Mathematical models of anti-angiogenic therapy and vessel normalisation



Lucy Hutchinson
Lincoln College
University of Oxford

A thesis submitted for the degree of
Doctor of Philosophy
Michaelmas 2016

For "Team Hutch": Mum, Dad, Phil, Anna, Granny, Dee, Danny and Christina.

Acknowledgments

I would like to thank my supervisors for guiding me through the last three years. Thank you to my Oxford supervisors: Helen Byrne, for being there through the ups and downs, for pushing me to reach my potential and making me believe that I could do it, Philip Maini for his endless positivity and his brilliant ideas and Eamonn Gaffney for all his support. I am also grateful to my supervisors at Roche for their perspective and support: to Alex Phipps who has provided me with opportunities far beyond what I could have hoped for and endless encouragement, to Ben Ribba for his professional and personal support throughout my time in Basel and to Jon Wagg for always being supportive of my work. I am grateful to Hans-Joachim Mueller, who provided us with preclinical data and whose biological explanations enabled the work in Chapter 3.

The Doctoral Training Centre, and especially SABS, has been such a valuable part of my DPhil experience. I thank the EPSRC and Hoffman-La Roche for their financial support that allowed me the opportunity to pursue this project. I am grateful to the members of the WCMB for their friendship and positivity.

Thank you to my friends at Lincoln College who made my last four years in Oxford so enjoyable and rewarding. I would like to thank my friends James, Claire and Anna who have provided me with so much joy and friendship for the last seven years, and Alisha, who has been by my side in times of difficulty and times of happiness, and who I can count on to support me, no matter what (even proof-reading my thesis!).

I am grateful to my brother, Phil, and my sister, Anna, who are my best friends and my inspiration. To my Granny and Dee, who are the perfect grandparents, and who always show me how proud they are. Of course, I am eternally grateful to my parents, Jackie and Ken, to whom I owe absolutely everything. Without their unwavering support I certainly would not be who or where I am now.

Finally, to Danny: my anchor and my role model, who makes me laugh every day, encourages me when the pressure rises, knows exactly when chocolate is the answer, and has made me happier than I have ever been.

Abstract

Angiogenesis is the formation of new blood vessels from existing ones, and is a key characteristic of tumour progression. The purpose of anti-angiogenic (AA) cancer therapies is to disrupt the tumour's blood supply in order to inhibit the delivery of oxygen and nutrients. However, such therapies have demonstrated limited benefit to cancer patients: although they delay tumour progression for some types of cancer, they do not consistently improve survival. Several preclinical experimental studies have reported that AA therapies lead to a period of vessel normalisation, during which vessels transition from the leaky, tortuous state that is typical of tumour vasculature to a more stable state where blood perfusion is increased. It has been suggested that normalisation is the reason why some AA therapies lack efficacy. In this thesis, we develop and study mathematical models of various aspects of angiogenesis and vessel normalisation, and we use our results to suggest effective AA therapy regimens.

Our first model represents the biochemical interactions and cellular dynamics involved in neovascularisation: we incorporate biological hypotheses to develop a spatially averaged ODE model of vessel formation, and we show that the model admits a number of vascular phenotypes characterised by their degrees of vessel normalisation. We showed that these phenotypes respond differently to different AA treatments. In our second model, we use preclinical tumour size data to develop and parametrise a mixed effects model of vascular tumour growth including vessel normalisation. We use our prediction about the timing of the transient normalisation window to further predict the potential benefits of combining chemotherapy and AA therapy. Lastly, we extend an existing PDE model of vascular tumour growth to incorporate AA therapy and vessel normalisation. We demonstrate that the oscillatory behaviour that arises in the spatially averaged version of the model induces spatial heterogeneity in the spatially extended version, and show that the vessel kill and normalisation parameters (among other parameters) can modulate tumour heterogeneity.

Contents

1 Introduction **1**

1.1 The biological basis of angiogenesis and vessel co-option 2

1.1.1 Vascular endothelial growth factor 3

1.1.2 The angiopoietins 4

1.1.3 Pericytes and platelet derived growth factor 5

1.1.4 Vessel normalisation 6

1.2 Anti-angiogenic therapies 9

1.2.1 Concomitant therapies 11

1.3 Mathematical models of angiogenesis 12

1.3.1 Continuum mathematical models of angiogenesis and vascular tumour growth 13

1.3.2 Discrete, hybrid and modular models of angiogenesis 18

1.3.3 Parameter estimation 19

1.3.4 Mixed effects modelling in quantitative systems pharmacology 21

1.3.5 Summary 25

1.4 Thesis structure 25

2 A non-spatial mathematical model of angiogenesis **27**

2.1 Introduction 27

2.2 Model development 29

2.2.1 Biochemical sub-models 31

2.2.2 Cell dynamics sub-model 37

2.2.3 Model summary 42

2.2.4 Initial conditions and numerical simulations of the full model 44

2.3 Simplified model 46

2.3.1 Steady state solutions 46

2.3.2 Linear stability analysis 49

2.4 Full model results 54

2.4.1 Corroboration of steady state results 54

2.4.2 Anti-angiogenic therapies 56

2.5 Discussion 63

3 Mixed effects modelling of preclinical tumour size data to identify transient dynamics 68
3.1 Introduction . . . 68
3.2 Preclinical data . . . 72
3.3 Model development . . . 73
3.3.1 Untreated tumours . . . 73
3.3.2 Tumours treated with anti-angiogenic therapy . . . 75
3.4 Non-linear mixed effects modelling and the SAEM algorithm . . . 78
3.4.1 SAEM algorithm . . . 79
3.4.2 Evaluation of mixed effects modelling techniques . . . 81
3.4.3 Summary of evaluation of mixed effects techniques for our dataset and model . . . 92
3.5 Model fitting results . . . 93
3.5.1 A simple vessel inhibition model does not capture non-monotonic dynamics . . . 93
3.5.2 Model selection: identifying the transient window of enhanced tumour growth . . . 95
3.5.3 Verification with histology data . . . 99
3.5.4 Theoretical administration of chemotherapy . . . 100
3.6 Discussion . . . 104

4 A non-spatial model of metastasis formation in a well vascularised region 108
4.1 Introduction . . . 108
4.2 Model development . . . 110
4.2.1 Control model and chemotherapy . . . 112
4.2.2 Anti-angiogenic therapy and normalisation . . . 114
4.2.3 Non-dimensionalisation . . . 116
4.2.4 Parameter values . . . 117
4.2.5 Quasi-steady state approximations . . . 117
4.2.6 Initial conditions . . . 120
4.3 Identification and characterisation of steady state solutions . . . 120
4.3.1 Anti-angiogenic therapy . . . 120
4.3.2 Summary of steady state and linear stability analysis . . . 126
4.4 Simulations of the ODE models . . . 128
4.4.1 Model comparison: quasi-steady state approximations . . . 128
4.4.2 Typical simulations . . . 129
4.5 Further simulations . . . 131
4.5.1 Non-oscillatory regimes . . . 131
4.5.2 Oscillatory regimes . . . 133

4.6 Discussion 135

5 A spatiotemporal model of vascular tumour growth 137
5.1 Introduction 137
5.2 Model development 139
5.2.1 Initial and boundary conditions 141
5.2.2 Numerical method 143
5.2.3 Parameter values 145
5.2.4 Typical model simulation 145
5.3 Oscillatory behaviour: $\lambda - \omega$ analysis 147
5.3.1 Model simplification 148
5.3.2 Results of $\lambda - \omega$ analysis 149
5.3.3 Simulations of regular and irregular travelling waves 150
5.4 Tumour spatial heterogeneity 156
5.5 Average tumour burden 161
5.6 Discussion 162

6 Spatially-averaged models that represent spatial systems: preliminary results 164
6.1 Introduction 164
6.2 Methods 165
6.3 Results 167
6.3.1 Parameter estimation 168
6.3.2 Model predictions 168
6.4 Discussion 171

7 Discussion 173
7.1 Summary and contextualisation 173
7.2 Future directions 178

A Parameter values for Chapter 2 181

B Individual fits for the no-normalisation model 189

C Model selection for Chapter 3 193

D Individual fits for the normalisation model 196

E $\lambda - \omega$ analysis for Chapter 5 200

List of abbreviations

AA	Anti-angiogenic
AIC	Akaike information criterion
Ang1	Angiopoietin 1
Ang2	Angiopoietin 2
BIC	Bayesian information criterion
CT	Computerised tomography
EC	Endothelial cell
FDA	Food and Drug Administration
IIV	Inter-individual variability
MRI	Magnetic resonance imaging
NLME	Non-linear mixed effects
ODE	Ordinary differential equation
PC	Pericyte cell
PDE	Partial differential equation
PDGF	Platelet derived growth factor
PET	Positron emission tomography
PKPD	Pharmacokinetic and pharmacodynamic
QSP	Quantitative systems pharmacology
r.s.e.	Relative standard error
SAEM	Stochastic approximation to expectation maximisation
TAF	Tumour angiogenic factor
VEGF	Vascular endothelial growth factor
VPC	Visual predictive check
WHO	World Health Organisation
WPB	Weibel Palade Body
WRES	Weighted residuals

Chapter 1

Introduction

The interactions between a tumour and its vasculature are key for the growth and spread of cancer cells. Vessels supply oxygen and nutrients that enable tumour cells to produce the energy they need to proliferate, to adapt to their surroundings and to evade immune suppression. Anti-cancer treatments that target tumour vasculature have shown promise in the clinic, and ongoing academic and pharmaceutical research aims to identify ways in which the process of tumour-induced blood vessel formation can be interrupted in order to reduce tumour burden and ultimately cure patients from cancer. Quantitative models that represent biological processes are increasingly used to elucidate mechanisms of action of drugs, and to identify new targets for therapy. This has led to the creation of the field of Quantitative Systems Pharmacology (QSP), wherein mathematical models and experimental data form the basis of studies of drug action in preclinical and clinical settings [165]. In this thesis we develop mathematical models that represent aspects of vascular tumour growth, with a focus on their application to the further development of anti-cancer therapies.

In this chapter, we begin by introducing the biological basis of blood vessel formation and vascular tumour growth, describing aspects that feature in our models in the later chapters. We then discuss existing therapies that target tumour vasculature, before reviewing the existing mathematical, computational and QSP models that have motivated our work. We conclude by describing the structure of

the remainder of the thesis.

1.1 The biological basis of angiogenesis and vessel co-option

Angiogenesis is the process by which new blood vessels are created from existing ones, in response to growth factors [75]. It is a key process for the growth and spread of cancer, and is described as one of Hanahan and Weinburg's original "Hallmarks of Cancer" [73]. Angiogenesis also plays a central role in wound healing and foetal development, and two diseases that affect the blood vessels in the eye (age-related macular degeneration and diabetic retinopathy), although in this thesis, we focus only on tumour angiogenesis [1, 5, 132].

When an avascular tumour reaches a size greater than approximately 1 millimetre in diameter, oxygen cannot reach some regions and oxygen-starved, or hypoxic, areas form within the tumour [129]. For further growth and progression, the tumour requires a sufficient blood supply from which it can obtain oxygen and nutrients. Angiogenesis is triggered by hypoxic signals from tumour cells, and maintained by a complex sequence of biochemical and physiological interactions. We focus on the biochemical basis for angiogenesis in our model in Chapter 2.

Folkman's seminal work on the therapeutic implications of tumour angiogenesis described the growth of neovasculature as "vigorous and continuous" [60, 158]. The most dominant pathway by which angiogenic blood vessel growth is stimulated is via the binding of vascular endothelial growth factor (VEGF) to its receptor, VEGFR2. In addition, there is a complex network of further biochemical interactions that also play a role in neovascularisation. Typically, angiogenic blood vessels grow rapidly and are tortuous, leaky and less effective than normal capillaries for delivering blood to the tumour. The consequences of tumour angiogenesis are improved oxygen and nutrient transport to the tumour (compared to the avascular case) and improved likelihood of metastasis, the spreading of cancer cells from a primary tumour to other parts of the body.

Tumours do not usually form in regions devoid of blood vessels; often tumour cells will proliferate in vascularised regions, where they have an immediately available source of oxygen and nutrients. The process by which tumour cells 'hijack' existing blood vessels is known as vessel co-option [50]. It has been reported that tumours that grow in an oxygen-sufficient environment can exert mechanical pressure on existing blood vessels, leading to their occlusion [82]. Furthermore, growth factors such as VEGF and angiopoietin-2 (Ang2), lead to vessel destabilisation, namely, the transition from stable, functioning vasculature to unstable and leaky vasculature [50, 82, 111]. Metastasis has been described as a process in which tumour cells aggregate in existing vessels and extravasate in a well oxygenated location, leading to the formation of secondary tumours [111]. Our models in Chapters 4-5 are motivated by vessel occlusion and vascular tumour growth in an oxygen-sufficient environment.

There have been many approaches to identify the most effective way to interrupt the tumour's blood supply in order to deprive it of essential oxygen and nutrients, and thereby to inhibit its growth. Antibodies that block VEGF and VEGFR2 lead to a decrease in total blood vessel density in the tumour, as expected, and have also revealed another layer of biological complexity known as vessel normalisation [53, 58, 176]. The structure of new vessels determines their ability to deliver oxygen, and the vessels that remain after VEGF or VEGFR2 therapy are less tortuous, less leaky, and less branched, resulting in improved perfusion compared to the pre-treatment vasculature [70]. The process by which vessels become more like the normal capillaries in the body is known as vessel normalisation and this must be taken into account when considering anti-angiogenic therapy [95]. Vessel normalisation features heavily in our mathematical models of vascular tumour growth and we investigate its role in determining treatment outcome in Chapters 3-5.

1.1.1 Vascular endothelial growth factor

VEGF is considered the key driver of angiogenesis. The ligand was first identified as a promoter of angiogenesis by Leung *et al.* [102] and its binding properties were characterised by Cunningham *et al.* [42]. VEGF is produced by tumour cells in

response to hypoxia in many different types of cancer [45, 81]. The VEGFA family encompasses four isoforms, which differ in the number of amino acids [56, 57]. The most abundant isoform of VEGFA, VEGFA-165, binds to the VEGFR2 receptor expressed by endothelial cells (ECs), stimulating a cascade of intracellular signalling events to trigger EC proliferation. This leads to the formation of capillary sprouts [88]. The cells at the leading edge of the sprout, known as tip cells, sense gradients of VEGF concentration and direct the growth of vessels towards high concentrations of VEGF [57]. It has been suggested that filopodia, finger-like projections on endothelial tip cells, can detect a gradient of VEGF, and therefore these cells guide the newly forming vessel towards the VEGF source. The rate of proliferation of the cells that constitute newly formed vessels may be determined by the local concentration of VEGF [68]. New sprouts are initiated along vessel stalks, leading to vessel branching and ultimately, a complex and tortuous vascular network is created [152]. While VEGF is the most heavily studied ligand involved in tumour angiogenesis, several other important ligands are involved.

1.1.2 The angiopoietins

The Tie2 receptor, which is expressed by ECs, binds two ligands: the angiopoietins, Ang1 and Ang2 [132]. There are different theories about the functions of Ang1 and Ang2. Ang1 has been associated with vessel maturation and normalisation, whereas Ang2 is thought to be an antagonist of Ang1. It has been reported that Ang2 does not induce signalling, but rather competes with Ang1 for binding to the Tie2 receptor and thus prevents maturation and promotes proliferation [79, 114, 188]. Other studies suggest that Ang2 activates the Tie2 receptor to promote EC proliferation [44]. The balance between Ang1 and Ang2 is considered to be a key factor in regulating the maturity of neovasculature [44, 63, 79].

Pericytes are smooth muscle cells that attach to the outside of blood vessels in order to increase vessel stability and support blood flow. Ang1 is highly expressed by pericyte cells (PCs) but not endothelial cells [166, 167]. An *in-vitro* study reported that addition of Ang1 to newly formed vascular structures led to cord-like vessels

with tight EC-EC adhesions. Inhibition of Ang1 abrogated EC elongation, leading to gaps characteristic of leaky vasculature [12, 167].

Ang2 synthesis occurs in ECs and it is stored in intracellular organelles known as Weibel Palade Bodies (WPBs). Exocytosis of Ang2 from WPBs is rapid and may be stimulated by histamine, thrombin or VEGF [59, 119]. The WPB stores rapidly refill after depletion and Ang2 has a short half-life once released into the extracellular environment [153]. It has been reported that Ang2 can limit the effectiveness of VEGF inhibitors in animal studies where tumour cells derived from human samples are inserted into a model organism (usually a mouse), known as xenograft studies. Inhibition of both Ang2 and VEGF has been observed to induce a more pronounced reduction in vascular volume and tumour burden than single-agent treatments [44, 96, 169]. This suggests that Ang2 plays a key role in stimulating endothelial cell proliferation, and in promoting an immature phenotype.

1.1.3 Pericytes and platelet derived growth factor

Pericytes are present throughout the body and provide different levels of vessel coverage, with the highest coverage observed in the central nervous system [11]. PCs adhere to the vessel wall by using finger-like projections to cling to ECs [65]. When gaps in a leaky vasculature have been plugged by PC attachment, a pressure gradient can be established across the newly formed blood vessels, allowing blood to flow [172].

The recruitment of PCs to neovasculature is regulated by platelet-derived growth factor (PDGF), which is expressed by ECs and binds to the PDGFR-β receptor expressed by PCs, stimulating PC proliferation and migration towards neovasculature [65, 108]. In particular, it has been suggested that migrating tip cells produce PDGF [11]. Furthermore, neutralisation of PDGF inhibits the recruitment of PCs [11], and combined VEGF and PDGF inhibition has been reported to lead to tumour blood vessel regression in animal studies [54].

1.1.4 Vessel normalisation

Anti-angiogenic therapy was first developed with the aim of starving the tumour by cutting off its supply of oxygen and nutrients. In fact, anti-angiogenic (AA) therapies (reviewed in more detail in Section 1.2) have not been shown to increase overall survival in the clinic when administered alone [6]. Instead, AA therapies have demonstrated prolonged survival when combined with other cancer treatments, such as chemotherapy [58]. Cytotoxic chemotherapy induces death in cancer cells that are normoxic, i.e. that have enough oxygen to proliferate. Since anti-angiogenic therapy, in theory, reduces the oxygen supply to the tumour, the combined benefit of chemotherapy and AA therapy observed in the clinic seems paradoxical. It was first suggested by Jain in 2001 that the apparent contradiction can be explained by the concept of vessel normalisation [94]. Vessel normalisation has now been widely studied in the context of anti-angiogenic therapy.

Vessel normalisation is the process by which angiogenic blood vessels adapt from their typical leaky, highly branched, tortuous phenotype to a phenotype similar to that of other vessels in the body: less branched, straighter and more robust. Moreover, normalised vessels are able to deliver oxygen, nutrients and cytotoxic molecules to the tumour. It has been widely reported that vessel normalisation occurs during anti-angiogenic therapy [48, 49, 77, 185]. Jain *et al.* propose that the increased delivery of cytotoxic chemotherapy and oxygen could be responsible for the success of combined AA therapy and chemotherapy [95].

There are several morphological and functional aspects that are characteristic of normalised vessels. In the previous subsection, we mentioned that the ligands Ang1, Ang2 and PDGF modulate the maturity and PC coverage of vessels. Here, we elaborate on some of the features that characterise normalised vessels.

- **Regularity of vessels**: Angiogenic blood vessels are typically tortuous and disorganised, whereas it has been shown that during anti-angiogenic therapy, vessels exhibit a more regular structure with fewer branching points, where vessels are less tortuous [49, 67].

- **Pericyte coverage:** Typically, tumour vasculature has a much lower PC coverage than "normal" blood vessels throughout the body. Several mouse xenograft studies have shown that PC coverage is enhanced during AA therapy [48, 185], and this results in vasculature that is more robust, less leaky, and therefore more capable of transporting blood.

- **Hyperpermeability:** The "leakiness" of angiogenic blood vessels, usually due to poor EC-EC adhesion and lack of PC coverage, means that a pressure gradient cannot be established across vessel segments. This hinders blood flow through vessels that exhibit large gaps between adjacent ECs [77].

- **Vessel diameter:** The width of intratumoural angiogenic blood vessels tends to be larger than normal capillaries and also extremely variable. Detailed images of tumour vasculature in [49] reveal that the diameter of tumour blood vessels in animals who had been treated with an anti-VEGF antibody was significantly smaller than for those who had not received an antibody.

Our list of factors that contribute to vessel normalisation is not exhaustive, but it includes the characteristics that will be most important in our study of angiogenesis and vessel normalisation. Further reviews of vessel normalisation in angiogenesis can be found in [70] and [95]. To date most evidence of vessel normalisation has been obtained from *in-vivo* studies in mice. It was shown in [47] that 24 hours after administration of an anti-VEGF antibody, the microvessel density in a neuroblastoma xenograft model had reduced, but the absolute number of pericytes covering the vessels was conserved, resulting in an effective increase in the fractional coverage of vessels by pericyte cells. Dickson *et al.* also showed that the permeability of vessels in treated tumours was reduced compared to pre-treatment measurements, resulting in increased perfusion, and this led to enhanced delivery of chemotherapy when administered within the transient period in which vessels appear to be normalised, compared to when chemotherapy was administered outside of this period. These findings are in agreement with other experimental studies [48, 120, 173].

There is limited evidence of vessel normalisation from clinical studies, and this

is likely to be due to the practical challenges associated with measuring normalisation parameters such as PC coverage or perfusion in patients. PC coverage was enhanced in a small sample of patients treated with an anti-VEGF antibody, as reported in [182], where several features of vessel normalisation were calculated from positron emission tomography (PET) and computerised tomography (CT) scans of tumours before and during therapy. Furthermore, in a small sample of glioblastoma multiforme patients treated with a VEGF receptor inhibitor, vessel size was reduced transiently during AA therapy and hyperpermeability was reduced for at least 112 days after the start of AA therapy [18], where magnetic resonance imaging (MRI) images were analysed to determine the level of vessel permeability. Results of a clinical study presented by Van der Veldt *et al.* suggested that AA therapy inhibits the delivery of a small cytotoxic molecule to the tumour [175], suggesting that perfusion is reduced. The authors showed that the influx rate of radiolabelled cytotoxic molecules decreased with AA treatment compared to chemotherapy alone for patients with non-small cell lung cancer. These controversial results that anti-angiogenic therapy can actually increase the delivery of blood to the tumour highlight the need for further investigation into vessel normalisation in a clinical setting.

It has been proposed that vessel normalisation is a transient process that begins shortly after the start of anti-angiogenic therapy and lasts a few days [48, 95, 185]. Furthermore, it has been shown in a preclinical (*in-vivo* mouse) model that the efficacy of chemotherapy is enhanced when administered within the normalisation window [185]. However, another preclinical study [47] suggests that some vessel normalisation parameters, such as permeability, are transiently changed, whereas other parameters, such as PC coverage, are permanently maintained at the normalised level. The time scale of normalisation cannot easily be determined for clinical studies, since normalisation measurements are typically taken at one time point following anti-angiogenic therapy [18, 182].

1.2 Anti-angiogenic therapies

Anti-angiogenic therapies are designed to reduce vessel density in order to inhibit the delivery of nutrients and oxygen to the tumour. A multitude of strategies to disrupt angiogenesis are currently in development. In this section we will introduce some existing AA therapies, along with their mechanisms of action and approval status.

The first FDA approved anti-angiogenic drug was the anti-VEGF monoclonal antibody, bevacizumab (Avastin, Genentech), as an addition to chemotherapy in most cases [6, 56, 58]. Bevacizumab neutralises VEGF-A molecules, rendering them unable to bind to their receptor, and, as a result, endothelial cell proliferation is inhibited. The antibody was combined with cytotoxic chemotherapy for treatment of first line metastatic colorectal cancer and non-small cell lung cancer with the rationale that dual targeting of endothelial cells and tumour cells would lead to a synergistic anti-tumour effect. It was shown in a Phase III clinical trial in 2004 that bevacizumab combined with the standard-of-care chemotherapy led to increased overall survival, compared to chemotherapy alone, for metastatic colorectal cancer. In addition to reducing the tumour's associated vessel density, it has also been observed in preclinical studies that anti-VEGF treatment normalises the vasculature, enhancing the delivery of small-molecule chemotherapy [95, 182]. Currently, bevacizumab has been approved to treat, in combination with chemotherapy: platinum-resistant recurrent epithelial ovarian, fallopian tube, or primary peritoneal cancer, metastatic cervical cancer, metastatic colorectal cancer, metastatic renal-cell carcinoma; and as a monotherapy: relapsed glioblastoma multiforme (Source: *www.cancer.gov/about-cancer/treatment/drugs/fda-bevacizumab*).

Other therapies also disrupt the VEGF-VEGFR2 pathway, mainly via receptor tyrosine kinase inhibitors. Sorafenib (Nexavar, Bayer Healthcare Pharmaceuticals Inc.) has been reported to inhibit VEGFR2 signalling, blocking endothelial cell proliferation [181]. This small molecule has been approved as a monotherapy for the treatment of hepatocellular carcinoma, renal cell carcinoma and thyroid cancer

(Source:*www.cancer.gov/about-cancer/treatment/drugs/fda-sorafenib-tosylate*). A multiple receptor tyrosine kinase inhibitor, sunitinib (Sutent, Pfizer), targets VEGFR2 and PDGFR-β, among several others, and has demonstrated clinical efficacy in improving progression-free-survival [36, 71, 148]. Sunitinib has been approved for treatment of pancreatic neuroendocrine tumours, kidney cancer and gastrointestinal stromal tumour, all as a monotherapy (Source: *www.cancer.gov/about-cancer/treatment/drugs/fda-sunitinib-malate*). Furthermore, a preclinical study reported that sunitinib induces transient vessel normalisation in mice [118].

Drugs that target the angiopoietins have not yet been approved for use in humans. Trebaninib (Amgen), an inhibitor of Ang1 and Ang2 binding, showed a small increase in progression-free survival but failed to show a statistically significant increase in overall survival for ovarian cancer patients when used in combination with chemotherapy [125].

Targeting of individual angiogenic factors or receptors has led to modest clinical benefit. Because of the multitude of angiogenic ligands and receptors, development of dual inhibitory molecules may offer added benefit. A bi-specific antibody that neutralises VEGF and Ang2 simultaneously is currently in Phase II trials for colorectal cancer as a monotherapy. The antibody, known in its early days as A2V or CrossMab, and now known as vanucizumab, was developed by Roche and has two different arms: one that is specific to VEGF, based on bevacizumab, and one that is specific to Ang2, based on an Ang2 specific antibody, LC06. When administered to mice expressing KPL-4 (breast cancer) or Colo205 (colon cancer) tumours, the antibody led to both tumour growth inhibition and a more mature vessel architecture [39, 96]. These results suggest that vessel normalisation is heightened following treatment with vanucizumab. Interestingly, there was no marked reduction in microvessel density after treatment with vanucizumab, and pericyte coverage was unchanged after treatment with vanucizumab, bevacizumab or LC06 compared to the control [14]. Both vanucizumab and bevacizumab will form the basis of our modelling studies in Chapters 2 and 3.

1.2.1 Concomitant therapies

Although the anti-VEGF antibody, bevacizumab, has been approved to treat several different types of cancer, it has not been approved as a monotherapy except in the case of relapsed glioblastoma multiforme; it is administered with chemotherapy for all its other approvals. The most frequently reported hypothesis for why anti-VEGF treatment works most effectively in combination with chemotherapy is that its normalising effects enhance chemotherapy delivery [56].

In recent years, a new type of anti-cancer therapy that harnesses a patient's immune system in order to kill the tumour "from within" has become the focus of much oncology research in pharmaceutical companies. So-called *immunotherapy* encompasses numerous new treatments that target pathways involved in the body's immune response to tumours [33]. Since several of the growth factors involved in angiogenesis also play a role in the immune response to tumours, there have been multiple studies where immunotherapies are combined with anti-angiogenic therapies [64, 84, 85, 121, 177]. Huang *et al.* showed that normalising doses of bevacizumab enhanced the efficacy of immunotherapeutic compounds by re-programming immune cells known as macrophages to attack tumour cells [85], or by enhancing the trafficking of cytotoxic T-cells to the tumour microenvironment [84].

The transient window of vessel normalisation that occurs during anti-angiogenic therapy provides a time period during which tumour oxygenation is improved [48, 185]. During this period, the efficacy of radiotherapy may also be enhanced due to improved oxygen uptake by tumour cells. After the window ends, the blood vessels return to their disorganised state. In general, radiotherapy preferentially kills tumour cells that have a good supply of oxygen [76]. The combination of anti-angiogenic therapy with radiotherapy has been shown to be efficacious in multiple studies [41, 43, 66] (among others, which are reviewed in [97]). For rectal cancer patients treated with bevacizumab and cytotoxic therapy prior to radiotherapy, a complete response was observed in a small sub-set of patients in a Phase I study [43]. The timing of radiotherapy with respect to the normalisation window is likely to be crucial for dose scheduling, but there is currently a lack of clinical evidence or

biomarkers that indicate when the normalisation window occurs for different cancer types in humans.

1.3 Mathematical models of angiogenesis

The complex interactions involved in angiogenesis make experimental studies expensive, time consuming and limited in scope. Mathematical models that reproduce selected features of angiogenesis and vascular tumour growth can provide mechanistic insight with fewer constraints. In addition to complementing existing experimental studies, mathematical and computational models of angiogenesis can be used to guide experiments by suggesting hypotheses based on modelling observations, such as the effectiveness of new anti-angiogenic drug targets, combination therapies or dosing regimens. Mathematical and QSP models are increasingly prevalent in the pharmaceutical industry for dose selection and to gain insight into mechanisms of action of novel therapies.

Collaboration with experimentalists, together with a thorough understanding of the relevant experimental literature, are important when developing mathematical and QSP models. In order to build realistic models, a detailed understanding of the appropriate biological processes is vital. Data from experiments can help to parametrise and validate models. In this section we highlight where biological data have been used to develop, validate and parametrise mathematical models of angiogenesis and vascular tumour growth.

There is a diverse range of mathematical and computational models of angiogenesis, and existing models cover several spatial and temporal scales, focussing on various aspects of angiogenesis. In this section, we focus on continuous mathematical models of angiogenesis and vascular tumour growth, since these have formed the basis for our models of angiogenesis. We include a summary of the discrete, hybrid and multi-scale, 'modular' models for completeness. Data-driven QSP models place emphasis on drug effect, usually focussing on measurable variables such as drug concentration, tumour size and vessel density. For this, we introduce mixed

effects modelling and review the literature surrounding mixed effects modelling of tumour growth and angiogenesis. Additional information about mathematical and computational models of angiogenesis can be found in the following excellent review articles [116, 137, 147, 154].

1.3.1 Continuum mathematical models of angiogenesis and vascular tumour growth

Continuum models of angiogenesis usually comprise a system of deterministic ordinary or partial differential equations (ODEs or PDEs) that are solved numerically and/or subjected to mathematical analysis. The equations represent processes associated with vessel growth such as biochemical interactions, vessel migration, new vessel formation ("budding"), normalisation or maturation and occlusion, among others. In this subsection, we introduce and describe some of the key continuum models of angiogenesis.

Simple models of vessel growth

Some early mathematical models of angiogenesis focus on the migration of blood vessels towards high concentrations of a growth factor [8, 15, 130]. These models feature chemotaxis, the migration of cells in response to spatial gradients in a diffusible chemical, or haptotaxis, movement in response to spatial gradients in adhesivity. A popular experimental assay for studying angiogenesis is the corneal pocket assay. In this assay, images are taken of blood vessels in the transparent tissue of the cornea as they grow and migrate towards an implanted VEGF source. The cornea pocket assay is a useful source of longitudinal vessel density data. The mathematical models presented in [8, 15, 130] consist of two to three coupled PDEs in time and one spatial dimension, describing the evolution of endothelial cells, angiogenic factors and fibronectin.

The process of capillary bud formation is modelled by Orme and Chaplain [130], where two PDEs represent the density of ECs and the local concentration

of fibronectin in one spatial dimension, respectively. The authors assume that fibronectin is secreted by ECs and that ECs proliferate and migrate towards high concentrations of fibronectin. Through this process, it is suggested that ECs in parent vessels aggregate in the existing vessel, resulting in the formation of a capillary sprout. A haptotaxis model in the same study describes stalk cell proliferation and migration up fibronectin gradients. Haptotaxis is also considered in the model presented by Anderson and Chaplain [8], where the relative contributions of haptotaxis and chemotaxis to vessel proliferation and migration are considered. By treating haptotactic migration, chemotactic migration and joint haptotactic and chemotactic migration cases separately, the authors qualitatively compare their simulation results with experimental data to conclude that the most realistic vessel growth model includes both chemotaxis and haptotaxis. In the PDE model presented by Balding and McElwain [15], chemotaxis, branching and anastomosis (loop formation) are modelled by introducing terms that account for the migration of vessels, production of tip cells for branching and loss of tip cells for anastomosis. The numerical simulations reproduce reasonable agreement with experimental data for the lengths of vessels in the cornea pocket assay. The models in [8, 15, 130] have formed the basis of many other models of angiogenesis, including those described in the remainder of this section.

Biochemical interactions and multi-scale models

Biochemical interactions, which typically act on a faster time-scale than processes such as vessel cell proliferation, add biological detail to mathematical models of angiogenesis. Models presented in [91, 103, 104, 142, 143] include the binding of a "tumour angiogenic factor" (TAF) to its receptor. A detailed treatment of VEGF binding is presented in [113], where the competition between VEGF and placental growth factor for binding to VEGFR receptors expressed by ECs is considered. Since ligand-receptor binding happens on a faster time-scale than cellular dynamics, receptor kinetics are often assumed to be in a quasi-steady state in models that consider processes on multiple time-scales. For example, the binding of TAFs to

their receptors is hypothesised to be in a quasi-steady state in [103, 104, 142].

Although the majority of mathematical models of angiogenesis focus on the role of VEGF, several models account for other biochemical interactions, such as those between the angiopoietins and the Tie2 receptor [21, 142, 143, 191], or the PDGF-PDGFR-β signalling axis that leads to the recruitment of pericytes [146, 191]. The balance between the angiopoietins, Ang1 and Ang2, regulates the maturity of neovasculature [114]. The model presented by Plank *et al.* [143] distinguishes between mature and immature vessel phenotypes, including the roles of Ang1 and Ang2 for regulating vessel maturity: PDEs represent the spatio-temporal evolution of the concentrations of Ang1 and Ang2. The authors assume that when the ratio of Ang1 to Ang2 exceeds a given threshold, vessels increase in maturity: similar assumptions are made in the models presented in [21, 191].

We describe models that account for processes on more than one length scale as multi-scale. The multi-scale models presented by Billy *et al.* [21] and Zheng *et al.* [191] comprise systems of PDEs that couple biochemical interactions with cellular dynamics. In [21], the authors account for angiopoietin-mediated blood vessel maturation and VEGF-driven EC proliferation. The authors model the oxygen concentration throughout the tumour, and simulate endostatin-based treatment administration. Several approaches to anti-angiogenic treatment are also investigated in [191], where oxygen concentration and tumour cells are not explicitly accounted for. The authors solve a system of PDEs that represent the biochemical interactions involved in angiogenesis in one spatial dimension. The PDE model is coupled to a biomechanical model that accounts for the mechanical forces experienced by the newly formed vasculature. Ang2, VEGF and PDGFR-β inhibition are simulated in order to make predictions comparing different angiogenic therapy targets. We discuss and adapt the model presented in [191] in more detail in Chapter 2.

Models of vascular tumour growth

Continuous models of vascular tumour growth are presented in [24, 80, 105, 161]. The model presented by Breward *et al.* [24] considers vessel growth and tumour

growth, accounting for biomechanical stress exerted on vessels by tumour cells: vessel occlusion is assumed to be an increasing, saturating function of the ratio of tumour cell density to vessel density. The same approach for vessel occlusion is incorporated in the model presented by Stamper *et al.* [161], where the authors extend the model to include oxygen concentration and investigate the effect of chemotherapy on vascular tumour growth. Oscillatory dynamics for tumour cell density and vessel density are observed when the vessel occlusion rate is large [161]. The spatial heterogeneity that arises from such oscillatory behaviour is assumed to contribute to the irregular blood flow that has been observed in tumours, and Stamper *et al.* demonstrate that different tumour growth scenarios (oscillatory vs. non-oscillatory) may respond differently to chemotherapy treatment. Our work in Chapters 4 and 5 extends the model presented in [161] to include anti-angiogenic therapy.

The model presented by Lignet *et al.* [105] includes tumour cells, vessels, oxygen and VEGF concentration. The authors simulate chemotherapy and anti-angiogenic therapy, and show how chemotherapy may be delivered more effectively when administered concomitantly with anti-angiogenic therapy. Chemotherapy and anti-angiogenic therapy are also simulated in the reaction-diffusion type PDE model presented by Hinow *et al.* [80], where subsets of tumour cells (hypoxic, apoptotic, and normoxic) are considered. The authors show that under anti-angiogenic therapy, the localisation of endothelial cells changes with respect to the hypoxic tumour cells, leading to a more dispersed vasculature. Chemotherapy simulations lead to an increased tumour mass for some parameter regimes, and a decreased post-treatment mass for other parameter regimes. The authors do not simulate concomitant chemotherapy and anti-angiogenic therapy [80].

Normalisation

As we discussed in Section 1.1.4, vessel normalisation is an important part of neovascularisation and cancer treatment, although the precise details of how normalisation is initiated and how long it lasts are controversial [95, 175]. Several models have taken into account aspects of normalisation such as the Ang1-Ang2 medi-

ated maturity and PC-EC interactions [21, 105, 143, 146, 191]. In the multi-scale model of vessel normalisation and vascular tumour growth presented by Lignet *et al.* [105], the authors compare the anti-tumour effects of anti-angiogenic drugs, cytotoxic chemotherapy and concomitant anti-angiogenic therapy and chemotherapy. The authors assume that the delivery of chemotherapy is enhanced by the normalisation process that occurs under anti-angiogenic therapy. However, according to this model, tumours treated with chemotherapy are more likely to be inhibited than those treated with concomitant therapy, since anti-angiogenic therapy also leads to increased oxygen and nutrient delivery during the normalisation period, and the enhancement of tumour growth outweighs the anti-tumour effects of anti-angiogenic therapy and chemotherapy.

Zheng *et al.* [191] include vessel maturity and PC coverage as contributors to vessel normalisation. The authors show that normalisation may be explained on a biochemical basis: model simulations show that VEGF inhibition leads to an increase in PC density from day 7 after VEGF inhibition until day 10. These results are reminiscent of the normalisation window proposed by Winkler *et al.* [185]. Our work in Chapter 2 builds on the model presented in [191], where we account for vessel maturity and pericyte coverage of vessels.

Steady state and linear stability analyses

For ODE and PDE models, steady state and linear stability analyses are often performed in order to explain observed model behaviours, and to predict outcomes in clinical or preclinical settings. Simple models with a small number of equations lend themselves to such analyses [2, 130, 161], whereas more complex models are often analytically intractable. Analysis of the models presented in [130] and [161] reveals oscillatory dynamics in the tumour or vessel cell densities, and a detailed description of Hopf bifurcations in alternative models of angiogenesis is presented in [2]. In cases where model parameters are not well defined in the experimental literature, steady state and linear stability analyses can be used to determine which parameters drive the long term behaviour in the model. In this thesis, we identify and characterise

the steady states of our models where possible, drawing comparisons between our findings for the long term model behaviours and corresponding biological outcomes.

1.3.2 Discrete, hybrid and modular models of angiogenesis

Discrete, hybrid or modular features are appropriate in models that emphasise the spatial structure of vessels. Discrete models often discretise a spatial domain by a lattice and adopt a rule-based [109, 134, 138, 139] or equation-based [90, 104, 142] approach to determine the behaviour of species on that lattice. Models of this type are also referred to as "agent-based". In hybrid models, discrete and continuous components are coupled in order to exploit their respective benefits, and in modular models, complex computational sub-models are integrated for modelling systems in one, two or three spatial dimensions. Discrete, hybrid and modular models of angiogenesis typically generate detailed information about the morphology of the vessel networks, such as branching points and anastomosis, and the results are usually compared to experimental data.

In models presented by Plank and Sleeman [142] and Levine *et al.* [104], endothelial cells migrate towards a source of VEGF via a biased random walk and are compared with experimental results [142].

A stochastic differential equation model is presented by Stokes and Lauffenburger [164], where the processes of budding, sprouting, branching and proliferation are taken into account. In this model, endothelial cells move on a two-dimensional domain, forming vessels and migrating via chemotaxis towards a growth factor source. Tip cells and stalk cells are treated separately, and the average cell density in each sprout determines whether the ECs in that sprout can continue to proliferate. The model simulation results show good agreement with experimental data for a large value of the migration coefficient for tip cells.

Multi-scale, cell-based models are presented in [19, 90, 134, 138]. In these models the behaviour of individual cells is regulated by stimuli such as growth factors. In

the model proposed by Jackson and Zheng [90], spatiotemporal profiles for VEGF, Ang1 and Ang2 are determined by solving a system of PDEs, whereas for the model proposed by Peirce *et al.* [138], rules determine the VEGF concentration at any given space and time. Experimental data from *in-vitro* and *in-vivo* assays were leveraged for model validation in [19, 90, 138], and close qualitative agreement between the appearance of simulated vessels and the experimental data was achieved.

Clinically relevant models of angiogenesis that account for mechanical aspects of vessel growth and vessel architecture are presented in [16, 134, 180]. Owen *et al.* [134] present a two-dimensional model of vascular tumour growth that accounts for blood flow, local oxygen concentration, pressure gradients along vessels and VEGF production, among other aspects of vascular tumour growth. Simulation results comprise a detailed vessel network and a realistic tumour growth profile, although the results are not compared directly to experimental data. Similar two-dimensional multi-scale models of vascular tumour growth are presented in [16, 180].

The model presented in [134] is extended from two to three dimensions by Perfahl *et al.* [139]. In the extended model, the authors incorporate anti-angiogenic therapy implicitly, by simulating an oxygen deprived environment. Data from a real vascular structure was used as an initial condition for the vasculature in the computational model. Conditions were defined under which this model predicts that the tumour will be completely eliminated. Steps are taken towards model validation, using data from multiphoton fluorescence microscopy experiments, which capture images of the three-dimensional structure of vessels through a dorsal window in mice. Other examples of three-dimensional computational models of vascular tumour growth are presented in the recent multi-scale modular mathematical models from Xu *et al.* [186] and Cai *et al.* [28].

1.3.3 Parameter estimation

The models of angiogenesis and vascular tumour growth described above generally encompass several biological processes that are governed by a set of parameters. Model parameters may correspond to biologically "measurable" processes, such as

the binding rates of ligands *in-vitro*, or to phenomenological processes, such as the probability of branching or the rate of maturation. In general, parameters that characterise angiogenesis and vascular tumour growth are difficult to estimate from clinical or preclinical data. Most mathematical models of angiogenesis rely on parameter values that were estimated from different experimental assays, different cell lines and different species [8, 15, 130, 134, 161, 191].

In order to investigate which parameters play an important role in determining model behaviour, sensitivity analysis may be performed. Local sensitivity analyses vary model parameters one-by-one and calculate the change in a given model output in response to changes in the model parameters [19, 191]. This method can be used to identify which parameters have the greatest effect on a particular model output when all other model parameters are held constant. Since it is not computationally expensive, this method is useful for models with large numbers of parameters, such as those presented in [19, 109, 191]. However, local sensitivity analyses are based on the assumption that the default parameter set is similar to the "true" parameter set for the biological system.

Global sensitivity analysis often involves Latin Hypercube sampling to sample the full parameter space and identifying correlations between parameters and model outputs. The method described in [117] for sampling the full parameter space of an ODE model involves simulating the model many times and ranking parameters based on the extent to which they contribute to model outputs. This method has been implemented for the mathematical models of the immune system presented in [74, 89]. For models that employ few parameters, the method is more reliable for identifying correlations between parameters and model outputs, however, incorrect results may be obtained if the subset of parameter space is incorrect, or if the effective averaging obscures important features. For larger parameter spaces the ability to fully search the parameter space becomes infeasible.

1.3.4 Mixed effects modelling in quantitative systems pharmacology

The continuous and discrete models described above are primarily mechanistic: qualitative and quantitative observations of biological systems have motivated models that capture biological processes in varying levels of detail. In many cases, data that are detailed enough to suggest that such models produce realistic biologically relevant results are not yet available, or are infeasible to collect with current technology. Data-driven modelling constitutes an alternative approach: where experimental observations are available, mathematical models are based on known biological mechanisms, and model selection is used to choose the model that best fits the experimental data. Model selection may uncover biological mechanisms and/or identify the factors that contribute most to variability within a population of patients or subjects. Data-driven approaches are often used in pharmaceutical research, and this field is known as QSP [165, 174].

Mixed effects modelling leverages data from a population of subjects in order to parametrise a mathematical model. Mixed effects models account for the population behaviour, that is proposed to represent an "average" subject, and the deviation of individual subjects from the average behaviour is known as inter-individual variability (IIV). The parameters of the mathematical model that describe data from individual subjects are expected to be sampled from population distributions. The terminology "mixed-effects" arises since the population parameter distributions are known as the "fixed" effect, and the difference between the population means and the parameters that best describe the data from an individual is known as the "random" effect. The random effect arises from biological variability between subjects [101, 165, 174].

In the context of longitudinal disease modelling, mixed effects models comprise a set of algebraic or differential equations that describe a particular aspect of a biological process. The development of the mathematical model depends heavily on the type, and quantity, of data available for model fitting. For example, the number

of dependent variables introduced to a mathematical model will depend on available experimental measurements [101].

Implementation and parametrisation of mixed effects models is usually undertaken using purpose-built software such as NONMEM (Icon plc.) or Monolix (Lixoft) which we use in Chapter 3. Algorithms implemented via these software tools include the stochastic approximation to expectation maximisation (SAEM) algorithm that is implemented in Monolix. The SAEM algorithm is based on maximising the likelihood that a parameter set describes the observed data [99]. In Chapter 3 we describe the SAEM algorithm in detail.

In order to select the model that best describes the experimental data, several metrics for comparison are used. Information criteria such as the Bayesian Information Criterion (BIC), or the Akaike Information Criterion (AIC) provide a numerical value that can be used to directly compare how closely the model fits the experimental data, incorporating a penalty for the number of model parameters to prevent selection of models that have been "over-fit" [145]. Diagnostic plots can also be used to compare how well the model predictions agree with the observed data. Visual predictive checks (VPCs) typically show a direct comparison between the 10th, 50th and 90th percentiles of experimental observations and model predictions. Residuals plots show the difference between of the observed data and the simulated data at the time points included in the dataset [83].

Mixed effects modelling has been used primarily for pharmacometric models, such as pharmacokinetic/pharmacodynamic (PKPD) models whose purpose is to model drug uptake, time course and the magnitude of the drug effect. Reviews of the history of mixed effects modelling in the context of PKPD can be found in [140, 141]. In the remainder of this subsection, we review mixed effects models of tumour growth and vascular tumour growth that motivate our work in Chapter 3.

Mixed effects models of tumour growth

Tumour size can be considered in terms of diameter or volume, depending on the method of tumour measurement. In clinical studies, tumour size is recorded as the

'sum of longest diameters' of the primary lesions obtained via medical imaging such as CT or MRI [22, 131], in accordance with the RECIST criteria: the guidelines by which response to treatment should be measured according to the World Health Organisation (WHO). In preclinical studies of tumour growth in mice, the tumour volume is usually estimated using the formula:

$$\text{Volume} = \frac{\text{length} \times \text{width}^2}{2},$$

where the length and width of the tumour are measured using callipers. The type of tumour size data, species and tumour cell line determine the type of tumour growth model that best describes the data. Tumour growth laws such as exponential growth, Gompertzian growth and logistic growth were surveyed by Gerlee *et al.* [69].

Preclinical xenograft experiments typically provide more data per subject than clinical studies because xenografted tumours in mice can be measured regularly with callipers, whereas human tumours are typically imaged at time points that may be weeks apart. However, due to ethical considerations, the number of mice used for each study is often much smaller than the number of humans enrolled in a clinical study. Mixed effects models developed for mouse xenograft data are presented in [17, 27, 133, 151, 159, 184]. The model developed by Simeoni *et al.* [159] and extended by Rocchetti *et al.* [151] describes tumour growth as a two-stage process in which exponential growth is observed before a certain timepoint, and linear growth is observed thereafter. The same two-stage model is also used by Bueno *et al.* [27]. Bastogne *et al.* [17] assume that the effective tumour diameter grows linearly, where effective tumour diameter is estimated by assuming

$$\text{tumour volume} = \frac{\text{length} \times \text{width}^2}{2},$$

and therefore that

$$\text{effective tumour diameter} = \sqrt[3]{\frac{3 \times \text{length} \times \text{width}^2}{\pi}}.$$

Models based on clinical data are presented in [37, 62, 133, 150, 162], and among these models, tumour growth (sum of longest diameters) for the control group is modelled by a linear function [162], an exponential function [37], a Gompertz function [62] and a logistic growth function [150].

Treatment effect is incorporated into mixed effects models of tumour growth in a number of ways. In some cases, pharmacokinetic data are available, and the concentration of the drug in the blood or tumour microenvironment is modelled explicitly [37, 159], or existing pharmacokinetic models are used alongside dose schedules to predict the local concentration of the drug [151]. Alternatively, a simple exponential clearance model may be proposed for the drug concentration as in the model presented by Ribba *et al.* [150]. The model proposed in [159] assumes that cytotoxic therapy administered in a preclinical study led to the death of proliferative tumour cells in a dose-dependent manner. Furthermore, resistance to treatment was considered in the models presented in [62] and [133], where the rate of tumour cell death due to chemotherapy decreases exponentially with time.

Vascular tumour growth and anti-angiogenic therapy are considered in the models proposed in [133] and [184]. In both cases, tumour growth is modelled by logistic growth, and the carrying capacity of the tumour is assumed to depend on the total vascular density within the tumour. The variable that represents a vascular dependent carrying capacity for the tumour is assumed to evolve as the square of the tumour size. Anti-angiogenic therapy and chemotherapy were both administered in the preclinical study described in [184], and a model in which the anti-angiogenic therapy and chemotherapy drugs interacted described the data more closely than where the therapies were assumed to have independent effects. In [133], the compound pazopanib is assumed to have anti-vascular and anti-tumour effects, and this model is validated for preclinical and clinical data.

Overall, mixed effects models of tumour growth and vascular tumour growth under various therapy regimens have been successful for describing clinical and preclinical data, and in many cases, model selection has been used to identify plausible mechanisms of action of anti-cancer therapies [133]. Working with our collabora-

tors at Hoffman La Roche, we developed a mixed effects model of vascular tumour growth based on preclinical data, and this work is presented in Chapter 3.

1.3.5 Summary

In this section we have reviewed existing mathematical models of angiogenesis and vascular tumour growth. Diverse approaches can be used to capture detail on multiple scales, and model simulation results can be compared to, and validated against experimental data. Modelling techniques that are popular in the pharmaceutical industry are driven by data, and allow the elucidation of biological mechanisms through model selection. However, since data on tumour growth are often limited in scope, these models are usually simplified. In conclusion, there has been progress in the field of mathematical modelling of angiogenesis and vascular tumour growth, but there is much work to be done before models are of an appropriate standard to provide detailed clinical predictions.

1.4 Thesis structure

The remainder of the thesis is organised as follows:

In Chapter 2 we introduce a spatially averaged model of angiogenesis that accounts for biochemical and cellular processes. The model is adapted from the ODE and PDE model presented by Zheng *et al.* [191]. In our analysis we identify four possible pre-treatment vessel phenotypes, and suggest how these could be used to identify "personalised" anti-angiogenic treatment based on pre-treatment phenotype and post-treatment goal. We also compare our model with published experimental data in the context of anti-VEGF and anti-Ang2 therapies. The work in Chapter 2 has been published in the *Journal of Theoretical Biology* [86].

In Chapter 3, we use preclinical data to develop a simple ODE model of vascular tumour growth incorporating a vascular normalisation window, and this model is parametrised using mixed effects methods. We demonstrate how our model could be used to identify an optimal treatment regimen for anti-angiogenic and chemotherapy

treatment by coordinating chemotherapy treatment with the normalisation window. The work in Chapter 3 has been published in *Clinical Pharmacology and Therapeutics: Pharmacometrics and Systems Pharmacology* [87].

While in Chapter 3 we investigate the pro-angiogenic effects of tumour cells, in Chapter 4 we consider the model of vascular tumour growth presented by Stamper *et al.* [161], which studies the anti-angiogenic effects of tumour cells through vessel occlusion. We extend this model to incorporate anti-angiogenic therapy. We demonstrate that our spatially averaged model exhibits oscillatory dynamics, similarly to the original model in [161], and that the parameters associated with anti-angiogenic therapy and normalisation (among others) can be modulated to access the oscillatory regime.

In Chapter 5, we extend the spatially averaged model from Chapter 4 to include spatial aspects of vascular tumour growth. We show that spatial heterogeneity of tumour cell and vessel density arises when the parameters correspond to the oscillatory case for the corresponding non-spatial model.

In Chapter 6, we motivate future work based on evaluating the suitability of spatially averaged models for capturing the dynamics of a spatially evolving phenomenon. We compare the outputs of our PDE and ODE models and show how data from the PDE model can be used to estimate the parameters of the corresponding ODE model. We investigate the conditions under which the ODE model provides reasonable predictions for the behaviour of the PDE model.

The final chapter of the thesis comprises a discussion of the results in the previous chapters and directions for future work.

Chapter 2

A non-spatial mathematical model of angiogenesis

The work in this chapter has been published in the Journal of Theoretical Biology [86].

2.1 Introduction

Our goal in this chapter is to use a mathematical model to categorize vessel phenotypes and to identify specific anti-angiogenic therapies that are suitable for treating each phenotype. Our model includes details of the biochemistry involved in angiogenesis, and accounts for vessel density and normalisation. We take a similar approach to Zheng *et al.* [191] by accounting for concentrations of free ligands and bound and unbound receptors explicitly, and also accounting for the cellular dynamics of vessel formation.

At the onset of angiogenesis, hypoxic tumour cells produce vascular endothelial growth factor (VEGF), which binds to VEGFR-2 receptors expressed by endothelial cells (ECs) of nearby vessels, inducing EC proliferation and migration [57]. Typically, newly formed tumour blood vessels surround the periphery of the tumour, and are tortuous and leaky, but the so-called normalisation of vessels [94], via maturation and coverage by smooth muscle cells, is essential for effective delivery of

blood. Normalisation may occur during anti-angiogenic (AA) therapy. A schematic of our interpretation of vessel maturation and normalisation is represented in Figure 2.1. The most well studied processes that drive normalisation involve the angiopoietin ligands and pericyte cells (PCs) [70]. The ligands Ang1 and Ang2 compete for binding to Tie2 receptors expressed by ECs. Furthermore, experimental work has reported that Ang1 promotes maturation, whereas the antagonist, Ang2, promotes vessel de-maturation. Attachment of PCs to new vessels promotes their stability by plugging gaps in otherwise leaky vasculature [55, 114, 169].

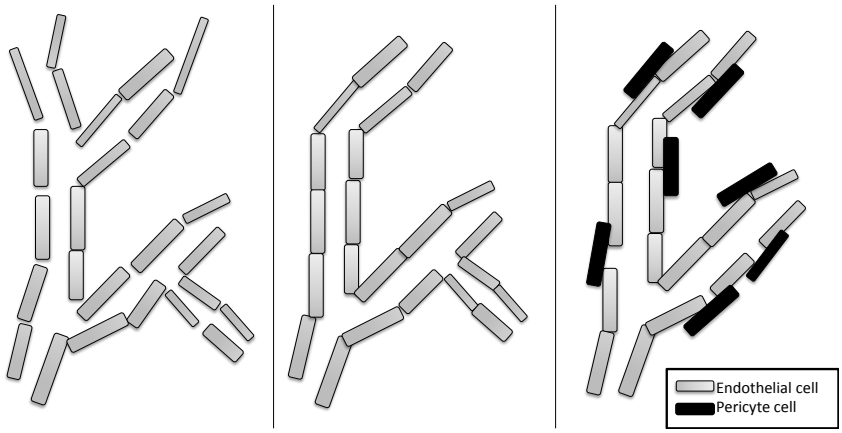


Figure 2.1: A schematic to illustrate our interpretation of immature, mature and normalised vessels. Left: tortuous, immature and leaky vessels with poor EC-EC adhesion and high branching. Centre: mature, less tortuous, less leaky vessels with good EC-EC adhesion. Right: normalised, mature vessels with good EC-EC adhesion and PC coverage to plug any gaps and support blood flow. Normal capilliaries in the body are similar to the figure on the right.

Two recent mathematical models incorporate vessel normalisation. Billy *et al.* present a pharmacologically driven, continuous, multi-scale PDE model of angiogenesis and vascular tumour growth that accounts for the effects of the angiopoietins on vessel maturation [21]. The model from [21] predicts a theoretical threshold level of endostatin gene therapy below which treatment loses efficacy. Zheng *et al.* present a one-dimensional, spatially resolved, continuous model of angiogenesis that couples biochemical effects with the processes of PC attachment and one-dimensional vessel growth [191]. They model ligand binding to the respective receptors and do not take tumour cells into account. Model simulations reveal that combined anti-VEGF/anti-PDGF therapy has a superior anti-angiogenic effect compared to anti-VEGF therapy

alone. In this work we adapt the model presented by Zheng *et al.* and investigate phenotype-specific AA treatment recommendations.

The remainder of this chapter is organised as follows. In Section 2.2, we develop our mathematical model and illustrate the behaviours it exhibits. In Section 2.3 we analyse a simplified version of the full model in order to gain insight into possible long-term behaviours. Section 2.4 contains our main results: we begin by demonstrating that the long term behaviour of the full model is similar to that of the simplified model, and we qualitatively validate the behaviour of the full model using experimental results from [96]. We predict the effects of different anti-angiogenic treatments on the different pre-treatment vascular phenotypes that our model exhibits. We simulate hypothetical drug treatments by perturbing the relevant model parameters, demonstrating that different pre-treatment vascular phenotypes require different perturbations for transition to a non-angiogenic phenotype. In the final section we discuss our findings and outline directions for future work.

2.2 Model development

Our model of angiogenesis comprises 16 time dependent, coupled, nonlinear ordinary differential equations (ODEs) that describe the evolution of ligands, receptors, ECs and PCs. Units of concentration, μM, are used to represent four ligands, three receptor types and two cell types. We focus on a small, isolated region of approximately homogeneous tumour tissue (for example, 0.5mm^3 is a reasonable volume to consider, since it is on the scale of the imaging data from a study of angiogenesis in mice in [49]). For simplicity, we neglect the dynamics of the tumour cells, and assume that the dynamics of the evolving vasculature in the region modelled are representative of the vasculature throughout the tumour. We assume there is no flux of ECs or PCs on the boundaries of the region represented. The terms density and concentration are used interchangeably when referring to cells. A schematic depicting all of the interactions that appear in the full model is shown in Figure 2.2.

The newly formed vessels in our model are described by the density of ECs, which

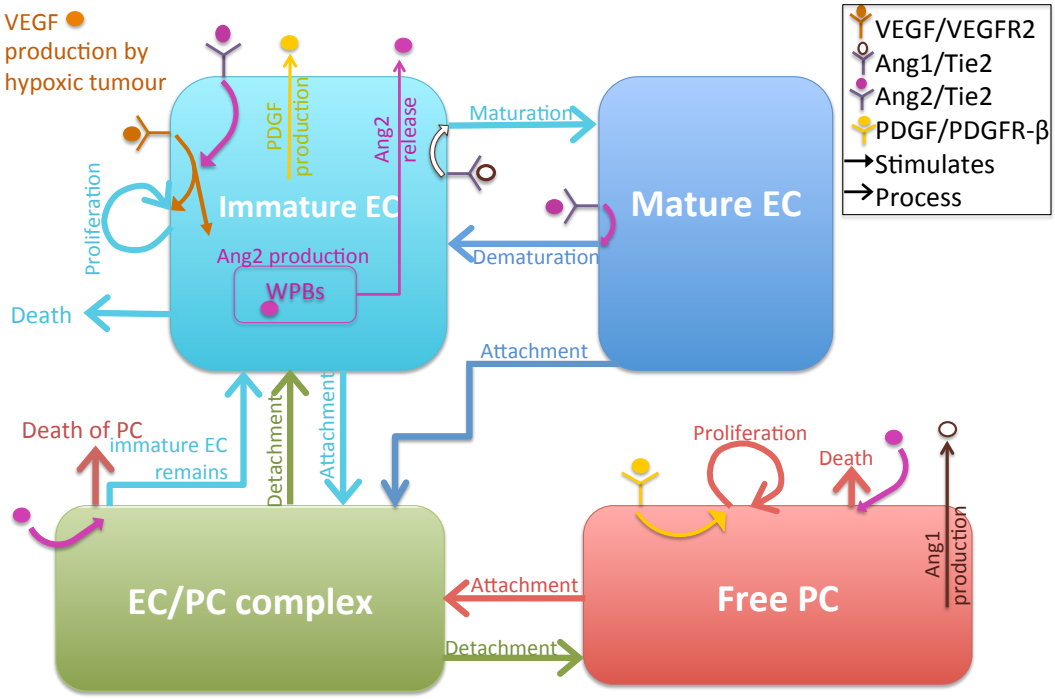


Figure 2.2: Schematic summary of the components of angiogenesis included in our model. VEGF is produced in response to hypoxia in the tumour (which we consider implicitly in our model), and binds to VEGFR2 receptors expressed by ECs. Bound VEGF increases the rate of production of Ang2 in Weibel Palade Bodies, from which it is released as the organelles become saturated. Immature ECs also produce PDGF at a constant rate, and die naturally via apoptosis. Ang2 competes with Ang1 for binding to the Tie2 receptor: an excess of bound Ang2 leads to de-maturation of ECs, whereas an excess of bound Ang1 leads to EC maturation. Ang2 binding also increases the proliferation rate of immature ECs. PDGF binds to PDGFR-β receptors expressed by PCs, upregulating PC proliferation. PCs die naturally and free Ang2 up-regulates PC death. PCs produce Ang1 and attach to both mature and immature ECs, forming the EC/PC complex that has no maturity rating, to increase the stability of vessels. PCs that are attached to ECs die naturally via apoptosis or due to high levels of extracellular Ang2, leaving behind a free EC which is automatically classed as immature.

are sub-divided into three categories: mature ECs, immature ECs, and ECs with PC coverage (the maturity of ECs with PC coverage is not specified). We assume that immature ECs proliferate and die, produce Ang2 and PDGF, and express VEGFR2 and Tie2 receptors [55, 57, 179]. Mature ECs and ECs with PC coverage also express VEGFR2 and Tie2 receptors, but do not proliferate, die or produce ligands in our model. We assume that immature ECs have loose EC-EC contacts and exhibit leakiness, whereas mature vessels have tight EC-EC contacts and are less leaky [55, 70]. PC coverage plugs gaps between ECs, makes vessels more sturdy and enhances blood flow (although inclusion of blood flow is beyond the scope of the current model) [63].

On the molecular scale, ligands are produced and bind to their respective receptors, and on the cellular scale, immature ECs and PCs proliferate. Production and release of VEGF, Ang1, Ang2 and PDGF are accounted for in our model. As illustrated in Figure 2.2, VEGF binds to VEGFR2 receptors expressed by ECs and stimulates EC proliferation. Similarly, Ang1 and Ang2 compete for binding to the Tie2 receptor, and their combined downstream effect is to modulate the maturity of new vessels. Finally, PDGF binds to PDGFR-β receptors expressed by PCs and stimulates their proliferation.

On the cellular scale, we assume that free PCs bind indiscriminately to mature and immature ECs. When PCs detach from ECs or the PC of an EC/PC complex dies, we assume, for simplicity, an immature EC remains. We also assume that de-maturation occurs when the ratio of bound Ang2/bound Ang1 exceeds a given threshold, and maturation occurs otherwise. The dependence of maturity on the angiopoietins is based on experimental observations in [114]. Table 2.1 summarises the dependent variables used in our model.

2.2.1 Biochemical sub-models

In this subsection we present the equations that describe the interactions included in the three sub-models that govern the biochemical aspects of our model.

VEGF sub-model

Similarly to the model presented in [191], we assume that free VEGF (v) binds reversibly to VEGFR2 receptors (r_v) to form VEGF/VEGFR2 complexes (b_v) via reactions of the form

$$\begin{aligned} v + r_v &\underset{k^v_{\text{off}}}{\overset{k^v_{\text{on}}}{\rightleftharpoons}} b_v, \\ b_v &\xrightarrow{k^v_{\text{int}}} \underset{product}{internal} + r_v, \end{aligned}$$

where k^v_{on} is the rate at which VEGF associates with VEGFR2 receptors to form a ligand/receptor complex, and k^v_{off} is the corresponding dissociation rate. We suppose that bound VEGF is internalised at rate k^v_{int}, and that this activates sub-cellular signalling pathways as the receptor is recycled to the cell surface. For simplicity, we assume instantaneous recycling of the VEGFR2 receptors, and that the "internal product" stimulates the onset of downstream signalling pathways.

Taking into consideration production, binding and decay, we assume that the evolution of extracellular VEGF concentration can be described by the following equation:

$$\underset{\text{VEGF:}}{\text{Extracellular}} \quad \frac{\mathrm{d}v}{\mathrm{d}t} = \underbrace{D(E_m, E_P)}_{\text{VEGF production}} \overbrace{-k^v_{\text{on}}\, v\, r_v + k^v_{\text{off}}\, b_v}^{\substack{\text{VEGF association} \\ \text{and dissociation}}} \underbrace{- \delta_v\, v}_{\text{VEGF decay}}, \quad (2.1)$$

where δ_v is the natural decay rate of extracellular VEGF. Since VEGF production is upregulated when tumour cells are hypoxic, we assume that the rate at which VEGF is produced is a decreasing function of oxygen tension, which is considered implicitly. We assume that ECs that are mature (E_m) or have PC coverage (E_P) can transport oxygen, reducing hypoxia, and therefore the VEGF production rate, $D(E_m, E_P)$, is given by

$$D(E_m, E_P) = \frac{\alpha_v}{\frac{E_m + E_P}{E_0} + 1},$$

where $(E_m + E_P)$ is the density of oxygen carrying vessels, E_0 is the carrying capacity of ECs (explained in more detail later in this section), and the constant, α_v,

represents the maximal VEGF production rate.

In our model, we assume that the total number of receptors is proportional to the cell density, and we expand on this when we introduce the equations for EC density later in this section. We assume that all cells have the same number of VEGFR2, Tie2 and/or PDGFR-β receptors, and we denote by ϕ the average number of VEGFR2, Tie2 or PDGFR-β receptors per cell. We base our estimate for ϕ on experimental work in [179]. Considering ligand binding and internalisation, and receptor generation and loss, the equations for unbound (r_v) and bound (b_v) VEGFR2 receptors are

$$\begin{aligned}
\text{VEGFR2:} \qquad \frac{\mathrm{d}r_v}{\mathrm{dt}} &= \underbrace{-k_{\text{on}}^v\, v\, r_v \quad + \quad (k_{\text{off}}^v + k_{\text{int}}^v)\, b_v}_{\substack{\text{VEGF association, dissociation} \\ \text{and internalisation}}} \\
&\quad \underbrace{+\phi \times (\text{EC proliferation rate})}_{\text{receptor generation}} \\
&\quad \underbrace{-\frac{r_v}{E_T}(\text{EC death rate})}_{\text{receptor loss}}, \\
\text{VEGF/VEGFR2 :} \qquad \frac{\mathrm{d}b_v}{\mathrm{dt}} &= \underbrace{k_{\text{on}}^v v\, r_v \quad - \quad (k_{\text{off}}^v + k_{\text{int}}^v)\, b_v}_{\substack{\text{VEGF association, dissociation} \\ \text{and internalisation}}} \\
&\quad \underbrace{-\quad \frac{b_v}{E_T}(\text{EC death rate})}_{\text{receptor loss}},
\end{aligned} \tag{2.2}$$

where $E_T = (E_i + E_m + E_P)$ is the total EC density and the functional forms of the EC proliferation and death rates are specified below. We suppose that when ECs proliferate, only unbound receptors, r_v, are produced, whereas both bound and unbound receptors, r_v and b_v, are lost as ECs die. The expression $\phi = \frac{r_v + b_v}{E_T}$ is used to derive the terms for receptor loss as cells die.

Hill Functions: In our model, there are several instances of switch-like behaviour. The model is continuous in cell density, representing the behaviour of a large number of cells. Although a switch in phenotype (or behaviour) of individual cells may occur rapidly when a threshold (of a ligand concentration, for example) is

reached, this threshold may be cell-specific and for a population of cells, distributed around the average threshold value. We capture this behaviour via second order Hill functions of the form

$$\mathrm{H}(a,b) = \frac{a^2}{a^2+b^2},$$

where a is a dependent variable and b is a threshold parameter, for instance. Functions of this type produce smooth switches between phenotypes and are more realistic than sharp switch functions when describing well-mixed cell populations. The order 2 is assumed a reasonable estimate.

Angiopoietins sub-model

The maturity of new vessels is controlled by the angiopoietins Ang1 and Ang2, which compete for binding to Tie2 receptors expressed by ECs. In our model we account for Ang1 internalisation and synthesis of both ligands [114]. Since Ang1 is produced by PCs, we assume that its production rate depends linearly on the PC density [63, 178]. Ang2 is produced and stored in sub-cellular organelles called Weibel Palade Bodies (WPBs) [59, 153], which we model explicitly.

We assume that only immature ECs (E_i) produce Ang2, that there is a maximum concentration of intracellular Ang2 per cell that cannot be exceeded, and that Ang2 is produced at a rate which is upregulated in response to VEGF binding. For clarity, we denote by v_b the fractional occupancy of VEGFR2 receptors. In our model, as WPBs become saturated, Ang2 is rapidly released to the extracellular space, and stored Ang2 is lost as ECs die. The total concentration of intracellular Ang2 across all ECs, a_w, is represented by the equation

$$\overset{\text{Intracellular Ang2}}{:} \quad \frac{\mathrm{d}a_w}{\mathrm{dt}} = \underbrace{\alpha_{a_w}(1+v_b)\left(\frac{A_0}{E_0}E_i - a_w\right)}_{\text{Ang2 production inside WPBs}} - \underbrace{\delta_{a_w}a_w}_{\text{decay}} - \underbrace{\alpha_{a2}\, a_w \mathrm{H}\left(a_w, \frac{A_0}{E_0}\frac{E_i}{2}\right)}_{\text{Ang2 exocytosis}} - \underbrace{\frac{a_w}{E_T}(\text{EC death rate})}_{\text{Ang2 loss as ECs die}}, \tag{2.3}$$

where $\frac{A_0}{E_0}$ is the maximum amount of intracellular Ang2 per cell and $\alpha_{a_w}, \delta_{a_w}$ and α_{a_2}

are positive constants representing the production, decay and release rates of Ang2, respectively. Since Ang2 is produced by immature ECs, its carrying capacity and exocytosis rate depend upon the density of immature ECs, E_i, the EC carrying capacity, E_0, and the maximum allowed intracellular Ang2, A_0. We assume that in the absence of VEGF stimulation, immature ECs produce Ang2 at a base rate α_{a_w}, and that the production rate is a linearly increasing function of bound VEGFR2 receptor fraction, v_b. Ang2 exocytosis is modelled as a function of the total immature EC density, E_i via a second order Hill function, where $\frac{A_0}{E_0}\frac{E_i}{2}$ is the concentration of intracellular Ang2 at which the release rate is half maximal. The functional form for the EC death rate is given below.

Extracellular Ang1, a_1, is produced by free and bound PCs. We assume that Ang1 binds Tie2 receptors, r_a, expressed by ECs, to form the Ang1/Tie2 complex, b_{a_1}, and also decays naturally. In our model, extracellular Ang2, a_2, is released by ECs as described above, and also binds to Tie2 receptors, r_a, to form the Ang2/Tie2 complex, b_{a_2}, and decays naturally. The evolution of the extracellular angiopoietins is modelled via the equations

$$\text{Extracellular Ang1:} \quad \frac{\mathrm{d}a_1}{\mathrm{dt}} = \underbrace{\alpha_{a_1}\ P_T}_{\text{Ang1 production}} - \overbrace{\left(k_{\text{on}}^{a_1}\ a_1\ r_a - k_{\text{off}}^{a_1}\ b_{a_1}\right)}^{\substack{\text{Ang1 association}\\ \text{and dissociation}}} - \underbrace{\delta_{a_1}\ a_1}_{\text{Ang1 decay}}, \tag{2.4}$$

$$\text{Extracellular Ang2:} \quad \frac{\mathrm{d}a_2}{\mathrm{dt}} = \underbrace{\alpha_{a_2}\ a_w \mathrm{H}\left(a_w, \frac{A_0}{E_0}\frac{E_i}{2}\right)}_{\text{Ang2 exocytosis}} - \underbrace{\left(k_{\text{on}}^{a_2}\ a_2\ r_a - k_{\text{off}}^{a_2}\ b_{a_2}\right)}_{\substack{\text{Ang2 association}\\ \text{and dissociation}}} - \underbrace{\delta_{a_2}\ a_2}_{\text{Ang2 decay}}. \tag{2.5}$$

In equation (2.4), α_{a_1} is the (constant) production rate of Ang1, $P_T = (P + E_P)$ is the total number of pericyte cells, the parameters that represent the association and dissociation rates for Ang1/Tie2 binding are $k_{\text{on}}^{a_1}$ and $k_{\text{off}}^{a_1}$, respectively, while $k_{\text{on}}^{a_2}$ and $k_{\text{off}}^{a_2}$ represent Ang2/Tie2 association and dissociation, respectively. The linear decay rates of Ang1 and Ang2 are represented by the constant parameters δ_{a_1} and δ_{a_2}, respectively.

As for the VEGF sub-model, we distinguish free and bound Tie2 receptors.

Assuming that each cell has ϕ receptors, we ensure that Tie2 receptors are generated as immature ECs (E_i) proliferate and lost as they die. The equations for Tie2 receptors, r_a, Ang1/Tie2 complex, b_{a_1}, and Ang2/Tie2 complex, b_{a_2} are:

$$\begin{aligned}\text{Tie2:}\quad \frac{\mathrm{d}r_a}{\mathrm{dt}} &= \underbrace{-k_{\text{on}}^{a_1}\, a_1\, r_a + k_{\text{off}}^{a_1}\, b_{a_1}}_{\substack{\text{Ang1 association}\\ \text{and dissociation}}} \underbrace{-\left(k_{\text{on}}^{a_2}\, a_2\, r_a - k_{\text{off}}^{a_2} b_{a_2}\right)}_{\substack{\text{Ang2 association}\\ \text{and dissociation}}} \\ &\quad \underbrace{+\, k_{\text{int}}^{a_1}\, b_{a_1}}_{\text{Ang1 internalisation}} + \underbrace{\phi \times (\text{EC proliferation rate})}_{\text{receptor generation}} \\ &\quad \underbrace{-\,\frac{r_a}{E_T}(\text{EC death rate})}_{\text{receptor loss}}, \end{aligned} \tag{2.6}$$

$$\begin{aligned}\text{Ang1/Tie2:}\quad \frac{\mathrm{d}b_{a_1}}{\mathrm{dt}} &= \underbrace{k_{\text{on}}^{a_1}\, a_1\, r_a - k_{\text{off}}^{a_1}\, b_{a_1}}_{\substack{\text{Ang1 association}\\ \text{and dissociation}}} - \underbrace{k_{\text{int}}^{a_1}\, b_{a_1}}_{\text{Ang1 internalisation}} \\ &\quad \underbrace{-\frac{b_{a_1}}{E_T}(\text{EC death rate})}_{\text{receptor loss}}, \end{aligned} \tag{2.7}$$

$$\text{Ang2/Tie2:}\quad \frac{\mathrm{d}b_{a_2}}{\mathrm{dt}} = \underbrace{k_{\text{on}}^{a_2}\, a_2\, r_a - k_{\text{off}}^{a_2}\, b_{a_2}}_{\substack{\text{Ang2 association}\\ \text{and dissociation}}} - \underbrace{\frac{b_{a_2}}{E_T}(\text{EC death rate})}_{\text{receptor loss}}, \tag{2.8}$$

where $k_{\text{int}}^{a_1}$ is the internalisation rate of Ang1. As Ang1 is internalised, we assume that receptors are recycled to the cell surface similarly to the VEGFR2 receptor in equations (2.2)-(2.3).

PDGF sub-model

In our model, PDGF, p, is produced by immature ECs, E_i, and binds to PDGFR-β receptors, r_p, expressed by PCs to form PDGF/PDGFR$-\beta$ complexes, b_p. The binding process may be represented by

$$p + r_p \underset{k_{\text{off}}^{p}}{\overset{k_{\text{on}}^{p}}{\rightleftharpoons}} b_p,$$

where k_{on}^{p} denotes the association rate of PDGF to PDGFR-β and k_{off}^{p} denotes the corresponding dissociation rate. Combining the above processes, we deduce that the

evolution of free PDGF may be described by the following ODE:

$$\text{Free PDGF:} \quad \frac{\mathrm{d}p}{\mathrm{dt}} = \underbrace{\alpha_p\, E_i}_{\substack{\text{PDGF production}\\ \text{by immature ECs}}} \overbrace{-k^p_{\text{on}}\, p\, r_p + k^p_{\text{off}}\, b_p}^{\substack{\text{PDGF association}\\ \text{and dissociation}}} - \underbrace{\delta_p\, p}_{\text{PDGF decay}} \tag{2.9}$$

where α_p is the assumed constant rate at which immature ECs produce PDGF, and δ_p is its natural decay rate.

As for the VEGF and angiopoietins sub-models described above, we assume that receptors are generated as PCs proliferate, and lost as they die. Assuming ϕ receptors per PC, we model the free and bound PDGFR-β receptors by the equations

$$\text{PDGFR-}\beta\text{:} \quad \frac{\mathrm{d}r_p}{\mathrm{dt}} = \overbrace{-k^p_{\text{on}}\, p\, r_p + k^p_{\text{off}}\, b_p}^{\substack{\text{PDGF association}\\ \text{and dissociation}}} + \underbrace{\phi \times (\text{PC proliferation rate})}_{\text{receptor generation}} - \underbrace{\frac{r_p}{P_T}(\text{PC death rate}),}_{\text{receptor loss}} \tag{2.10}$$

$$\text{PDGF/PDGFR-}\beta\text{:} \quad \frac{\mathrm{d}b_p}{\mathrm{dt}} = \underbrace{k^p_{\text{on}}\, p\, r_p - k^p_{\text{off}}\, b_p}_{\substack{\text{PDGF association}\\ \text{and dissociation}}} - \underbrace{\frac{b_p}{P_T}(\text{PC death rate}),}_{\text{receptor loss}} \tag{2.11}$$

The functional forms of the terms for PC proliferation and death are described below.

2.2.2 Cell dynamics sub-model

In our model we consider two types of cells: ECs and PCs. We subdivide the ECs into three subclasses: immature (E_i), mature (E_m) and ECs with PC coverage (E_P) and denote by P the concentration of free PCs. We assume that ECs undergo three processes: proliferation, death and attachment to PCs. Similarly, we assume that PCs proliferate, die and attach to ECs. PCs are assumed to bind to mature and immature ECs at the same rate, ζ. For simplicity, we assume that when PCs detach, the ECs to which they were bound become immature, regardless of their previous status. The attachment and detachment of PCs to ECs can be represented by the

following reactions:

$$\begin{aligned} E_m + P &\xrightarrow{\zeta} E_P, \\ E_i + P &\xrightarrow{\zeta} E_P, \\ E_P &\xrightarrow{\nu} E_i + P, \\ E_P &\xrightarrow{\epsilon} E_i. \end{aligned}$$

where ϵ scales the PC death rate. We assume that when attached PCs die, the remaining ECs are immature.

In our model, the proliferation of immature ECs is stimulated by VEGF binding and upregulated by Ang2 binding. The death of immature ECs occurs when there is insufficient bound VEGF for proliferation. Similarly, we assume that the proliferation of free PCs is stimulated by PDGF binding. According to experimental data, PCs die when local levels of extracellular Ang2 are high [136], and we take this into account, via the free Ang2 concentration in accordance with the experimental data (the authors showed a correlation between PC death and Ang2 concentration), when we model PC death. We assume that vessel maturity is regulated by the ratio of bound Ang1 and Ang2, similarly to models presented in [90, 191] and based on experimental results in [114].

Endothelial cells

Using the law of mass action to represent the attachment and detachment of PCs to ECs, and including exchange terms between mature and immature ECs, the equation

for the evolution of immature ECs takes the form

$$\begin{aligned}\text{Immature ECs:}\quad \frac{\mathrm{d}E_i}{\mathrm{dt}} = {} & \underbrace{\theta\,\mathrm{H}\left(v_b, c_{ep}\right)\left(1+\mathrm{H}(a_b,c_a)\right)\left(1-\frac{E_T}{E_0}\right)E_i}_{\text{EC proliferation}} - \underbrace{\rho\,\mathrm{H}\left(c_d, v_b\right)E_i}_{\text{EC death}} \\ & \underbrace{-\zeta\,PE_i + \nu\,E_P}_{\substack{\text{association and dissociation}\\ \text{of PCs with ECs}}} + \underbrace{\epsilon\left(\frac{a_2}{A_0}+\mathrm{H}(c_{ep},p_b)\right)E_P}_{\substack{\text{PC death due}\\ \text{to high Ang2 levels}\\ \text{or low PDGF levels}}} \\ & \underbrace{-\eta\,\mathrm{H}\left(\lambda,\frac{b_{a_2}}{b_{a_1}}\right)E_i}_{\text{maturity increase}} + \underbrace{\mu\,\mathrm{H}\left(\frac{b_{a_2}}{b_{a_1}},\lambda\right)E_m}_{\text{maturity decrease}}, \end{aligned} \tag{2.12}$$

where the parameter θ represents the half-maximal proliferation rate of immature ECs and ρ represents the maximum death rate of immature ECs. In our model, EC proliferation is switched on when the fractional occupancy of VEGFR2 receptors, v_b, reaches the threshold, c_{ep}, and logistic growth of immature ECs is assumed. Furthermore, EC death is switched on when the concentration of bound VEGFR2 receptors falls below a threshold, c_d. In our model, the proliferation rate of immature ECs is upregulated when the fraction of Tie2 receptors bound by Ang2, a_b, reaches the threshold, c_a, similarly to the model presented in [191].

We model both the increase and decrease in maturity via second order Hill functions (these are given by the fifth and sixth bracketed terms on the right hand side of equation (2.12)) and denote by η and μ the maximum de-maturation and maturation rates. The parameter λ is the ratio of bound Ang2 to bound Ang1 above which ECs transition to an immature phenotype.

In our model, mature ECs do not proliferate or die, and PCs are assumed to attach to mature and immature ECs at the same rate. Taken together, we deduce that the equation governing the evolution of mature ECs is

$$\begin{aligned}\text{Mature ECs:}\quad \frac{\mathrm{d}E_m}{\mathrm{dt}} = {} & \underbrace{-\zeta\,P\,E_m}_{\substack{\text{association of PCs}\\ \text{with ECs}}} + \underbrace{\eta\,\mathrm{H}\left(\lambda,\frac{b_{a_2}}{b_{a_1}}\right)E_i}_{\text{maturity increase}} \\ & \underbrace{-\mu\,\mathrm{H}\left(\frac{b_{a_2}}{b_{a_1}},\lambda\right)E_m}_{\text{maturity decrease}}. \end{aligned} \tag{2.13}$$

Receptor conservation

We account for the total number of receptors present via the receptor generation and loss terms in equations (2.2), (2.3), (2.4), (2.6)-(2.8) and (2.10)-(2.11). For each receptor type, we assume that there are, on average, ϕ receptors per cell. Therefore the total number of each receptor included in our model can be expressed as follows

$$\begin{aligned}
&\text{VEGFR2 receptors} && r_v + b_v && = \phi(E_i + E_m + E_P);\\
&\text{Tie2 receptors} && r_a + b_{a1} + b_{a2} && = \phi(E_i + E_m + E_P);\\
&\text{PDGFR-}\beta\text{ receptors} && r_p + b_p && = \phi(P + E_P).
\end{aligned}$$

Using VEGFR2 receptors as an example, it must hold that

$$\frac{\mathrm{d}r_v}{\mathrm{d}t} + \frac{\mathrm{d}b_v}{\mathrm{d}t} = \phi\left(\frac{\mathrm{d}E_i}{\mathrm{d}t} + \frac{\mathrm{d}E_m}{\mathrm{d}t} + \frac{\mathrm{d}E_P}{\mathrm{d}t}\right),$$

and therefore the receptor generation and loss terms in equations (2.2), (2.3), (2.4) and (2.6)-(2.8) are

$$(\text{EC proliferation rate}) = \theta\ \mathrm{H}\left(v_b, c_{ep}\right)\left(1 + \mathrm{H}\left(a_b, c_a\right)\right)\left(1 - \frac{E_T}{E_0}\right)E_i,$$

and

$$(\text{EC death rate}) = \rho\ \mathrm{H}\left(c_d, v_b\right)E_i.$$

Similar expressions for PDGFR-β receptors are explained below.

Pericyte cells

We suppose that the processes dominating the time evolution of free PCs are proliferation, death and attachment to ECs. Combining these processes yields the following

ODE:

$$\text{Free pericytes:} \quad \frac{\mathrm{d}P}{\mathrm{dt}} = \underbrace{\kappa\, \mathrm{H}(p_b, c_{pp}) \left(1 - \frac{P_T}{P_0}\right) P}_{\text{PC proliferation}} \quad \underbrace{- \epsilon \left(\frac{a_2}{A_0} + \mathrm{H}(c_{pp}, p_b)\right) P}_{\substack{\text{PC death due} \\ \text{to high Ang2 levels} \\ \text{or low PDGF levels}}}$$
$$\underbrace{- \zeta\, P\, (E_i + E_m) + \nu\, E_P}_{\substack{\text{association and dissociation} \\ \text{of PCs with ECs}}}, \tag{2.14}$$

where κ is the maximum proliferation rate of PCs, ϵ scales the PC death rate and P_0 is the carrying capacity of PCs. We assume PCs obey a logistic growth function, competing for space with one another but not with ECs. Experimental observations from [11] suggest that PC coverage in normal vessels ranges from 10%-50%. In our model, therefore, we assume that the maximum carrying capacity of PCs, P_0, is half that of ECs, E_0. We further assume that PC proliferation is switched on when the fractional occupancy of PDGFR-β receptors, p_b, reaches the threshold value, c_{pp}. When the proportion of bound PDGF/PDGFR-β falls below c_{ep}, or when Ang2 levels are high (compared to the reference concentration, A_0) the PC death rate increases.

Endothelial cell/pericyte complex

In our model, ECs with PC coverage are quiescent; they do not proliferate or die, and are not classed as either mature nor immature. Taking into account the association and dissociation of PCs to ECs, and the death of PCs due to a high extracellular Ang2 concentration, we represent the EC/PC complex, E_P, by the equation

$$\text{EC/PC complex:} \quad \frac{\mathrm{d}E_P}{\mathrm{dt}} = \underbrace{\zeta\, P\, (E_i + E_m) - \nu\, E_P}_{\substack{\text{association and dissociation} \\ \text{of PCs with ECs}}}$$
$$\underbrace{- \epsilon \left(\frac{a_2}{A_0} + \mathrm{H}(c_{pp}, p_b)\right) E_P}_{\substack{\text{PC death due} \\ \text{to high Ang2 levels} \\ \text{or low PDGF levels}}}. \tag{2.15}$$

We assume that PCs bound to ECs die at the same rate as free PCs and that the ECs to which they were attached are immature.

In equations (2.10) and (2.11), PDGFR-β receptor generation and loss depend on the proliferation and death rates of PCs. Combining equations (2.14) and (2.15), the evolution of the total PC density, $P_T = P + E_P$, satisfies

$$\frac{\mathrm{d}P_T}{\mathrm{dt}} = \kappa\ \mathrm{H}(p_b, c_{pp}) \left(1 - \frac{P_T}{P_0}\right)\ P - \epsilon \left(\frac{a_2}{A_0} + \mathrm{H}(c_{pp}, p_b)\right)\ P_T.$$

Further we deduce that

$$(\text{PC proliferation rate}) = \kappa\ \mathrm{H}(p_b, c_{pp}) \left(1 - \frac{P_T}{P_0}\right)\ P,$$

and

$$(\text{PC death rate}) = \ \epsilon\ \left(\frac{a_2}{A_0} + \mathrm{H}(c_{pp}, p_b)\right)\ P_T.$$

These expressions are used in equations (2.10) and (2.11) to determine the rate at which PDGFR-β receptors are created and lost.

2.2.3 Model summary

Our model comprises 16 time dependent ODEs. Twelve of these equations represent biochemical interactions between ligands and receptors; four represent cell dynamics. The full set of equations is listed below for completeness.

Free VEGF:
$$\frac{\mathrm{d}v}{\mathrm{dt}} = \frac{\alpha_v}{\frac{E_m+E_P}{E_0} + 1} - k^v_{\text{on}}\ v\ r_v + k^v_{\text{off}}\ b_v - \delta_v\ v, \tag{2.1}$$

VEGFR2:
$$\begin{aligned}\frac{\mathrm{d}r_v}{\mathrm{dt}} = &-k^v_{\text{on}}\ v\ r_v + (k^v_{\text{off}} + k^v_{\text{int}})\ b_v \\ &+\phi\ \theta\ \mathrm{H}\left(v_b, c_{ep}\right)\left(1 + \mathrm{H}(a_b, c_a)\right)\left(1 - \frac{E_T}{E_0}\right)\ E_i \\ &-\rho\ \mathrm{H}(c_d, v_b)\frac{E_i}{E_T}\ r_v,\end{aligned} \tag{2.2}$$

VEGF/VEGFR2:
$$\frac{\mathrm{d}b_v}{\mathrm{dt}} = k^v_{\text{on}}\ v\ r_v - (k^v_{\text{off}} + k^v_{\text{int}})\ b_v - \rho\ \mathrm{H}(c_d, v_b)\frac{E_i}{E_T}\ b_v, \tag{2.3}$$

Free Ang1:
$$\frac{\mathrm{d}a_1}{\mathrm{dt}} = \alpha_{a_1}\ P_T - k^{a_1}_{\text{on}}\ a_1\ r_a + k^{a_1}_{\text{off}}\ b_{a_1} - \delta_{a_1}\ a_1, \tag{2.4}$$

Intracellular Ang2:
$$\frac{\mathrm{d}a_w}{\mathrm{dt}} = \alpha_{a_w}\ (1+v_b)\left(\frac{A_0}{E_0}E_i - a_w\right) - \delta_{a_w}\ a_w - \alpha_{a_2}\ a_w\ \mathrm{H}\left(a_w, \frac{E_i}{E_0}\frac{A_0}{2}\right) - \rho\ \mathrm{H}\left(c_d, v_b\right)\frac{E_i}{E_T}\ a_w, \tag{2.5}$$

Free Ang2:
$$\frac{\mathrm{d}a_2}{\mathrm{dt}} = \alpha_{a_2}\ a_w\ \mathrm{H}\left(a_w, \frac{A_0}{E_0}\frac{E_i}{2}\right) - k^{a_2}_{\mathrm{on}}\ a_2\ r_a + k^{a_2}_{\mathrm{off}}\ b_{a_2} - \delta_{a_2}\ a_2, \tag{2.6}$$

Tie2:
$$\frac{\mathrm{d}r_a}{\mathrm{dt}} = -k^{a_1}_{\mathrm{on}}\ a_1\ r_a + (k^{a_1}_{\mathrm{off}} + k^{a_1}_{\mathrm{int}})\ b_{a_1} - k^{a_2}_{\mathrm{on}}\ a_2\ r_a + k^{a_2}_{\mathrm{off}}\ b_{a_2} + \phi\ \theta\ \mathrm{H}\left(v_b, c_{ep}\right)\left(1+\mathrm{H}(a_b, c_w)\right)\left(1-\frac{E_T}{E_0}\right)\ E_i - \rho\ \mathrm{H}\left(c_d, v_b\right)\frac{E_i}{E_T}\ r_a, \tag{2.7}$$

Ang1/Tie2:
$$\frac{\mathrm{d}b_{a_1}}{\mathrm{dt}} = k^{a_1}_{\mathrm{on}}\ a_1\ r_a - (k^{a_1}_{\mathrm{off}} + k^{a_1}_{\mathrm{int}})\ b_{a_1} - \rho\ \mathrm{H}\left(c_d, v_b\right)\frac{E_i}{E_T}\ b_{a_1}, \tag{2.8}$$

Ang2/Tie2:
$$\frac{\mathrm{d}b_{a_2}}{\mathrm{dt}} = k^{a_2}_{\mathrm{on}}\ a_2\ r_a - k^{a_2}_{\mathrm{off}}\ b_{a_2} - \rho\ \mathrm{H}\left(c_d, v_b\right)\frac{E_i}{E_T}\ b_{a_2}, \tag{2.9}$$

Free PDGF:
$$\frac{\mathrm{d}p}{\mathrm{dt}} = \alpha_p\ E_i - k^p_{\mathrm{on}}\ p\ r_p + k^p_{\mathrm{off}}\ b_p - \delta_p\ p, \tag{2.10}$$

PDGFR-β:
$$\frac{\mathrm{d}r_p}{\mathrm{dt}} = -k^p_{\mathrm{on}}\ p\ r_p + k^p_{\mathrm{off}}\ b_p + \phi\ \kappa\ \mathrm{H}(p_b, c_{pp})\left(1-\frac{P_T}{P_0}\right)\ P - \epsilon\ \left(\frac{a_2}{A_0} + \mathrm{H}(c_{pp}, p_b)\right)\ r_p, \tag{2.11}$$

PDGF/PDGFR-β:
$$\frac{\mathrm{d}b_p}{\mathrm{dt}} = k^p_{\mathrm{on}}\ p\ r_p - k^p_{\mathrm{off}}\ b_p - \epsilon\ \left(\frac{a_2}{A_0} + \mathrm{H}(c_{pp}, p_b)\right)\ b_p, \tag{2.12}$$

Immature ECs:
$$\frac{\mathrm{d}E_i}{\mathrm{dt}} = \theta\ \mathrm{H}\left(v_b, c_{ep}\right)\left(1+\mathrm{H}(a_b, c_a)\right)\left(1-\frac{E_T}{E_0}\right)\ E_i - \rho\ \mathrm{H}\left(c_d, v_b\right)\ E_i - \zeta\ P\ E_i + \nu\ E_P + \epsilon\ \left(\frac{a_2}{A_0} + \mathrm{H}(c_{pp}, p_b)\right)\ E_P - \eta\ \mathrm{H}\left(\lambda, \frac{b_{a_2}}{b_{a_1}}\right)\ E_i + \mu\ \mathrm{H}\left(\frac{b_{a_2}}{b_{a_1}}, \lambda\right)\ E_m, \tag{2.13}$$

Mature ECs:
$$\frac{\mathrm{d}E_m}{\mathrm{dt}} = -\zeta\ P\ E_m + \eta\ \mathrm{H}\left(\lambda, \frac{b_{a_2}}{b_{a_1}}\right)\ E_i - \mu\ \mathrm{H}\left(\frac{b_{a_2}}{b_{a_1}}, \lambda\right)\ E_m, \tag{2.14}$$

Free pericytes:
$$\frac{\mathrm{d}P}{\mathrm{dt}} = \kappa\ \mathrm{H}(p_b, c_{pp})\left(1-\frac{P_T}{P_0}\right)\ P - \epsilon\ \left(\frac{a_2}{A_0} + \mathrm{H}(c_{pp}, p_b)\right)\ P - \zeta\ P\ (E_i + E_m) + \nu\ E_P, \tag{2.15}$$

EC/PC complex:
$$\frac{\mathrm{d}E_P}{\mathrm{dt}} = \zeta\ P\ (E_i + E_m) - \nu\ E_P - \epsilon\ \left(\frac{a_2}{A_0} + \mathrm{H}(c_{pp}, p_b)\right)\ E_P, \tag{2.16}$$

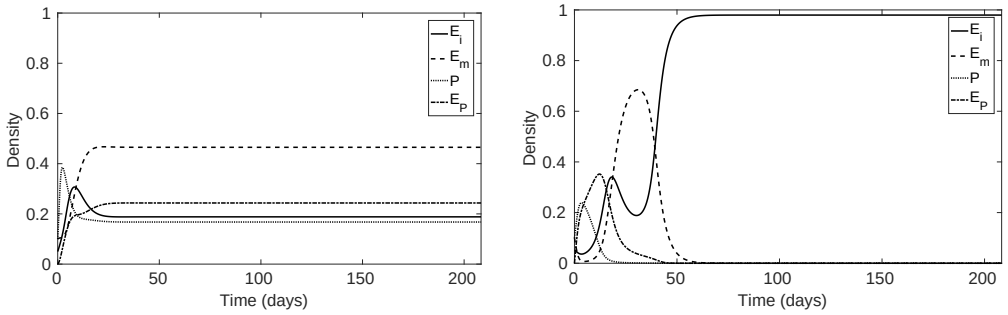
where all variables and derived quantities are defined in Table 2.1.

Of the 39 parameters, 22 were estimated from the literature. Where no ap-

propriate data were available, parameters were typically estimated from values of parameters in similar systems, or from existing mathematical models. Otherwise, we made order of magnitude estimates for parameters. The default parameter values used in model simulations, and their sources, are explained in detail in Appendix A.

2.2.4 Initial conditions and numerical simulations of the full model

We simulate the full model with initial conditions that represent the onset of angiogenesis. We assume that ECs ($E_i + E_m + E_P$) have a density that is 15% of their carrying capacity, that all PCs are free (no PC coverage) and that $\frac{2}{3}$ of ECs are mature. The initial conditions for all variables are given in Table 2.1. Figure 2.3 shows two typical simulations of the full model. They indicate that there are multiple long-term behaviour regimes of the full model for different parameter sets: we show cases where all cell types coexist and where only immature ECs have non-zero density. By increasing the PC attachment rate, ζ, (shown in 2.3b) fewer PCs are available to produce Ang1, and this drives the ECs into an immature state, where they produce Ang2, which leads to the death of PCs.



(a) **(b)**

Figure 2.3: Numerical simulations of the full model equations (2.1)-(2.15) with initial conditions from Table 2.1. Parameter values as per Table A.1 except the PC attachment rate, ζ, is ten times larger than the default value in (b).

In the next section, we turn to a simplified version of the full model in order to explore analytically the possible long term behaviours.

Name	Description	Initial value	Units
v	Free VEGF concentration	8×10^{-5}	μM
r_v	Total unbound VEGFR2 receptors	6×10^{-4}	μM
b_v	Total bound VEGFR2 receptors	6×10^{-4}	μM
a_1	Free Ang1	8×10^{-5}	μM
a_w	Total Ang2 stored in all WPBs	8×10^{-5}	μM
a_2	Free Ang2	8×10^{-5}	μM
r_a	Total unbound Tie2 receptors	6×10^{-4}	μM
b_{a_1}	Total bound Ang1/Tie2	3×10^{-4}	μM
b_{a_2}	Total bound Ang2/Tie2	3×10^{-4}	μM
p	PDGF-B	8×10^{-5}	μM
r_p	Total unbound PDGFR-β receptors	4×10^{-4}	μM
b_p	Total bound PDGFR-β receptors	4×10^{-4}	μM
E_i	Number density of immature ECs	4×10^{-9}	μM
E_m	Number density of mature ECs	8×10^{-9}	μM
P	Number density of free pericytes	8×10^{-9}	μM
E_P	Number density of ECs with pericyte coverage	0	μM
E_T	$(E_i + E_m + E_P)$ Total endothelial cells	-	μM
P_T	$(P + E_P)$ Total pericyte cells	-	μM
v_b	$\left(\frac{b_v}{r_v + b_v}\right)$ Bound fraction of VEGFR2 receptors	-	none
a_b	$\left(\frac{b_{a_2}}{r_a + b_{a_1} + b_{a_2}}\right)$ Fraction of Tie2 receptors bound by Ang2	-	none
p_b	$\left(\frac{b_p}{r_p + b_p}\right)$ Bound fraction of PDGFR-β receptors	-	none

Table 2.1: Definitions of dependent variables and variable groupings in the full ODE model of angiogenesis, along with the default initial conditions used for numerical simulations. See Section 2.2.4 for explanations of the initial conditions.

2.3 Simplified model

In this section we analyse a decoupled version of the cell dynamics sub-model in order to gain insight into the possible long-term behaviours of the full model. The results are used both to identify possible vascular phenotypes, and to recommend specific anti-angiogenic treatments to suit them.

The simplified model is obtained from the full model by viewing the proliferation and death rates for ECs and PCs and the maturation/de-maturation rates of ECs as constants, rather than depending on VEGF, Ang1, Ang2 and PDGF. Under these assumptions, equations (2.13)-(2.16) reduce to give:

$$\text{Immature ECs:} \quad \frac{\mathrm{d}E_i}{\mathrm{dt}} = \hat{\theta}\left(1-\frac{E_i+E_m+E_P}{E_0}\right)E_i - \hat{\rho}\,E_i - \zeta\,P\,E_i + \nu\,E_P + \hat{\epsilon}\,E_P - \hat{\eta}\,E_i + \hat{\mu}\,E_m, \tag{2.17}$$

$$\text{Mature ECs:} \quad \frac{\mathrm{d}E_m}{\mathrm{dt}} = -\zeta\,P\,E_m + \hat{\eta}\,E_i - \hat{\mu}\,E_m, \tag{2.18}$$

$$\text{Free pericytes:} \quad \frac{\mathrm{d}P}{\mathrm{dt}} = \hat{\kappa}\left(1-\frac{P+E_P}{P_0}\right)P - \hat{\epsilon}\,P - \zeta\,P\,(E_i+E_m) + \nu\,E_P, \tag{2.19}$$

$$\text{EC/PC complex:} \quad \frac{\mathrm{d}E_P}{\mathrm{dt}} = \zeta\,P\,(E_i+E_m) - \nu\,E_P - \hat{\epsilon}\,E_P, \tag{2.20}$$

wherein the constants $\hat{\theta}, \hat{\rho}, \hat{\kappa}, \hat{\epsilon}, \hat{\eta}$ and $\hat{\mu}$ replace the corresponding functional forms in the full model:

$$\theta\,\mathrm{H}\,(v_b, c_{ep})\,(1+\mathrm{H}(a_b, c_a)) \to \hat{\theta}; \qquad \rho\,\mathrm{H}\,(c_d, v_b) \to \hat{\rho}; \qquad \kappa\,\mathrm{H}(p_b, c_{pp}) \to \hat{\kappa};$$
$$\epsilon\left(\frac{a_2}{A_0}+\mathrm{H}(c_{pp}, p_b)\right) \to \hat{\epsilon}; \qquad \eta\,\mathrm{H}\left(\lambda, \frac{b_{a_2}}{b_{a_1}}\right) \to \hat{\eta}; \qquad \mu\,\mathrm{H}\left(\frac{b_{a_2}}{b_{a_1}}, \lambda\right) \to \hat{\mu}.$$

2.3.1 Steady state solutions

With $\frac{\mathrm{d}}{\mathrm{d}t} = 0$ in equations (2.17)-(2.20), we identify five steady state solutions, including two vessel-free solutions for which $E_i = E_m = E_P = 0$. A third steady solution is devoid of PCs so that $E_P = P = 0$ and $E_i, E_m > 0$. For the final two steady solutions, all cell types coexist. We identify the regions of existence and linear

stability for each steady state solution in terms of the ratios of the proliferation and death rates of ECs and PCs, respectively: $\frac{\hat{\rho}}{\hat{\theta}}$ and $\frac{\hat{\epsilon}}{\hat{\kappa}}$, since these ratios could theoretically be modulated via drug treatments, and we assume all other parameters are fixed to those listed in Table 2.2. The first three steady state solutions, for which one or more of E_i, E_m, P, E_P are zero, can be written as follows:

$$\begin{aligned}
&\text{(i)} && E_i = 0; && E_m = 0; && P = 0; && E_P = 0;\\
&\text{(ii)} && E_i = 0; && E_m = 0; && P = P_0\left(1 - \frac{\hat{\epsilon}}{\hat{\kappa}}\right); && E_P = 0;\\
&\text{(iii)} && E_i = \frac{E_0\left(1 - \frac{\hat{\rho}}{\hat{\theta}}\right)}{\left(1 + \frac{\hat{\eta}}{\hat{\mu}}\right)}; && E_m = \frac{E_0\left(1 - \frac{\hat{\rho}}{\hat{\theta}}\right)}{\left(1 + \frac{\hat{\mu}}{\hat{\eta}}\right)}; && P = 0; && E_P = 0.
\end{aligned}$$

Solution (i) represents the trivial, non-angiogenic phenotype. It corresponds to tumour sub-regions in which angiogenesis does not take place. Solution (ii) corresponds to an alternative non-angiogenic steady state in which only free PCs are non-zero. This solution is physically realistic in regions of parameter space for which the PC death rate is smaller than the PC proliferation rate, $\frac{\hat{\epsilon}}{\hat{\kappa}} \leq 1$. The third steady state, (iii), is physically realistic when $\frac{\hat{\rho}}{\hat{\theta}} \leq 1$, i.e. the proliferation rate of immature ECs exceeds the death rate of immature ECs. Steady state (iii) is characterised by the coexistence of mature and immature ECs; this corresponds to a highly angiogenic vascular phenotype with no PC normalisation. The balance between mature and immature ECs depends on the parameters $\hat{\eta}$ and $\hat{\mu}$, which are coupled to the concentrations of bound Ang1 and Ang2 in the full model. Specifically, if $\hat{\eta} > \hat{\mu}$, then $E_m > E_i$ and vice-versa.

For the fourth and fifth steady states, all cell types have non-zero densities and the corresponding values of P, denoted P_+ and P_-. The steady states are known functions of P_+ and P_-:

$$\begin{aligned}
&\text{(iv),(v)} && E_i = \frac{E_0(1 - \frac{\hat{\rho}}{\hat{\theta}})(\nu + \hat{\epsilon})(\zeta P_\pm + \hat{\mu})}{(\nu + \hat{\epsilon} + \zeta P_\pm)(\hat{\eta} + \hat{\mu} + \zeta P_\pm)}, && E_m = \frac{\hat{\eta} E_i}{\zeta P_\pm + \hat{\mu}},\\
&&& P = P_\pm, && E_P = \frac{\zeta\left(1 - \frac{\hat{\rho}}{\hat{\theta}}\right) P_\pm}{\nu + \hat{\epsilon} + \zeta P_\pm},
\end{aligned}$$

where $P_\pm$ are given by

$$P_\pm = \frac{1}{2}\left[-a \pm \sqrt{a^2 - 4b}\right],$$

where

$$a = \left[\left(E_0\left(1 - \frac{\hat{\rho}}{\hat{\theta}}\right) - P_0\left(1 - \frac{\hat{\epsilon}}{\hat{\kappa}}\right)\right) + \frac{(\nu + \hat{\epsilon})}{\zeta}\right],$$

and

$$b = P_0\left[\frac{\hat{\epsilon}}{\hat{\kappa}}E_0\left(1 - \frac{\hat{\rho}}{\hat{\theta}}\right) - \left(1 - \frac{\hat{\epsilon}}{\hat{\kappa}}\right)\frac{(\nu + \hat{\epsilon})}{\zeta}\right].$$

The solutions for $P_\pm$ can be classified as follows:

Case 1 $a^2 > 4b \quad \rightarrow \quad P_\pm \in \mathbb{R}$:

Case 1.1 $b > 0$:

Case 1.1.1 $a < 0 \quad \rightarrow \quad P_+ > P_- > 0$: two positive roots;

Case 1.1.2 $a > 0 \quad \rightarrow \quad P_\pm < 0$: two negative roots;

Case 1.2 $b < 0$: one positive, one negative root;

Case 2 $a^2 < 4b \quad \rightarrow \quad P_+, P_- \in \mathbb{C}$: no real roots;

Case 3 $a^2 = 4b$:

Case 3.1 $b > 0$: repeated negative root;

Case 3.2 $b < 0$: repeated positive root.

We require for $E_P, E_i > 0$ that $\frac{\hat{\rho}}{\hat{\theta}} < 1$. For two real positive solutions for $P_\pm$ (**Case 1.1.1**) we require

$$a < 0 < b,$$

which is equivalent to

$$\frac{\hat{\kappa}}{\hat{\epsilon}}\left(\frac{\nu + \hat{\epsilon}}{\zeta}\right)\left(1 - \frac{\hat{\epsilon}}{\hat{\kappa}}\right) < E_0\left(1 - \frac{\hat{\rho}}{\hat{\theta}}\right) < P_0\left(1 - \frac{\hat{\epsilon}}{\hat{\kappa}}\right) - \left(\frac{\nu + \hat{\epsilon}}{\zeta}\right), \tag{2.21}$$

or

$$\frac{\nu + \hat{\epsilon}}{\zeta} < P_0\frac{\hat{\epsilon}}{\hat{\kappa}}\left(1 - \frac{\hat{\epsilon}}{\hat{\kappa}}\right),$$

and therefore, since $\nu, \hat{\epsilon}, \zeta > 0$, we must have $\frac{\hat{\epsilon}}{\hat{\kappa}} < 1$. Using the parameter values in Table 2.2 for all other parameters, condition (2.21) is not satisfied where $\frac{\hat{\rho}}{\hat{\theta}} < 1$ and $\frac{\hat{\epsilon}}{\hat{\kappa}} < 1$. Therefore the conditions for **Case 1.1.1** are not met and we do not expect two real, positive solutions for steady solutions (iv) and (v).

In **Case 1.2**, where $b < 0$, and for $\frac{\hat{\rho}}{\hat{\theta}} < 1$, the condition

$$\left(\frac{\hat{\kappa}}{\hat{\epsilon}} - 1\right)(\nu + \hat{\epsilon}) > \zeta E_0 \left(1 - \frac{\hat{\rho}}{\hat{\theta}}\right) > 0 \tag{2.22}$$

must hold for a biologically realistic solution for (iv) where $P_+ > 0$.

Parameter	Normalised value(s)	Units
$\hat{\rho}$	[0.001, 0.08] (0.02)	h^{-1}
$\hat{\epsilon}$	[0.01, 0.08] (0.02)	h^{-1}
$\hat{\eta}$	0.01	h^{-1}
$\hat{\mu}$	0.01	h^{-1}
$\hat{\theta}$	0.04	h^{-1}
$\hat{\kappa}$	0.04	h^{-1}
ζ	0.1	h^{-1}
ν	0.05	h^{-1}
E_0	1	dimensionless
P_0	0.5	dimensionless

Table 2.2: Normalised parameter values for analysis of the uncoupled cell dynamics sub-model. The default values for $\hat{\rho}$ and $\hat{\epsilon}$ are given in round brackets. The ranges of values used to generate Figure 2.4 are given in square brackets. See Table A.1 for sources of parameters.

2.3.2 Linear stability analysis

Since there are multiple steady states that are biologically realistic in some regions of parameter space, we perform a linear stability analysis in order to assess whether bistability may occur in some parameter regimes.

Figure 2.4 decomposes $\left(\frac{\hat{\rho}}{\hat{\theta}}, \frac{\hat{\epsilon}}{\hat{\kappa}}\right)$ parameter space into distinct regions based on where each of solutions (i)-(iv) is biologically feasible and/or linearly stable for the parameter values listed in Table 2.2.

The local stability of each steady state is determined in the standard way, by linearising the system of equations (2.17)-(2.20) around that steady state and de-

termining if the solution

$$(\tilde{E}_i, \tilde{E}_m, \tilde{E}_P, \tilde{P})e^{\psi t},$$

grows or decays. The latter is determined by the sign of the real part of ψ. The values for ψ are the eigenvalues of the associated Jacobian matrix of the linearised system, J, where

$$J = \begin{pmatrix} \tilde{\theta} - \hat{\rho} + \zeta P - \hat{\eta} & -\hat{\theta}\frac{E_i}{E_0} + \hat{\mu} & -\zeta E_i & -\hat{\theta}\frac{E_i}{E_0} + \nu + \hat{\epsilon} \\ \hat{\eta} & \zeta P - \hat{\mu} & -\zeta E_m & 0 \\ -\zeta P & -\zeta P & \tilde{\kappa} - \hat{\epsilon} - \zeta(E_i + E_m) & -\hat{\kappa}\frac{P}{P_0} + \nu \\ \zeta P & \zeta P & \zeta(E_i + E_m) & -(\nu + \hat{\epsilon}) \end{pmatrix},$$

evaluated at the steady state of interest, and where $\tilde{\theta} = \hat{\theta}\left(1 - \frac{(2E_i + E_m + E_P)}{E_0}\right)$, $\tilde{\kappa} = \hat{\kappa}\left(1 - \frac{(E_P + 2P)}{P_0}\right)$. If $\Re(\psi_j) < 0 \quad \forall j$, then the steady state solution is linearly stable. If $\Re(\psi_j) \geq 0$ for any j then the steady state solution is unstable.

We first analyse the linear stability of solutions (i)-(iii) (defined in Section 2.3.1), when one or more cell types are zero. Next, we analyse solution (iv), where all cell types coexist. The parameter combinations $\frac{\hat{\rho}}{\hat{\theta}}$ and $\frac{\hat{\epsilon}}{\hat{\kappa}}$ are used as bifurcation parameters and we examine the stability of the steady states in regions of parameter space where they are biologically feasible.

The eigenvalues of the Jacobian evaluated at the trivial steady state, (i), reveal that it is linearly stable for $\frac{\hat{\rho}}{\hat{\theta}} > 1, \frac{\hat{\epsilon}}{\hat{\kappa}} > 1$, but unstable otherwise. The eigenvalues, ψ, of the Jacobian evaluated at (i) are

$$\psi_{i1} = -(\nu + \hat{\epsilon}); \qquad \psi_{i2} = \hat{\kappa} - \hat{\epsilon};$$
$$\psi_{i3} = \frac{1}{2}\left[(\hat{\theta} - \hat{\rho} - \hat{\eta} - \hat{\mu}) + \sqrt{(\hat{\theta} - \hat{\rho} - \hat{\eta} - \hat{\mu})^2 + 4\hat{\mu}(\hat{\theta} - \hat{\rho})}\right];$$
$$\psi_{i4} = \frac{1}{2}\left[(\hat{\theta} - \hat{\rho} - \hat{\eta} - \hat{\mu}) - \sqrt{(\hat{\theta} - \hat{\rho} - \hat{\eta} - \hat{\mu})^2 + 4\hat{\mu}(\hat{\theta} - \hat{\rho})}\right].$$

The linear stability of (i) depends on the ratios $\frac{\hat{\rho}}{\hat{\theta}}$ and $\frac{\hat{\epsilon}}{\hat{\kappa}}$ as can be seen by the following argument. Firstly, $\psi_{i2} < 0$ when $\frac{\hat{\epsilon}}{\hat{\kappa}} > 1$. Next, if $\frac{\hat{\rho}}{\hat{\theta}} < 1$ then ψ_{i3}, ψ_{i4} are real and positive, whereas if $\frac{\hat{\rho}}{\hat{\theta}} > 1$ then the real part of ψ_{i3}, ψ_{i4} is negative. Therefore for linear stability, we require $\frac{\hat{\rho}}{\hat{\theta}} > 1$ and $\frac{\hat{\epsilon}}{\hat{\kappa}} > 1$.

It is biologically realistic that when the death rates of ECs and PCs are both

greater than their respective proliferation rates, there is a stable steady state where $E_i = E_m = P = E_P = 0$. In the other regimes, where the proliferation rates of ECs and/or PCs are greater than the corresponding death rates, the trivial steady state is linearly unstable.

For steady states (ii) and (iv), the eigenvalues are calculated numerically in Matlab and, for (iii), they are calculated analytically. From the signs of the eigenvalues evaluated at (ii), we deduce that the steady state solution (ii), where $E_i = E_m = E_P = 0$, and $P > 0$, is linearly stable in region D (defined in Figure 2.4), where $\frac{\hat{\rho}}{\hat{\theta}} > 1$ and $\frac{\hat{\epsilon}}{\hat{\kappa}} < 1$ in the current parameter regime. Biologically, this is a non-angiogenic phenotype and suggests in the absence of ECs, free PCs remain in the tumour region.

The eigenvalues of the Jacobian evaluated at (iii) are:

$$
\begin{aligned}
\psi_{iii1} &= -(\eta + \hat{\mu}),\\
\psi_{iii2} &= \frac{\hat{\mu}(\hat{\rho} - \hat{\theta})}{\hat{\eta} + \hat{\mu}},\\
\psi_{iii3} &= -\frac{1}{2}\left(\nu + 2\hat{\epsilon} - \hat{\kappa} + \zeta E_0\left(1 - \frac{\hat{\rho}}{\hat{\theta}}\right)\right)\\
&\quad + \frac{1}{2}\sqrt{\left(\nu + 2\hat{\epsilon} - \hat{\kappa} + \zeta E_0\left(1 - \frac{\hat{\rho}}{\hat{\theta}}\right)\right)^2 - 4\left((\nu + \hat{\epsilon})(\hat{\epsilon} - \hat{\kappa}) + \hat{\epsilon}\zeta E_0\left(1 - \frac{\hat{\rho}}{\hat{\theta}}\right)\right)},\\
\psi_{iii4} &= -\frac{1}{2}\left(\nu + 2\hat{\epsilon} - \hat{\kappa} + \zeta E_0\left(1 - \frac{\hat{\rho}}{\hat{\theta}}\right)\right)\\
&\quad - \frac{1}{2}\sqrt{\left(\nu + 2\hat{\epsilon} - \hat{\kappa} + \zeta E_0\left(1 - \frac{\hat{\rho}}{\hat{\theta}}\right)\right)^2 - 4\left((\nu + \hat{\epsilon})(\hat{\epsilon} - \hat{\kappa}) + \hat{\epsilon}\zeta E_0\left(1 - \frac{\hat{\rho}}{\hat{\theta}}\right)\right)}.
\end{aligned}
$$

From ψ_{iii3} and ψ_{iii4} we identify a region of linear stability of (iii) bounded below by $\frac{\hat{\rho}}{\hat{\theta}} = 1$, and

$$\left(\frac{\hat{\kappa}}{\hat{\epsilon}} - 1\right)(\nu + \hat{\epsilon}) < \zeta E_0\left(1 - \frac{\hat{\rho}}{\hat{\theta}}\right), \tag{2.23}$$

which encompasses all of region A and a subset of region C in the current parameter regime. The region of parameter space corresponding to this condition for linear stability shares a boundary with (2.22), which bounds the region of existence of (iv). This is plotted in Figure 2.4.

From the signs of the eigenvalues of the Jacobian evaluated numerically at steady state (iv), we deduce that solution (iv) is linearly stable for all parameter values where it is feasible, as illustrated in Figure 2.4. The bifurcations observed at the transitions between steady state regimes are all transcritical bifurcations.

In Figure 2.4 we summarise the results of our steady state and linear stability analyses by showing where in $\left(\frac{\hat{\rho}}{\hat{\theta}}, \frac{\hat{\epsilon}}{\hat{\kappa}}\right)$ parameter space each of solutions (i)-(iv) is physically realistic and linearly stable.

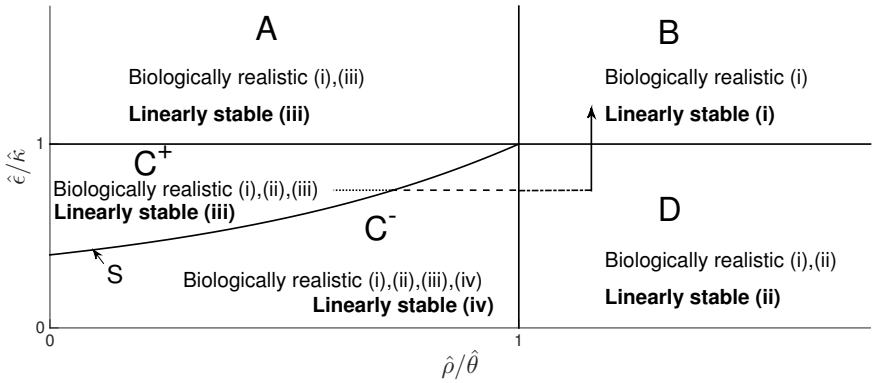


Figure 2.4: Schematic diagram showing how the existence and linear stability of steady states (i)-(iv) changes as parameters $\left(\frac{\hat{\rho}}{\hat{\theta}}, \frac{\hat{\epsilon}}{\hat{\kappa}}\right)$ vary. Region C is subdivided into two regions by the curve S on which $\left(\frac{\hat{\kappa}}{\hat{\epsilon}} - 1\right)(\nu + \hat{\epsilon}) = \zeta E_0 \left(1 - \frac{\hat{\rho}}{\hat{\theta}}\right)$ (see condition (2.23) for details). The arrow shows an example of a path in $\left(\frac{\hat{\rho}}{\hat{\theta}}, \frac{\hat{\epsilon}}{\hat{\kappa}}\right)$ space that transitions from an angiogenic to a non-angiogenic phenotype (for details, see main text). The system is always monostable. Parameter values as per Table 2.2.

Our analysis showns that the cell dynamics sub-model from equations (2.17)-(2.20) does not exhibit bistability in the current parameter regime (see Figure 2.4). Moreover, the transitions between regions defined in Figure 2.4 are of biological interest. They indicate how, when treating the angiogenic phenotypes (iii) or (iv), the ratios of $\frac{\hat{\rho}}{\hat{\theta}}$ and $\frac{\hat{\epsilon}}{\hat{\kappa}}$ can be modulated to switch to a non-angiogenic phenotype such as (i) or (ii).

An example of a path in $\left(\frac{\hat{\rho}}{\hat{\theta}}, \frac{\hat{\epsilon}}{\hat{\kappa}}\right)$ space that could lead from an angiogenic phenotype to a non-angiogenic phenotype is shown by the arrow in Figure 2.4, which starts in region C^+, where (iii) is linearly stable, and passes through regions C^-

and D, ending in B, where the trivial non-angiogenic solution (i) is linearly stable. In region C^+, steady states (i) and (ii) are biologically feasible, but unstable. The real parts of the eigenvalues of the Jacobian evaluated at (iii) are all negative in region C^+, but for increasing $\frac{\hat{\rho}}{\hat{\theta}}$ and fixed $\frac{\hat{\epsilon}}{\hat{\kappa}}$, the real part of one of the eigenvalues of the Jacobian becomes positive, so (iii) is no longer linearly stable after the curve S is crossed. Furthermore, as S is crossed, the solutions for (iv) become biologically feasible and linearly stable, and all cell types coexist in this region. Continuing to increase $\frac{\hat{\rho}}{\hat{\theta}}$ at fixed $\frac{\hat{\epsilon}}{\hat{\kappa}}$, the concentrations of E_i, E_m and E_P decrease until they all become zero at $\frac{\hat{\rho}}{\hat{\theta}} = 1$. At this point, solution (iv) reduces to solution (ii). In region D, the real parts of the eigenvalues of the Jacobian evaluated at (ii) are negative. Now increasing $\frac{\hat{\epsilon}}{\hat{\kappa}}$ for some fixed value of $\frac{\hat{\rho}}{\hat{\theta}} > 1$, steady state (ii) reduces to steady state (i) when $\frac{\hat{\epsilon}}{\hat{\kappa}} = 1$, and in region B, the trivial, non-angiogenic steady state solution (i) is linearly stable.

The concentrations of the cell types within the stable steady states are shown in Figure 2.5. The plots indicate that there are no discontinuities at the boundaries between parameter regions.

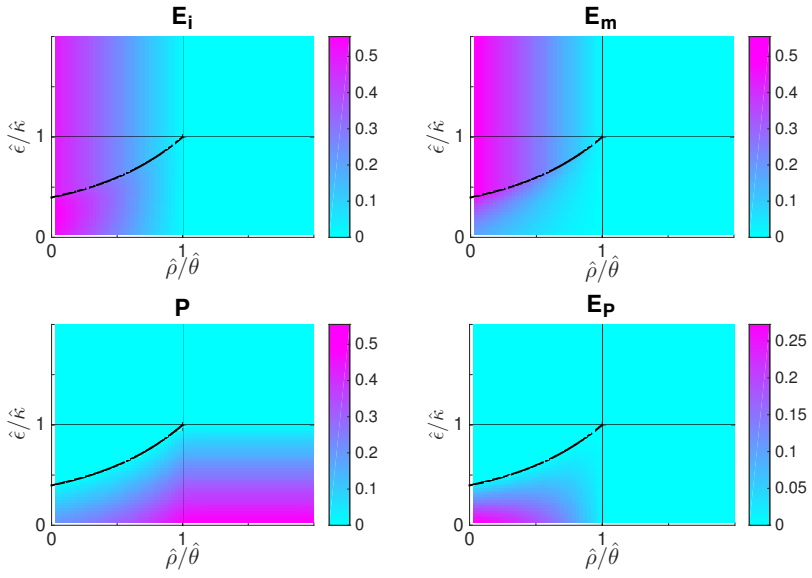


Figure 2.5: Plots to show the stable steady state solutions for E_i, E_m, P and E_P according to the simplified model equations (2.17)-(2.20). The boundary of the region of feasibility of (iv) is shown by a thick black line and arises from inequality (2.23). Parameter values as per Table 2.2.

Summary of linear stability analysis

- There are four biologically feasible ($E_i, E_m, P, E_P \geq 0$) steady state solutions to the simplified cell dynamics sub-model in the current parameter regime. One additional solution is not feasible in the current parameter regime but may be feasible in others.
- The feasibility and stability of the steady state solutions depend on the ratios $\frac{\hat{\rho}}{\hat{\theta}}$ and $\frac{\hat{\epsilon}}{\hat{\kappa}}$.
- There are no regions of bistability in the current parameter regime, and all steady states are linearly stable in exactly one region of the positive quadrant of $\left(\frac{\hat{\rho}}{\hat{\theta}}, \frac{\hat{\epsilon}}{\hat{\kappa}}\right)$ space.

In the next section, cell density plots will be directly compared with others generated from the full model.

2.4 Full model results

In this section we revert to the full model, identifying conditions under which its behaviour is the same as that of the simplified one. We use experimental data to qualitatively validate the model predictions, and we simulate AA treatment for various pre-treatment phenotypes.

2.4.1 Corroboration of steady state results

To compare the stable steady states of the full model with those of the simplified model, equations (2.1)-(2.16) were solved for values of the EC proliferation rate, θ, and the PC proliferation rate, κ, that span several orders of magnitude (with the values of all other parameters fixed). The steady state concentrations of E_i, E_m, P, E_P were recorded and the results are shown in Figure 2.6.

In Figure 2.6, the parameter space defined by the EC and PC proliferation rates, θ and κ, is divided into distinct regions where model simulations settle into

linearly stable steady states. We note that there may be more than one steady state that is linearly stable in each parameter regime for the full model. Some similarities between the steady state behaviour of the full model and the simplified model shown in Figure 2.5 are as follows: there is a region of parameter space in which free and bound PCs are non-zero and the bounding region given by the curve marked S in Figures 2.1 and 2.5 is qualitatively similar in Figure 2.6; immature EC density attains its maximum for large θ and small κ; mature and immature ECs reach higher densities in the steady state for large θ; free PCs have a higher density for small θ and the EC/PC complex has a larger density for large θ.

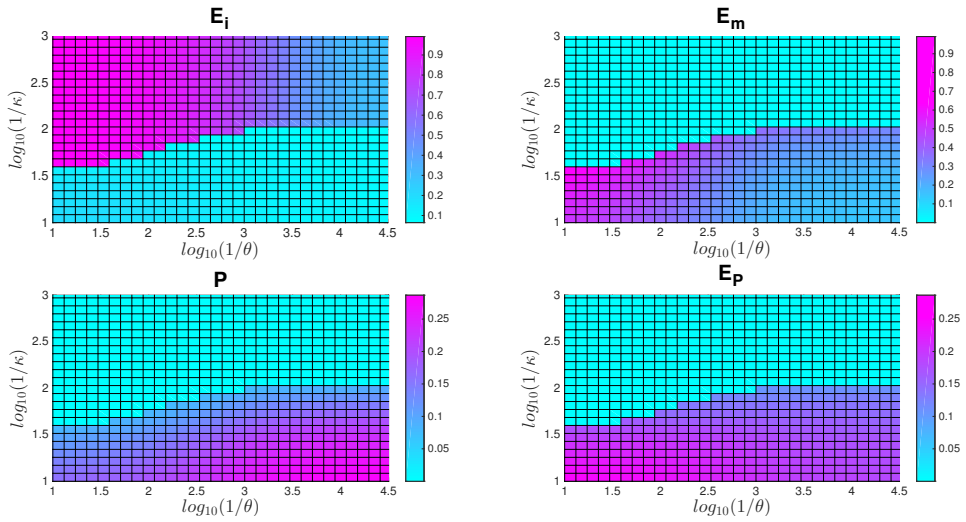


Figure 2.6: Stable steady state solutions for E_i, E_m, P and F using the full model (equations (2.1)-(2.16)) for values of $10^{-4.5} \leq \theta \leq 10^{-1}$ and $10^{-3} \leq \kappa \leq 10^{-1}$ and with all other parameters as per Table A.1. We assume that equations (2.1)-(2.16) have reached a steady state when the time derivative of the full system is less than $10^{-5}h^{-1}$.

The most notable discrepancy between Figures 2.5 and 2.6 is that $E_m \ll E_i$ for low κ (where no PCs are present), and $E_i \ll E_m$ for high κ (where PCs are present) in Figure 2.6. In contrast, in Figure 2.5 for low $\frac{\hat{\rho}}{\hat{\theta}}$ and low $\frac{\hat{\epsilon}}{\hat{\kappa}}$, immature ECs and PCs coexist at similar densities. The absence of immature ECs in regions with high PC concentration in the stable steady states of the full model can be explained in terms of the biochemical interactions between Ang1 and Ang2. Where it exists, steady state (iii) of the simplified model takes the form $E_m = \frac{\hat{\eta}}{\hat{\mu}} E_i$; in other words, the ratio of immature to mature vessels is the ratio of the de-maturation to maturation

functions. For the full model, PCs produce Ang1 that is needed for maturation, while Ang2 produced by immature ECs leads to further de-maturation (a positive feedback loop for Ang2 induces de-maturation). Consequently,

$$P_T = 0 \implies \mu \, \mathrm{H}\left(\frac{b_{a_2}}{b_{a_1}}, \lambda\right) \gg \eta \, \mathrm{H}\left(\lambda, \frac{b_{a_2}}{b_{a_1}}\right) \implies E_i \gg E_m,$$

and

$$P_T \neq 0 \implies \eta \, \mathrm{H}\left(\lambda, \frac{b_{a_2}}{b_{a_1}}\right) \gg \mu \, \mathrm{H}\left(\frac{b_{a_2}}{b_{a_1}}, \lambda\right) \implies E_m \gg E_i.$$

In both cases, one EC type becomes dominant. Figure 2.6 also reveals that a very small value of θ would be required to observe steady states (i) and (ii).

2.4.2 Anti-angiogenic therapies

The application of AA drugs to tumours has revealed that many candidate drugs normalise vessels and stimulate vessel regression [70]. While the anti-tumour benefit of normalised vessels remains unclear, it has been suggested that they aid the delivery of chemotherapeutic agents, and/or improve oxygen delivery and thereby reduce hypoxia-induced VEGF production [95]. Consequently, an alternative goal of AA therapy is to improve vessel normalisation while decreasing vessel density compared to the pre-treatment case. In the context of our model, this corresponds to a post-therapy phenotype (iv), with high normalisation.

The simplified and full models can be used to identify paths in parameter space that connect the basin of attraction of a highly angiogenic steady state (for example, solutions (iii) and the coexistence steady state, (iv), with low normalisation), to an alternative steady state solution (such as (i) or steady state (iv) characterised by a high degree of vessel normalisation). Highly angiogenic vascular networks are associated with poor clinical outcome, whereas less dense, normalised networks are typically associated with a more positive clinical outcome (see Table 1 in [95] for a summary).

In the following sections, we simulate the effects of anti-VEGF, anti-Ang2 and a combined anti-VEGF/anti-Ang2 antibody on vessels of two alternative pre-treatment

phenotypes. Next, we investigate transitions from highly angiogenic, (iii), or angiogenic, (iv), pre-treatment phenotypes to non angiogenic, (i), or the highly normalised region of (iv), end-points.

Anti-VEGF and anti-Ang2 antibodies: Mature pre-treatment phenotype

In this section, we perform a qualitative validation of the full model against experimental data.

In experiments described in [96], KPL-4 tumour-bearing mice were treated with either an anti-VEGF antibody, an anti-Ang2 antibody, a bispecific anti-VEGF/anti-Ang2 antibody (CrossMab) or a control treatment after the mean tumour volume for each group reached 150mm^3. The number of vessels per mm^3 of viable tumour tissue and the PC coverage of vessels were quantified by histology at the end of the study (day 63). Animals treated with anti-VEGF or CrossMab treatment had lower vessel densities than the control group on average, but the result was not statistically significant ($p> 0.05$) due to large variability and a small sample size. PC coverage was greater in all treatment groups compared to the control group, and treatment with CrossMab resulted in a statistically significant ($p< 0.05$) increase in PC coverage compared to anti-VEGF treatment, anti-Ang2 treatment and the control group. The experimental levels of total EC density and PC coverage are superimposed on our simulated results in Figure 2.7.

Since PCs were present for all experimental groups, we focus on the coexistence pre-treatment phenotype. Anti-VEGF antibodies are known to neutralise free VEGF, while anti-Ang2 antibodies neutralise free Ang2 and CrossMab neutralises both ligands [96]. We simulate anti-VEGF therapy by increasing the VEGF clearance rate, δ_v, and anti-Ang2 therapy by increasing the Ang2 clearance rate, δ_{a_2}. This simple approach avoids the need for new variables and parameters in the model. CrossMab treatment is simulated by increasing both clearance rates simultaneously. In the absence of detailed experimental data, we are unable to fully parametrise our model. Consequently, we do not claim that our model can generate quantitative

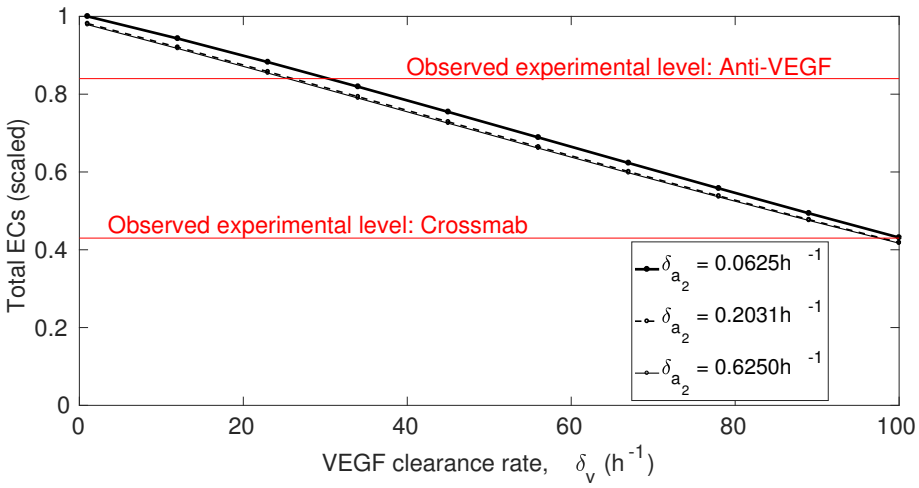
results, although we can validate its qualitative predictions against the observations of [96].

Using initial conditions corresponding to steady state (iv), anti-VEGF and anti-Ang2 therapies were simulated for a range of values of δ_v and δ_{a_2}. The simulation results presented in Figure 2.7 show that, as expected, anti-VEGF treatment leads to a decrease in vessel density and an increase in PC coverage, in line with experimental results (also indicated on the plots) [96]. Increasing the rate of Ang2 clearance also increases PC coverage in the steady state. The effect of anti-Ang2 therapy on PC coverage saturates when the PDGF concentration exceeds the value at which all extracellular Ang2 is neutralised. While simulations predict that the addition of anti-Ang2 therapy to anti-VEGF therapy will not reduce the total EC density, (see Figure 2.7a), it will increase PC coverage (see Figure 2.7b).

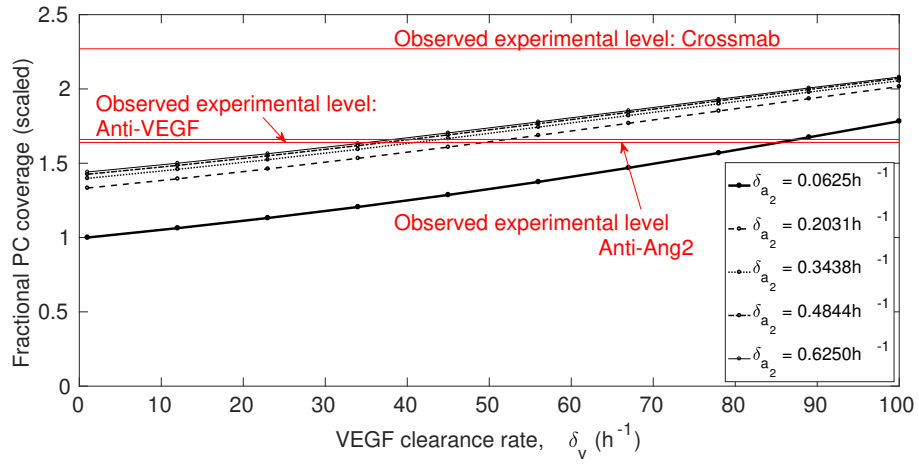
In conclusion, the full model produces results in qualitative agreement with experimental data for PC coverage following anti-angiogenic treatment. Although experimental results showed a decrease in vessel density following CrossMab therapy compared to anti-VEGF therapy alone, as shown in Figure 2.7, the result was not statistically significant. Our simulations, predict that CrossMab therapy will not lead to a larger decrease in EC density than anti-VEGF therapy alone.

Model predictions: Immature pre-treatment phenotype

We use the full model to predict the impact of anti-VEGF, anti-Ang2 and combined treatments on an immature vessel network. Figure 2.8 shows the stable ($E_m + E_P$) and immature (E_i) cell densities after initiation of anti-VEGF, anti-Ang2 and Cross-Mab treatments. Simulation of anti-VEGF treatment results in a decrease in immature vessel density, but does not effect a transition from the immature vessel phenotype, i.e. only immature ECs have non-zero density. Simulation of anti-Ang2 treatment leads to an initial "lag" period, during which there is a small reduction in immature EC density, followed by a transition to a normalised phenotype approximately 100 days post treatment. Close inspection of the cell densities and biochemical variables during this lag period (results not shown) reveals that for



(a)



(b)

Figure 2.7: Simulations of equations (2.1) - (2.16) for values of the VEGF clearance rate $1h^{-1} \leq \delta_v \leq 100h^{-1}$ (indicated by the x axis) and the Ang2 clearance rate $0.0625h^{-1} \leq \delta_{a_2} \leq 0.625h^{-1}$ (indicated by different line styles). (a) Steady state values for total ECs, E_T, divided by the total ECs for the control simulation, from numerical simulations indicated by black points with interpolated line, and the experimental results are indicated in red. (b) Steady state values of fractional PC coverage (E_P/E_T), divided by the PC coverage for the control simulation, from numerical simulations, are indicated by black points with interpolated line. Experimental results were scaled by dividing the EC density and PC coverage post-treatment results by the results for the control at the same time point. These are indicated in red. Initial conditions are the steady state (iv).

anti-Ang2 treatment, PCs (which have a very low, but non-zero density) begin to proliferate since there is less free Ang2 to suppress them. The PCs produce Ang1, which binds to Tie2 receptors, eventually reaching a concentration that activates the maturation switch. This leaves fewer immature ECs producing Ang2, and therefore PC suppression remains low, allowing their rapid growth. Decreasing the threshold ratio of $\frac{\text{bound Ang2}}{\text{bound Ang1}}$ for maturation delays the switch from an immature to a mature phenotype (results not shown) which supports this explanation.

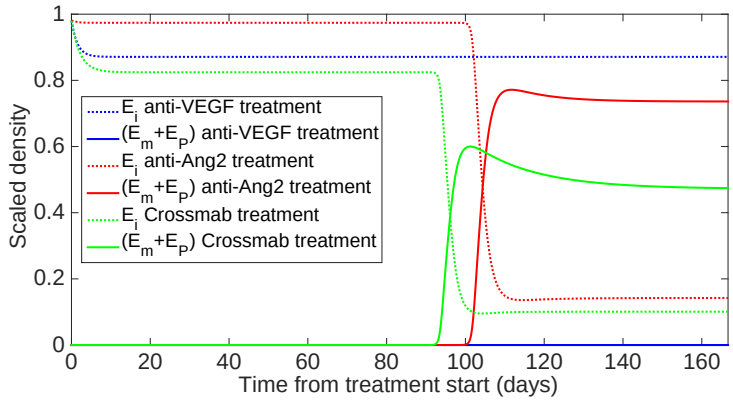


Figure 2.8: Simulations of equations (2.1) - (2.16) with anti-VEGF, anti-Ang2 and CrossMab treatment where the initial conditions are given by the immature pre-treatment phenotype (iii). For anti-VEGF treatment, $\delta_v = 60h^{-1}$ and for anti-Ang2 treatment $\delta_{a_2} = 0.4h^{-1}$, for CrossMab treatment $\delta_v = 60h^{-1}$ and $\delta_{a_2} = 0.4h^{-1}$ and treatment begins at day 0. Parameters as per Table A.1 except $\delta_{a_2} = 0.02h^{-1}$.

For an immature pre-treatment phenotype, anti-VEGF and anti-Ang2 monotherapy simulations decreased the total EC density by 11% and 10% respectively, while CrossMab therapy simulations decreased the total EC density by 41%, as seen in Figure 2.8. In this case, there is a strong synergistic effect when the two AA therapies are combined, i.e. the sum of the anti-vascular effects due to anti-VEGF and anti-Ang2 therapy alone are less than the total effect from combined anti-VEGF/anti-Ang2 therapy.

Our model simulations predict that the switch to a normalised phenotype, with PC coverage, occurs after administration of either anti-Ang2 or CrossMab therapies. The fractional PC coverage increases after simulations of anti-Ang2 therapy and

CrossMab therapy, but not anti-VEGF therapy.

Phenotype-specific treatment recommendations

In this subsection we identify parameters in the full model that could be varied to effect a transition from an angiogenic to a non-angiogenic phenotype. The parameters $\hat{\theta}, \hat{\rho}, \hat{\kappa}$ and $\hat{\epsilon}$ that appear in the simplified model are coupled to upstream biochemical processes in the full model, and the biochemical parameters can be perturbed to effect the desired transition from one behaviour regime to another.

The EC proliferation rate depends on the fractional occupancy of VEGFR2 receptors in the full model. Perturbations to parameters that control VEGF production, binding or decay should aid a transition from a stable coexistence steady state to one where E_i and E_m are small (from the left to the right side of Figure 2.6). Similarly, since the proliferation rate of PCs depends on the fractional occupancy of PDGFR-β receptors, perturbations to parameters that control PDGF production, binding and decay should aid a transition from the coexistence steady state (iv) to one with a lower PC density (from bottom to top of Figure 2.6). For a normalised angiogenic pre-treatment phenotype, we perturb VEGF and PDGF related parameters simultaneously to approach the least angiogenic phenotype (i).

Figure 2.9 shows how simultaneous perturbations to VEGF and PDGF associated parameters impact a normalised pre-treatment phenotype (steady state (iv)). A transition from the coexistence steady state to an immature steady state with low EC density can be achieved by decreasing the VEGF production rate, α_v, and perturbing one of the PDGF associated parameters α_p, k_{on}^p or δ_p.

For the "runaway angiogenesis" highly immature pre-treatment phenotype (iii) where $E_i \gg E_m$ and $P, E_P \approx 0$, we decrease VEGF associated parameters to decrease E_T, moving from the upper left to the upper right region of Figure 2.6. Results are shown in Figure 2.10: for an immature pre-treatment phenotype in the current parameter regime, a perturbation to the VEGF production rate, α_v, has a stronger anti-angiogenic effect than perturbations to the VEGF binding rate, k_{on}^v, or VEGF decay rate, δ_v (results for perturbations to δ_v are similar to those for perturbations

to k_{on}^{v}, and are therefore not shown). From this result we propose that decreasing the VEGF production rate by a factor of 50 is preferable to decreasing the VEGF binding rate by a factor of 100 or increasing the VEGF clearance rate by a factor of 100 for effecting a transition from a highly angiogenic pre-treatment phenotype to a non-angiogenic phenotype.

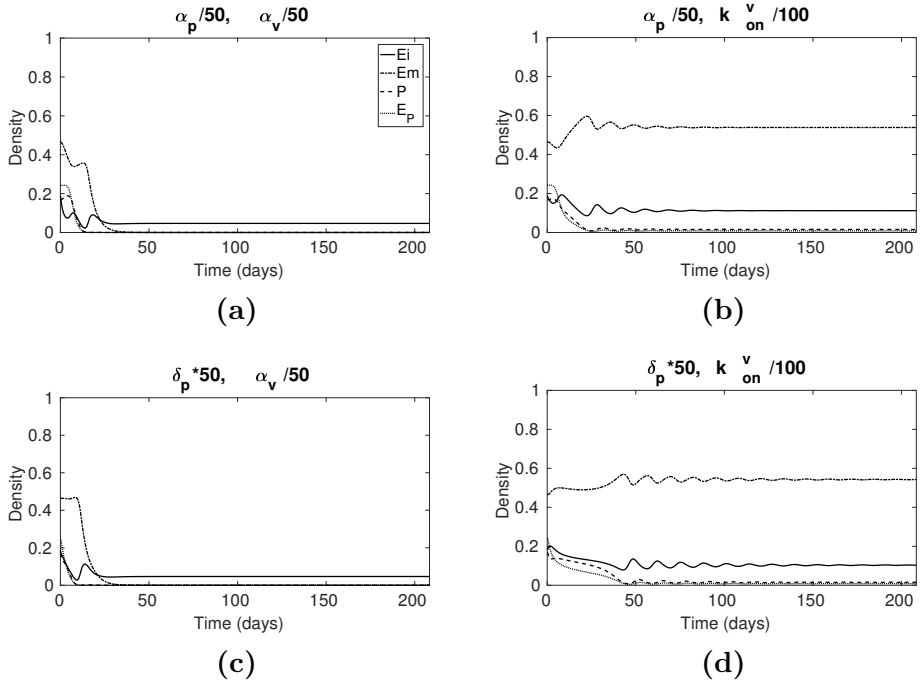
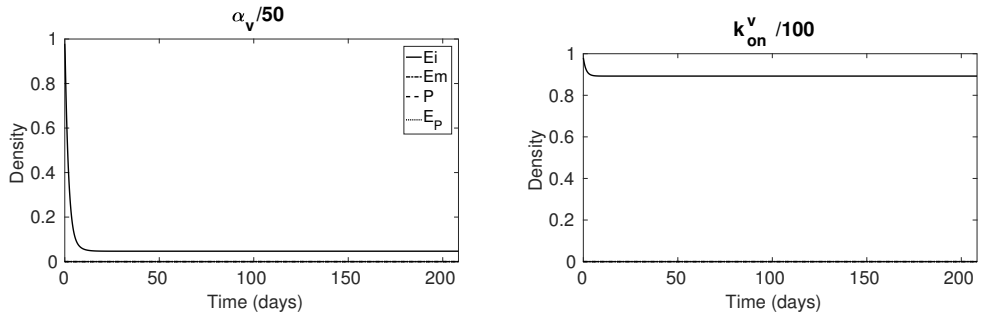


Figure 2.9: Simulations of theoretical anti-angiogenic treatments applied to equations (2.1)-(2.15), when the initial conditions correspond to a steady state of type (iv), all unperturbed parameters are as per Table A.1 and treatment begins at t=0. In (a) and (c), all cell types except E_i are equal to zero. Parameters are as per the default parameter set up until $t = 0$ when the relevant parameters undergo a 'step' change as indicated in individual plot titles.

In preclinical experiments, antibodies for VEGF and PDGF are administered at a dose such that a large percentage of the free ligand is neutralised, and tumour growth can be inhibited by up to 90% [58]. The magnitude of the perturbations to the clearance rates of VEGF and PDGF in Figures 2.9 and 2.10 are such that the free VEGF or PDGF concentrations decrease to less than 30% of their pre-treatment concentrations, and that the fractional occupancy of VEGF receptors falls below the threshold for EC proliferation. Similarly, inhibitors of downstream effects of ligand



(a) **(b)**

Figure 2.10: Simulations of theoretical anti-angiogenic treatments applied to equations (2.1)-(2.15), when the initial conditions correspond to a steady state of type (iii) for all variables. All unperturbed parameters are as per Table A.1, except $\kappa = 0.008h^{-1}$, and treatment begins at $t = 0$. In both cases, all cell types except E_i are equal to zero. Parameters are as per the default parameter set up until $t = 0$ when the relevant parameters undergo a 'step' change as indicated in individual plot titles.

binding significantly reduce the receptor occupancy [160]. The magnitude of the perturbations to binding rates of VEGF and PDGF are such that the post-treatment occupancy of receptors is around 19%, which is below the threshold for proliferation in our model. The orders of magnitudes for our perturbations to the production rates of VEGF and PDGF by tumour cells and ECs, respectively, are estimates to reflect *in-vitro* predictions.

2.5 Discussion

Both experimental and clinical results have shown that anti-angiogenic therapies are of limited value as monotherapies, and searches for biomarkers of angiogenic response to treatment have had limited success. We have attempted to improve our understanding of how these results may arise from the biochemical basis of angiogenesis.

In this chapter, we have developed an ODE model representing the interactions between processes involved in angiogenesis, and the impact of the interactions on the effects of anti-angiogenic therapies on neovasculature. We have shown that the model gives results that are qualitatively consistent with the limited available

experimental data. Quantitative validation cannot yet be achieved due to high parameter dimensionality and poor data availability. A simplified version of the model was used to identify the expected long-term behaviour of the full model.

The steady state behaviours exhibited by the full and simplified models are physically realistic, representing vessel phenotypes (for high quality 3D images of tumour vessels that exhibit immature and normalised phenotypes, see [49], and for our interpretation of phenotypical features, see Figure 2.1). We acknowledge that the full model may exhibit other steady state solutions in addition to the four solutions considered above. However, the high dimensional nature of the parameter space makes an analytical treatment of the full model impractical.

Simulation of AA treatment with the full model includes regulatory dependencies, which it is not possible to capture in the simplified model. Transitions from angiogenic to non-angiogenic phenotypes are considered as an indication for response to treatment. If measurable, the pre- and post-treatment phenotypes of vascular sub-regions could be used as a biomarker of response to treatment for preclinical experiments.

The conclusions that we draw from our investigations are summarised below:

1. The simplified model identifies four possible long term behaviours for ECs and PCs in the parameter regimes studied. Two behaviours are angiogenic and two are non-angiogenic. The regions of parameter space in which these solutions exist and are locally stable can be determined. The full model exhibits similar long-term behaviours.

2. The full model is in good qualitative agreement with experimental results in which VEGF, Ang2 and combined VEGF/Ang2 inhibition stimulate an increase in PC coverage. We note that our model may not be unique in its qualitative agreement with the simplified model, and a simpler model may produce similar results.

3. A transition from the normalised angiogenic steady state (iv) to the non-angiogenic steady state (i) can be effected by decreasing the VEGF and

PDGF production rates or by increasing the rate of PDGF clearance (see Figure 2.9).

4. A transition from the runaway angiogenic steady state (iii) to the non-angiogenic steady state (i) can be effected by decreasing the VEGF production rate (see Figure 2.10).

5. According to our model in the current parameter regime, combination anti-VEGF/anti-Ang2 therapy has a synergistic effect when administered to a highly angiogenic pre-treatment phenotype, but not when administered to a normalised pre-treatment phenotype as shown in Figure 2.7.

Our model was inspired by an earlier model proposed by Zheng *et al.*, which accounts for similar biochemical variables (VEGF, Ang1, Ang2, PDGF) but places greater emphasis on the biomechanical aspects of one-dimensional vessel growth such as friction and sprout elongation [191]. The authors compare model outputs with experimental corneal angiogenesis data. Given the rationale that simplifying some aspects of the biology would yield a model that is analytically tractable, and in the absence of spatially resolved data with which to validate our model, we chose to adopt a spatially averaged approach. This approach led to a significant reduction in the total number of parameters in our model compared to [191] at the expense of spatial information. We adapted several features for our model, such as Ang2 dependent EC proliferation, the generation of receptors as cells proliferate, and loss as they die and the details of the exocytosis of Ang2 from WPBs. We also developed a new cell dynamics sub-model from which we gained insight into possible long term model behaviours.

The identification of distinct vascular phenotypes has formed the basis of our conclusions. We anticipate robustness of our simulated treatment results as it is the end states rather than the transients that are most important for our conclusions, and these end states are well understood from the simplified model analysis. We note that more long term behaviour regimes may exist for the full model. Several mathematical models of angiogenesis recommend treatment on a one-size-fits-all

basis, where treatment is applied to only one pre-treatment phenotype [21, 93, 191], whereas we have taken into account the effects of treatments on different vascular phenotypes.

Our model does not capture tumour spatial heterogeneity, since it represents a small, well-mixed volume of tumour tissue. The phenotypes described in this chapter apply to an individual, approximately homogeneous portion of the tumour, and we envision that a tumour would be made up of several such sections that exhibit different phenotypes. In reality, a tumour contains sections with different characteristics, and these regions are physically connected. In Chapter 5 we develop a spatial model of vascular tumour growth that underlines some conditions under which spatial heterogeneity in tumour and vessel cells can arise.

In addition to the non-spatial nature of our model, we are limited by a lack of experimental data with which to estimate system parameters and validate our model. Accurate parametrisation and model validation are often challenges that face modellers of biological systems. Many of the parameter values in the full model are estimated from the resultant model behaviour, or taken from *in-vitro* studies, as described in detail in Appendix A.

The experimental study that we used to compare to our model simulations showed that CrossMab treatment or anti-VEGF treatment led to a significant decrease in primary tumour volume, but anti-Ang2 treatment did not. The inclusion of tumour cells in our model could enhance the understanding of the role played by angiogenesis in the growth and spread of cancer cells. Since tumour size is measured in most preclinical experiments relating to anti-angiogenic therapies, further validation of our model may be possible if a tumour compartment were included. Tumour cells are incorporated in the models in the following chapters in order to gain insight into the interactions between the tumour and its vasculature.

In Chapter 3 we develop a simple, spatially-averaged model of vascular tumour growth, motivated by preclinical data from AA-treated mice, and we simplify the interactions that constitute vessel normalisation from the model presented in this chapter in order to use the experimental data to identify the time at which vessel

normalisation occurs. Where the model presented in this chapter focusses on the early stages of vascular formation, in the following chapter, we assume that the tumour has already established its vasculature.

Chapter 3

Mixed effects modelling of preclinical tumour size data to identify transient dynamics

Much of the work in this chapter has been published in Clinical Pharmacology and Therapeutics: Pharmacometrics and Systems Pharmacology (CPT:PSP) [87].

3.1 Introduction

In the previous chapter we developed a spatially averaged model of the early stages of angiogenesis, accounting for growth factors, pericyte cells and mature and immature endothelial cells. In this chapter we focus on the growth of a tumour with established vasculature. We use a quantitative systems pharmacology (QSP) approach to develop a simple, data driven ordinary differential equation (ODE) model of vascular tumour growth in mice who are treated with anti-angiogenic (AA) therapy.

It is now clear that anti-angiogenic therapy not only causes vascular regression, but also affects processes that include vessel permeability, perfusion, diameter and pericyte coverage; and thereby normalises the vasculature [94]. It has been suggested that vessel normalisation plays a key role in tumour progression, since it

may enhance the delivery of oxygen and nutrients to the tumour microenvironment [95]. There is evidence that anti-angiogenic drug induced vessel normalisation increases the efficacy of chemotherapy and radiotherapy during a finite time window [47, 128]. If this normalisation window were identified for individual patients, then combination treatment schedules could be designed that coordinate administration of chemotherapy or radiotherapy with the normalisation window to maximise the therapeutic response.

Normalisation has been observed in preclinical models of anti-angiogenic therapy both from histology [96, 169] and via real-time imaging methods such as window chamber assays [176, 189]. For reviews on the role of normalisation in neovascular development, see [31] and [70]. Evidence from mouse xenograft studies suggests that vessel normalisation is transient: it begins shortly after the onset of anti-angiogenic therapy and ends a few days later [48, 185]. Furthermore, some clinical studies are consistent with anti-angiogenic therapy stimulating a reduction in vessel permeability for glioblastoma [18] and rectal cancer [183]. In both [185] and [48] radiotherapy was found to be most efficacious when administered within the transient window of increased tumour oxygenation. In particular, in [185] a synergistic tumour growth delay was observed when radiotherapy was administered 4-6 days after the first dose of anti-angiogenic therapy. It has also been suggested that normalised vessels allow efficient delivery of chemotherapy since improved perfusion allows effective extravasation of small molecules [47, 49].

Bevacizumab is an anti-vascular endothelial growth factor (VEGF) antibody that has been approved for treatment of numerous cancers including renal cell carcinoma, non-small-cell lung cancer and colorectal cancer. Vanucizumab is a bispecific antibody that recognises VEGF with one arm (based on bevacizumab) and angiopoietin-2 (Ang2) with the other arm (based on LC06, an Ang2 specific antibody). Vanucizumab is currently in Phase 2 trials to treat locally advanced or metastatic solid tumours (NCT01688206), and in combination with FOLFOX for metastatic colorectal cancer (NCT02141295). It is thought that since both VEGF and Ang2 promote angiogenesis, simultaneous inhibition of the ligands will result

in an additive or even synergistic effect on tumour vessel regression [96]. Anti-angiogenic therapies are principally used in combination with cytotoxic therapies or radiotherapy. It has been shown that the timing of such concomitant treatments is important for the therapeutic outcome in preclinical experiments [47, 128]. In order to further elucidate some of the mechanisms by which anti-angiogenic therapy can improve treatment outcome when administered alone or in combination with chemotherapy, we have developed a mathematical model of vascular tumour growth. Our model can be used to identify a period of enhanced tumour growth that could correspond to the vessel normalisation window within which cytotoxic or radiotherapeutic efficacy may be increased.

The development of mathematical models of angiogenesis has been driven by experimental observations. Continuous, discrete and hybrid models can be used to represent vessel growth dynamics, and tumour growth, in one, two or three dimensions and may account for intricate biological details [21, 105, 139, 143, 191] (for a review, see [154]). Without suitable experimental data, these models can yield qualitative mechanistic insight; with appropriate data, the models can be validated and parametrised and, thereby, their predictive power increased. Mathematical models can also be used to investigate the impact of mechanistic perturbations to angiogenesis and to design optimal therapy regimens.

For model development and parametrisation, non-linear mixed effects (NLME) modelling enables a data-driven approach [99]. A maximum likelihood approach is used to estimate population and individual parameters from experimental data. The method has been used widely to integrate tumour growth data with ODE models that characterise tumour growth kinetics in the presence and absence of cytotoxic treatments [62, 149, 150, 159, 184]. Typically these models comprise a term that represents an empirical tumour growth law (eg. logistic, Gompertzian, or exponential growth), and another term to represent tumour growth inhibition due to chemotherapy. For example, in [159] a two-stage tumour growth law (exponential followed by linear) is modified to account for a cytotoxic therapy that acts directly to kill the tumour cells. This model is extended in [151] to account for anti-angiogenic

therapy which is assumed to indirectly slow the tumour's growth rate, however, there is no variable for the tumour's vascular density.

Hahnfeldt *et al.* proposed a simple model of vascular tumour growth in which the tumour and the vasculature are treated separately [72]. Vascular density is assumed to regulate the equilibrium size of the tumour while the tumour is assumed to promote angiogenesis [72]. In [133], Ouerdani *et al.* develop a model of vascular tumour growth in which a logistic tumour growth law is assumed, and the equilibrium tumour size is the vessel-dependent carrying capacity. The authors use preclinical and clinical data to parametrise the model in the presence and absence of the dual cytotoxic and anti-angiogenic drug, pazopanib. Similarly, in [184], Wilson *et al.* present a logistic tumour growth model with a dynamic carrying capacity term that is parametrised for administration of anti-angiogenic therapy alone and in combination with chemotherapy. The model is used to predict an optimal time for the administration of chemotherapy following administration of anti-angiogenic tyrosine kinase inhibitor. The authors suggest that vascular normalisation could play a key role in the identification of the optimal treatment schedule, although normalisation is neglected in their model.

While vessel normalisation may play a key role in vascular tumour growth, parameters associated with normalisation are rarely measured and existing mixed effects models have not explicitly considered the dynamics of vessel normalisation. Motivated by the transient dynamics apparent from the experimental data in the KPL-4 preclinical mouse (xenograft) model of breast cancer, we extend existing mathematical models of vascular tumour growth under anti-angiogenic therapy to account for normalisation. Our model could be used to characterise normalisation in clinical studies, and we demonstrate how the model can be used to predict the optimal time, relative to the transient window, to schedule chemotherapy.

The remainder of this chapter is structured as follows. In Section 3.2, we introduce the preclinical dataset that we use for model parametrisation. In Section 3.3 we develop our mathematical model of vascular tumour growth. Before presenting the results from model fitting in Section 3.5, we investigate the suitability of mixed

effects modelling for our data and mathematical model in Section 3.4. Finally, we discuss our findings in Section 3.6.

3.2 Preclinical data

The preclinical data were collected by our experimental collaborators at Hoffman La Roche. Thirty immuno-suppressed mice were injected with human tumour cells from a breast cancer (KPL-4) cell line (immuno-suppression avoids tumour rejection). The tumours were measured regularly with callipers until the mean tumour volume of the entire cohort was 70mm^3, which occurred at day 38 after inoculation. At this stage, animals were randomly allocated to three experimental groups. The control group received an antibody that does not affect tumour growth (omalizumab), and the other two groups received bevacizumab and vanucizumab, respectively. Treatment was administered once per week for 5 weeks and tumour size was measured twice per week [1], resulting in a total of 10 measurements per animal.

Bevacizumab is an anti-VEGF antibody, vanucizumab is a bispecific anti-VEGF/anti-Ang2 antibody that neutralises both ligands, and omalizumab was included as a control. Each antibody was administered via i.v. injection at a dose of 10mg/kg, once per week, starting 38 days after inoculation. The raw data are presented in Figure 3.1.

[Experimental details: Female SCID beige mice, aged 8 weeks, were housed in specific-pathogen-free conditions according to committed guidelines (GV-Solas, Felasa, TierschG) and injected with a suspension of 3×10^6 KPL-4 tumour cells into the right, penultimate, inguinal mammary fat pad.]

[1] Measurements of tumour length and width were taken using callipers, where the length and width of the tumour were the longest dimension of the tumour, and the shortest dimension lying at 90° to the longest, respectively. Tumour volume, T, was calculated using the formula $T = \frac{\text{length} \times \text{width}^2}{2}$.

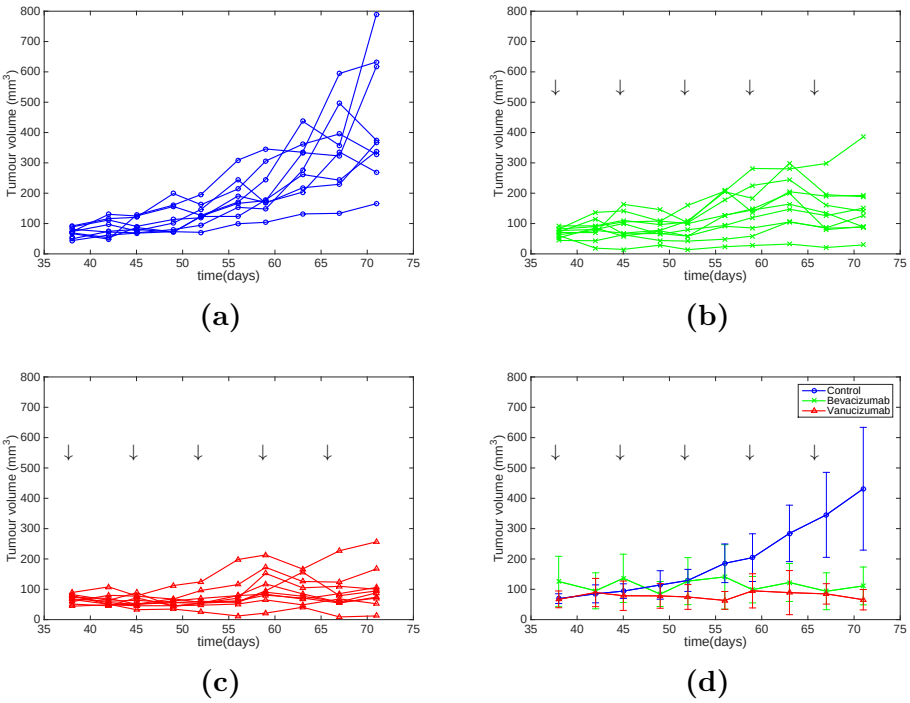


Figure 3.1: Individual tumour size data for (a) control tumours (n=10), (b) bevacizumab treated animals (n=10), (c) vanucizumab treated animals (n=10), (d) mean tumour volume of individual groups. Treatment times are shown by vertical arrows in plots (b) - (d). The error bars on (d) represent the standard deviation of the tumour size measurements at each time point.

3.3 Model development

3.3.1 Untreated tumours

The model that we propose comprises two ODEs to describe time-dependent tumour growth and the associated vessel-dependent carrying capacity. Our model is inspired by one developed by Hahnfeldt *et al.*, [72]. Tumour size is the observed variable; vessel-dependent carrying capacity has not been measured experimentally. We assume that all individual parameters are distributed log-normally, which is generally anticipated for growth rates and reaction rates and avoids negative values for parameters [101, 106].

The biological interpretation of the carrying capacity is the maximum tumour size that can be supported by the associated vasculature. The anti-angiogenic therapies that we consider affect vessel growth, but are not directly cytotoxic to tumour

cells. We view tumour volume, T (measured in mm^3), and the carrying capacity, V (also in mm^3), as distinct dependent variables. A simple logistic growth model for T was chosen for the untreated case (see equation (3.1)). Tumour growth has been represented using a logistic or generalised logistic growth term in several related models [133, 150, 184]. In recent publications [133, 184], the evolution of the carrying capacity was assumed to depend only on T. However, we take a similar approach to [72], where we assume that the carrying capacity of the tumour, V, depends on the local vascular density and its quality. In the model presented by Hahnfeldt *et al.* [72], the evolution of the carrying capacity depends on the tumour cell density according to the following ODE, where V represents the carrying capacity and T represents tumour cell density:

$$\frac{\mathrm{d}V}{\mathrm{d}t} = -aV + bT - dVT^{2/3},$$

where a, b and d are positive constants. The authors assume that the tumour produces vessel stimulating factors that increase the carrying capacity according to the term bT, and that inhibitors from the tumour will impact the vessel growth at a rate that depends on the tumour surface area, $T^{2/3}$. In our model, we propose a simpler case where the net effect of tumour cells on the carrying capacity is positive. Furthermore, we assume that the carrying capacity also depends on the existing vascular density since new vessels sprout from existing ones. The untreated model of tumour size and dynamic carrying capacity can be written:

$$\frac{\mathrm{d}T}{\mathrm{d}t} = \alpha_T\, T\left(1 - \frac{T}{V}\right), \tag{3.1}$$

$$\frac{\mathrm{d}V}{\mathrm{d}t} = \alpha_V\, T^a\, V^b, \tag{3.2}$$

where α_T is the maximal tumour growth rate, and α_V is the growth rate of the vascular-dependent carrying capacity. Since in equation (3.2) the exponents a and b are not identifiable via model simulations, we fixed them at physiologically based values. Vessel growth is stimulated by growth factors (such as VEGF) that are

released at the tumour surface, which follows $T^{2/3}$. Accordingly, we fix $a = \frac{2}{3}$. Furthermore, we assume that since vessels grow from existing ones, the growth of the carrying capacity depends also on the radius of the effective vascular density, which follows $V^{1/3}$, since T and V both have units of volume. We use a value of $b = \frac{1}{3}$, which also ensures that vessel growth is exponential at long times (which appears to be the case from our dataset). We note that there may be several combinations of a and b that describe the experimental data well.

3.3.2 Tumours treated with anti-angiogenic therapy

We assume that anti-angiogenic therapy has two effects: (1) it causes blood vessel regression and (2) it leads to a transient period during which tumour growth is enhanced due to increased blood flow. We start by taking only effect (1) into account, and then suppose both effects are active. We incorporate effects (1) and (2) into our mathematical model by including a term for vessel regression and a function that transiently increases the carrying capacity (this change being stimulated by increased tumour perfusion due to improved vascular quality during the transient normalisation window).

In the absence of pharmacokinetic data from the experiment and to avoid introducing further unknown model parameters, we do not explicitly model drug levels in the tumour microenvironment; we assume that from the onset of treatment, the concentration of each anti-angiogenic drug in the blood stream is maintained at a high enough level to ensure maximum efficacy. The long half-life (around 8 days in preclinical models) of bevacizumab supports this assumption [107], and we assume that vanucizumab has a similarly long half-life since it has a similar structure to bevacizumab. Data presented by [107] and [96] show that a weekly dose of 10mg/kg of bevacizumab or vanucizumab results in maximum efficacy with respect to tumour growth inhibition in mice, further supporting our argument for a constant efficacy

throughout the treated period. The full model can be written

$$\frac{\mathrm{d}T}{\mathrm{d}t} = \alpha_T\, T\left(1 - \frac{T}{NV}\right), \tag{3.3}$$

$$\frac{\mathrm{d}V}{\mathrm{d}t} = \alpha_V\, T^{2/3}\, V^{1/3} - \delta_V\, V, \tag{3.4}$$

$$N(t) = \begin{cases} 1 \text{ for } t \leq t_{norm1} \text{ and } t \geq t_{norm2}, \\ N_{max} \text{ for } t_{norm1} < t < t_{norm2}, \end{cases} \tag{3.5}$$

where the constant δ_V corresponds to the vessel death rate, t_{norm1} and t_{norm2} are the start and end times of the window of enhanced tumour growth, respectively, and $N_{max} \geq 1$ is the maximum factor by which the carrying capacity is enhanced during the transient window. For the first case, where only effect (1) is accounted for, $N_{max} = 1$ for all time.

The initial condition for T, denoted T_0, is the experimental value of the tumour volume at the first measurement time (day 38). We assume that the initial value for V, which we denote V_0, is linearly related to T_0 for individuals through the parameter $K = \frac{V_0}{T_0}$, which is estimated for individuals (since we estimate K for individuals, this is equivalent to estimating V_0 itself.). Typical model simulations for various values of δ_V and N_{max} are presented in Figure 3.2.

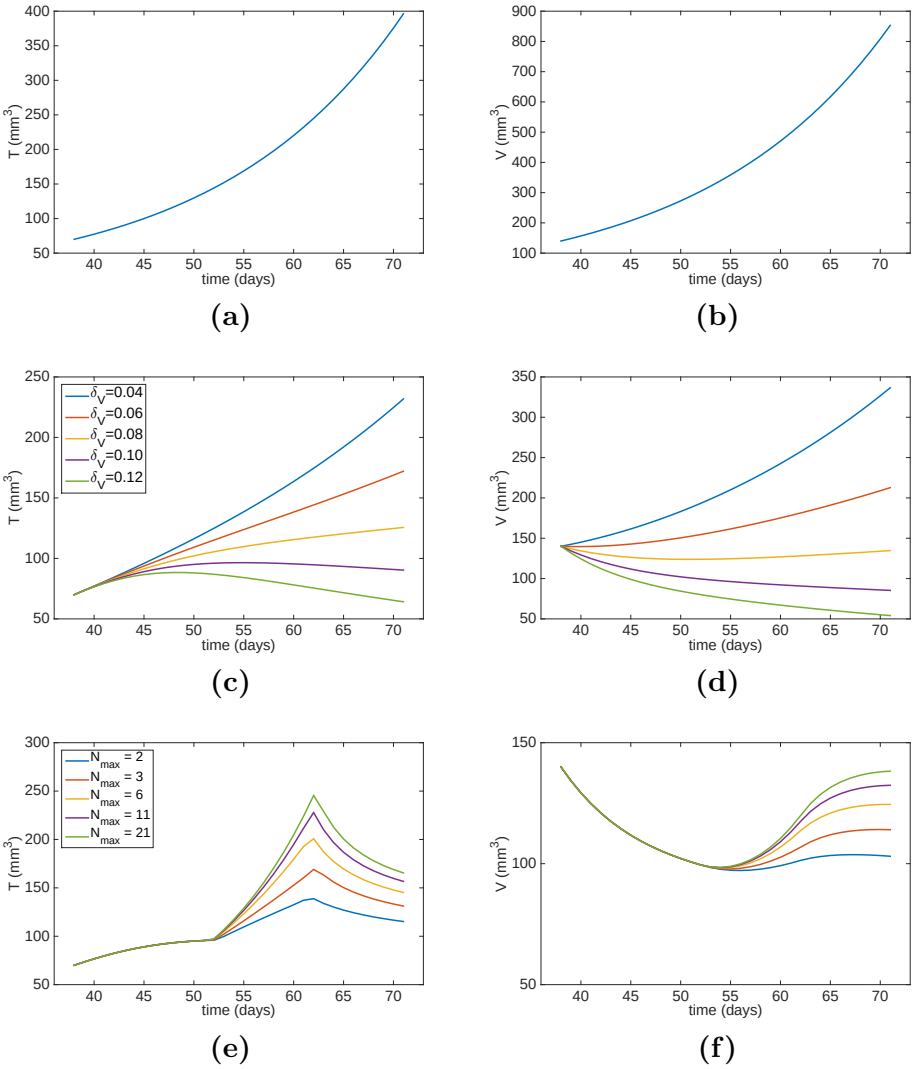


Figure 3.2: Typical model simulations. (a), (c), (e) represent the tumour volume $T(t)$ and (b), (d), (f) represent the vessel dependent carrying capacity $V(t)$. (a)-(b) Control simulations (equations (3.1)-(3.2)) with $\alpha_T = 0.1$ day^{-1}, $\alpha_V = 0.09$ day^{-1}, $K = 2$, $T_0 = 70$mm^3. (c)-(d) Treatment model simulations (equations (3.3)-(3.5)) with $N_{max} = 1$, δ_V values 0.04 day^{-1} $-$ 0.12 day^{-1} and all other parameters the same as (a)-(b). (e)-(f) Treatment model simulations (equations (3.3)-(3.5)) where $t_{norm1} = 52$ days, $t_{norm2} = 62$ days, N_{max} values $2 - 21$, $\delta_V = 0.1$ day^{-1} and all other parameters the same as (a)-(b).

3.4 Non-linear mixed effects modelling and the SAEM algorithm

A general non-linear model may describe observed experimental data, y, such that the data are expected to follow some underlying structural model and also to contain some experimental error. The non-linear model that describes observed data from a given subject may be written

$$y = f(t, \phi) + g(t, \phi)\epsilon,$$

where the structural model, $f(t, \phi)$, describes the deterministic processes that give rise to the data and depends on time (t) and the underlying model parameters (ϕ), and where $g(t, \phi)\epsilon$ is a function that describes the measurement error. Common error models include constant error: $g(t, a) = a$, where a is a constant for all t, and proportional error: $g(t, \phi) = bf(t, \phi)$, where b is a constant. It is assumed that since experimental error occurs at random, ϵ is a random number, and in simulations, it is drawn randomly from a normal distribution: $\epsilon \sim \mathcal{N}(0, 1)$ for each observation.

In the case where experimental data are collected from a population of subjects, such as a patient cohort or a group of mice, a mixed effects model may be used to describe the observed data. In this case, we assume that parameter values will differ between subjects. Now, ϕ is a matrix of parameters where each row represents a parameter that describes the structural model, e.g. a growth rate, and each column represents the values of parameters belonging to a given subject. The entries of the matrix, ϕ_{ij}, that represent parameter i and subject j can be expressed as

$$\phi_{ij} = \beta_i + \eta_{ij},$$

where β_i is the "population" value for parameter i, usually the mean value for each parameter, and η_{ij} is the deviation of the value for parameter i, belonging to subject j, from its population value, β_i (thus η_{ij} may be positive or negative). The column vector of individual values for individual j, which we denote ψ^j, are expected to be

distributed with mean, β, and variance, ω^2. For instance, if a normal distribution is assumed for the parameters, then

$$\psi^j \sim \mathcal{N}(\beta, \omega^2),$$

where ω^2 is the vector containing the variance of the parameters in the rows of ψ^j, known as the inter-individual variability (IIV) and β is the vector containing the population values for all parameters.

The term "mixed effects" modelling comes from the assumption that individual parameters can be described in terms of the population mean β (the "fixed" effect) and IIV (the "random" effect).

For our model, we use the Stochastic Approximation to Expectation Maximisation (SAEM) algorithm (described below) to estimate

- the population parameters: $\{\beta_{\alpha T}, \beta_{\alpha V}, \beta_K, \beta_{\delta V}, \beta_{Nmax}, \beta_{tnorm1}, \beta_{tnorm2}\}$;
- the IIV parameters: $\{\omega_{\alpha T}, \omega_{\alpha V}, \omega_K, \omega_{\delta V}, \omega_{Nmax}, \omega_{tnorm1}, \omega_{tnorm2}\}$;
- values for the parameters $\{\alpha_T, \alpha_V, K, \delta_V, N_{max}, t_{norm1}, t_{norm2}\}$ belonging to each individual.

3.4.1 SAEM algorithm

Our non-linear mixed effects model was implemented using Monolix software, which allows estimation of the population parameters, IIV, and individual parameters via the SAEM algorithm [100].

The SAEM algorithm is a likelihood based method that requires initial estimates of the parameter distributions. The algorithm is summarised in Figure 3.3, and comprises 3 main steps:

1. **Simulation:** Parameter values for individual subjects are drawn from the population distributions, and using these parameter values, a synthetic dataset is generated. Differences between the experimental data, y, and

the simulated data, f, are calculated and these residuals are used to calculate the likelihood that this parameter set describes the experimental data. If the likelihood improves compared to the previous iteration, values for individual parameters are updated with a given probability (this method is known as the Metropolis Hastings algorithm [78]).

2. **Stochastic approximation:** "Sufficient" statistics are calculated to summarise the parameters estimated for the model. The sufficient statistics calculated at step l using ψ notation as defined above, are

$$\begin{aligned} s_{1,l} &= \sum_j \psi^j; \\ s_{2,l} &= \sum_j \psi^j \cdot \psi^{jT}; \end{aligned}$$

and for the error model,

$$\begin{aligned} s_{3,l} &= \sum_i \sum_j \left(y_{ij} - f(t_{ij}, \phi_i)\right)^2; \quad \text{(constant error model) or} \\ s_{3,l} &= \sum_i \sum_j \frac{\left(y_{ij} - f(t_{ij}, \phi_i)\right)^2}{f(t_{ij}, \phi_i)^2}; \quad \text{(proportional error model).} \end{aligned}$$

These statistics are used to update the quantities, $S_{m,l}$:

$$S_{m,l} = S_{m,l-1} + \gamma_l(s_{m,l} - S_{m,l-1}),$$

where $m = \{1, 2, 3\}$, l is the iteration number of the SAEM algorithm, and γ is a decreasing sequence of numbers such that $\sum_{l=1}^{\infty} \gamma_l = \infty$ and $\sum_{l=1}^{\infty} \gamma_l^2 < \infty$ (these conditions are required for convergence, as shown in [46]). If $\gamma = 0$, then there is no memory of previous iterations in the algorithm.

3. **Maximisation:** The population distributions defined by $\hat{\beta}$ and $\hat{\omega}$, from which individual values shall be drawn in the next iteration of the algorithm

are updated such that:

$$\hat{\beta}_l = \frac{S_{1,l}}{N}; \qquad \hat{\omega}_l = \frac{S_{2,l}}{N} - \left(\frac{S_{1,l}}{N}\right) \cdot \left(\frac{S_{1,l}}{N}\right)^T,$$

where N is the number of individuals.

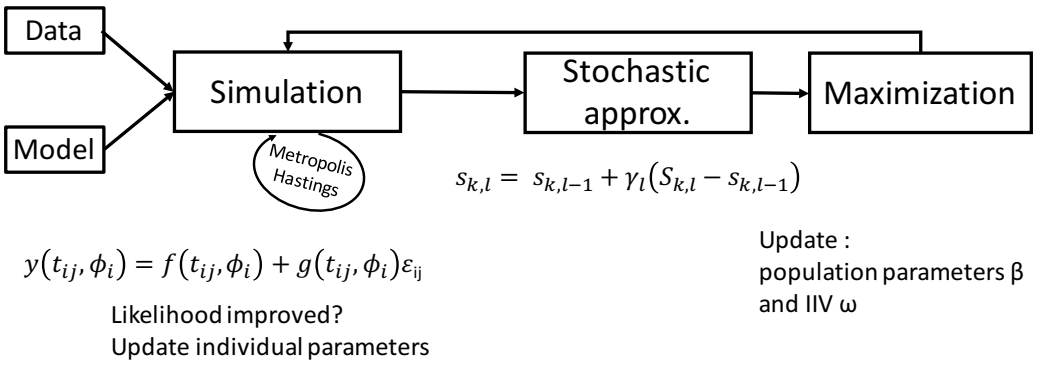


Figure 3.3: A summary of the steps of the SAEM algorithm. See text for full description.

Using Monolix software, which implements the SAEM algorithm, we attempt to estimate parameters for several versions of the same model, where we fix some parameters instead of estimating them in some cases. Model selection is informed by comparing the Bayesian Information Criterion (BIC) for each model, alongside diagnostic plots and relative standard error (r.s.e.) of population parameters and IIV. The BIC is a penalized likelihood criterion calculated by the formula BIC = $-2\mathcal{LL}_y(\phi) + log(n)d$, where $\mathcal{LL}$ is the log-likelihood, n is the number of observations, ϕ is the vector containing the individual parameters and d is the total number of parameters.

3.4.2 Evaluation of mixed effects modelling techniques

Returning to our model, we use synthetic data to investigate the suitability of the SAEM algorithm in Monolix for estimating model parameters from the experimental

data. The investigation will inform whether we take a sequential or pooled approach to model fitting, and will also identify the accuracy we can expect from our results. A sequential approach involves using the control data to parametrise the untreated model in equations (3.1)-(3.2), then fixing these parameters for the treated model in equations (3.3)-(3.5) to estimate the treatment parameters. A pooled approach involves using the entire dataset (control and treatment data) to estimate the model parameters.

In the following treatment, we use synthetic data to examine the structural identifiability of the parameters α_T, α_V and K using the control model (equations (3.1)-(3.2)) and the treated model (equations (3.3)-(3.5)). We then generate additional synthetic datasets and use Monolix to compare the accuracy of the parameter estimates as the size of the dataset varies.

Identifiability considerations

Parameter identifiability depends on the structural model and the data available for parametrisation. Given a particular dataset, a model is considered to be structurally identifiable if the parameters could all, in theory, be uniquely identified using perfect, noise-free data for the observed variable(s). A model is termed practically identifiable if the parameters are uniquely identifiable given the experimental dataset, including noise. There are several methods to investigate the structural identifiability of parameters in linear models [13, 20, 110], and some analytical methods for structural identifiability of non-linear models [32, 144]. Here we investigate the structural identifiability of our non-linear model using a method from Pohjanpalo, which was also used by Chappell and Godfrey [32, 144]. We then investigate the practical identifiability of our control and treatment models using synthetic data.

The method that we employ for finding global structural identifiability of non-linear models has three steps:

1. Expand y, the observed variable, as a Taylor series

$$y(t,p) = y(0,p) + y^{(1)}(0,p)t + y^{(2)}(0,p)\frac{t^2}{2} + y^{(3)}(0,p)\frac{t^3}{3} + ...y^{(n)}(0,p)\frac{t^n}{n}$$

where $y^{(i)}$ is the ith derivative of y with respect to time, and p is the set of model parameters;

2. Find the coefficients of $y^{(i)}$ up to $i = \text{length}(p)$;

3. Find the Jacobian of the vector of coefficients with respect to the model parameters;

4. If the Jacobian has full rank, then the parameters are globally structurally identifiable. If the rank is less than full, the parameters are not globally structurally identifiable.

For our model, the first tumour size measurement is at $t = 38$, so we introduce $\tau = t - 38$ for the purposes of our expansion. The measured variable is tumour size, T. Using the structural model in equations (3.1)-(3.2), we expand $y(\tau, p)$, where $p = \{\alpha_T, \alpha_V, K\}$ and $\frac{V_0}{T_0} = K$. The expansion can be written:

$$\frac{T(\tau,p)}{T_0} \approx 1 + T^{(1)}(0,p)\tau + T^{(2)}(0,p)\frac{\tau^2}{2} + T^{(3)}(0,p)\frac{\tau^3}{3}$$

where

$$\begin{aligned}
T^{(1)}(0,p) &= \alpha_T\left(1 - \frac{1}{K}\right);\\
T^{(2)}(0,p) &= \alpha_T^2 + 2\frac{\alpha_T^2}{K^2} + \frac{\alpha_T\alpha_V}{K^{5/3}} - 3\frac{\alpha_T^2}{K};\\
T^{(3)}(0,p) &= \alpha_T^3 - 6\frac{\alpha_T^3}{K^3} - \frac{20}{3}\frac{\alpha_T^2\alpha_V}{K^{8/3}} - \frac{5}{3}\frac{\alpha_T\alpha_V^2}{K^{7/3}} + 12\frac{\alpha_T^3}{K^2} + \frac{17}{3}\frac{\alpha_T^2\alpha_V}{K^{5/3}} - 7\frac{\alpha_T^3}{K}.
\end{aligned}$$

We find the rank of the Jacobian J, where

$$J = \begin{pmatrix}
\frac{\partial T^{(1)}(0,p)}{\partial \alpha_T} & \frac{\partial T^{(1)}(0,p)}{\partial \alpha_V} & \frac{\partial T^{(1)}(0,p)}{\partial K}\\
\frac{\partial T^{(2)}(0,p)}{\partial \alpha_T} & \frac{\partial T^{(2)}(0,p)}{\partial \alpha_V} & \frac{\partial T^{(2)}(0,p)}{\partial K}\\
\frac{\partial T^{(3)}(0,p)}{\partial \alpha_T} & \frac{\partial T^{(3)}(0,p)}{\partial \alpha_V} & \frac{\partial T^{(3)}(0,p)}{\partial K}
\end{pmatrix}.$$

Since the columns of the Jacobian are linearly independent, the rank of J is 3, and therefore there exists a unique solution for the parameters α_T, α_V and K that

would describe an "ideal" dataset, and the control model parameters are structurally identifiable.

Structural identifiability does not guarantee practical identifiability. We have demonstrated that the parameters of the control model are structurally identifiable, by showing that perturbations to each parameter result in a different effect on T, since all coefficients of the Taylor expansion are linearly independent in α_T, α_V, K space. In practice, the change in T resulting from perturbations to α_T, α_V and K may not be pronounced enough to distinguish parameters, and therefore practical identifiability may not be achieved.

To investigate the practical identifiability of the control model parameters using data from measurements of tumour volume, T, only, we simulated equations (3.1)-(3.2) using the parameter values $\alpha_T = 0.1$ day^{-1}, $\alpha_V = 0.09$ day^{-1}, $K = \frac{V_0}{T_0} = 2$ and the initial condition $T_0 = 70$ mm^3, for $38 \leq t \leq 71$ days and the results for T constitute the vector $y(t)$. There was no error in $y(t)$ and the value of T was recorded at $t = 38, 39, 40, ...71$. Next, we sampled α_T, α_V and K within the intervals

$$\begin{aligned} 0.02 \leq \quad & \alpha_T \quad \leq 0.3, \\ 0.02 \leq \quad & \alpha_V \quad \leq 0.3, \\ 0.5 \leq \quad & K \quad \leq 5. \end{aligned}$$

We took 50 values for each parameter, resulting in $50 \times 50 \times 50$ simulations of the control model. For each model simulation, the resulting vector of T values, $f(t)$, was used to calculate the sum of squared residuals, SS, for that simulation, where $SS = \sum_j (y_j - f_j)^2$. In Figure 3.4, we show that there is a curve in parameter space where the sum of squared residuals is small. This results in practical identifiability problems, since several combinations of α_T, α_V and K give a small value of SS. Therefore, although the control model is structurally identifiable, it is not practically identifiable.

For the treatment model, we take a similar approach to investigate the practical identifiability of parameters α_T, α_V and K. For simplicity, we hold fixed all the

extra parameters of the treatment model ($\delta_V, N_{max}, t_{norm1}$ and t_{norm2}) and scan the parameter space mapped out by varying α_T, α_V and K. We generate a new dataset by solving equations (3.3)-(3.5), where the model parameters are fixed to their control values. We vary α_T, α_V and K as for the control model above, and the sum of squared residuals are shown in Figure 3.5. In this case, the parameter values that result in the minimum value of SS coincide with the true parameter values. From these simulations, it appears that for the treatment model, the parameters α_T, α_V and K are practically identifiable via a least-squares method when other model parameters are known and fixed.

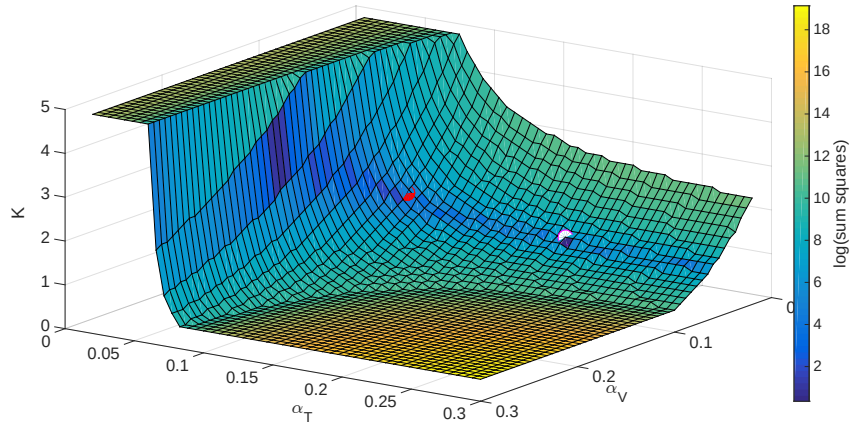
Our analytical and simulation results for the no-treatment case suggest that the control parameters are structurally, but not practically, identifiable using tumour size measurements only. This observation is relevant to our model fitting with experimental data as it suggests that a sequential approach where control parameters are estimated first using control data only, and the control parameters are fixed in simulations to estimate the treatment parameters, is inappropriate. A pooled approach where the full dataset is used to estimate control and treatment parameters may be more appropriate. However, we note the limitations of our treatment: we fixed the extra parameters to their known values, and did not attempt to estimate them. Including all parameter values in this treatment may yield different results.

In the next section, we compare sequential and pooled approaches to estimate the parameters of a synthetic dataset using Monolix.

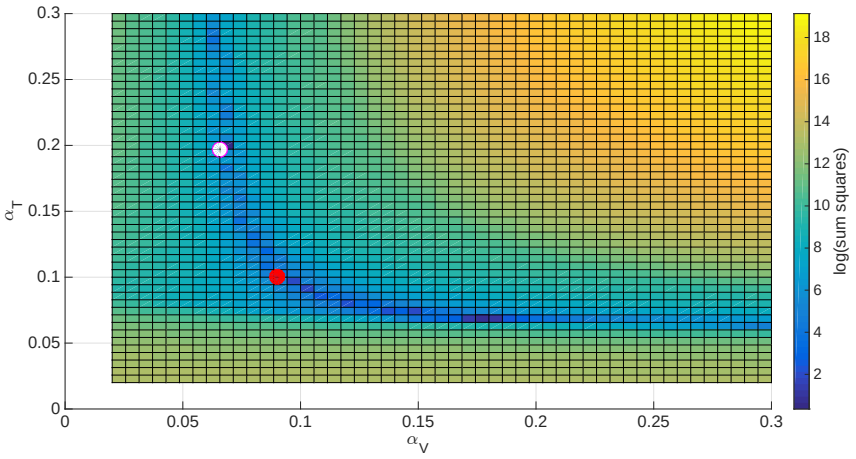
Synthetic data

Here we assess the accuracy of parameter estimates using Monolix software for a sequential fitting approach (estimating control parameters first and fixing these when estimating the treatment parameters) and a pooled approach (where parameters are estimated simultaneously using all available data).

We generated synthetic data for T and V by solving equations (3.1)-(3.2) for the control model and equations (3.3)-(3.5) for the treatment model, using parameter values from lognormal distributions defined by a population parameter, β, and

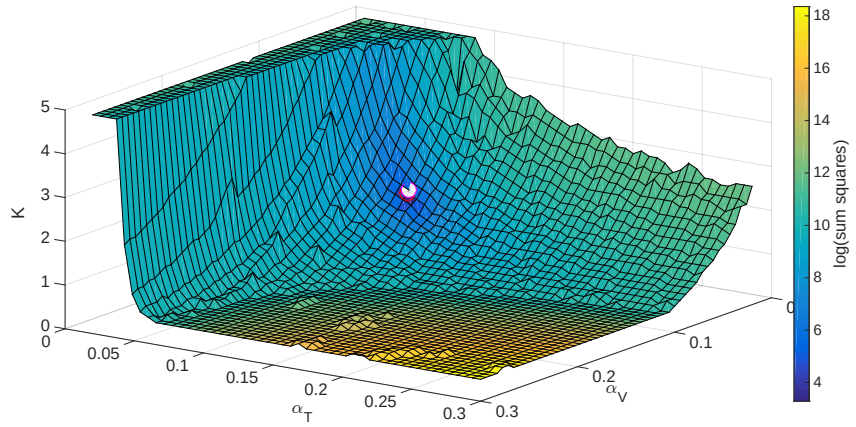


(a)

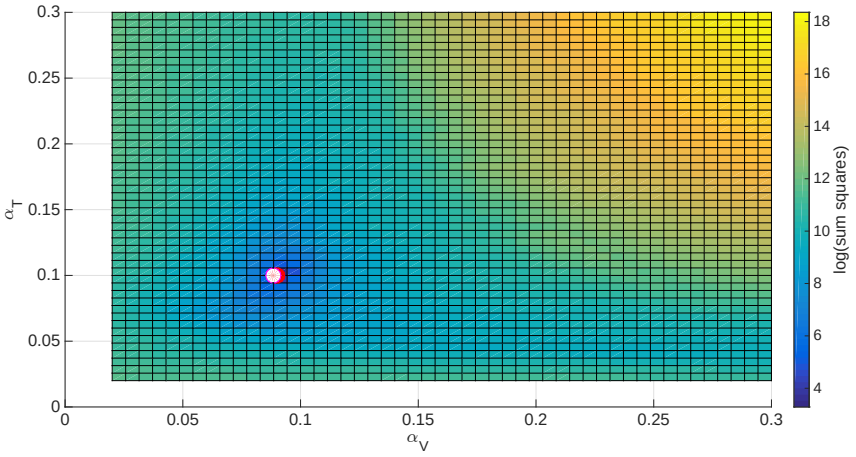


(b)

Figure 3.4: Sum of squared residuals between simulations of equations (3.1)-(3.2) for parameter values sampled from a $50 \times 50 \times 50$ parameter space, and the test data y. For simulations, $0.02 \leq \alpha_T \leq 0.3$, $0.02 \leq \alpha_V \leq 0.3$, and $0.5 \leq K \leq 5$. (a) The surface that corresponds to the value of K at which the value of the sum of squares is minimised for a combination of values for α_V and α_T. The colourmap on the surface corresponds to the value of the sum of squared residuals at that point. The filled red circle indicates the true parameter values used to simulate y and the filled white circle indicates the combination of α_T, α_V and K that results in the lowest value for the sum of squared residuals. (b) Projection onto (α_T, α_V) parameter space.



(a)



(b)

Figure 3.5: Sum of squared residuals between simulations of equations (3.3)-(3.5), where the following parameters are fixed: $d_V = 0.1, N_{max} = 5, t_{norm1} = 52, t_{norm2} = 62$. Parameter values were sampled from a $50 \times 50 \times 50$ parameter space. For simulations, $0.02 \leq \alpha_T \leq 0.3$, $0.02 \leq \alpha_V \leq 0.3$, and $0.5 \leq K \leq 5$. (a) The surface that corresponds to the value of K at which the value of the sum of squares is minimised for a combination of values for α_V and α_T. The colourmap on the surface corresponds to the value of the sum of squared residuals at that point. The filled red circle indicates the true parameter values used to simulate y and the filled white circle indicates the combination of α_T, α_V and K that results in the lowest value for the sum of squared residuals. (b) Projection onto (α_T, α_V) parameter space.

standard deviation, ω, with added noise to represent the experimental measurement error. The magnitude of the noise was proportional to the tumour size at that time, i.e. we used a proportional error model. The datasets contain values of T and V at times $t = 38, 42, 45, 49, 52, 56, 59, 63, 67, 71$ days. The true parameter distributions that were sampled to generate the data are listed in Table 3.1.

Parameter	Distribution	Population parameter (β)	Standard Deviation (ω)
T_0 (not estimated)	uniform(50,90)	–	–
α_T	lognormal	0.1	0.3
α_V	lognormal	0.09	0.3
K	lognormal	2	0.845
t_{norm1}	none	52	0
t_{norm2}	none	62	0
N_{max}	lognormal	10	0.3
δ_V	lognormal	0.1	0.3
b	none	0.2	–
ϵ	normal	0	b

Table 3.1: The distributions of parameters used to generate the synthetic data. A proportional error model was used such that $y = f + fb\epsilon$ and $\epsilon = \mathcal{N}(0, 1)$.

The synthetic datasets were of size $N = 10$ per group or $N = 100$ per group, and we considered three values of the proportional error parameter: $b = 0.05$, 0.1 and 0.2. We also attempted to fit the model parameters using only tumour volume data, and using data for both V and T. In total, 12 datasets were generated.

First, we used a sequential approach to estimate the model parameters. Using only data from the control group, we estimated the parameters for the control model (population, β, and IIV, ω, were estimated for the parameters α_T, α_V and K). Next, the estimated population parameter distributions from the control model were fixed while the treatment parameters (population and IIV for N_{max}, δ_V and population only for t_{norm1} and t_{norm2}) were estimated. The accuracy of our estimates is indicated in Figures 3.6 and 3.7, where we also include the relative standard error (r.s.e.) for parameter estimates using Monolix. For the sequential fitting, larger datasets did not always result in more accurate parameter estimates. In general, estimates for N_{max} were the least accurate.

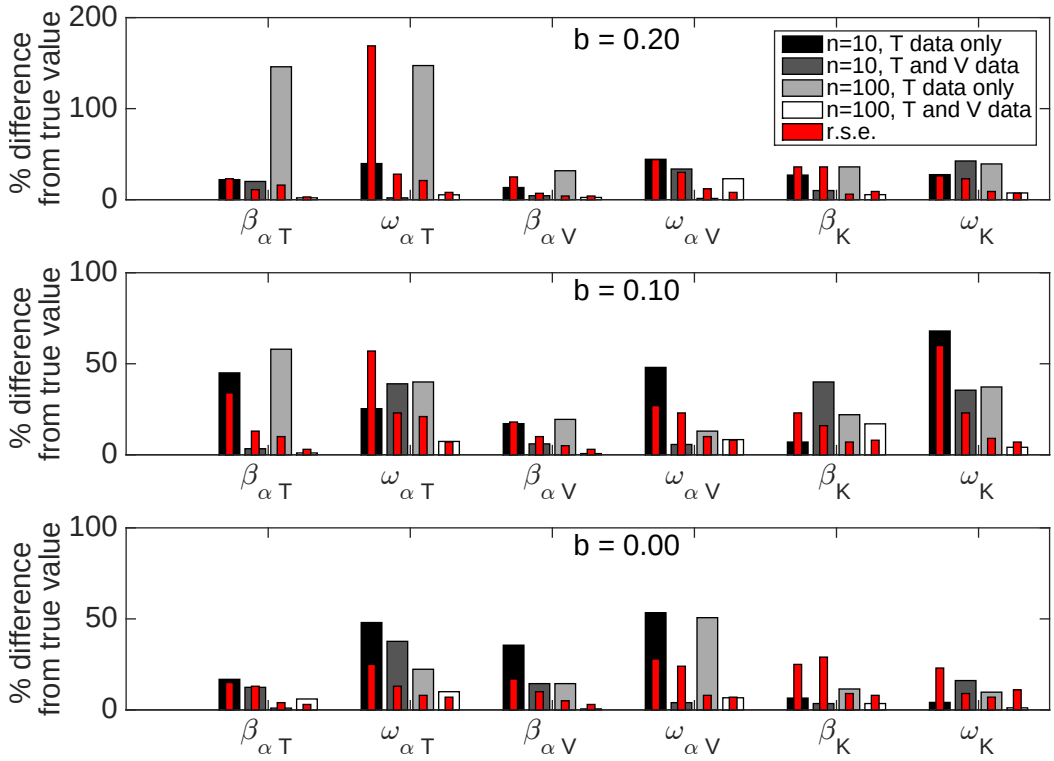


Figure 3.6: Sequential parameter estimation: control group. Bar charts showing the percentage difference between population parameter estimates from Monolix and the true parameter values, and the r.s.e. for each dataset using a sequential fitting approach. Parameters labelled β represent the population mode and parameters labelled ω represent the standard deviation (IIV).

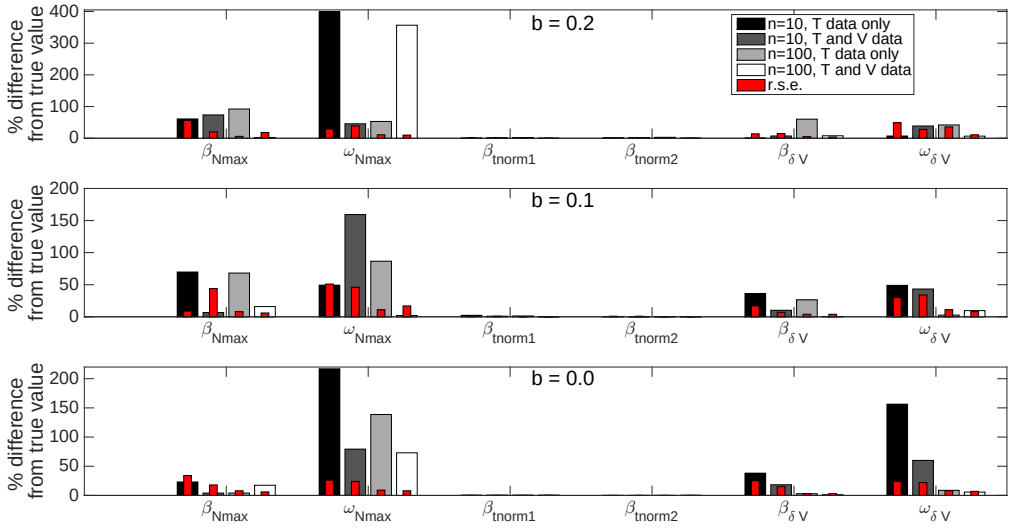


Figure 3.7: Sequential parameter estimation: treatment group. Control model parameters were fixed to the population results obtained from estimates shown in Figure 3.6. Bar charts showing the percentage difference between population parameter estimates from Monolix and the true parameter values, and the r.s.e. for each dataset using a sequential fitting approach. Parameters labelled β represent the population mode and parameters labelled ω represent the standard deviation (IIV).

Figure 3.8 shows the results of the parameter estimates using a pooled approach, where all data were used to estimate control and treatment model parameters simultaneously. It is clear that the r.s.e. values are largest at all error levels for the β_{Nmax} and ω_{Nmax} parameters: from equation (3.3), when $N \times V \gg T$, then $\frac{\mathrm{d}T}{\mathrm{d}t} \approx \alpha_T T$ and simulations for different large values of N are indistinguishable. As a result, the likelihood is relatively insensitive to N_{max}. In most cases, r.s.e. values decrease as more data are used for the simulations. In most cases, fitting with T and V data results in more accurate parameter estimates than fitting T data only. From our simulations, when $b = 0.1$, the parameter estimates are more accurate than when $b = 0.2$. This suggests, unsurprisingly, that parameter estimates can be improved by reducing experimental error.

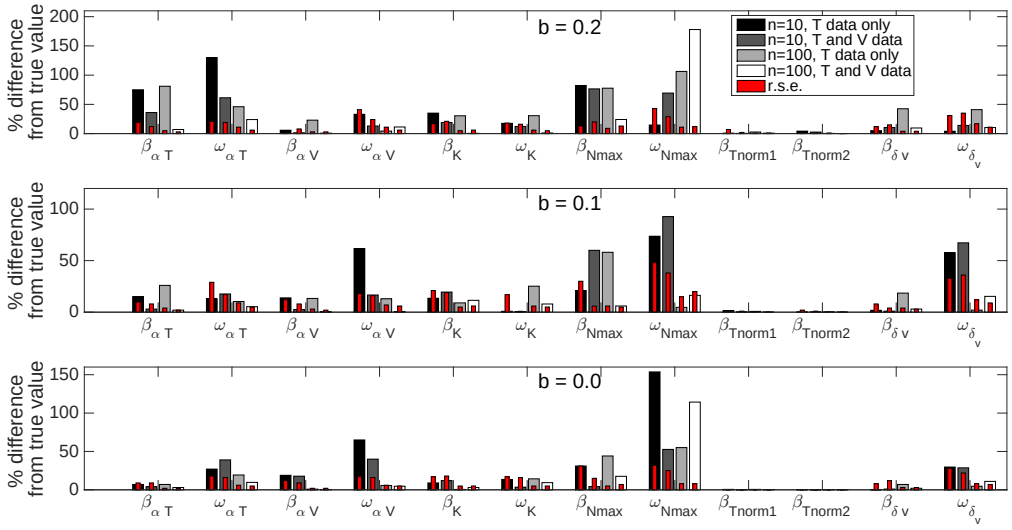


Figure 3.8: Bar charts showing how the percentage difference between population parameter estimates from Monolix and the true parameter values, and the r.s.e. for each dataset. Parameters labelled β represent the population mode and parameters labelled ω represent the standard deviation (IIV).

Finally, we directly compare estimates for the model parameters using sequential and pooled approaches. The results in Figure 3.9 show that the pooled approach does not always produce more accurate estimates than the sequential approach. Our simulations for both the sequential and pooled approaches have shown that it is not always the case that more data lead to more accurate estimates of parameters.

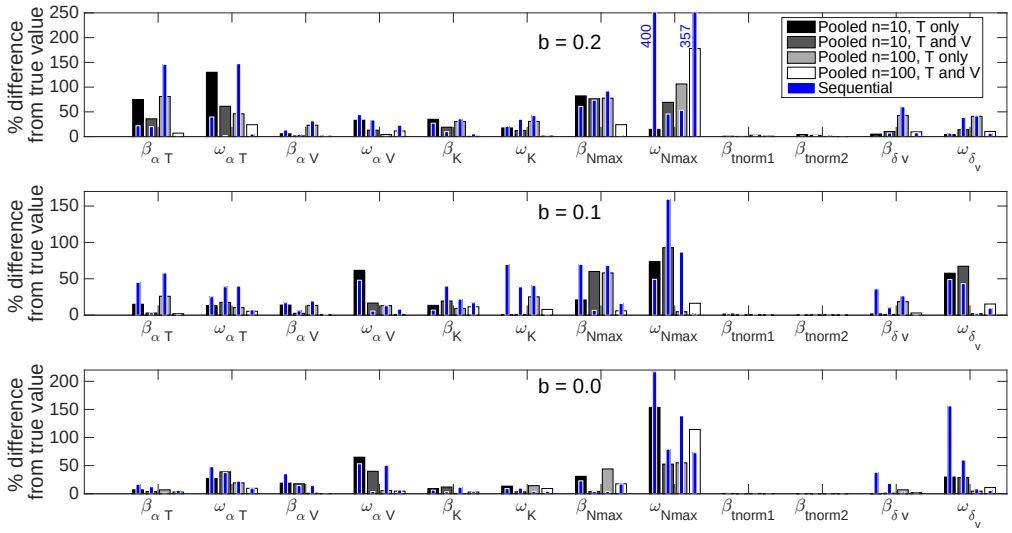


Figure 3.9: Direct comparison between parameter estimation results using sequential and pooled approaches. Bar charts showing the percentage difference between population parameter estimates from Monolix and the true parameter values for pooled and sequential approaches. Parameters labelled β represent the population mode and parameters labelled ω represent the standard deviation (IIV).

3.4.3 Summary of evaluation of mixed effects techniques for our dataset and model

We conclude that, for our model, a pooled approach to parameter estimation may produce more reliable parameter estimates than a sequential approach, and that in general, when using a pooled approach, results are more accurate when larger datasets are used (although this was not always the case for our synthetic data investigation in the previous subsection). We note the limitations of our study: from Figures 3.6-3.9, there are cases where using data for T and V produced poorer estimates than those produced using only T data, and in some cases, larger sample sizes did not improve parameter accuracy. This could be due to the stochastic nature of the process or parameter identifiability issues associated with local minima. Repeats of the same investigation may yield slightly different results, and therefore when using real data to infer parameters, caution should be taken when using the parameter estimates.

3.5 Model fitting results

3.5.1 A simple vessel inhibition model does not capture non-monotonic dynamics

Model simulations that account for drug-induced vessel regression, but not normalisation (see equations (3.3)-(3.4) with $N_{max} = 1$), produced a poor fit to the experimental data as illustrated in Figure 3.10; the fit could be improved by accounting for the transient increase in the rate of tumour growth, as detailed in the following subsection. The individual fits, weighted residuals and observations versus predictions are shown in Figure 3.10. As seen in the typical individual fits shown in Figures 3.10a-f, the data are consistently overestimated at $t = 49$ days and underestimated at $t = 59$ and $t = 63$, as is most clear in Figure 3.10h, although in the plot of observed versus predicted data in Figure 3.10(g), these features do not influence the overall closeness of fit of the model to the data. Individual fits for the entire dataset using the monotonic model are shown in Appendix B. In the next subsection we account for the non-monotonic tumour growth dynamics. A summary of the parameter estimates obtained by fitting the monotonic model to the experimental data is presented in Table 3.2. Large r.s.e. values were associated with the parameter estimates for this model, suggesting that the parameter estimates may not be accurate.

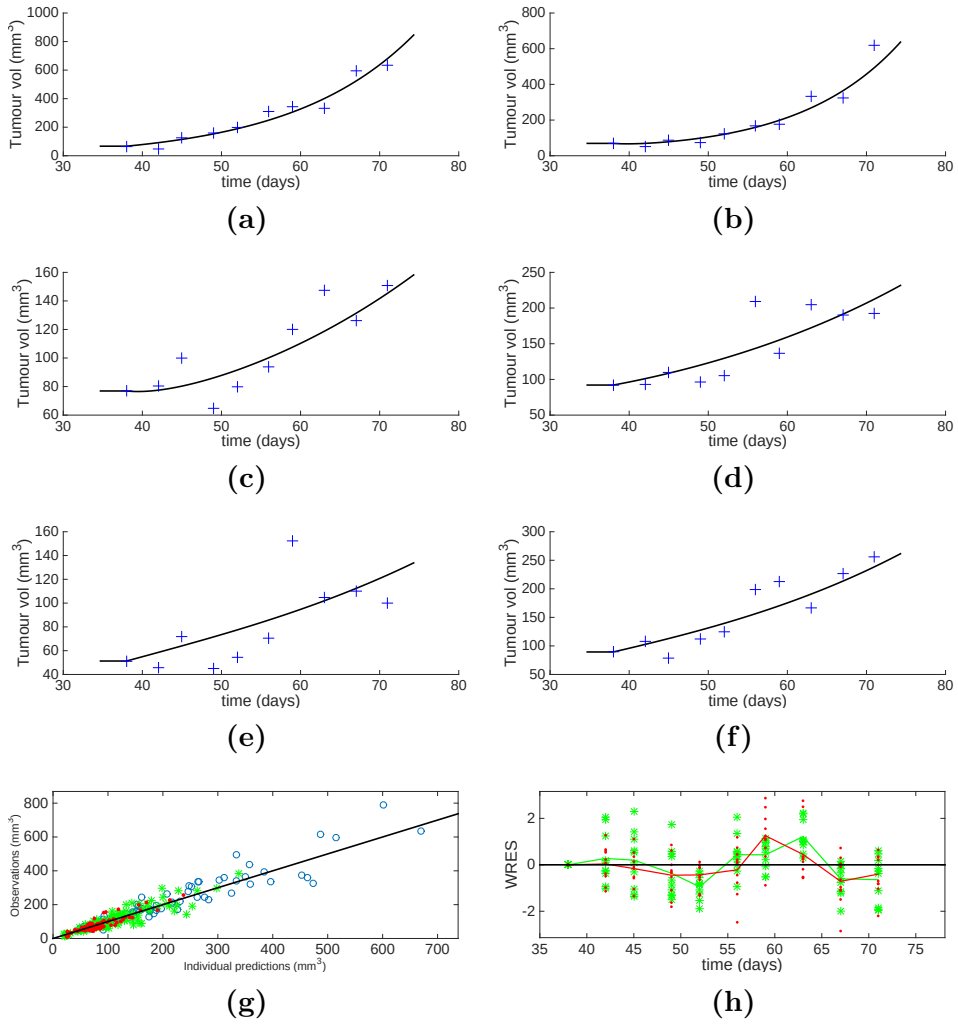


Figure 3.10: Fits, using Monolix, of the model with drug-induced vessel regression but without vessel normalisation (equations (3.3)-(3.5) with $N_{max} = 1$), to the experimental data shown in Figure 3.1. Because there is no vessel normalisation in this model, all tumour volume trajectories are monotonic increasing in time. (a)-(f) Typical individual fits selected at random for (a)-(b) control; (c)-(d) bevacizumab, and (e)-(f) vanucizumab groups using experimental data. Key: Blue '+' - experimental data, solid black lines - predicted tumour volume, T, using individual parameters estimated by Monolix. (g) Experimental (observed) results for tumour volume plotted against predicted results for tumour volume for individuals and coloured by group. (h) Weighted residuals (WRES) plots for the no-normalisation model. Solid green and red lines indicate the mean weighted residuals at each time point for bevacizumab and vanucizumab groups, repectively. Key: blue circles - control, green stars - bevacizumab, red dots - vanucizumab.

3.5.2 Model selection: identifying the transient window of enhanced tumour growth

Following experimental observations in [48, 185], where the time frame in which vessel normalisation occurred was similar for all animals treated with bevacizumab, we assume that the duration of the transiently enhanced tumour growth window is similar for all animals injected with a given tumour cell line and receiving a particular anti-angiogenic treatment. Furthermore, we assume that normalisation remains at control levels before and after the transient window. Therefore, in our model selection process, we fix the variance of the population distributions for t_{norm1} and t_{norm2} to the relatively small value of 0.1 and allow individual parameter values to be chosen from this pre-defined distribution.

When assuming the anti-angiogenic treatment stimulates both vessel regression and normalisation, equations (3.3)-(3.5) were used to estimate population and individual parameter values. During model selection, we tested several cases where the treatment parameters $\delta_V, N_{max}, t_{norm1}$ and t_{norm2} were fixed or free, and the details of our model fitting attempts can be found in Appendix C. The model that gave the best fit to the experimental data assumed different values of δ_V for each treatment group, and the same values of N_{max}, t_{norm1} and t_{norm2} for both treatment groups. A measure by which to judge the appropriateness of a model to describe the data is by calculating the shrinkage. Shrinkage compares the distributions of the individual parameters to the distributions of the population parameters from which they were chosen and is calculated as: shrinkage $= 1 - \frac{Var(\hat{\eta})}{\omega^2}$, where $Var(\hat{\eta})$ is the variance of the estimated individual parameters and ω^2 is the variance of the population distribution from which individual parameters were chosen. A small absolute value for shrinkage indicates that the individual parameters are distributed as expected within the population parameter distributions. A larger value for shrinkage suggests that although individual parameters may produce a close fit to observed data, they do not represent the distribution from which they were chosen well, i.e. a disproportionate number of individual parameter values may lie on the tails of the population

parameter distribution. The parameter estimates along with their r.s.e. values and shrinkage are listed in Table 3.2.

Param	Units	Monotonic model: Population parameter β (r.s.e. %)	Monotonic model: IIV ω (r.s.e. %)	Monotonic model: Shrink-age (%)	Final model: Population parameter β (r.s.e. %)	Final model: IIV ω (r.s.e. %)	Final model: Shrink-age (%)
α_T	day^{-1}	0.11(25)	0.134 (274)	-12	0.109 (12)	0.422 (25)	-6
α_V	day^{-1}	0.0886(20)	0.345 (47)	24	0.119 (7)	0.177 (34)	6
K	none	1.26(20)	0.941 (16)	16	1.14 (15)	0.711 (15)	9
t_{norm1}	days	-	-		53.3 (4)	0.1 FIX	-
t_{norm2}	days	-	-		59.2 (3)	0.1 FIX	-
N_{max}	none	-	-		6.7 (27)	0.55 (41)	
δ_V (bev)	day^{-1}	0.0633 (33)	0.674(2.3e3)		0.113 (11)	0.208 (47)	-
δ_V (van)	day^{-1}	0.0733 (32)	0.219 (176)		0.115 (12)	0.293 (33)	-
b	%	22.7 (5)	-		18.5 (5)	-	-

Table 3.2: Population parameters and inter-individual variability (IIV) for the monotonic model (equations (3.3)-(3.4) with $N_{max} = 1$) and final model (equations (3.3)-(3.5)). The IIV is the standard deviation (ω) and relative standard error (r.s.e.) estimated using Monolix sofware. A proportional error model was used and the percentage error is listed as parameter b. Parameters marked "FIX" were held at stated values, and not estimated.

The individual fits for all animals in the dataset are included in Appendix D, and we show two typical fits from each experimental group in Figures 3.11a-f. Figure 3.11g shows that, similarly as for the no-normalisation model, there is close agreement between the observed and predicted data. Residual errors for the final model are shown in Figure 3.11h, where we have included a line that indicates the mean values for the weighted residuals for both treated groups in order to highlight that the bias at time points either side of the normalisation window is not present as it was in Figure 3.10h. Visual predictive checks (VPCs), split by experimental group, are shown in Figure 3.12. These results show that the enhanced tumour growth window model describes individual and population data well for all groups.

In order to compare the appropriateness of a proportional error model with a constant error model, we repeated the model fitting using a constant error model and compared the log-likelihood obtained from fittings with each error model using

the Wald test. The test statistic,

$$W = 2(\log\mathcal{L}_{const} - \log\mathcal{L}_{prop}),$$

where $\mathcal{L}_{const}$ and $\mathcal{L}_{prop}$ are the likelihoods of the constant and proportional error models, respectively, was compared with the χ^2 distribution. The conclusion of the statistical test was that the data are better described using a proportional error model than a constant error model, since the change in the log-likelihood between the two model fittings was significantly lower using the proportional error model than using the constant error model.

We selected the transient normalisation model as the most appropriate to represent the experimental data based on the diagnostic plots, shrinkage, parameter estimates and r.s.e. values, compared to the no-normalisation model (equations (3.3)-(3.5) with $N_{max} = 1$). The BIC for the transient dynamics model, BIC_T, was larger than the BIC for the monotonic model, BIC_M, ($BIC_T = 2865, BIC_M = 2797$). However, we do not reject the transient dynamics model based on the BIC, and we propose that the other evidence for model appropriateness (diagnostic plots, r.s.e., shrinkage) suggests that the normalisation model describes the data better than the monotonic model. In particular, the BIC accounts for the total difference between simulated and observed data via the likelihood, $\mathcal{L}$, but information on the consistent underestimation of the monotonic model at $t = 63$ is not taken into account. In this case, comparison of an information criterion is insufficient to compare models and diagnostic plots must also be considered.

The estimated value of the population parameter $N_{max} = 6.7$. An interpretation of this result is that, during the transient window, the vasculature provides sufficient oxygen and nutrients to support a tumour 6.7 times larger than it was able to support before the period of enhanced tumour growth.

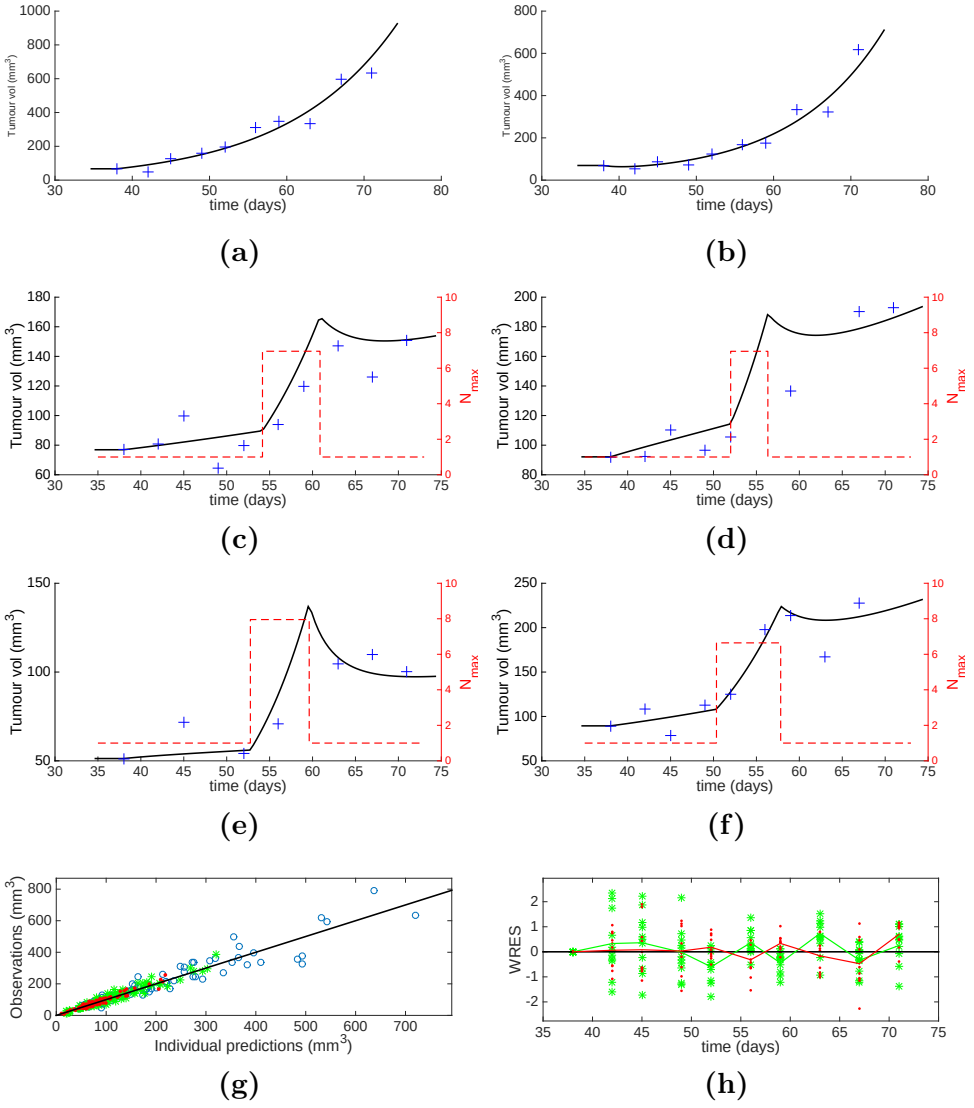


Figure 3.11: Fits, using Monolix, of the model with drug-induced vessel regression and transient vessel normalisation (equations (3.3)-(3.5)), to the experimental data shown in Figure 3.2, under the assumptions for fixed and free parameters given in Table 3.2. (a)-(f) Typical individual fits selected at random for (a)-(b) control; (c)-(d) bevacizumab, and (e)-(f) vanucizumab groups using experimental data. Key: Blue '+' - experimental data, solid black lines - predicted tumour volume, T, red dashed lines - normalisation windows for individuals. (g) Experimental (observed) results for tumour volume plotted against predicted results for tumour volume for individuals and coloured by group. (h) Weighted residuals (WRES) plots for the non-monotonic model. Solid green and red lines indicate the mean weighted residuals at each time point for bevacizumab and vanucizumab groups, repectively. Key: blue circles - control, green stars - bevacizumab, red dots - vanucizumab.

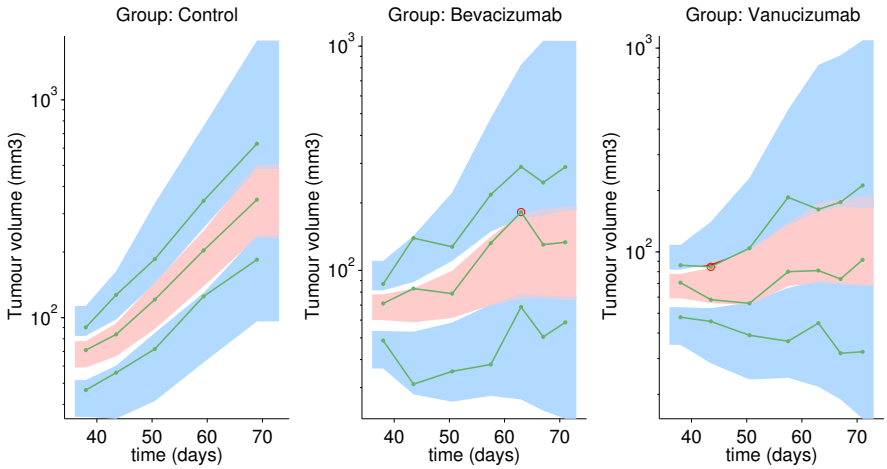


Figure 3.12: Visual predictive check (VPC) for equations (3.3)-(3.5), split by group. Parameters of the final model are listed in Table 3.2. Green, solid lines show the 10%, 50% and 90% quantiles of the observed data and the shaded regions represent the 90% prediction intervals on the theoretical 10% (blue region, lower), 50% (pink region, middle) and 90% (blue region, upper) quantiles from 100 simulations with the estimated parameters
. Outliers are highlighted by red circles.

3.5.3 Verification with histology data

We compare our estimate of the vessel dependent carrying capacity, V, at the end of the model simulations (day 71) with histological data (tumours harvested at day 71) for vessel density. Our experimental collaborators at Hoffman La Roche collected the histology data. Vessel number and size were automatically quantified on entire slides (samples were taken from 5 tumours from each experimental group) and microvessel density was calculated as vessels per mm^2 viable tissue.

Since our simulation results for the vessel dependent carrying capacity are measured as a volume (mm^3), we can only make qualitative comparisons with the histological data.

We compared the vessel density from histology with the effective vessel density from our model, calculated as V/T using the estimated population parameters from the final model for each experimental group. For the histology and simulated data, we scaled our results by dividing by the vessel density for the control group. The results presented in Figure 3.13 show good qualitative agreement between the simulated control and vanucizumab vessel dependent carrying capacities and the

histology results, although the results for the bevacizumab treated group were not in agreement. In our simulations, V corresponds to the vascular-dependent carrying capacity of the tumour, and theoretically, this includes the vasculature within the tumour and surrounding it, although our well-mixed approach does not capture spatial information. For the histology results, only vessels inside viable tumour regions were quantified: this could explain the discrepancy between the simulated and observed results for vessel density in the case of bevacizumab treatment.

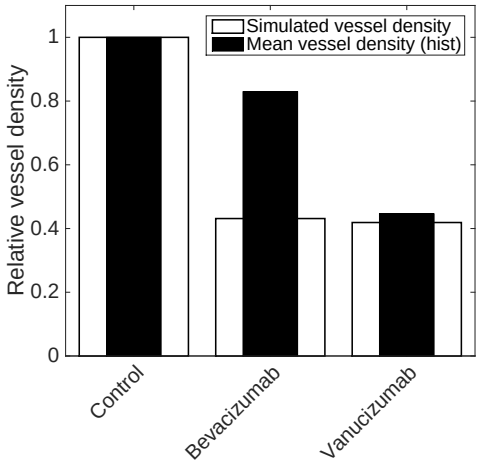


Figure 3.13: A bar chart to compare the simulated vessel density, V/T, at day 71 to the vessel density at day 71 from histology data, which was measured as vessels per mm^2. Each experimental group has been normalised by dividing by the vessel density for the control group.

3.5.4 Theoretical administration of chemotherapy

We now simulate the administration of a cytotoxic drug, $C(t)$ and investigate whether there is a more pronounced difference in tumour volume when chemotherapy is administered during the normalisation window. We assume that the cytotoxic drug is delivered to the tumour at a rate proportional to $N \times V$, and that it kills tumour cells at a rate proportional to its concentration in the tumour. Our chemotherapy model is based on one used in [62], to investigate the effects of docetaxel and capecitabine on tumour growth. For simplicity, we based our parameter estimates on the population parameters from [62]. The equations for vascular tumour growth

in response to combined anti-angiogenic and chemotherapy are given by:

$$\frac{\mathrm{d}T}{\mathrm{d}t} = \alpha_T\, T\left(1-\frac{T}{N\times V}\right) - \delta_T\, C\, T e^{-\lambda(t-t_{on})}, \tag{3.6}$$

$$\frac{\mathrm{d}V}{\mathrm{d}t} = \alpha_V\, T^{2/3}\, V^{1/3} - \delta_V\, V, \tag{3.7}$$

$$C(t) = \alpha_C(t) N V e^{-k\ \mathrm{mod}(t,1)}, \tag{3.8}$$

$$N(t) = \begin{cases} 1 \text{ for } t \le t_{norm1} \text{ and } t \ge t_{norm2}, \\ N_{max} \text{ for } t_{norm1} < t < t_{norm2}, \end{cases} \tag{3.9}$$

and

$$\alpha_C(t) = \begin{cases} 0 \text{ for } t \le t_{on} \text{ and } t \ge t_{off}, \\ \tilde{\alpha}_C \text{ for } t_{on} < t < t_{off}, \end{cases} \tag{3.10}$$

where $\delta_T, \lambda, \tilde{\alpha}_C$ and k are positive constants that represent the tumour cell kill rate, emergence of resistance to chemotherapy, dose of chemotherapy and clearance rate of chemotherapy in the blood, respectively. In equation (3.6), $C(t)$ is the concentration of the cytotoxic drug in mgml^{-1} inside the tumour. We perform simulations using the population values for the model parameters in response to vanucizumab, and fix the new parameters to the values obtained in [62]: $\tilde{\alpha}_C = 1\mathrm{mg\ ml}^{-1}\mathrm{mm}^{-3}, k = 0.9\ \mathrm{day}^{-1}$, $\delta_T = 0.12\ \mathrm{mg}^{-1}\mathrm{ml\ day}^{-1}, \lambda = 0.08\ \mathrm{day}^{-1}$. We consider three regimens:

1. Chemotherapy is administered once daily for a one week period **before** the transient window, so that $(t_{on}, t_{off}) = (42, 49)$,

2. Chemotherapy is administered once daily for one week **during** the transient window, so that $(t_{on}, t_{off}) = (54, 61)$,

3. Chemotherapy is administered **throughout** a three-week period that starts on the same day as anti-angiogenic therapy, and overlaps with the normalisation window so that $(t_{on}, t_{off}) = (38, 59)$.

The third regimen is likely to be the most realistic, and represents treatment when the timing of the normalisation window is not known. The total amount of chemotherapy administered is larger in regimen 3 than in regimens 1 and 2. The results of our

simulations are shown in Figure 3.14. The tumour volume at day 71 for each treatment regimen is summarised in Figure 3.15. When chemotherapy is administered before the transient window (regimen 1), tumour growth is reduced, but chemotherapy is more efficacious when administered during the transient window (regimen 2) due to the 6-fold enhancement in N, leading to a more pronounced decrease in tumour volume that is clearly visible in Figure 3.15. Our model predicts that chemotherapy as per regimen 3 above leads to a smaller reduction in tumour volume than chemotherapy administered only within the normalisation window, even though the total amount of chemotherapy administered was greater. In the chemotherapy model, a resistance to chemotherapy term (see parameter λ in equation (3.6)) leads to the counter-intuitive result that a lower total dose of chemotherapy in regimen 2 can lead to more pronounced tumour regression compared to the larger total dose of chemotherapy administered in regimen 3.

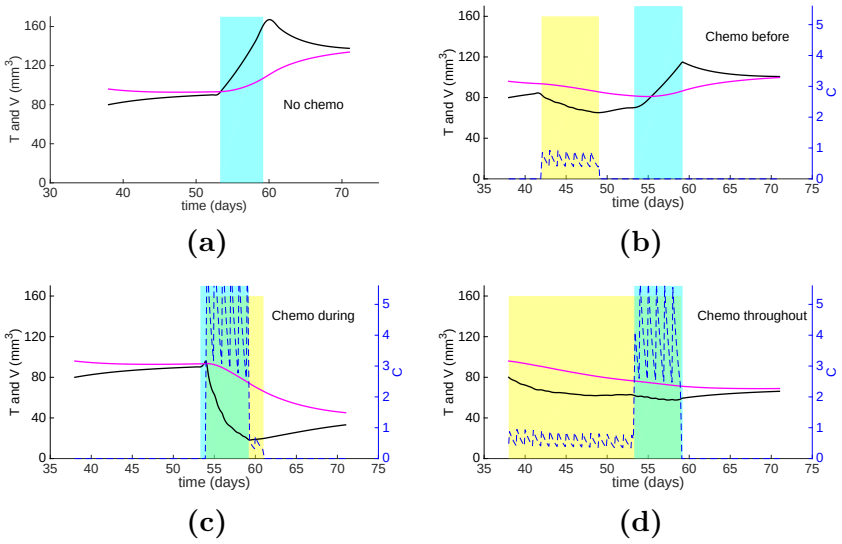


Figure 3.14: Model simulations for anti-angiogenic monotherapy, and three alternative theoretical regimens that combine anti-angiogenic therapy and chemotherapy (see equations (3.6)-(3.8)). Key: Black lines - tumour volume (T), magenta lines - vessel dependent carrying capacity (V), dashed blue lines - intratumoural concentration of the cytotoxic drug, C. Blue shaded regions represent the normalisation window and yellow shaded regions represent the delivery period of chemotherapy. (a) No chemotherapy, (b) Regimen 1: chemotherapy administered before the transient window, (c) Regimen 2: chemotherapy administered during the transient window (d) Regimen 3: chemotherapy administered for a three week period from day 38 to day 59. Anti-angiogenic therapy is administered from day 38 as in the preclinical study for all regimens.

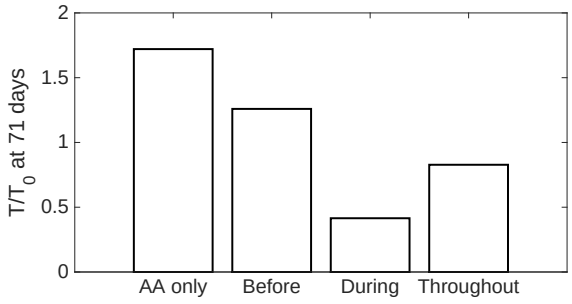


Figure 3.15: A bar chart to summarise the chemotherapy simulation results (see equations (3.6)-(3.8)): tumour cell density at the end of the experimental period compared to the initial condition for tumour cell density, T/T_0, for three chemotherapy regimens as summarised in Figure 3.14.

3.6 Discussion

In this chapter we have continued our investigation of angiogenesis and vascular tumour growth by focussing on AA therapy and normalisation. In contrast to the model presented in Chapter 2, we introduced a simple vascular tumour growth model and utilised mixed effects methods to parametrise it with experimental data. We evaluated the suitability of the mixed effects method for our model and dataset, and concluded that a pooled fitting approach is marginally preferable to a sequential fitting approach due to identifiability issues associated with the control model parameters. If data for the dynamic carrying capacity, which depends on vascular density, were available, then estimation of the control model parameters using control data only may be more accurate. Since vascular carrying capacity is a phenomenological variable, it cannot directly be measured. Assuming carrying capacity depends linearly on vessel density in the case of no normalisation, at least two measurements of the vascular density would be required in order to identify the parameters for the control case, and these measurements could be taken via histology or micro-CT [49, 96].

We used synthetic datasets to show that the accuracy and precision of parameter estimates using Monolix are improved by using more data in general, and that using data for both tumour size and vessel density usually, but not always, leads to more accurate parameter estimates. The accuracy and precision of parameter estimates is also usually improved for a smaller magnitude of the proportional error on the data. In practice, it is unethical to sacrifice 100 animals per group, and the experimental error is limited by the instruments used. Our synthetic data investigation showed that it is not always the case that more data with smaller experimental error improves parameter estimation accuracy. This may be due to the stochastic nature of the estimation method and also the tendency of the method to locate local minima in likelihood. Alternative methods to improve parameter inference potential would be to measure vascular density at at least two time points, as well as tumour volume, or to use more precise methods to identify tumour volume, such as CT scans [49].

To our knowledge, this is the first semi-mechanistic mixed effects model that accounts explicitly for the effects of vessel normalisation in response to anti-angiogenic therapy. Our model was motivated by the identification of non-monotonic dynamics in the experimental data (data shown in Figure 3.1), and builds upon recent, similar models by incorporating mathematical representations for the transient tumour growth dynamics [133, 184]. Based on our results we conclude that mixed effects modelling can be used to locate and parametrise the window of enhanced tumour growth, which may be a direct or indirect effect of the vessel normalisation window, for KPL-4 xenografts, leveraging only tumour size data. In addition, our model predicts that cytotoxic therapies would lead to a greater decrease in tumour volume if administered within the transient window. We note the limitations of our model, and make the above conclusions with caution, since there is uncertainty associated with the parameter estimates, and the BIC of the monotonic model was smaller than for the normalisation model.

We hypothesise that the transient window that we identify from our experimental data can be attributed to multiple processes, including increased pericyte coverage, increased vessel perfusion and decreased vessel permeability (leakiness). These physiological variables are assumed directly to increase tumour oxygenation and to increase the efficacy of chemotherapy, due to increased perfusion, and radiotherapy, due to increased oxygenation. Techniques such as window chamber assays and fluorescent staining are available to measure such physiological variables *in-vivo*. The next step of model validation involves performing experiments that can measure dynamic vessel characteristics such as perfusion and leakiness, to investigate whether the window of enhanced tumour growth that we identify corresponds to the above aspects of vessel normalisation, and whether chemotherapy is more efficacious when administered within the window.

Experiments performed on mouse xenografts suggest that normalisation can occur 3 days after the onset of treatment [48, 128, 172, 185]. The transient window that we identified begins 15 days after the start of anti-angiogenic treatment. It is possible that the enhanced tumour growth period that we have identified is a

downstream effect of vessel normalisation, and that the normalisation begins earlier. Further experiments are required to resolve this discrepancy.

Previous experiments have shown that, during the transient normalisation window, the efficacy of radiotherapy and chemotherapy are enhanced [47, 48, 128, 185]. If the window is not taken into account when investigating the efficacy of combined anti-angiogenic therapy with radiotherapy or chemotherapy, then inconsistencies in efficacy measurements may result. With validation, our model has the potential to provide a thorough understanding of the likely effect on efficacy measurements that the changing vasculature may have.

We developed and parametrised the model using longitudinal tumour size data, and the dynamic carrying capacity was inferred. The scope of our semi-mechanistic model is limited by the quality, quantity and type of available experimental data. A pooled approach was used for parameter estimation, to maximise the amount of data used to estimate the tumour and vessel growth parameters. For the final model, we fixed the IIV of t_{norm1} and t_{norm2} to 0.1 in order to allow small variations in the estimates for the start and end times of the transient window. No other parameter values were manipulated or fixed, except for the parameters for the chemotherapy simulations.

The results for the vascular volume after treatment were in reasonable qualitative agreement with histology data, although there is inconsistency in the reduction in vessel density in the bevacizumab group for simulated and observed data.

In the future, models such as the one presented in this chapter could be used to identify the transient window associated with other anti-angiogenic treatments and tumour cell lines, in both preclinical and clinical settings. We end by noting that our model could also be used to identify the optimal time for combination treatment, especially given the experimental observations in [185] and [48] suggest that combination therapies in which radiotherapy or chemotherapy are administered during the normalisation window achieve better outcomes than when administered before or after the window.

In the model presented in this chapter, we used a simple expression for the evo-

lution of the vessel dependent carrying capacity, assuming that the tumour had a positive effect on blood vessels. In the next chapter we develop a new model of vascular tumour growth, taking into account the negative effects that tumour cells have on vasculature, such as vessel occlusion and destabilisation. We use the concept of the normalisation window that was introduced in this chapter to investigate the behaviour of the vascular tumour growth model when different normalisation functions are implemented. We also build on the results in this chapter for concomitant chemotherapy and AA therapy to investigate the importance of the timing of chemotherapy with respect to the normalisation window.

Chapter 4

A non-spatial model of metastasis formation in a well vascularised region

4.1 Introduction

In the previous chapters, we considered a tumour that formed in a low-oxygen environment, such that the predominant mediators of tumour vascularisation were growth factor signals produced by tumour cells in response to hypoxia. In our previous models, the net effect of the tumour cells on existing vessels is positive, i.e. tumour cells stimulate formation of new blood vessels. In this chapter we consider a tumour that forms in a well vascularised region, with a good blood supply. As in Chapters 2 and 3, we focus on the effects of anti-angiogenic therapy and the role of vessel normalisation.

It was shown over 60 years ago that most tumours begin to grow directly around existing blood vessels [170]. Several studies have shown that vessel co-option, the recruitment of existing blood vessels by a tumour, is an important process for tumour progression. Tumours that grow in an oxygen-sufficient, well vascularised environment such as the brain, liver or lung are among the most aggressive [34, 82, 111, 168].

In such situations, the initial effect of the tumour on the blood vessels may be negative: the high density of tumour cells surrounding vessels causes them to collapse, inhibiting their perfusion via a process known as vessel occlusion [82]. The survival of co-opted vessels within the tumour microenvironment is influenced by an array of molecular and biomechanical processes, including the production of growth factors such as VEGF, Ang2 and PDGF, and pericyte coverage of vessels [50]. VEGF and Ang2 typically destabilise vessels, and reduce perfusion of intratumoural vessels. A study of breast cancer brain metastasis in mice showed that in the early stages of metastasis, cancer cells that have been transported in the blood from a primary tumour localise on the interior vessel wall of existing blood vessels and, in some cases, begin to proliferate before they extravasate, forming a solid tumour mass that surrounds the co-opted blood vessel [111].

Mathematical models that account for vessel co-option are proposed in [24, 28, 29, 139, 161]. Discrete modelling approaches are used in [28, 29, 139], where a pre-existing vascular network is proposed, and oxygen tension is modelled explicitly. In [139], the authors assume that a tumour forms around a pre-existing blood vessel, and new vessel sprouts form as the tumour cells proliferate. A three-dimensional vascular network initialises computational models in [28, 29], designed to reproduce pathophysiological phenomena associated with glioblastoma growth. By contrast, in [24, 161], systems of coupled PDEs describe the evolution of tumour and vessel densities through time and one spatial dimension. In [24], local oxygen concentration is assumed to be directly proportional to local vessel density, and in [161], oxygen levels in the tumour microenvironment are modelled explicitly. These models provide insight into how the oxygen tension varies throughout the tumour.

The PDE model presented by Stamper *et al.* [161] focusses on tumour cells, vessels, oxygen and chemotherapy, and identifies conditions under which vessel occlusion and tumour cell proliferation may lead to oscillatory dynamics. In more detail, the model comprises a set of reaction-diffusion equations for tumour cell density, vessel density and oxygen concentration, which may exhibit limit cycle solutions when spatial effects are neglected. In this chapter, we extend the spatially-averaged

version of Stamper *et al.*'s model to include aspects of anti-angiogenic (AA) therapy. We derive conditions under which oscillatory behaviour is expected during AA therapy, and show how the balance between AA-induced vessel kill and vessel normalisation influences the system dynamics. We also incorporate chemotherapy into our model in order to examine how different combination therapy regimens affect treatment outcome. In particular, we simulate chemotherapy administration inside and outside the vessel normalisation window. Our model describes the growth of a metastasis in a well vascularised region, however, the model could also represent a larger tumour in a well oxygenated region.

The structure of this chapter is as follows: in Section 4.2, we introduce our ODE model and describe the conditions under which it reduces to the model proposed in [161]. We identify the steady states and characterise their linear stability in Section 4.3 and in Section 4.4 we present typical simulation results. In Section 4.5 we simulate the model with two different normalisation functions, in the case of oscillatory and non-oscillatory behaviour, and in the cases of AA therapy alone and combined AA therapy and chemotherapy. In Section 4.6, we summarise our findings from the non-spatial model and motivate the model extensions that we undertake in the next chapter.

4.2 Model development

We base our model of vascular tumour growth on the spatially averaged version of a model proposed by Stamper *et al.* [161]. The model presented in [161] accounts for oxygen-dependent tumour growth, vessel growth, vessel occlusion due to local tumour cell density, oxygen delivery to the tumour, chemotherapy delivery to the tumour, and tumour growth inhibition due to chemotherapy. The key interactions, including our model extensions, are depicted in Figure 4.1. In this chapter, we simplify the model by neglecting spatial behaviour, and extend the model to account for vessel kill and normalisation due to AA therapy.

Our model describes the growth of a tumour in a well vascularised region, where

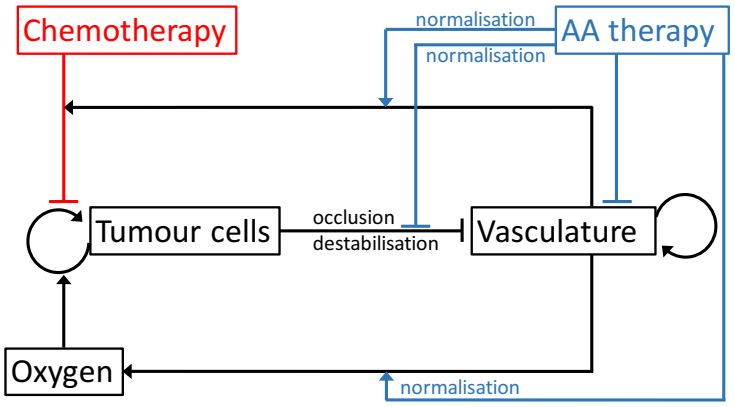


Figure 4.1: A schematic highlighting the key interactions in Stamper *et al.*'s model [161] and our model extensions (these are indicated in blue). Oxygen delivered via the vasculature enhances tumour cell proliferation. If the density of tumour cells is high then vessels are occluded and destabilised by growth factors produced by tumour cells and the density of functioning vasculature falls. Chemotherapy inhibits the proliferation of tumour cells and in our extended model, anti-angiogenic therapy acts to kill vessels and normalise the remaining vessels. Normalisation enhances the delivery of oxygen and chemotherapy to the tumour, and inhibits occlusion.

the net influence of the tumour cells on the vasculature is inhibitory: as tumour cells that surround vessels proliferate, they increase the pressure on those vessels, and this may lead to vessel collapse. Furthermore, tumour cells produce growth factors such as VEGF and Ang2 that may destabilise blood vessels and render them more prone to collapse, thus reducing the density of functioning vasculature. We do not account explicitly for VEGF and Ang2 in our model; we assume that the net effects of occlusion and destabilisation can be described simply and phenomenologically. A model that accounts for ligand concentrations may describe the system more accurately than our model, but such complexity would preclude detailed mathematical analysis. Depending on initial conditions, our model may also represent a tumour such as a metastasis that has established itself and created its own vasculature.

We simulate chemotherapy treatment using the model from [161], which is based on doxorubicin, to represent treatment with docetaxel, since both drugs act by killing proliferating tumour cells [124, 126]. Docetaxel is a small cytotoxic molecule that has been approved for treatment of breast, prostate, non-small cell lung cancer, stomach, and head and neck cancers [126], and has been administered in combination with

anti-angiogenic therapy [25, 123].

We assume that after the start of anti-angiogenic therapy, vessels become normalised: they undergo a transformation whereby perfusion is increased and the vasculature delivers oxygen and chemotherapy more effectively. In addition, normalised vessels are sheathed by pericytes, making them more robust and less likely to be occluded. An AA therapy that has been shown to induce vessel normalisation and reduce total vessel density, as described in the previous chapters, is bevacizumab [10, 171].

4.2.1 Control model and chemotherapy

In this subsection we introduce the model equations from [161] and in the next subsection we introduce our model extensions.

Following [161], we introduce the dependent variables T, V, S and C, which represent tumour cell density, vessel density, local oxygen concentration and local chemotherapy concentration, respectively, and focus on their time evolution in a well mixed environment.

The variable $T(t)$ represents the total number of tumour cells in a given tissue volume at time t. It is assumed that tumour cells proliferate at a rate that is an increasing, saturating function of the local oxygen concentration, $S(t)$, and that proliferating tumour cells are killed directly by cytotoxic chemotherapy. We also assume that tumour cells die naturally via apoptosis. The equation that represents tumour cells is

$$\frac{\mathrm{d}T}{\mathrm{d}t} = \underbrace{\frac{\beta S T}{s_\beta + S}\left(1 - 2\frac{C}{c+C}\right)}_{\substack{\text{cell proliferation,}\\ \text{modulated by chemotherapy}}} - \underbrace{d_p T}_{\text{apoptosis}}, \tag{4.1}$$

where the positive constants β and s_β characterise the maximum rate of tumour cell proliferation, and the concentration of oxygen at which tumour cell proliferation is half-maximal, respectively. Tumour growth is inhibited by chemotherapy, $C(t)$, and the constant, c, is the concentration of $C(t)$ at which chemotherapy has half-maximal efficacy.

Stamper *et al.* [161], assume that the variable $V(t)$ represents the surface area of vessels per unit volume of tissue, and that it includes existing vasculature and any new vessels formed via angiogenesis. We assume that the vessels undergo logistic growth, with growth rate η and carrying capacity V_0. The rate of vessel occlusion and destabilisation is assumed to be an increasing function of the ratio T/V, such that vessels are more likely to be occluded or destabilised when the ratio of tumour cells to vessel density is large. The equation for the vessel density is

$$\frac{\mathrm{d}V}{\mathrm{d}t} = \underbrace{\eta V\left(1-\frac{V}{V_0}\right)}_{\text{logistic growth}} - \underbrace{\frac{\delta T}{(k_\delta V+T)}V}_{\substack{\text{vessel occlusion}\\ \text{and destabilisation}}}, \tag{4.2}$$

where the parameter δ is the maximum rate of vessel occlusion and destabilisation and the parameter k_δ is the value of the ratio T/V at which occlusion and destabilisation are half maximal.

In the model presented in [161], blood oxygen concentration, S_b, is assumed constant, and oxygen delivery to the tumour is mediated by the blood vessels. The variable $S(t)$ represents oxygen concentration in units of volume of oxygen per unit volume of tissue. We assume that the transfer of oxygen from the blood vessels to the tissue depends on S_b and the permeability of the vessels, h_S. We suppose further that oxygen is consumed by tumour cells and other cells at rates σ and d_S, respectively. Thus, the equation for oxygen concentration is

$$\frac{\mathrm{d}S}{\mathrm{d}t} = \underbrace{h_S(S_b-S)V}_{\text{oxygen delivery}} - \underbrace{\sigma TS}_{\substack{\text{uptake by}\\ \text{tumour cells}}} - \underbrace{d_S S}_{\substack{\text{uptake by}\\ \text{other cells}}}. \tag{4.3}$$

Finally, the concentration of chemotherapy, in units of mass per unit volume in the tumour microenvironment, is denoted by $C(t)$. It is delivered via blood vessels by transcapilliary transfer and is cleared naturally at rate d_C. The equation for the time evolution of the chemotherapy is given by

$$\frac{\mathrm{d}C}{\mathrm{d}t} = \underbrace{h_C(C_b-C)V}_{\text{chemotherapy delivery}} - \underbrace{d_C C}_{\text{natural clearance}}, \tag{4.4}$$

where h_C is the permeability of the blood vessels to the chemotherapeutic drug and C_b is its concentration in the blood. We assume that chemotherapy is administered into the blood stream via multiple bolus injections, and that C_b is given by

$$C_b = C_b(t) = C_0 \; e^{-k(t \bmod t_{per})}, \tag{4.5}$$

where C_0 is the administered dose of chemotherapy, k is the clearance rate from the vasculature and t_{per} is the time between successive doses.

The model that we have described so far is identical to the one presented in [161].

4.2.2 Anti-angiogenic therapy and normalisation

Our extensions to equations (4.1)-(4.4) account for two aspects of anti-angiogenic therapy: vessel kill and vessel normalisation. With our extensions, ODEs (4.1)-(4.4) become

$$\frac{\mathrm{d}T}{\mathrm{d}t} = \frac{\beta S T}{s_\beta + S}\left(1 - 2\frac{C}{c+C}\right) - d_p T, \tag{4.6}$$

$$\frac{\partial V}{\partial t} = \eta V\left(1 - \frac{V}{V_0}\right) - \underbrace{\frac{\delta T V}{N(t)(k_\delta V + T)}}_{\substack{\text{vessel occlusion} \\ \text{impeded by normalisation}}} - \underbrace{d_V(t) V}_{\text{vessel kill}}, \tag{4.7}$$

$$\frac{\mathrm{d}S}{\mathrm{d}t} = \underbrace{h_S(S_b - S)N(t)V}_{\substack{\text{oxygen delivery} \\ \text{enhanced by normalisation}}} - \sigma T S - d_S S, \tag{4.8}$$

$$\frac{\mathrm{d}C}{\mathrm{d}t} = \underbrace{h_C(C_b - C)N(t)V}_{\text{chemotherapy delivery}} - \underbrace{d_C C}_{\text{natural clearance}}, \tag{4.9}$$

where $d_V(t)$ is the vessel kill rate, ($d_V(t) = 0$ in the absence of AA and $d_V(t) > 0$ in the presence of AA), and $N(t)$ is the normalisation function. We assume that normalisation leads to more sturdy vessel walls that withstand vessel occlusion, and also to higher perfusion, leading to more effective delivery of oxygen and chemotherapy.

We assume that the rate of vessel kill increases quickly from the time of administration of AA therapy to its maximum rate, and remains at its highest rate for

the duration of AA treatment. The AA therapy that we consider is an antibody, which exhibits different pharmacokinetics to chemotherapy drugs, and therefore the AA therapy terms are not similar to the chemotherapy delivery terms. As such, we define

$$d_V(t) = d_V^{max}\left(\frac{1}{\exp(-\gamma_A(t-t_{AA}))+1}\right), \tag{4.10}$$

where d_V^{max} is the maximum value for the vessel kill rate. The width of this smooth step function is characterised by the positive constant, γ_A. For the simulations in this chapter and the following chapter, we assume that AA therapy reaches its most efficacious concentration in the tumour microenvironment within two days, in line with the pharmacokinetics study in [112], and therefore we assume that $\gamma_A = 2.5$ day^{-1} and $(t_{AA} - 1)$ is the time at which AA therapy is administered.

In this chapter, we will investigate two alternative forms for the normalisation function, $N(t)$. Firstly, we assume that normalisation is transient (similar to in Chapter 3, and the experimental studies in [48, 185]), in which case,

$$N(t) = 1 + N_{max}\exp\left(-\frac{(t-t_{norm})^2}{\epsilon}\right), \tag{4.11}$$

where the maximum value of normalisation is $(1 + N_{max})$, the peak occurs at $t = t_{norm}$ and the duration of the normalisation window is governed by ϵ. We also consider a smooth step function for $N(t)$, which increases from 1 to its maximum value. Such dynamics are assumed to occur in experimental studies from Tong *et al.* and Tolaney *et al.* [171, 172]. The smooth step normalisation function is:

$$N(t) = 1 + N_{max}\left(\frac{1}{1+\exp(-\gamma(t-t_{norm}))}\right), \tag{4.12}$$

where t_{norm} controls the time at which normalisation increases from 1 and γ controls the width of the smooth step. We sketch the alternative normalisation functions in Figure 4.2.

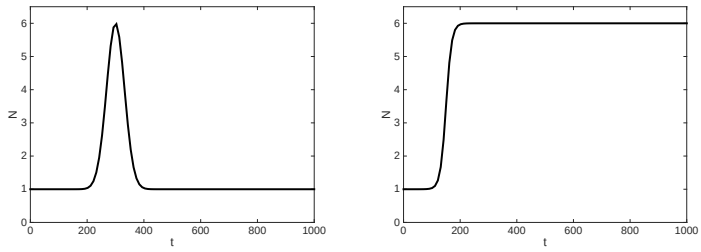


Figure 4.2: Plots of the alternative normalisation functions. Left: transient normalisation function given in equation (4.19) with $N_{max} = 5$, $t_{norm} = 300$ and $\epsilon = 2000$ days. Right: smooth step normalisation function given in equation (4.20), with $N_{max} = 5, \gamma = 0.1$ day^{-1} and $t_{norm} = 150$.

4.2.3 Non-dimensionalisation

In order to reduce the number of model parameters, equations (4.4)-(4.8) are rescaled as follows:

$$T^* = \frac{T}{k_\delta V_0}, \quad V^* = \frac{V}{V_0}, \quad S^* = \frac{S}{S_b}, \quad C^* = \frac{C}{C_0}, \quad C_b^* = \frac{C_b}{C_0}, \quad t^* = \beta t.$$

In terms of the parameter groupings:

$$\begin{array}{lllll} s_\beta^* = \dfrac{s_\beta}{S_b}, & d_p^* = \dfrac{d_p}{\beta}, & \delta^* = \dfrac{\delta}{\beta} & \eta^* = \dfrac{\eta}{\beta}, & \delta^* = \dfrac{\delta}{\beta}, \\ h_S^* = \dfrac{h_S V_0}{\beta}, & \sigma^* = \dfrac{\sigma k_\delta V_0}{\beta}, & d_s^* = \dfrac{d_s}{\beta}, & h_C^* = \dfrac{h_c V_0}{\beta}, & d_C^* = \dfrac{d_C}{\beta}, \\ k^* = \dfrac{k}{\beta}, & t_{per}^* = \beta t_{per}, & c^* = \dfrac{c}{C_0}, & d_V^* = \dfrac{d_V}{\beta}, & \gamma_A^* = \dfrac{\gamma}{\beta}, \\ \epsilon^* = \beta^2 \epsilon, & \gamma^* = \dfrac{\gamma}{\beta}, & & & \end{array}$$

the non-dimensionalised model can be written as (where * notation has been dropped for clarity):

$$\frac{\mathrm{d}T}{\mathrm{d}t} = \frac{S\,T}{s_\beta + S}\left(1 - 2\frac{C}{c+C}\right) - d_p T, \tag{4.13}$$

$$\frac{\mathrm{d}V}{\mathrm{d}t} = \eta V(1-V) - \frac{\delta T V}{N(t)(V+T)} - d_V(t)V, \tag{4.14}$$

$$\frac{\mathrm{d}S}{\mathrm{d}t} = h_S(1-S)N(t)V - \sigma T S - d_S S \tag{4.15}$$

$$\frac{\mathrm{d}C}{\mathrm{d}t} = h_C(C_b - C)N(t)V - d_C C, \tag{4.16}$$

$$C_b(t) = e^{-k(t \bmod t_{per})}, \tag{4.17}$$

where $d_V(t)$ and the two alternative functions for $N(t)$ are unchanged:

$$d_V(t) = d_V^{max}\left(\frac{1}{\exp(-\gamma_A(t - t_{AA})) + 1}\right), \tag{4.18}$$

$$\text{Transient: } N(t) = 1 + N_{max}\exp\left(-\frac{(t - t_{norm})^2}{\epsilon}\right), \tag{4.19}$$

$$\text{Smooth step: } N(t) = 1 + N_{max}\left(\frac{1}{1 + \exp(-\gamma(t - t_{norm}))}\right). \tag{4.20}$$

For the remainder of this chapter, the non-dimensional forms of variables and parameters will be used.

4.2.4 Parameter values

We refer the reader to [161] for estimates of most parameter values. Table 4.1 details dimensional parameter values, and Table 4.2 details dimensionless ones. We base our estimates for the tumour cell proliferation rate, β, and the vessel kill rate, d_V, on the results of our mixed effects model in Chapter 3, assuming that the estimates for these parameters obtained are a reasonable approximation to describe the well mixed system in this chapter.

4.2.5 Quasi-steady state approximations

We assume that the kinetics of oxygen and chemotherapy delivery occur on a much faster time scale than the dynamics of tumour and vessel growth: the parameter values that characterise the transfer of oxygen and chemotherapy support this assumption. Therefore, as in [161], we suppose that the oxygen concentration is in a quasi-steady state, and the local chemotherapy concentration is in a quasi-steady state throughout the treated period. Setting the right hand sides of equations (4.15)

Param	Description	Value	Units	Reference
β	Tumour cell proliferation rate	0.5	day^{-1}	Estimate from Chapter 3
d_P	Tumour cell apoptosis rate	0.1	day^{-1}	One fifth of β
s_β	Oxygen concentration for half maximal tumour growth rate	1	none	[161]
c	Concentration of chemotherapy for half maximal efficacy	0.1	mg ml^{-3}	[161]
η	Vessel proliferation rate	0.25	day^{-1}	0.5× the rate of tumour cell proliferation (order of magnitude estimate)
δ	Vessel occlusion rate	0.35	day^{-1}	Order of magnitude estimate based on vessel growth rate
k_δ	T/V ratio for half maximal vessel occlusion	4.5×10^5	cells mm	[135, 161]
d_V^{max}	Maximal vessel kill rate (AA therapy)	1	day^{-1}	Population estimate from Chapter 3 (we vary this parameter)
h_S	Vessel permeability to oxygen	620	mm day^{-1}	[161, 190]
S_b	Oxygen concentration in blood	1	none	[161]
σ	Oxygen uptake by tumour cells	2.3×10^{-3}	$\text{cell}^{-1}\text{day}^{-1}$	Order of magnitude estimate [161]
d_S	Oxygen degradation and uptake by other cells	2480	day^{-1}	[161]
h_C	Vessel permeability to chemotherapy	62	mm day^{-1}	[52, 161]
d_C	Decay rate of chemotherapy	1.4×10^{-4}	day^{-1}	[52, 161]
V_0	Vessel carrying capacity	10	mm^{-1}	[52, 161]
C_0	Reference chemotherapy concentration	1	mg mm^3	[161]
t_{per}	Time between chemotherapy doses	21	days	[161]
k	Clearance rate of chemotherapy	0.45	day^{-1}	[161]

Table 4.1: Default parameter set with units and references where applicable.

and (4.16) equal to zero, we obtain

$$S = S_{qss2} = \frac{NV}{NV + \tilde{\sigma}T + \tilde{d}_S}, \tag{4.21}$$

$$C = C_{qss} = \frac{C_b NV}{NV + \frac{d_C}{h_C}}, \tag{4.22}$$

Parameter	Description	Value
s^*_β	$\frac{s_\beta}{S_b}$	1
c^*	$\frac{c}{C_0}$	0.1
d^*_P	$\frac{d_P}{\beta}$	0.2
η^*	$\frac{\eta}{\beta}$	0.5
δ^*	$v\frac{\delta}{\beta}$	0.7
d_V^{max*}	$\frac{d_V}{\beta}$	0.01-1 (varies)
h^*_S	$\frac{h_S\ V_0}{\beta}$	1.24×10^4
σ^*	$\frac{\sigma K_\delta V_0}{\beta}$	2.1×10^4
$\tilde{\sigma}^*$	$\frac{\sigma *}{h^*_S}$	1.7
d^*_S	$\frac{d_S}{\beta}$	2.48×10^3
$\tilde{d}^*_S$	$\frac{d^*_S}{h_S}$	0.4
h^*_C	$\frac{h_C V_0}{\beta}$	1.24×10^3
d^*_C	$\frac{d_C}{\beta}$	2.8×10^4
k^*	$\frac{k}{\beta}$	0.9

Table 4.2: Non-dimensionalised parameter values.

where $\tilde{\sigma} = \frac{\sigma}{h_S}$ and $\tilde{d}_S = \frac{d_S}{h_S}$. With $S = S_{qss}$ and $C = C_{qss}$, equations (4.13)-(4.16) become

$$\frac{\mathrm{d}T}{\mathrm{d}t} = \frac{N(t)VT}{(N(t)V + s_\beta(N(t)V + \sigma T + d_S))}\frac{(h_- N(t)V + 1)}{(h_+ N(t)V + 1)} - d_p T \quad = f_c(T, V), \tag{4.23}$$

$$\frac{\mathrm{d}V}{\mathrm{d}t} = \eta V(1 - V) - \frac{\delta TV}{N(t)(V + T)} - d_V(t)V \quad = g_c(T, V), \tag{4.24}$$

where $h_+ = \frac{h_c}{d_C}\left(1 + \frac{C_b}{c}\right)$, $h_- = \frac{h_c}{d_C}\left(1 - \frac{C_b}{c}\right)$, and $N(t)$ is defined by either equation (4.19) or (4.20) in the case of AA therapy, and $N = 1, d_V = 0$ when no AA therapy is applied. Henceforth, we drop ˜ notation.

4.2.6 Initial conditions

We assume that, at $t = 0$, a small tumour has established itself in a normally vascularised tissue, such that

$$(T(0), V(0)) = (0.01, 1).$$

In the remainder of this chapter, we identify and characterise the steady state solutions of equations (4.23)-(4.24), and simulate the model for alternative therapy regimens.

4.3 Identification and characterisation of steady state solutions

As in Chapter 2, in this section, we use linear stability analysis to analyse the steady state behaviour of equations (4.23)-(4.24) in the cases of no therapy and AA therapy, noting that the case with $C_b = d_V = 0, N = 1$ was analysed in [161]. We assume that the vessel kill rate, d_V, and normalisation, N, are constant in this analysis.

4.3.1 Anti-angiogenic therapy

4.3.1.1 Steady states

The nullclines of the AA therapy model in equations (4.23)-(4.24), with $C = 0$ are identified by setting $\frac{\mathrm{d}T}{\mathrm{d}t} = 0$ in equation (4.23). The nullclines on which $\frac{\mathrm{d}T}{\mathrm{d}t} = 0$ are given by

$$T = 0, \tag{4.25}$$

$$T = \frac{(1 - d_P - s_\beta d_p)}{d_P s_\beta \sigma} NV - \frac{d_s}{\sigma}, \tag{4.26}$$

where (4.26) lies in a physically realistic region ($T, V \geq 0$) for

$$NV \geq \frac{d_S d_p s_\beta}{1 - d_p - s_\beta d_p}.$$

The nullclines on which $\frac{\mathrm{d}V}{\mathrm{d}t} = 0$ are given by

$$V = 0, \tag{4.27}$$

$$T = \frac{V(\eta(1-V) - d_V)}{d_V + \frac{\delta}{N} - \eta(1-V)}, \tag{4.28}$$

where (4.28) is physically realistic if

$$\begin{cases} 1 - \frac{d_V}{\eta} - \frac{\delta}{\eta N} < V \leq 1 - \frac{d_V}{\eta} & \text{if} \quad \Gamma = 1 - \frac{d_V}{\eta} - \frac{\delta}{\eta N} \geq 0, \\ 0 \leq V \leq 1 - \frac{d_V}{\eta} & \text{if } \Gamma < 0, \end{cases}$$

and an asymptote occurs at $V = \Gamma$.

The intersections of the nullclines define the fixed points of the system. It is straightforward to show that there are three physically realistic ($T, V \geq 0$) steady states:

$$(T, V) = \begin{cases} (0, 0), \\ \left(0, 1 - \frac{d_V}{\eta}\right), \\ (T_{ss}, V_{ss}), \end{cases} \tag{4.29}$$

where T_{ss} and V_{ss} denote the coexistence steady state associated with the intersection of the (4.26) and (4.28), so that

$$2V_{ss} = -A \pm \sqrt{A^2 - 4B} \tag{4.30}$$

and

$$T_{ss} = \frac{\Lambda N V_{ss} - d_S}{\sigma} = \frac{V_{ss}\left(1 - V_{ss} - \frac{d_V}{\eta}\right)}{V_{ss} - \Gamma}, \tag{4.31}$$

where

$$\begin{aligned} A &= \frac{d_V}{\eta} - 1 + \frac{\frac{\Lambda\delta}{\eta} - d_S}{\Lambda N + \sigma}\,, \\ B &= \frac{d_S(\eta - d_V - \frac{\delta}{N})}{\eta(\Lambda N + \sigma)} = \frac{d_S\Gamma}{\Lambda N + \sigma}, \\ \Lambda &= \frac{1 - d_P(1 + s_\beta)}{d_P s_\beta}. \end{aligned}$$

In Figure 4.3, we sketch phase planes for equations (4.23)-(4.24) for the default parameter set. We highlight qualitatively different cases where $\Gamma \geq 0$ and $\Gamma < 0$. We have indicated trajectories for three alternative initial conditions. There is always, at most, one physically realistic solution for (T_{ss}, V_{ss}), which can be deduced from the phase plane diagrams in Figure 4.3, along with the expressions for the nullclines in equations (4.25)-(4.28): For $\Gamma < 0$, two intersections in the positive quadrant of the (T, V) phase plane, between the curve defined by equation (4.28) and the line defined by equation (4.26), will occur only if the line crosses the T axis where $T > 0$, and this is not possible since the intersection occurs at $T = -\frac{d_s}{\sigma} < 0$, where $d_s, \sigma > 0$. In the case that $\Gamma \geq 0$, there can be only one intersection between the line defined by equation (4.26) and the curve defined by equation (4.28) in the positive quadrant of phase space.

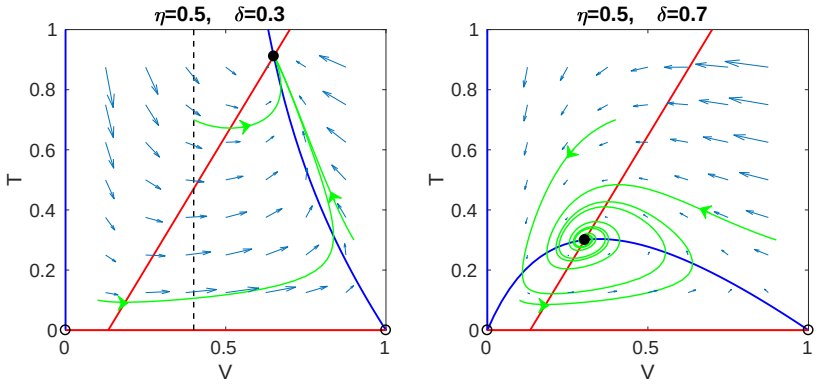


Figure 4.3: Phase plane diagrams to indicate the nullclines, steady states and example trajectories for the equations (4.23)-(4.24) in the case of no therapy for $\eta = 0.55$, $\Gamma > 0$ $(\delta = 0.3)$, where Γ is indicated by a vertical dashed line, and $\Gamma < 0$ $(\delta = 0.7)$ as indicated. Nullclines on which $\frac{\mathrm{d}T}{\mathrm{d}t} = 0$ are shown in red; nullclines on which $\frac{\mathrm{d}V}{\mathrm{d}t} = 0$ are shown in blue, typical trajectories are shown in green. Arrows indicate the direction and magnitude of $\frac{\mathrm{d}T}{\mathrm{d}t}$ and $\frac{\mathrm{d}V}{\mathrm{d}t} = 0$ for points in phase space. Unstable steady states are shown by open circles and stable steady states are shown by closed circles. Parameter values are as in Table 4.2 with δ indicated for each plot, $d_V = 0, N = 1$ and $C_b = 0$.

4.3.1.2 Linear stability and bifurcations

The linear stability of each steady state solution can be found by calculating the eigenvalues of the Jacobian, J, where

$$J = \begin{pmatrix} \frac{\partial f_c}{\partial T} & \frac{\partial f_c}{\partial V} \\ \frac{\partial g_c}{\partial T} & \frac{\partial g_c}{\partial V} \end{pmatrix},$$

and where

$$\frac{\partial f_c}{\partial T} = \frac{NV(NV(1+s_\beta)+s_\beta d_S)}{(NV(1+s_\beta)+s_\beta\sigma T+s_\beta d_S)^2} - d_p, \tag{4.32}$$

$$\frac{\partial f_c}{\partial V} = \frac{NT(s_\beta\sigma T+s_\beta d_s)}{(NV(1+s_\beta)+s_\beta\sigma T+s_\beta d_S)^2}, \tag{4.33}$$

$$\frac{\partial g_c}{\partial T} = -\frac{\delta V^2}{N(T+V)^2}, \tag{4.34}$$

$$\frac{\partial g_c}{\partial V} = \eta(1-2V) - \frac{\delta T^2}{N(T+V)^2} - d_V, \tag{4.35}$$

evaluated at the steady state in question. In [161], oscillatory behaviour was observed for certain parameter values in the absence of therapy. In this section, we determine whether AA therapy can generate oscillatory dynamics that may lead tumour reduction followed by relapse. A bifurcation diagram in which we vary the vessel kill rate, d_V, is shown in Figure 4.4.

The eigenvalues of the Jacobian matrix evaluated at the tumour free steady state where $(T, V) = (0, 0)$ are $-d_p$ and $(\eta - d_V)$, and therefore this steady state is linearly stable when the vessel kill rate exceeds the vessel growth rate ($d_V > \eta$) and an unstable saddle otherwise. This suggests that a dose of AA therapy that leads to net regression of the blood vessels will eliminate the tumour, and also the surrounding vasculature.

At the second tumour-free steady state, where $(T, V) = \left(0, 1 - \frac{d_V}{\eta}\right)$, the Jacobian has negative eigenvalues if

$$1 - d_P \left(1 - s_\beta \left(1 + \frac{d_S}{N}\right)\right) < \frac{d_V}{\eta} < 1. \tag{4.36}$$

and therefore this steady state is physically realistic and locally stable under these conditions. We consider this the optimal outcome from AA therapy. This steady state is not physically realistic when $d_V > \eta$; a transcritical bifurcation occurs when $d_V = \eta$, since the steady state loses linear stability.

The linear stability of the coexistence steady state depends on the sign of Γ. When $\Gamma \geq 0$, the nullcline given by equation (4.28) is a decreasing function of V that is physically realistic for $\Gamma < V < 1 - \frac{d_V}{\eta}$. Substituting the expression for T_{ss} in terms of V_{ss} and Λ, given by equation (4.31), into the expression for $\frac{\partial f_c}{\partial T}$, given by equation (4.32), we derive the condition for which $\frac{\partial f_c}{\partial T} \leq 0$:

$$NV \geq \frac{d_S d_p s_\beta}{1 - d_p - s_\beta d_p}.$$

This condition is the same as that for which the nullcline given by equation (4.26) lies in the physically realistic region: where T_{ss} and V_{ss} are physically realistic the condition is fulfilled. Similarly, by substituting the expression T_{ss} in terms of V_{ss}

and Γ, given by equation (4.31), into the expression for $\frac{\partial g_c}{\partial V}$, given by equation (4.35), we obtain the quadratic

$$-\Gamma\left(1-\frac{d_V}{\eta}\right)+2\Gamma V-V^2\leq 0$$

for $\frac{\partial g_c}{\partial V}\leq 0$. For $\Gamma\geq 0$, this inequality holds. Therefore for $\Gamma\geq 0$, the trace of the Jacobian evaluated at the coexistence steady state is negative, the coexistence steady state is linearly stable where it exists, and Hopf bifurcations do not occur.

The linear stability of the coexistence steady state for $\Gamma<0$ is calculated numerically in Matlab by evaluating the eigenvalues of the Jacobian evaluated at the coexistence steady state, determining its stability from their signs. The results are shown the bifurcation diagram in Figure 4.4. In the default parameter regime, two Hopf bifurcations occur for the coexistence steady state at values of d_V that we will refer to as d_V^{crit+} and d_V^{crit-}, respectively. For $d_V^{crit-}<d_V<d_V^{crit+}$, the coexistence steady state is an unstable spiral. It can be shown by the Poincare-Bendixson theorem that since the other steady states are linearly unstable, a limit cycle occurs for $d_V^{crit-}<d_V<d_V^{crit+}$. Our numerical simulations in Figure 4.4 show the amplitude of the limit cycle oscillations. The values of d_V^{crit+} and d_V^{crit-} can be evaluated by equating the trace of the Jacobian evaluated at the coexistence steady state to zero. At $d_V^{crit-}<d_V<d_V^{crit+}$ the real parts of the eigenvalues are positive, and for $d_V<d_V^{crit-}$ and $d_V>d_V^{crit+}$, the real parts of the eigenvalues are negative. On the phase plane diagram in Figure 4.3, the effect of increasing d_V would be to change the shape of the nullcline on which $\frac{\mathrm{d}V}{\mathrm{d}t}=0$, and the nullcline on which $\frac{\mathrm{d}T}{\mathrm{d}t}=0$ would not be affected. If $V_{ss}=1-\frac{d_V}{\eta}$, then $T_{ss}=0$ and a transcritical bifurcation occurs for the coexistence steady state.

The linear stability of the steady states is summarised in Table 4.3.

In Figure 4.5, we show that as N increases, the range of values of d_V for which a limit cycle occurs shifts to the right and decreases in width. In practice, oscillatory values for the tumour cell density are not desirable; a transient decrease in tumour volume may be misinterpreted as an apparent cure. Therefore, treatment protocols

Range of values of d_V	$(T,V)=(0,0)$	$(T,V)=\left(0,1-\frac{d_V}{\eta}\right)$	$(T,V)=(T_{ss},V_{ss})$
$d_V \leq d_V^{crit-}$	Unstable	Unstable	Linearly stable
$d_V^{crit-} < d_V < d_V^{crit+}$	Unstable	Unstable	Unstable spiral (limit cycle occurs)
$d_V^{crit+} \leq \eta\left[1-d_P\left(1-s_\beta\left(1+\frac{d_S}{N}\right)\right)\right]$	Unstable	Unstable	Linearly stable
$\eta\left[1-d_P\left(1-s_\beta\left(1+\frac{d_S}{N}\right)\right)\right] < d_V < \eta$	Unstable	Linearly stable	Unphysical
$d_V \geq \eta$	Linearly stable	Unphysical	Unphysical

Table 4.3: Summary of the linear stability of each of the three steady states for the model in equations (4.23)-(4.24) with $C_b = 0$ (no chemotherapy), $\Gamma < 0$.

that drive the system into the limit cycle regime are not desirable. Furthermore, the more pronounced the normalisation, the larger the value of d_V that is required to access the linearly stable steady state where $d_V > d_V^{crit+}$. In Figure 4.5, for smaller values of d_V, larger values of N give rise to a higher tumour cell density in the coexistence steady state. This indicates that normalisation due to AA therapy can have a negative effect on patients by leading to a larger tumour cell density in the coexistence steady state.

4.3.2 Summary of steady state and linear stability analysis

There are three possible steady state solutions for the model with no therapy or AA therapy. The coexistence steady state is linearly stable under certain conditions, and limit cycle behaviour is predicted in certain regions of parameter space. There is at most one linearly stable steady state in each region of parameter space. AA therapy at a concentration for which the vessel kill rate is greater than the vessel proliferation rate ($d_V > \eta$), will in theory lead to the unhealthy tumour free and vessel free state where $(T,V) = (0,0)$, and lower concentrations of AA therapy stabilise either the steady state for which $(T,V) = \left(0, 1-\frac{d_V}{\eta}\right)$, which could be considered a cure, or the coexistence steady state (see Table 4.3).

As shown in Figure 4.5, in some cases, the combination of values for N and d_V can lead to a larger steady state tumour cell density than the control case. The parameter d_V can be varied to access the limit cycle regime when $\Gamma < 0$ and the

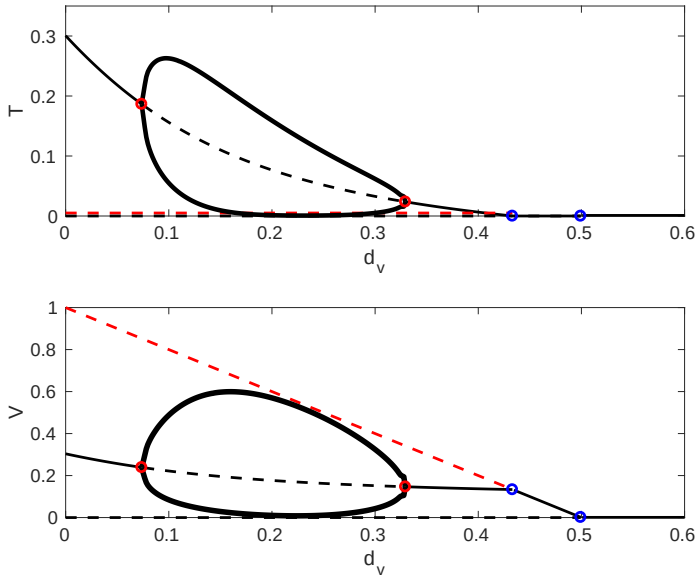


Figure 4.4: Bifurcation diagrams for T and V in the case of AA therapy for the equations (4.23)-(4.24). Bifurcation parameter: $0 \leq d_V \leq 0.6$. Thin solid lines represent linearly stable steady states, thick solid lines represent the magnitude of the limit cycle, and dashed lines represent all other linearly unstable steady states (the unstable region of the steady state where $(T, V) = \left(0, 1 - \frac{d_V}{\eta}\right)$ is shown in red for clarity). The amplitudes of the limit cycle oscillations were calculated from simulations for individual values of d_V. Hopf bifurcation points are indicated by red circles and transcritical bifurcation points are indicated by blue circles. Parameter values as per Table 4.2 with $N = 1$.

range of values for which a limit cycle occurs varies with N. Therefore it is the combination of N and d_V, among other parameter combinations, that determines the long term behaviour of the model.

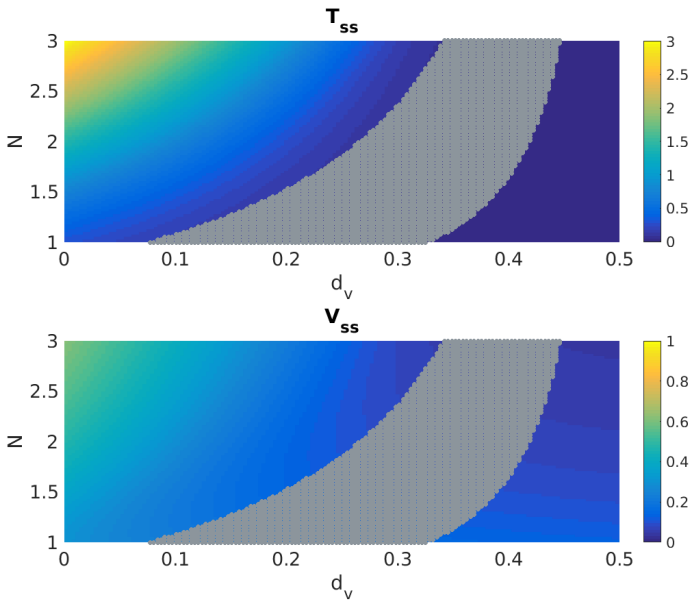


Figure 4.5: Bifurcation diagrams highlighting the region of parameter space in which equations (4.23)-(4.24) admit a limit cycle solution. Bifurcation parameters are d_V and N. Coloured areas indicate regions in which the coexistence steady state is linearly stable; the corresponding values of T_{ss} and V_{ss} are indicated by the colour maps. Grey areas indicate where limit cycles occur. The values of T_{ss} and V_{ss} at each point were identified from individual simulations for values of d_V and N. Parameter values are as in Table 4.2.

4.4 Simulations of the ODE models

4.4.1 Model comparison: quasi-steady state approximations

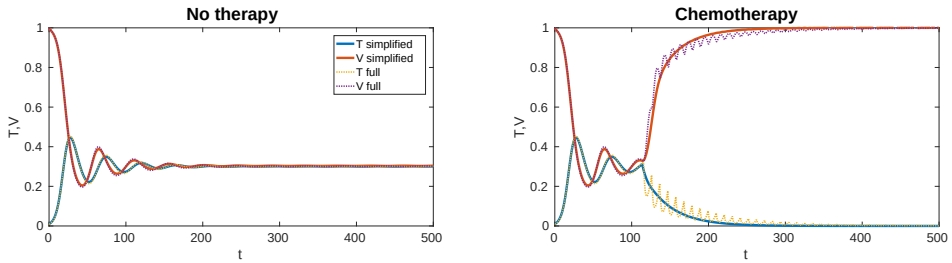
Our first goal is to determine the validity of the quasi-steady state approximations for $C(t)$ and $S(t)$. We simulate the full model without quasi-steady state approximations for $S(t)$ and $C(t)$ (equations (4.13)-(4.17)) and compare with the results of the simplified model (equations (4.23)-(4.24)) to demonstrate that our approximations are valid and in good agreement with the full model. In Figure 4.6 we present results for the cases of no therapy, AA therapy, chemotherapy, and combined AA and chemotherapy. For simulations of the full model, chemotherapy was administered once every three weeks, and this gives rise to the fast dynamics that are not present in the simplified model simulations, where the concentration of chemotherapy in the

blood is considered constant. We chose $C_b = 0.11$ for the simplified model simulations, since this produces similar results to the full model for chemotherapy treatment effect. In light of the close agreement between results with the quasi-steady state approximations, we continue to use the simplified model for the remainder of the simulations in this chapter and the following chapter. In the following chapter, we introduce a PDE model that we solve using a numerical method. The method is not suited to simulating systems where fast dynamics are prescribed, such as those in the full chemotherapy model. Therefore, we assume that chemotherapy is at a concentration in the blood for simulations in the following chapter, and, for consistency, in this chapter.

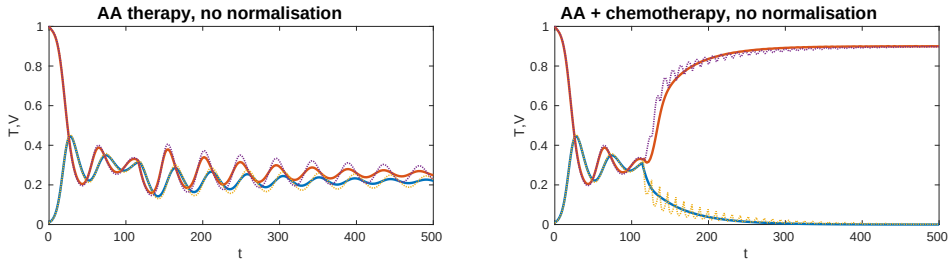
The results presented in Figure 4.6 show that with chemotherapy, $(T, V) \to \left(0, 1 - \frac{d_V}{\eta}\right)$ as $t \to \infty$, i.e. that the tumour evolves to the healthy, tumour-free steady state. However, in practice, due to the toxicity of most chemotherapy drugs, an ongoing regimen such as this is unrealistic.

4.4.2 Typical simulations

We simulate the model in equations (4.23)-(4.24) for values of d_V that give rise to linearly stable or oscillatory behaviour, illustrating our results in Figure 4.7. We choose values of d_V for which the coexistence steady state is linearly stable, the oscillatory regime and the critical value for which a Hopf bifurcation occurs. In the simulation of AA therapy that leads to the linearly stable steady state, we observe oscillations that decay to the linearly stable steady state. Limit cycle oscillations occur for the value of d_V that leads to the oscillatory regime, and when the value of d_V is close to the Hopf bifurcation point, periodic, damped oscillations occur.



(a)



(b)

Figure 4.6: Simulations of the full (equations (4.13)-(4.17)) and simplified ((4.23)-(4.24)) ODE models in the cases of no therapy, AA therapy and chemotherapy as indicated. For chemotherapy simulations (right), chemotherapy was switched on at $t = 115$ and in the simplified model, $C_b = 0.11$ during chemotherapy administration. (a) $d_V = 0$ throughout. (b) d_V as in equation (4.18) where $t_{AA} = 116, \gamma = 5, d_V^{max} = 0.2$. The initial conditions for simulations were $(T, V, S, C) = (0.01, 1, 0.01, 0)$. Parameter values as per Table 4.2 with $N = 1$.

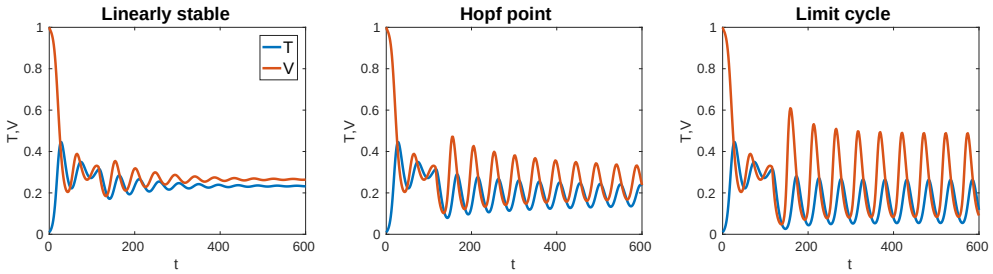


Figure 4.7: Typical simulations of equations (4.23)-(4.24) with AA therapy. Vessel kill rate, d_V is as in equation (4.18). Left: Linearly stable regime, $d_V^{max} = 0.04$. Middle: Hopf bifurcation point $d_V^{max} = 0.0736$. Right: oscillatory regime $d_V^{max} = 0.1$. The initial conditions for simulations were $(T, V) = (0.01, 1)$. Parameter values as per Table 4.2 with $N = 1, C_b = 0$.

4.5 Further simulations

In this section, we simulate the quasi-steady state approximation model in equations (4.23)-(4.24) and investigate several clinically relevant treatment regimens for AA and chemotherapy. We showed in the previous section that this model provides a good approximation to the full model. We also investigate two alternative normalisation functions. Typically, docetaxel is administered once every 3 weeks for 6 cycles [126], while bevacizumab is administered once every two weeks until disease progression (an increase in tumour volume) is observed [6]. Our non-dimensional time units correspond to 2 days. For our simulations we assume that chemotherapy is administered once every three weeks from $t = 115$ for a total of 6 doses. Since, as we showed in Figure 4.6, the assumption that chemotherapy is at a constant concentration in the blood throughout treatment is a good approximation, we assume that $C_b = 0.11$ for the entire 18 week period (63 time units) of administration.

4.5.1 Non-oscillatory regimes

AA therapy prolongs the time taken to reach steady state: The simulations with no treatment in Figure 4.8a show that the system has reached a steady state within 300 time units. However, in Figure 4.8b, where the maximum vessel kill rate, d_V^{max} is less than d_V^{crit-} and when $N = 1$ throughout the simulation, a steady state is not reached within 600 time units. Including chemotherapy for both cases further prolongs the time taken until steady state is reached.

We also simulated the case where $d_V < d_V^{crit-}$ assuming a transient normalisation function from equation (4.19), varying the time at which chemotherapy is administered. In the simulations of AA only with the transient normalisation function in Figure 4.9, we observe an initial peak in tumour cell density as the normalisation increases due to increased oxygenation. The peak is suppressed when chemotherapy is administered during the transient normalisation period, but not when chemotherapy is administered before the normalisation period.

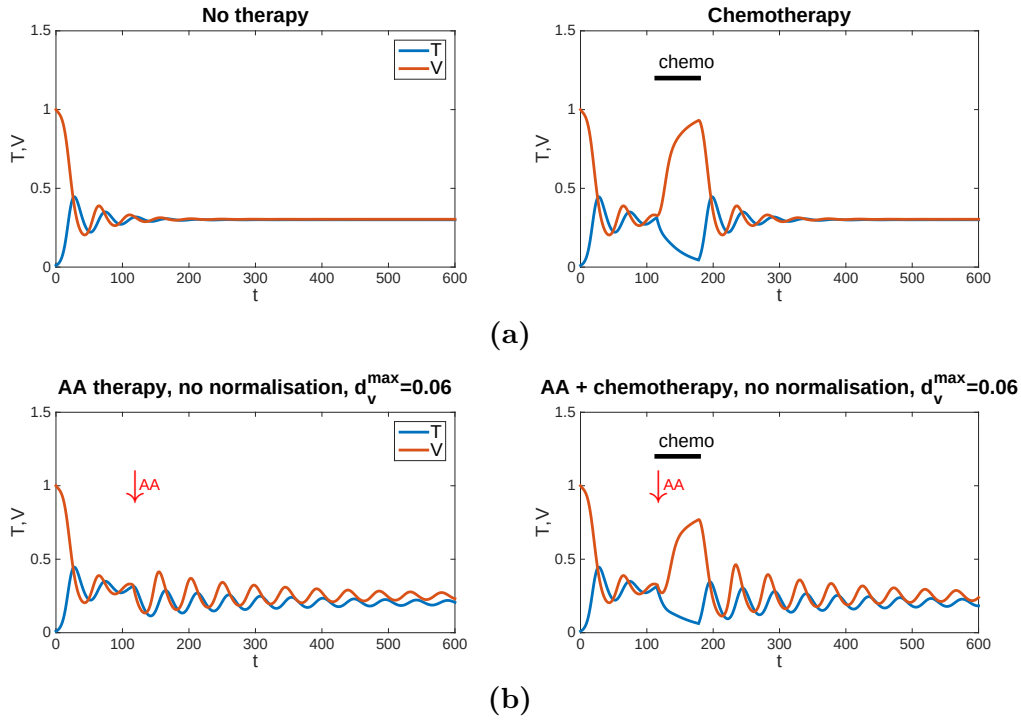


Figure 4.8: Simulations of equations (4.23)-(4.24) in the cases of no therapy, AA therapy and chemotherapy as indicated. Thick black lines indicate the period of chemotherapy treatment for $115 \leq t \leq 178$. (a) $d_V = 0$ throughout. (b) d_V as in equation (4.18) with $d_V^{max} = 0.06 < d_V^{crit-}$, and $N = 1$ for all time. The initial conditions for all simulations were $(T, V) = (0.01, 1)$. Parameter values as per Table 4.2 and $C_b = 0.11$ during the chemotherapy period.

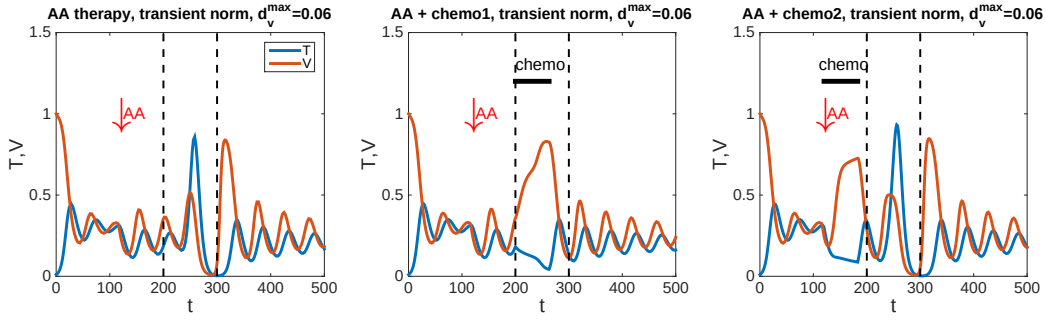


Figure 4.9: Simulations of equations (4.23)-(4.24) in the cases of AA therapy and chemotherapy as indicated, with a transient normalisation function as in equation (4.19) with $N_{max} = 1, \epsilon = 50, t_{norm} = 130$. Thick black lines indicate the period of chemotherapy treatment for $115 \leq t \leq 178$ (middle) or $145 \leq t \leq 208$ (right). Vertical dashed lines indicate the transient normalisation window. AA therapy as in equation (4.18) with $d_V^{max} = 0.06 < d_V^{crit-}$. The initial conditions for all simulations were $(T, V) = (0.01, 1)$. Parameter values as in Table 4.2 and $C_b = 0.11$ during the chemotherapy period.

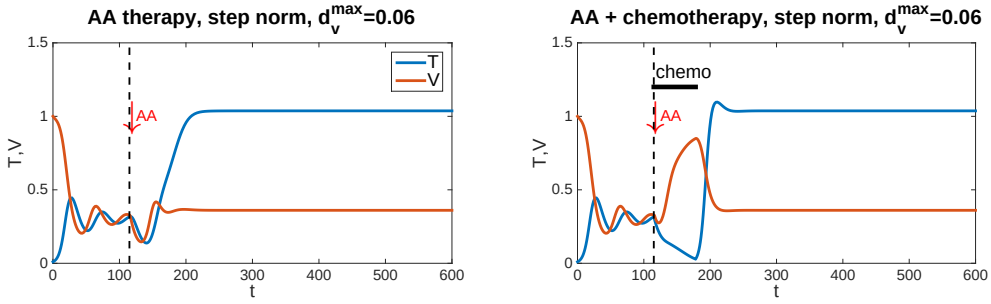


Figure 4.10: Simulations of equations (4.23)-(4.24) in the cases of AA therapy and chemotherapy as indicated with a step normalisation function as in equation (4.20) with $N_{max} = 1, \gamma = 0.5, t_{norm} = 125$. The thick black line indicates the period of chemotherapy adminstration for $115 \leq t \leq 178$. Vertical dashed lines indicate the start of the normalisation period. AA therapy as in equation (4.18) with $d_V^{max} = 0.06 < d_V^{crit-}$. The initial conditions for all simulations were $(T, V) = (0.01, 1)$. Parameter values as in Table 4.2 and $C_b = 0.11$ during the chemotherapy period.

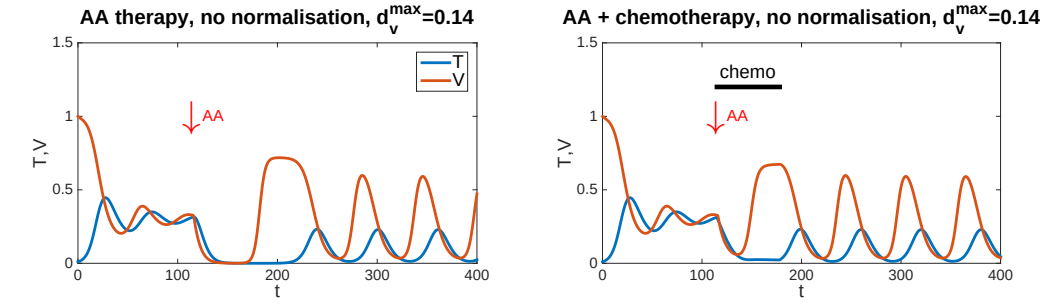
Some combinations of d_V and N lead to an increased post-treatment tumour cell density compared to the pre-treatment tumour cell density: The simulation results presented in Figure 4.10 show that when normalisation is modelled via a smooth step function as in equation (4.20), the long term tumour cell density may be larger than the pre-treatment tumour cell density. This behaviour arises when the vessel kill term is small and normalisation is large. Clearly this is not a desirable clinical outcome. For concomitant chemotherapy and AA therapy, an initial reduction in tumour cell density occurs during the chemotherapy period.

4.5.2 Oscillatory regimes

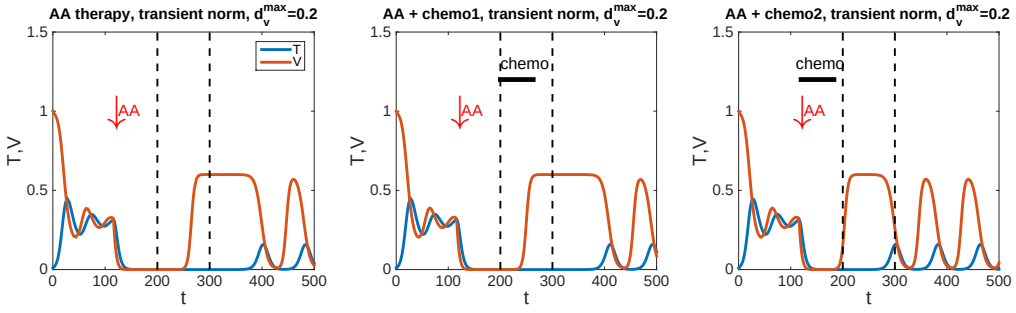
If AA therapy leads to more severe vessel kill, such that $d_V^{crit-} < d_V < d_V^{crit+}$, then our model may yield oscillatory behaviour, as demonstrated in the previous section. Figure 4.5 indicates the regions of (d_V, N) parameter space in which oscillatory behaviour occurs. By including transient and step normalisation functions, we simulate transitions between regions in which oscillatory solutions are expected and regions in which they are not.

Chemotherapy in combination with AA therapy can reduce the tumour-free period compared to AA alone: We simulated a smooth step normalisation function, as in equation (4.20), for which $d_V = 0.14$ and the steady state is unstable (oscillatory) for $N = 1$. The results of our simulations with and without chemotherapy are shown in Figure 4.11a. The tumour and vessel densities transition from a linearly stable steady state to an oscillatory regime. Including chemotherapy during the oscillatory phase leads to a reduced period where $T \ll 1$.

Finally, we apply a transient normalisation function, as in equation (4.19), to the case where $d_V = 0.2$. The model is in the linearly unstable regime when $N = 1$, and a transition to the linearly stable regime occurs as N increases past some critical value, before returning to the linearly unstable regime as N decreases. The results of our simulations for AA therapy alone, and for two different schedules of chemotherapy, are shown in Figure 4.11b. In all cases, AA therapy leads to an initial period where $T, V \ll 1$, and as N increases during the transient period, V increases but $T \ll 1$. Eventually, when N decreases, the system resumes limit cycle oscillations. For chemotherapy administered before the transient normalisation window, the period where $T \ll 1$ is shorter compared to AA alone. These results suggest that the timing of chemotherapy relative to the normalisation window can influence the expected time before relapse, but does not affect the long term treatment outcome.



(a)



(b)

Figure 4.11: Simulations of equations (4.23)-(4.24) in the cases of AA therapy and chemotherapy as indicated. For AA therapy, d_V as in equation (4.18). (a) No normalisation ($N = 1$), $d_V^{max} = 0.14$. Chemotherapy is administered for $120 < t < 183$ as shown by the thick black line. (b) $d_V^{max} = 0.2$, N behaves as the transient function in (4.19) with $N_{max} = 1, \epsilon = 500, t_{norm} = 250$, and the start and end times of the normalisation window are shown by vertical dashed lines. Chemotherapy is administered for $200 < t < 263$ (middle) or for $120 < t < 183$ (right) as indicated by the thick black line. The initial conditions for all simulations were $(T, V) = (0.01, 1)$. Parameter values as in Table 4.2.

4.6 Discussion

In this chapter we have developed a well-mixed model for tumour growth in a well vascularised tissue. Our model accounts for vessel occlusion and destabilisation and provides insight into the expected response to AA therapy and chemotherapy. Our steady state and linear stability analyses revealed three possible steady state behaviours that exist and are linearly stable in regions of parameter space that can be accessed by varying the vessel kill rate, d_V. We have shown that several model parameters, including the parameter that represents the vessel kill rate for AA therapy, can lead to oscillatory behaviour and moreover that the balance between

the aspects of AA therapy - vessel kill and vessel normalisation - can be crucial in determining the therapeutic outcome. Scheduling of chemotherapy relative to the normalisation window, in the case of transient vessel normalisation, can influence the time until relapse. This result is (qualitatively) clinically relevant for a combined AA and chemotherapy regimen where AA therapy leads to prolonged progression-free survival, but not overall survival [6].

The model that we present in this chapter is subject to several assumptions and simplifications, including a well-mixed assumption, the neglect of phenotypic differences in tumour cell types, and neglect of normal, 'healthy' cells, among others. The model could be extended to include chemokine concentrations such as VEGF and Ang2, and also to include normal cells. These extensions would provide a more realistic model, but would prohibit analytical progress and furthermore, introduce extra parameters that are difficult to estimate. We proposed that our model represents the formation of a micrometastasis in a well vascularised region, such as that described in [111]. The preclinical study provides a qualitative description of the process of breast cancer brain metastasis formation, however, longitudinal data for such an experimental system are difficult to obtain due to the spontaneous nature of metastasis formation.

Although our model is too simplistic to provide quantitative predictions regarding vascular tumour growth and AA therapy, it can be used to gain insight into the range of potential treatment outcomes from the model in different parameter regimes. Furthermore, our non-spatial model provides insight into the growth of a vascular tumour in a well vascularised tissue, but does not provide information about whether the interior of the tumour is spatially homogeneous or heterogeneous in each treatment case. In particular, similarly to [161], where the authors showed that the oscillatory regime gives rise to tumour heterogeneity in the absence of AA therapy, we wish to investigate how AA therapy may also give rise to spatial heterogeneity, which could affect drug delivery to the tumour. In the following chapter, we extend our model by including diffusion-like terms that allow spatial variation in one and two spatial dimensions.

Chapter 5

A spatiotemporal model of vascular tumour growth

5.1 Introduction

In the previous chapter, we developed a spatially averaged ordinary differential equation (ODE) model of vascular tumour growth, accounting for vessel occlusion and destabilisation. We considered tumour formation in a well vascularised region, where the tumour has a negative effect on the vessels due to occlusion and destabilisation. For the spatially averaged model, we showed that oscillatory behaviour is possible, and the parameters that represent anti-angiogenic (AA) therapy, among other parameters, can be modulated to access the oscillatory regime. We showed that administration of chemotherapy after the transient normalisation window can result in a prolonged time until relapse compared to chemotherapy administered during the normalisation window, but did not affect the long-term treatment outcome.

In this chapter we extend the model to include spatial effects, similarly to [161], introducing a set of reaction-diffusion partial differential equations (PDEs). The aim of our study is to investigate how the inclusion of AA therapy in the model may affect the known results from [161] regarding spatial heterogeneity in tumour cell density and vessel density that emerges in the oscillatory regime.

Tumour heterogeneity refers to either genetic differences between populations of tumour cells, or spatial differences in tumour cell density within the tumour. Although both types of heterogeneity are important for understanding cancer, in the remainder of this work, we refer only to spatial heterogeneity. It has been suggested that characterising tumour spatial heterogeneity via textural analysis of medical images can improve the prognostic power of imaging techniques such as positron emission tomography (PET), and could lead to personalised treatment design [35]. Furthermore, heterogeneity in blood vessel density throughout the tumour could affect drug delivery to tumour regions. A recent MRI and ultramicroscopy study showed that anti-VEGF treatment for mice with brain tumours reduced the "chaotic" nature of highly angiogenic regions on the tumour periphery, and also transiently increased tumour perfusion [51]. Tumour heterogeneity has implications for the expected delivery of drugs to the tumour. Mechanistic mathematical models provide insight into how tumour heterogeneity arises, and can be used to recommend further treatments for tumour elimination [163]. Since therapies such as chemotherapy and radiotherapy rely on tumour oxygenation, tumour heterogeneity may have a significant effect on such therapies. In this study, we simulate our spatiotemporal model of vascular tumour growth in one and two spatial dimensions, and show that, under certain conditions, the model simulations predict a spatially heterogeneous tumour with necrotic and hypoxic regions.

We extend the bifurcation analysis from Chapter 4 to investigate the behaviour of the spatial model in the neighbourhood of the Hopf bifurcation points. Following [161] and [156], we show that under certain conditions and at long times, stable or unstable travelling wave solutions to the PDEs are predicted as a result of AA therapy. We also show that similar stable or unstable travelling wave solutions are observed in the oscillatory regime when parameters are further from the Hopf bifurcation.

The remainder of this chapter is structured as follows: in Section 5.2 we introduce our model extensions and present typical simulations of the spatial model. In Section 5.3 we present the results of our analysis of the behaviour at the Hopf bifurcation

points and show simulation results for stable and unstable travelling wave solutions. We also show that similar behaviour is observed for parameter sets that do not correspond to the Hopf bifurcation point. We present clinically relevant simulations that give rise to tumour heterogeneity in Section 5.4. Finally, in Section 5.5, we compare the average tumour burden for several AA and chemotherapy treatment regimens. We summarise our findings and suggestions for future work in Section 5.6.

5.2 Model development

In the previous chapter, we developed a model to represent the evolution of tumour cells, vessels, oxygen concentration and chemotherapy concentration in time. We made quasi-steady state approximations for the concentrations of oxygen and chemotherapeutic agent, and we continue to use these approximations in this chapter. The non-dimensional ODE model equations presented in the previous chapter, including the quasi-steady state approximations for oxygen and chemotherapy, are

$$\frac{\mathrm{d}T}{\mathrm{d}t} = \frac{N(t)VT}{(N(t)V + s_\beta(N(t)V + \sigma T + d_S))}\frac{(h_- N(t)V + 1)}{(h_+ N(t)V + 1)} - d_p T \quad = f_c(T,V), \quad (5.1)$$

$$\frac{\mathrm{d}V}{\mathrm{d}t} = \eta V(1-V) - \frac{\delta TV}{N(t)(V+T)} - d_V(t)V \qquad = g_c(T,V), \quad (5.2)$$

where $h_+ = \frac{h_c}{d_C}\left(1 + \frac{C_b}{c}\right)$, $h_- = \frac{h_c}{d_C}\left(1 - \frac{C_b}{c}\right)$, and h_C, c and d_C represent the permeability of vessels to chemotherapy, the concentration of therapeutic agent at which its effect is half-maximal and the natural clearance rate of chemotherapy, respectively. The parameters $s_\beta, \sigma, d_S, d_P, \eta$, and δ are positive constants, the variable $N(t)$ represents the level of vessel normalisation, which evolves in time if AA therapy is administered or is fixed to $N = 1$ otherwise, and the variable d_V obeys a smooth step function, described in the previous chapter and repeated below. Definitions of all model parameters are given in Table 4.1 in Chapter 4, and in Table 5.1 in this chapter.

Our spatial model comprises two coupled PDEs that represent the evolution of

variables $T(x, y, t)$ and $V(x, y, t)$ for tumour cells and vessel density, respectively, in space (x, y) and time (t), where the relevant spatial domain is a section of tissue that is constrained by boundaries at $x = 0, y = 0, x = L$, and $y = L$, where L is the length and width of the domain. We introduce spatial terms that represent the random motion of tumour cells and vessels in two dimensions to equations (5.1)-(5.2) to obtain

$$\frac{\partial T}{\partial t} = D_T \frac{\partial^2 T}{\partial x^2} + D_T \frac{\partial^2 T}{\partial y^2} + f_c(T, V), \tag{5.3}$$

$$\frac{\partial V}{\partial t} = D_V \frac{\partial^2 V}{\partial x^2} + D_V \frac{\partial^2 V}{\partial y^2} + g_c(T, V), \tag{5.4}$$

where D_T and D_V are both positive constants that represent the random motility coefficients of tumour cells and vessels, respectively. We assume that tumour cells are able to migrate, and that the vasculature is constantly remodelling such that its movement is well described by a diffusion-like term. In reality, endothelial tip cells migrate towards high concentrations of VEGF; our model represents a spatial domain in the immediate vicinity of the tumour, and since we do not take into account biochemical interactions in this model, we assume that the diffusion term sufficiently captures vessel spreading. We assume further that tumour and vessel spreading are isotropic. As in the previous chapter, we consider the two alternative normalisation functions,

$$\text{transient normalisation:} \quad N(t) = 1 + N_{max} \exp\left(-\frac{(t - t_{norm})^2}{\epsilon}\right), \tag{5.5}$$

and

$$\text{step normalisation:} \quad N(t) = 1 + N_{max}\left(\frac{1}{1 + \exp(-\gamma(t - t_{norm}))}\right), \tag{5.6}$$

where N_{max} characterises the extent of vessel normalisation, ϵ and γ characterise the width of the Gaussian and step functions, respectively, and t_{norm} characterises the time at which normalisation is half-maximal for the smooth step function, or the time at which normalisation is maximal for the transient function. In our model,

we assume that AA drug concentration and normalisation are isotropic in space. In reality they are likely to depend on local vascular density and quality.

Equations (5.1)-(5.2) have been rescaled and non-dimensionalised as described in the previous chapter. We rescale the spatial independent variables:

$$x^* = \frac{x}{\sqrt{D_T/\beta}}, \quad y^* = \frac{y}{\sqrt{D_T/\beta}},$$

where β is the dimensional tumour growth rate. We introduce the parameter grouping:

$$D_V^* = \frac{D_V}{D_T},$$

so that equations (5.3)-(5.4) become

$$\frac{\partial T}{\partial t} = \frac{\partial^2 T}{\partial x^2} + \frac{\partial^2 T}{\partial y^2} + f_c(T, V), \tag{5.7}$$

$$\frac{\partial V}{\partial t} = D_V \frac{\partial^2 V}{\partial x^2} + D_V \frac{\partial^2 V}{\partial y^2} + g_c(T, V), \tag{5.8}$$

where we have dropped the $*$ notation for clarity.

As in the previous chapter, we assume that for AA administration, the vessel kill rate, d_V, obeys

$$d_V(t) = d_V^{max}\left(\frac{1}{\exp(-\gamma_A(t - t_{AA})) + 1}\right), \tag{5.9}$$

and that throughout AA treatment, the AA drug reaches its maximum effective concentration, and this is denoted d_V^{max}. The width of the smooth step function is characterised by the positive constant, γ_A, as described in the previous chapter.

5.2.1 Initial and boundary conditions

In our numerical simulations, we suppose that the tumour forms in a well vascularised organ, and that its growth is constrained by tissue boundaries. We perform simulations in one and two spatial dimensions.

For our two-dimensional simulations, we assume that there is a small, circular

mass of tumour cells at the centre of the $L \times L$ domain that is well vascularised, such that the variables $T(x, y, t)$ and $V(x, y, t)$ satisfy

$$(T(x, y, 0), V(x, y, 0)) = \left(T_0 \exp\left(-\frac{\left(x - \frac{L}{2}\right)^2 + \left(y - \frac{L}{2}\right)^2}{\kappa_1} \right), V_0 \right),$$

where T_0 and κ_1 are positive constants that describe the initial Gaussian distribution of tumour cells at the centre of the domain.

For our one-dimensional simulations, we simulate the growth of a small tumour implanted at the left of the well vascularised domain, such that the variables $T(x, t)$ and $V(x, t)$ satisfy

$$(T(x, 0), V(x, 0)) = (T_0 \exp(-x^2/\kappa), V_0),$$

where T_0 and κ are positive constants that describe the initial Gaussian tumour cell distribution at the left hand boundary for $t = 0$. We assume that our simulations represent the propagation of the tumour front in one direction, on a domain of length L and that tissue boundaries constrain the growth of the tumour at $x = 0$ and $x = L$. Similarly to [161], the growth can be interpreted as growth of a two-dimensional tumour averaged along one spatial dimension.

For the one- and two-dimensional simulations, we assume no-flux boundary conditions such that

$$\begin{aligned} \frac{\partial T}{\partial x}(0, y, t) = \frac{\partial V}{\partial x}(0, y, t) = \frac{\partial T}{\partial y}(x, 0, t) = \frac{\partial V}{\partial y}(x, 0, t) = 0, \\ \frac{\partial T}{\partial x}(L, y, t) = \frac{\partial V}{\partial x}(L, y, t) = \frac{\partial T}{\partial y}(x, L, t) = \frac{\partial V}{\partial y}(x, L, t) = 0, \\ \text{for } 0 \leq x \leq L, \text{ and } 0 \leq y \leq L, \end{aligned}$$

to represent tissue boundaries that do not allow cells or substances to flow in or out of the domain.

5.2.2 Numerical method

We implemented the implicit Euler method to simulate the PDEs. This method is known to be stable for systems of stiff differential equations [40]. The implicit Euler method applies to the time-stepping (t) and we apply central differences for the stepping in space (x), assuming a regular grid for both time and space steps. To explain our method, we describe how the implicit Euler method can be applied for a general reaction-diffusion equation for variable $U(x,t)$. Such an equation can be written

$$\begin{aligned} \frac{\partial U(x,t)}{\partial t} &= D\frac{\partial^2 U(x,t)}{\partial x^2} + f(U(x,t)), \\ U(x,0) &= h(x), \\ \frac{\partial U(0,t)}{\partial x} &= \frac{\partial U(L,t)}{\partial x} = 0, \end{aligned}$$

where D is a positive constant, L is the length of the domain, and we have assumed no-flux boundary conditions. We discretise the equation in time and space so that $\Delta x = L/N$ is the space step, indexed by $1 \leq i < N$ and $\Delta t = t_{end}/M$ is the time step, indexed by $1 \leq j < M$ and switch to superscript/subscript notation:

$$\frac{U^i_{j+1} - U^i_j}{\Delta t} = \frac{D}{\Delta x^2}\left[U^{i+1}_{j+1} - 2U^i_{j+1} + U^{i-1}_{j+1}\right] + f(U^i_j),$$

This expression can be rearranged an expressed in matrix form:

$$\begin{bmatrix} 1+2\beta & -\beta & & & & \\ -\beta & 1+2\beta & -\beta & & & \\ & -\beta & 1+2\beta & -\beta & & \\ & & \ddots & \ddots & \ddots & \\ & & & \ddots & \ddots & \ddots \end{bmatrix} \begin{bmatrix} \vdots \\ U^{i-1}_{j+1} \\ U^i_{j+1} \\ U^{i+1}_{j+1} \\ \vdots \end{bmatrix} = \begin{bmatrix} \vdots \\ U^{i-1}_j \\ U^i_j \\ U^{i+1}_j \\ \vdots \end{bmatrix} + \begin{bmatrix} \vdots \\ f(U^{i-1}_j) \\ f(U^i_j) \\ f(U^{i+1}_j) \\ \vdots \end{bmatrix},$$

where $\beta = \frac{D\Delta t}{\Delta x^2}$. We solved the matrix system using the backslash method in Matlab.

Our model incorporates no-flux boundary conditions. These were implemented in our solver by adapting the first and last rows of the finite differencing matrix to

conserve mass at the edges of the domain. We undertook a number of tests to check that simulations using our PDE solver produced reliable results.

Test 1. Solving for a well-mixed system We used our implementation of the implicit Euler method to solve the equation:

$$\frac{\partial Z}{\partial t} = D\frac{\partial^2 Z}{\partial x^2} + aZ(1-Z),$$

where a is a positive constant, for initial conditions such that $Z = 0.01$ on a domain of length $L = 50$ with $\Delta x = 0.5$, for a total of 100 time units where $\Delta t = 1$. The results of our simulation were in agreement with the results of simulations of the corresponding ODE equation simulated using ODE45 in Matlab (data not shown).

Furthermore, we implemented the PDE model in equations (5.3)-(5.4) for well-mixed initial conditions for both T and V. We obtained close agreement with simulations of the corresponding ODE equations (5.1)-(5.2) using a time-step of $\Delta t = 0.1$ in the case of no therapy as shown in Figure 5.1.

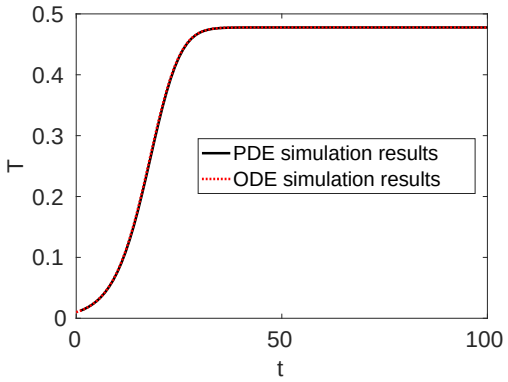


Figure 5.1: $T(50, t)$ from simulation of PDE equations (5.3)-(5.4) and $T(t)$ from simulation of ODE equations (5.1)-(5.2) with no treatment and for uniform initial conditions $(T, V) = (0.01, 1)$. The PDE solver settings were: $L = 100, \Delta x = 0.5, \Delta t = 0.1$. Parameter values as per Table 5.2.

Test 2. Solving the heat equation We used our solver to simulate the one-dimensional heat equation,

$$\frac{\partial Z}{\partial t} = D\frac{\partial^2 Z}{\partial x^2}.$$

We chose a time step of $\Delta t = 0.1$ and a domain where $L = 50$ and $\Delta x = 0.5$. For a Gaussian initial condition with the arbitrary initial condition $Z(x, 0) = 0.06\exp((x - 25)^2/100)$, we observed that the initial density distribution spread out as expected until a layer of uniform density (whose integral was the same as the integral of the initial condition) was left across the domain.

Test 3. Choosing Δx and Δt We chose the space and time steps for each simulation performed in the remainder of this chapter by choosing the smallest time and space steps that provide the expected simulation results (according to our model analysis) while allowing the simulations to run in a reasonable amount of time (typically overnight or less). Δx and Δt are specified for each simulation.

5.2.3 Parameter values

Model parameter values can be found in their dimensional form in Table 4.1 in the previous chapter. In Table 5.1, we state the values of the parameters that have been introduced for the spatial model. In Table 5.2 we repeat the non-dimensional parameter values used for our model simulations.

Parameter	Description	Value	Units	Reference
D_T	Diffusion coefficient of tumour cells	8.6×10^{-6}	$\text{cm}^2\text{day}^{-1}$	Based on estimate in [7, 161]
D_V	Diffusion coefficient of vessels	8.6×10^{-6}	$\text{cm}^2\text{day}^{-1}$	Same as tumour cell diffusion rate

Table 5.1: Additions to the default parameter set given in Table 4.1 with units and references where applicable.

5.2.4 Typical model simulation

We present a typical simulation of the control model from equations (5.3)-(5.4) in one spatial dimension ($T = T(x, t), V = V(x, t)$) in Figure 5.2. The tumour cells and vessel density consist of a non-monotonic propagating wavefront that leaves behind values of T and V that correspond to the stable coexistence steady state. The steady state of the corresponding non-spatial model is a stable spiral for our parameter set

Parameter	Description	Value
s^*_β	$\frac{s_\beta}{S_b}$	1
c^*	$\frac{c}{C_0}$	0.1
d^*_P	$\frac{d_P}{\beta}$	0.2
η^*	$\frac{\eta}{\beta}$	0.5
δ^*	$v\frac{\delta}{\beta}$	0.7
d_V^{max*}	$\frac{d_V}{\beta}$	0.01-1 (varies)
h^*_S	$\frac{h_S\ V_0}{\beta}$	1.24×10^4
σ^*	$\frac{\sigma K_\delta V_0}{\beta}$	2.1×10^4
$\tilde{\sigma}^*$	$\frac{\sigma *}{h^*_S}$	1.7
d^*_S	$\frac{d_S}{\beta}$	2.48×10^3
$\tilde{d}^*_S$	$\frac{d^*_S}{h_S}$	0.4
h^*_C	$\frac{h_C V_0}{\beta}$	1.24×10^3
d^*_C	$\frac{d_C}{\beta}$	2.8×10^4
k^*	$\frac{k}{\beta}$	0.9

Table 5.2: Non-dimensionalised parameter values.

(see the phase plane diagram in Figure 4.3 in the previous chapter), and this leads to the non-monotonic dynamics at the leading edge of the wavefront. The wavefront propagates across the domain since tumour cells proliferate in regions near to vessels due to oxygen availability. In our model, the tumour cells have a negative effect on the vessels that occupy the same region. This represents mechanical stress applied to vessels, known as occlusion, and the release of destabilising factors such as Ang2 and VEGF, reducing the density of functioning vasculature in regions populated by tumour cells.

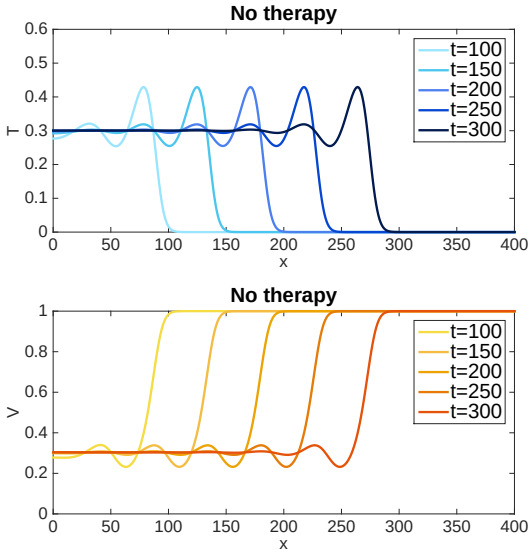


Figure 5.2: One-dimensional simulation of equations (5.3)-(5.4) with no treatment. The PDE solver settings were: $L = 400, \Delta x = 1, \Delta t = 0.1$. The initial conditions were $(T(x,0), V(x,0)) = (0.01\exp(-x^2/100), 1)$. Parameters were as per Table 5.2.

5.3 Oscillatory behaviour: $\lambda - \omega$ analysis

In the previous chapter, we showed that Hopf bifurcations occur for some values of the vessel-kill parameter, which we denoted d_V^{crit}, when all other parameters are held constant. We also showed that there is a subset of parameter space for which a limit cycle occurs, and in this region the spatially averaged model exhibits oscillatory dynamics. Here we employ $\lambda - \omega$ analysis, as described in [156, 157, 161] for analysing oscillatory behaviour of reaction-diffusion PDEs in order to investigate the conditions under which regular and irregular travelling waves follow the invading front of tumour cells. We interpret our results in terms of tumour spatial heterogeneity. The detailed mathematical analysis is presented in Appendix E, and in this section, we explain the model simplifications necessary for the application of $\lambda - \omega$ analysis, and present the results of our analysis. We perform the analysis for the one-dimensional case where $T = T(x,t), V = V(x,t)$. It is important that the analysis is performed for values near the Hopf bifurcation since we assume that solutions for $T(x,t)$ and $V(x,t)$ can be described by elliptical terms in phase space (see Appendix E).

5.3.1 Model simplification

To make analytical progress, we set the oxygen uptake rate by tumour cells, σ, equal to zero. We propose that the total oxygen uptake by tumour cells and normal cells is captured in the oxygen uptake rate by other cells, d_S. We consider only AA therapy. The model equations become

$$\frac{\partial T}{\partial t} = \frac{\partial^2 T}{\partial x^2} + f_s(T,V), \tag{5.10}$$

$$\frac{\partial V}{\partial t} = \frac{\partial^2 V}{\partial x^2} + g_s(T,V), \tag{5.11}$$

where

$$f_s(T,V) = \frac{NVT}{NV(1+s_\beta)+s_\beta d_S} - d_p T,$$

$$g_s(T,V) = \eta V(1-V) - \frac{\delta TV}{N(V+T)} - d_V V,$$

and in the case of no therapy, $N = 1$ and $d_V = 0 \ \forall \ t$. With $\frac{\partial}{\partial x} = 0$, equations (5.10)-(5.11) reduce to give

$$\frac{\mathrm{d}T}{\mathrm{d}t} = f_s(T,V), \tag{5.12}$$

$$\frac{\mathrm{d}V}{\mathrm{d}t} = g_s(T,V). \tag{5.13}$$

The nullclines of equations (5.12)-(5.13) are shown in the phase plane diagram in Figure 5.3, where trajectories for several initial conditions are also shown. In the no-treatment case, the coexistence steady state of equations (5.12)-(5.13), for these parameters, is a stable spiral. This gives rise to a non-monotonic propagating wavefront in simulations of the PDEs (5.10)-(5.11), as can be seen in Figure 5.4. In addition, we adapt some parameter values in order to access the oscillatory behaviour in biologically realistic parameter regimes. All parameter values are given in figure legends.

Equations (5.12)-(5.13) are similar to the predator-prey model presented in [156],

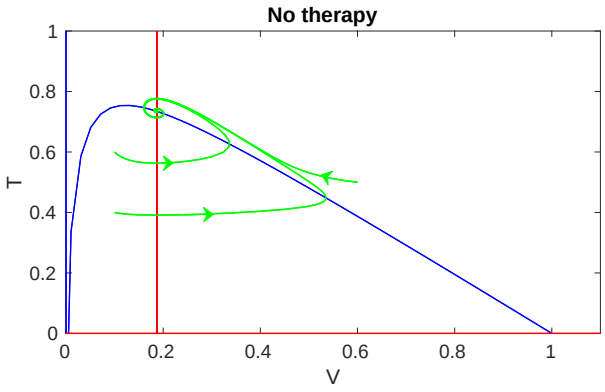


Figure 5.3: Phase plane diagram showing the nullclines and trajectories in phase space for equations (5.12)-(5.13). Nullclines where $\frac{\mathrm{d}T}{\mathrm{d}t} = 0$ are shown in red and nullclines where $\frac{\mathrm{d}V}{\mathrm{d}t} = 0$ are shown in blue. Sample trajectories calculated by solving equations (5.12)-(5.13) for $d_V = 0, N = 1$ are shown in green. Parameter values: $\delta = 10.2, d_p = 0.2, s_\beta = 1, d_S = 0.56, \eta = 10$.

which also exhibits a Hopf bifurcation. For more information on how the Hopf bifurcation arises in our model, see Chapter 4. In [156], it was shown, using conditions derived in [98, 157], that regular, periodic or irregular travelling wave solutions typically follow the propagating wavefront that connects the stable $(T, V) = \left(0, 1 - \frac{d_V}{\eta}\right)$ steady state to the unstable coexistence steady state for solutions near the Hopf bifurcation point. Similarly to work in [161], we state the conditions under which our model exhibits regular or irregular travelling wave solutions. We also show typical simulations of each case in one spatial dimension in Figure 5.6.

5.3.2 Results of $\lambda - \omega$ analysis

In this subsection we summarise the results of our $\lambda - \omega$ analysis, for which the mathematical details can be found in Appendix E.

The condition, as derived in [98], under which stable, periodic, travelling wave solutions follow the propagating wavefront that connects the steady state where $(T, V) = \left(0, 1 - \frac{d_V}{\eta}\right)$ to the unstable coexistence steady state is

$$\left(\frac{\omega_1}{\lambda_1}\right)^2 < 1.148, \tag{5.14}$$

and in Appendix E we show that for our model, λ_1 and ω_1 can be approximated

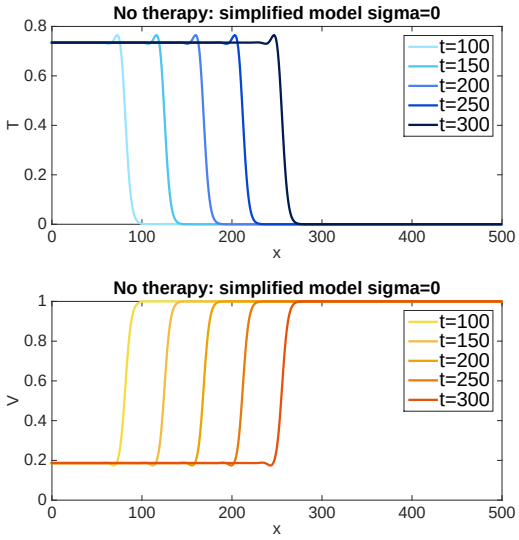


Figure 5.4: Simulation of equations (5.10)-(5.11) for fixed $N = 1$ and $d_V = 0$ for all time. The PDE solver settings were: $L = 500, \Delta x = 1, \Delta t = 0.1$. Initial conditions: $(T, V) = (0.01\exp(-x^2/100), 1)$. Parameter values: $\eta = 10, d_p = 0.2, \delta = 10.2, s_\beta = 1, d_S = 0.56$.

as functions of T and V that depend on the model parameters. In Figure 5.5 we indicate the region in $(N - d_S)$ parameter space (where N is the normalisation coefficient and d_S is the oxygen uptake rate) in which inequality (5.14) holds. For clarity, we also indicate the contours on which d_V^{crit} is constant, since this analysis is relevant only when $d_V \approx d_V^{crit}$. Regular waves are predicted for a small subset of the values of d_S and N that we examined, where N and d_S are large.

5.3.3 Simulations of regular and irregular travelling waves

We demonstrate that regular and irregular travelling waves follow the propagating wavefront that connects the stable steady state where $(T, V) = \left(0, 1 - \frac{d_V}{\eta}\right)$ to the unstable coexistence steady state in one spatial dimension in Figure 5.6. The vessel kill parameter, d_V, was assumed constant from $t = 0$ in all simulations.

The regular, periodic travelling wave solutions and the irregular travelling wave solutions described in this section occur under some specific conditions; in particular, the vessel kill rate, d_V, must take a value close to the Hopf bifurcation point for our approximations in Appendix E to be valid. Our analysis does not indicate whether

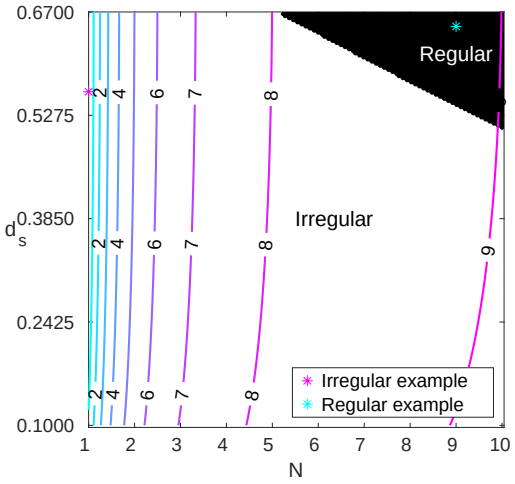


Figure 5.5: A map to indicate the regions of parameter space for which regular or irregular periodic waves follow the invading front for the simplified PDE model given by equations (5.10)-(5.11), in the region of the Hopf bifurcation. The black area represents the region where regular waves are expected according to condition (5.14), and in the white regions the travelling waves are expected to be irregular. Contour lines indicate the surface on which $d_V = d_V^{crit}$ and the numbers on the lines give the value of d_V^{crit} on each contour. The values of N and d_S that we used as examples in our simulations below are indicated in the legend. Parameter values: same as Figure 5.4.

we may expect the same behaviour elsewhere in parameter space. As can be seen in Figure 5.6a, for the parameter regime in which we expect irregular waves to follow the propagating wavefront, the irregularities arise at long times ($t = 3000$ is equivalent to 16 years in real-time) and before this, the waves appear periodic. In Figure 5.6b, waves were periodic and regular throughout the simulated period, as expected.

We have shown that regular and irregular travelling waves arise for parameter regimes near the Hopf bifurcation, where $(d_V - d_V^{crit}) = 0.1$. We now simulate equations (5.10)-(5.11) for parameters further from the Hopf bifurcation, for parameter regimes such that irregular and regular travelling waves are predicted as per Figure 5.5. For our simulation of irregular waves, we choose $d_V = d_V^{crit} + 0.5$. Our simulation in Figure 5.7a shows that irregular waves appear behind the propagating tumour front on a time-scale shorter than the simulation in Figure 5.6a. For the parameter regime where periodic, regular waves are predicted by the $\lambda - \omega$ analysis,

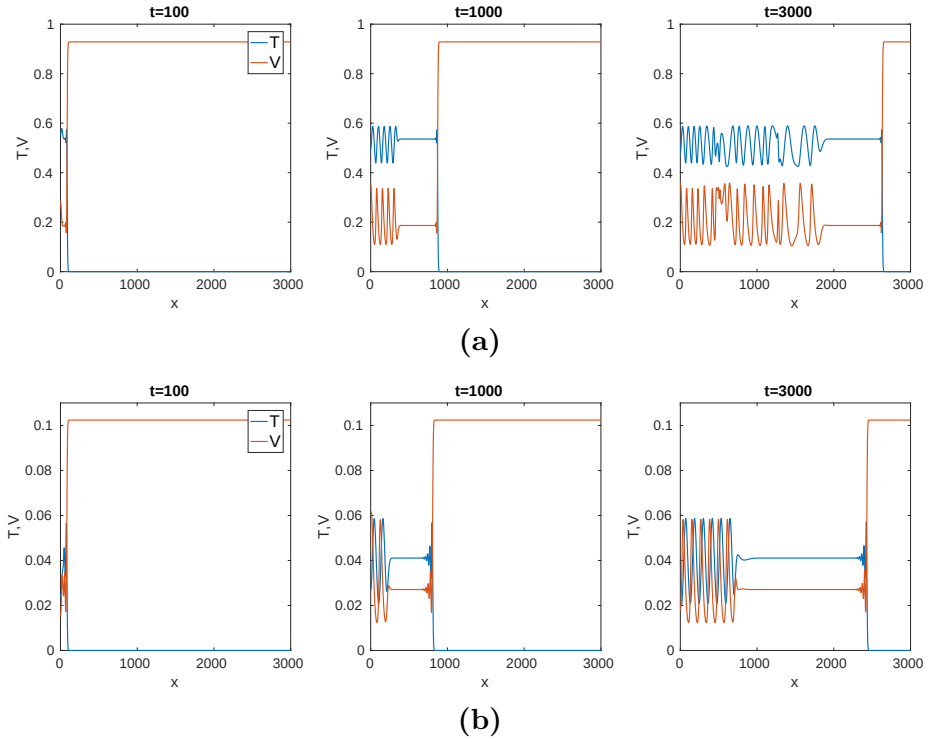


Figure 5.6: Examples of simulations of equations (5.10)-(5.11) demonstrating the regimes where regular and irregular travelling waves follow the invading tumour front. (a) Irregular travelling waves follow the propagating wavefront. $N = 1, d_V = 0.71, d_V^{crit} = 0.61, d_S = 0.56\eta = 10, \delta = 10.2$. (b) Regular travelling waves follow the propagating wavefront. $N = 8, d_V = 8.97, d_V^{crit} = 8.87, d_S = 0.65, \eta = 10, \delta = 10.2$. The initial conditions as in Figure 5.4. Other parameter values as in Figure 5.4 except where specified and d_V and N were constant.The solver settings were $L = 3000, \Delta x = 2, \Delta t = 1$.

a narrow range of values for d_V and N provide oscillatory solutions (we calculated the values of d_V^{crit+} and d_V^{crit-} in Matlab using analytical expressions for T_{ss} and V_{ss} as presented in the previous chapter). We simulate equations (5.10)-(5.11) with $d_V = d_V^{crit} + 0.2$. In this case, the simulation in Figure 5.7b indicates that regular travelling wave solutions appear behind the propagating wavefront as expected.

We simulated the same cases presented in Figure 5.7 to visualise the emergence of regular and irregular waves in two spatial dimensions, and the results are shown in Figures 5.8-5.9. For the irregular wave simulation in Figure 5.8, irregular behaviour is observed in the central region of the tumour. Irregular travelling waves that correspond to those in Figure 5.7a, appear to give rise to spatial heterogeneity within the tumour volume. The symmetry of the heterogeneous patterning in this

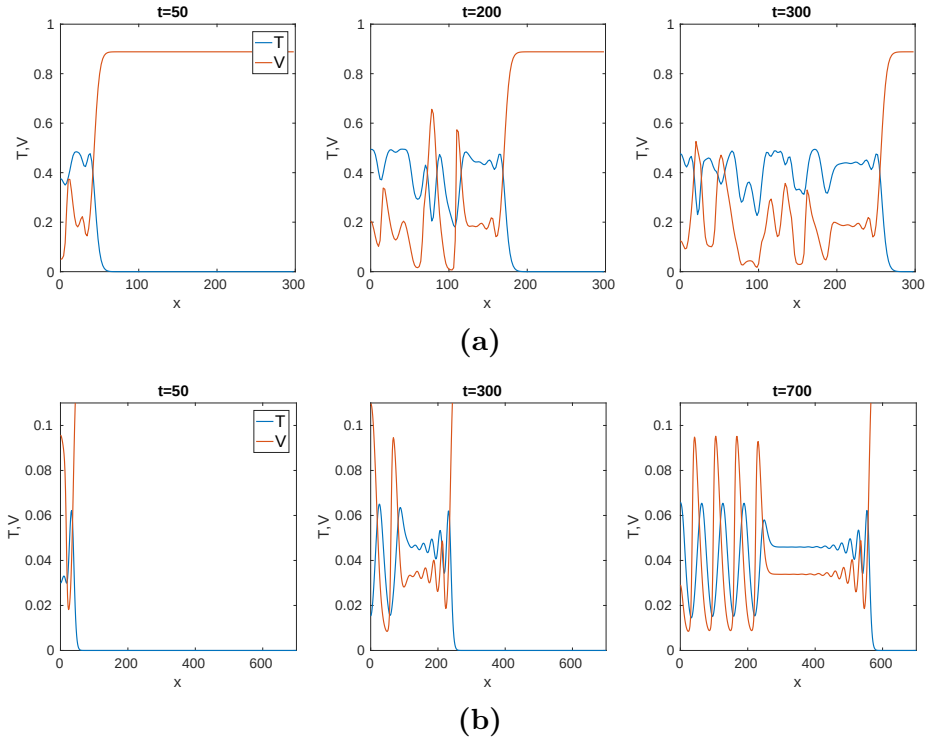


Figure 5.7: Examples of simulations of equations (5.10)-(5.11) demonstrating the regimes where stable and unstable travelling waves follow the invading tumour front. (a) Irregular travelling waves follow the propagating wavefront. $N = 1, d_V = 1.11, d_V^{crit} = 0.61, d_S = 0.56, \eta = 10, \delta = 10.2$. (b) Regular travelling waves follow the propagating wavefront. $N = 6.5, d_V = 8.83, d_V^{crit} = 8.63, d_S = 0.66, \eta = 10, \delta = 10.2$. Other parameter values as for Figure 5.4 and d_V and N were constant. The initial conditions and solver settings were the same as in Figure 5.4.

simulation may be due to grid effects from discretising in space in two spatial dimensions. For the simulation of the emergence of stable waves in Figure 5.9, regular concentric circles of equal width and tumour cell density are observed at the centre of the tumour: we consider in this case the heterogeneity in tumour cell density and vessel density occurs in uniform 'layers'.

We have shown that our predictions for when stable and unstable travelling wave solutions occur near the Hopf bifurcation from the $\lambda - \omega$ analysis in Appendix E also applies in the simulations that we have performed for values of d_V that give rise to the irregular steady state but are less close to the Hopf bifurcation, and the predictions can be illustrated in one- and two-dimensional simulations.

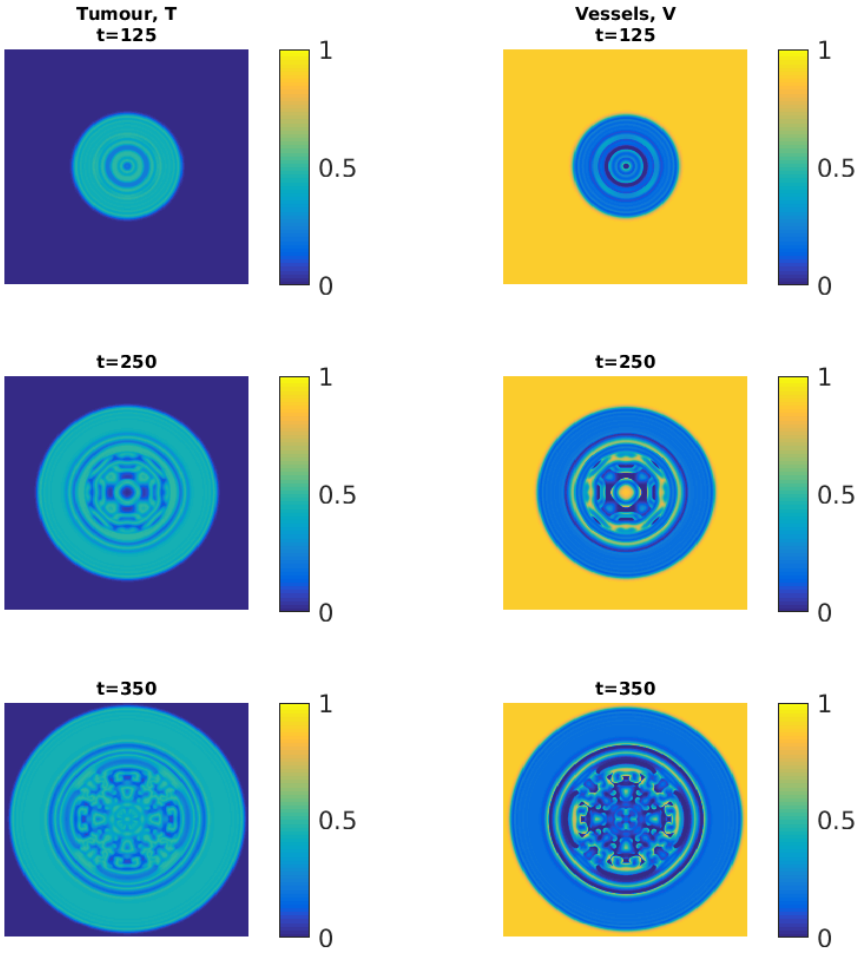


Figure 5.8: Two-dimensional simulations of equations (5.10)-(5.11) for fixed N and d_V, demonstrating the emergence of unstable travelling wave solutions. Initial conditions represent a circular tumour in the centre of the domain: $(T(x,y,0), V(x,y,0)) = \left(0.01\exp\left(-\frac{(x-400)^2+(y-400)^2}{1000}\right), 1\right)$. Solver settings were $\Delta T = 0.1, \Delta x = 2, L = 800$. Parameter values as per Table 5.2 except $N = 1, d_V = 1.11, d_V^{crit} = 0.61, d_S = 0.56, \eta = 10, \delta = 10.2$.

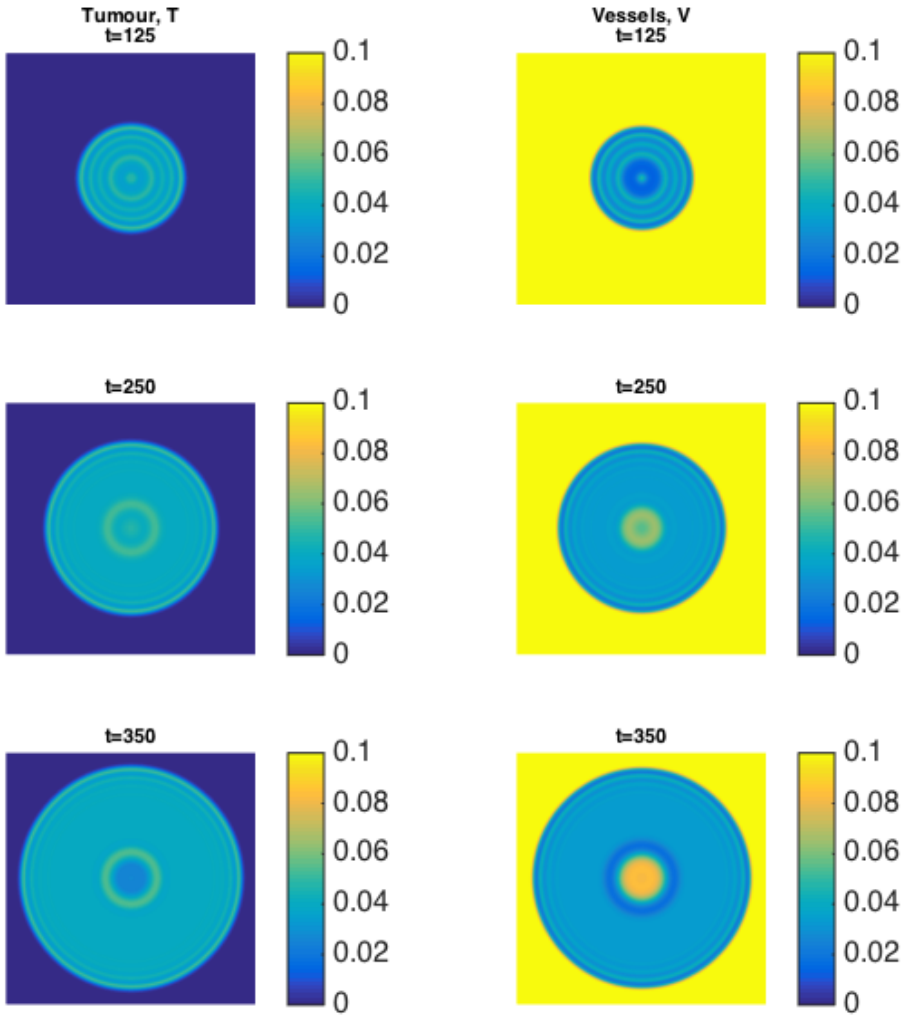


Figure 5.9: Two-dimensional simulations of equations (5.10)-(5.11) for fixed N and d_V, demonstrating the emergence of stable travelling wave solutions. Initial conditions represent a circular tumour in the centre of the domain: $(T(x,y,0),V(x,y,0)) = \left(0.01\exp\left(-\frac{(x-400)^2+(y-400)^2}{1000}\right),1\right)$. Solver settings were $\Delta T = 0.1, \Delta x = 2, L = 800$. Parameter values as per Table 5.2 except $N = 6.5, d_V = 8.83, d_V^{crit} = 8.63, d_S = 0.66, \eta = 10, \delta = 10.2$.

5.4 Tumour spatial heterogeneity

In the previous chapter we showed that limit cycle behaviour is possible for the corresponding non-spatial model, and that one of the model parameters that can be modulated to access limit-cycle oscillations is the vessel-kill rate, d_V. For mathematical tractability in the previous section, we set $\sigma = 0$, and in this section, we return to the model with $\sigma > 0$ in equations (5.3)-(5.4). We investigate further how tumour heterogeneity can arise on clinically relevant time-scales due to oscillatory behaviour in the corresponding non-spatial model. Tumour and vessel heterogeneity that arises from AA therapy could have implications for concomitant therapies such as radiotherapy or chemotherapy, since some regions of a spatially heterogeneous tumour are less well oxygenated than others.

Oscillatory behaviour of the corresponding ODE model is expected when $d_V = 0.2$ with no normalisation ($N = 1$), according to Figure 4.5 in the previous chapter. We simulate this case for the spatial model in equations (5.3)-(5.4). The simulation results in Figure 5.10 show that heterogeneous tumour cell density is observed for this value of AA therapy with no normalisation, as expected.

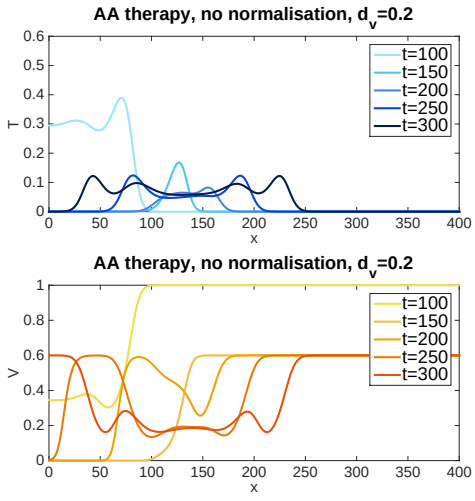


Figure 5.10: Simulations of equations (5.3)-(5.4) with AA therapy and no normalisation ($N = 1$). Initial conditions $(T, V) = (0.01\exp(-x^2/100), 1)$. Parameters as per Table 5.2. d_V as in equation (5.9) where $d_V^{max} = 0.2$.

In Figure 5.11 we present the results of simulations of equations (5.3)-(5.4) where

AA therapy is administered such that oscillatory behaviour is predicted for the corresponding non-spatial model for two different normalisation functions. Figure 5.11a shows that tumour cells and vessels are highly heterogeneous throughout the tumour volume in simulations of a transient normalisation function, and irregular behaviour persists for times after the normalisation window has ended, as expected in this parameter regime. In Figure 5.11b, the simulations show that administration of chemotherapy after the normalisation window reduces the extent of tumour heterogeneity, and the overall tumour cell density at $t = 300$.

Simulations of normalisation as a step function in Figures 5.11c and 5.11d show that a non-monotonic wavefront propagates across the domain, compressing vessels behind it. Figure 5.11d shows that administration of chemotherapy in this case delays the propagation of the wavefront across the domain.

Our two-dimensional simulation of the heterogeneous tumour and vessel densities that arise from transient normalisation is presented in Figure 5.12. Narrow concentric rings of high tumour cell density characterise the heterogeneous behaviour. The rings have different widths, similarly to the irregular behaviour of the corresponding one-dimensional simulation in Figure 5.11a. Regions of low vessel density could be interpreted as hypoxic, and regions of low tumour cell density could be considered as regions of necrotic tumour tissue, such as the central region. Figure 5.13 shows a simulation of equations (5.3)-(5.4) in two dimensions with the step normalisation function. 'Layers' of high and low tumour and vessel densities show similar characteristics to the corresponding one-dimensional simulation in Figure 5.11c for corresponding time-points. The centre of the tumour is devoid of vessels, and this could be interpreted as a hypoxic region. Vessels may recover at longer times in regions with low tumour cell density.

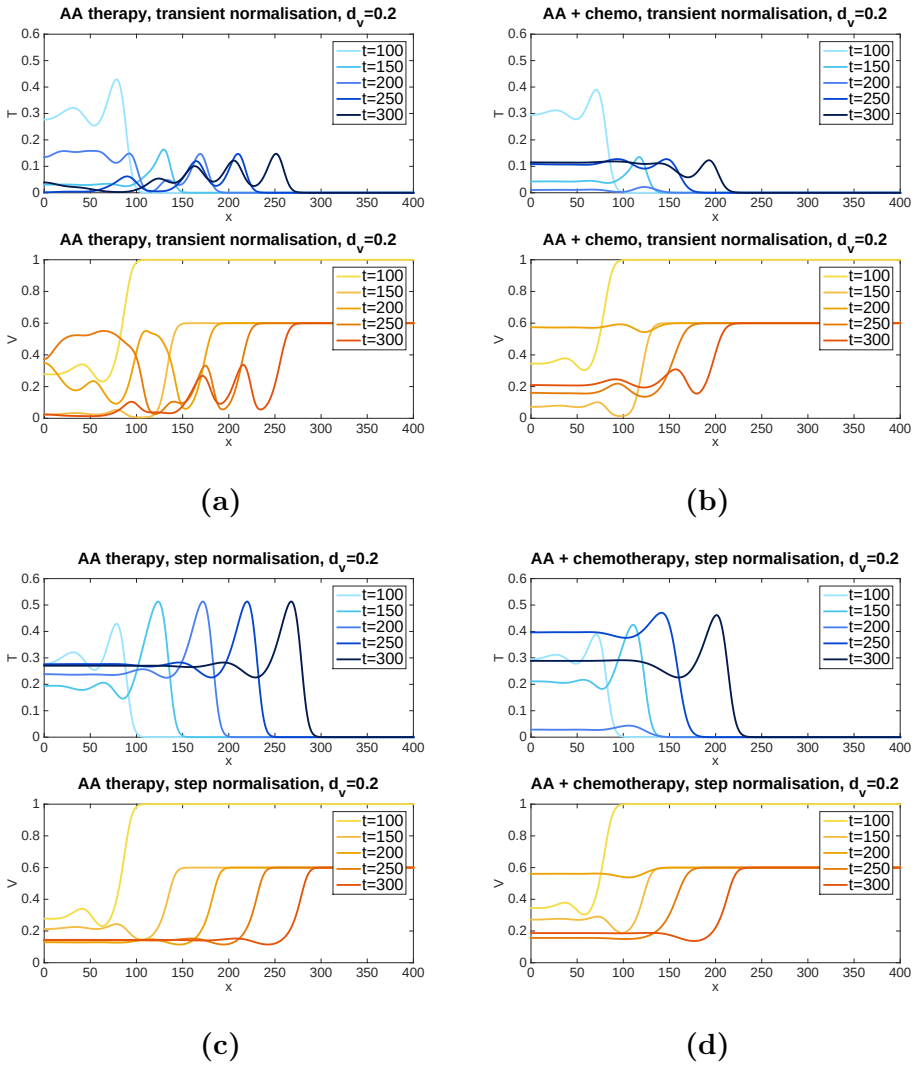


Figure 5.11: Simulations of equations (5.3)-(5.4) with AA therapy and AA therapy + chemotherapy. (a),(b): Transient N as in equation (5.5) with $N_{max} = 1, \epsilon = 50, t_{norm} = 130$. (c),(d): Smooth step function N as in equation (5.6) with $N_{max} = 1, \gamma = 0.5, t_{norm} = 125$. (b),(d): Chemotherapy administered with $C_b = 0.1$ for $120 < t < 183$. Initial conditions $(T, V) = (0.01\exp(-x^2/100), 1)$. Parameters as per Table 5.2. d_V as in equation (5.9) where $d_V^{max} = 0.2$.

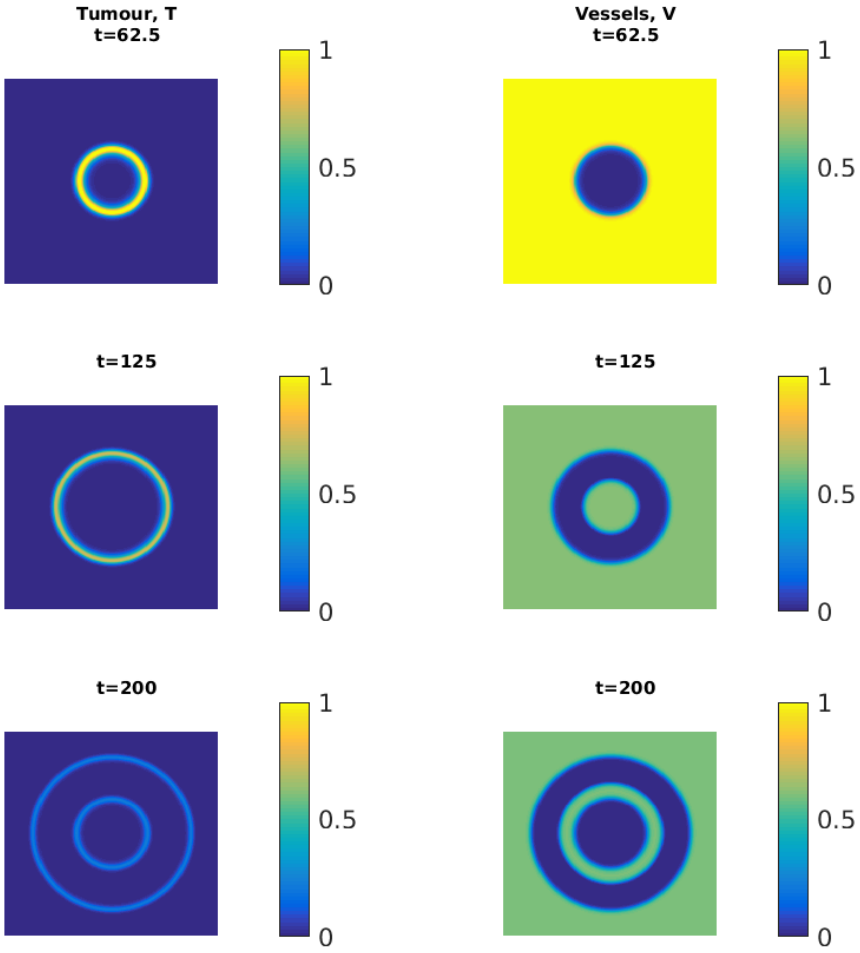


Figure 5.12: Two-dimensional simulations of equations (5.3)-(5.4) with AA therapy where $d_V^{max} = 0.2$ and transient normalisation according to equation (5.5) with $N_{max} = 1, \epsilon = 100, t_{norm} = 130$. Solver settings were $\Delta x = \Delta y = 2, L_x = L_y = 700, \Delta t = 0.05$ and the initial conditions correspond to a Gaussian distribution of tumour cells in a uniformly vascularised region such that $(T(x,y,0), V(x,y,0)) = \left(0.01\exp\left(-\frac{(x-350)^2+(y-350)^2}{100}\right), 1\right)$. Model parameters are given in Table 5.2.

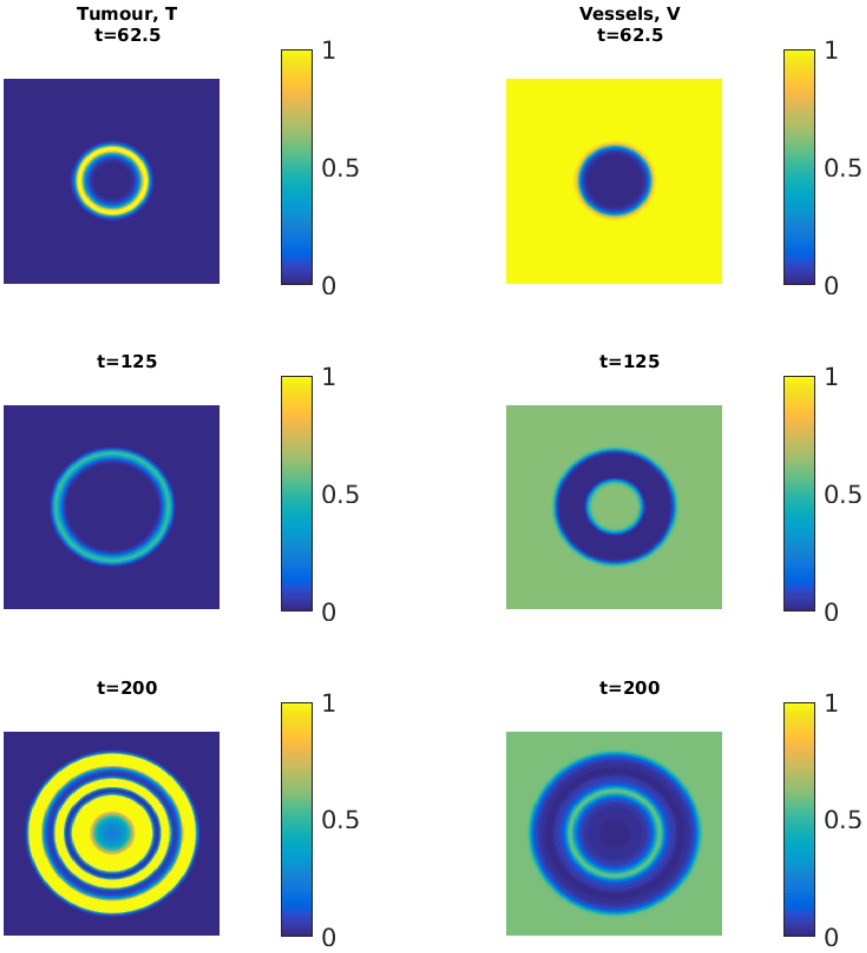


Figure 5.13: Two-dimensional simulations of equations (5.3)-(5.4) with AA therapy where $d_V^{max} = 0.2$ and step normalisation according to equation (5.6) with $N_{max} = 1, \gamma = 0.5, t_{norm} = 125$. Solver settings were $\Delta x = \Delta y = 2, L_x = L_y = 700, \Delta t = 0.05$ and the initial conditions correspond to a Gaussian distribution of tumour cells in a uniformly vascularised region such that $(T(x,y,0), V(x,y,0)) = \left(0.01\exp\left(-\frac{(x-350)^2+(y-350)^2}{100}\right), 1\right)$. Model parameters are given in Table 5.2.

5.5 Average tumour burden

In this section we return to our one-dimensional PDE model. We note that the average tumour per unit length of tissue at a given time is equal to

$$\text{average tumour burden, } \langle T(t) \rangle = \frac{1}{L} \int_0^L T(x,t) \mathrm{d}x, \tag{5.15}$$

where L is the length of the domain. Using average tumour burden as a metric allows direct comparison between different therapies. In experimental studies, the tumour volume is usually the measured variable. In imaging studies, such as PET, total tumour tissue may be quantified by integrating over the total metabolising tumour cells that are visible on a scan, and in this case the measurement is similar to $\langle T \rangle$. However, in experiments where volume is measured using longest diameters of a tumour, necrotic tissue is also included and this is not comparable to $\langle T \rangle$.

In Figure 5.14 we show the average tumour burden for several treatment schedules. Our simulations of a low vessel kill rate, $d_V^{max} = 0.06$, show that concomitant chemotherapy and AA therapy leads to a lower average tumour burden compared to AA therapy or chemotherapy alone. Furthermore, administration of chemotherapy during or after the normalisation window does not significantly affect $\langle T \rangle$, and both schedules have a similar long-term outcome. By considering $\langle T \rangle$ at $t = 500$, for both chemotherapy schedules combined with AA where $d_V^{max} = 0.06$, the reduction in $\langle T \rangle$ compared with the control is greater than the sum of the reduction in $\langle T \rangle$ from AA therapy alone or chemotherapy alone. In other words, chemotherapy and AA therapy act synergistically in this case.

Simulations where $d_V^{max} = 0.2$ demonstrate a much lower tumour cell density compared to the simulations where $d_V^{max} = 0.06$. Chemotherapy has no added benefit in these cases in the longer term for these simulations.

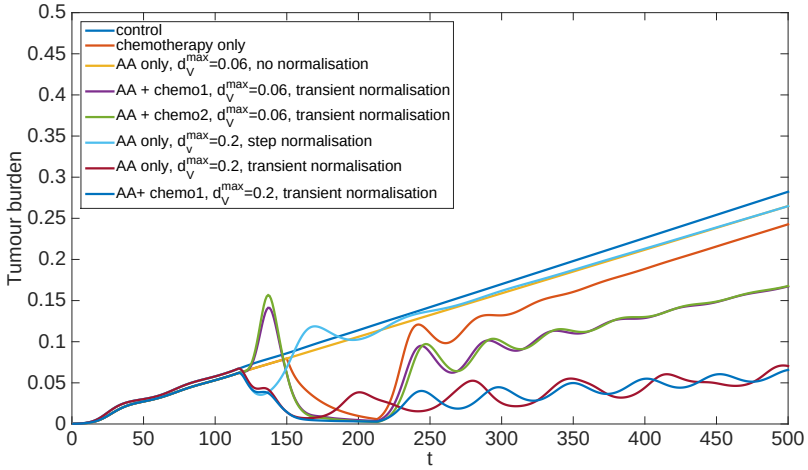


Figure 5.14: Average tumour burden as defined in equation (5.15), calculated using the trapezium rule from results of the simulations of equations (5.3)-(5.4) in one spatial dimension on a domain of length $L = 500$. (a) Chemotherapy was administered for $120 < t < 183$ for chemotherapy alone and the simulations of "chemo1", and for $150 < t < 213$ for the simulation called "chemo2". AA therapy was administered with $d_V^{max} = 0.06$ or $d_V^{max} = 0.2$ from $t = 115$ and the transient normalisation function was as in equation (5.5) with $\epsilon = 50, t_{norm} = 130, N_{max=1}$. Model parameters are given in Table 5.2.

5.6 Discussion

In this chapter we extended the non-spatial model of vascular tumour growth from the previous chapter to include spatial terms that represent the spreading of tumour cells and vessels in one and two spatial dimensions. We investigated the behaviour of the model at points in parameter space that correspond to the vicinity of the Hopf bifurcation points for the non-spatial model, demonstrating that regular and irregular wave-train solutions follow the propagating tumour front under certain conditions. Furthermore, we showed that values of the bifurcation parameter that are further away from the Hopf bifurcation point produce regular and irregular wave-train solutions on a shorter time-scale.

In the previous chapter we demonstrated that transient and smooth step normalisation functions result in different tumour growth profiles for the spatially averaged model. In this chapter, we showed that transient normalisation, or no normalisation, leads to a heterogeneous tumour and that a smooth step normalisation function leads to a homogeneous tumour in one spatial dimension. Our simulations in one

and two spatial dimensions show that tumour heterogeneity can arise for parameter regimes that correspond to the oscillatory regime of the non-spatial model, and that the vessel kill rate and normalisation can be modulated to access such a regime. The recent MRI study from Dominietto *et al.* reported that anti-VEGF treatment increases heterogeneity in intratumoural vessel density in some cases, in qualitative agreement with the results for transient normalisation simulations in this chapter [51]. In the spatially averaged model, such detail was not captured.

Average tumour burden per unit length of tissue was introduced as a metric by which to compare the efficacy of different treatment regimens, and we showed that the long term tumour burden is the same for chemotherapy administered during the transient normalisation window or after the normalisation window for an example of AA therapy. Similarly, in the previous chapter, we showed that timing of concomitant chemotherapy and AA therapy with respect to the normalisation window may affect short-term behaviour, whereas the long term behaviour is not affected. We also demonstrated that for a large value for the vessel kill rate, the tumour burden is very low compared to the control simulation, and this case could be considered a cure.

Our model provides a mathematical framework with which to consider vascular tumour growth on a one- or two-dimensional domain. As we mentioned in the previous chapter, our model is subject to several simplifying assumptions, and we emphasise that the model cannot yet be used to make quantitative biological predictions. The model could be extended to include a biochemical basis for vessel normalisation, and this would require explicit modelling of ligand concentrations, such as VEGF and Ang2. Furthermore, a natural extension of our work would be to perform simulations in three spatial dimensions.

In the following chapter, we directly compare the results of the PDE model simulations with simulations of the ODE model presented in Chapter 4. We briefly investigate whether a spatially averaged model is sufficient to capture the dynamics of a spatial system, and show an example of parameter estimation using our ODE model and data obtained from the PDE model.

Chapter 6

Spatially-averaged models that represent spatial systems: preliminary results

6.1 Introduction

In Chapter 4 we introduced a spatially-averaged model of vascular tumour growth and in Chapter 5 we extended the model to account for spatial aspects of tumour growth and vessel development. We demonstrated that tumour spatial heterogeneity can arise for the spatial model when model parameters correspond to the oscillatory regime for the non-spatial model. By making a well-mixed assumption in developing the ODE model, such detail was lost. In this short chapter, we further compare the ODE model and the PDE model results in order to assess the predictive power of the ODE model with respect to data obtained from PDE model simulations. As such, we assume that the results of the PDE model simulations are the "ground truth" for tumour growth, and we investigate whether the ODE model simulations are able to predict the behaviour of the PDE model, including response to treatment. Our findings motivate further study into whether spatially averaged models, such as those developed earlier in this thesis, are appropriate to represent systems that are,

in reality, evolving spatially.

6.2 Methods

The dimensionless equations for the ODE model under the quasi-steady state assumptions for oxygen concentration and chemotherapy concentration, as introduced in detail in Chapter 4, are

$$\frac{\mathrm{d}T}{\mathrm{d}t} = \frac{NVT}{(N(t)V + s_\beta(NV + \sigma T + d_S))}\frac{(h_- NV + 1)}{(h_+ NV + 1)} - d_p T \quad = f_c(T, V), \tag{6.1}$$

$$\frac{\mathrm{d}V}{\mathrm{d}t} = \eta V(1 - V) - \frac{\delta TV}{N(V + T)} - d_V V \quad = g_c(T, V), \tag{6.2}$$

where $T(t)$ represents tumour cell density, $V(t)$ represents vessel density and s_β, σ, d_S, h_-, h_+, d_p, η and δ are positive constants, and we assume that d_V and N are positive constants for the treatment in this chapter. Including spatial evolution of tumour cells and vessels in one spatial dimension leads to the dimensionless equations

$$\frac{\partial T}{\partial t} = \frac{\partial^2 T}{\partial x^2} + f_c(T, V), \tag{6.3}$$

$$\frac{\partial V}{\partial t} = D_V \frac{\partial^2 V}{\partial x^2} + g_c(T, V), \tag{6.4}$$

where D_V is the rate of vessel spread, and $T(x, t)$ and $V(x, t)$ are the densities of tumour cells and vessels at space x and at time t. The definitions of model parameters can be found in Tables 4.1 and 5.1.

In Chapter 5 we introduced the average tumour burden, $\langle T \rangle$, which represents the integral of the tumour cell density with respect to the spatial variable, x. In this chapter we also introduce vessel burden, $\langle V \rangle$, and we compare the average tumour burden calculated from simulations of the PDE model with simulations of the spatially averaged ODE model. The average tumour burden and average vessel

burden are defined by

$$\text{average tumour burden } \langle T(t)\rangle = \frac{1}{L}\int_0^L T(x,t)\mathrm{d}x, \tag{6.5}$$

$$\text{average vessel burden } \langle V(t)\rangle = \frac{1}{L}\int_0^L V(x,t)\mathrm{d}x, \tag{6.6}$$

where L is the length of the spatial domain. When the initial conditions for the corresponding PDEs are such that the density of tumour cells and vessels is uniform throughout the domain, and such that

$$(T(x,0),V(x,0)) = \frac{1}{L}(T_0,V_0) \text{ for } 0 \leq x \leq L,$$

where $(T(0),V(0)) = (T_0,V_0)$ for the ODE model, then the results for the tumour burden agree exactly with the results for the ODE simulations. In this case, the system behaves as if it is well mixed (results not shown).

When the initial conditions for $T(x,0)$ and $V(x,0)$ in equations (6.3)-(6.4) represent a small tumour at the left side of the domain, similar to our earlier simulations in Chapter 6, the simulation results for average tumour burden calculated from the PDE model and the ODE model simulations differ.

In Figure 6.1 we present the results for the tumour burden calculated from simulations of equations (6.3)-(6.4) with a Gaussian initial condition for $T(x,0)$ and a uniform initial condition for $V(x,0)$ such that

$$\begin{aligned}\frac{1}{L}\int_0^L T(x,0)\mathrm{d}x &= T_0,\\ \frac{1}{L}\int_0^L V(x,0)\mathrm{d}x &= V_0,\end{aligned}$$

where T_0 and V_0 are the initial conditions for $T(t)$ and $V(t)$ in the corresponding ODE model simulations. We show the results for tumour burden calculated from the PDE model simulations for several different values of the diffusion coefficient, D_T, with no therapy and with AA therapy. In Chapter 5, we non-dimensionalised such that $D_T = 1$, and here we vary D_T from its default value of 1. Closer agreement

between the ODE model and the tumour burden from the PDE model is achieved for larger values of D_T in the control case, since the domain fills uniformly with tumour cells quickly and therefore fulfils the spatially homogeneous assumption. Where the tumour cells are distributed normally throughout the domain, their effect on the vessels is the same throughout the domain, and therefore the vessels are also uniform. In the AA treatment case, the system is in the oscillatory regime. For the simulation where $D_T = 100$, there is close agreement between the ODE model and the PDE model results.

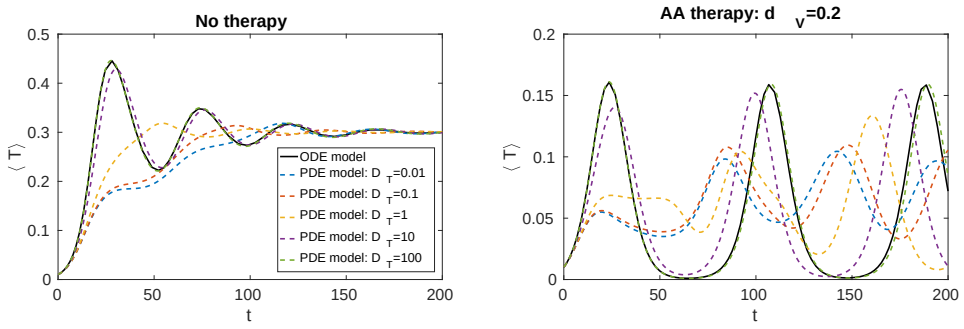


Figure 6.1: Simulations of the ODEs (6.1)-(6.2) and the PDEs (6.3)-(6.4). The initial conditions for the ODE simulations were $(T, V) = (0.01, 1)$ and for the PDE simulations were $(T, V) = (0.0564\exp(-x^2/100), 1)$ (such that $\frac{1}{L}\int_0^L T(x, 0)\mathrm{d}x = 0.01$) and $L = 50$. The left hand plot shows the average tumour burden as defined in equation (6.5) with no therapy ($d_V = 0, C = 0, N = 1$) and the right hand plot shows the tumour burden with AA therapy where $d_V = 0.2$ administered from $t = 0$. Parameters as per Table 5.2.

In the following section, we demonstrate how results for average tumour burden and average vessel burden can be used to estimate parameters for ODE model simulations.

6.3 Results

Spatially averaged models are often developed to represent spatial phenomena, particularly when spatially resolved data are not available. In this section we demonstrate how data derived from a spatial system can be used to estimate the parameters of the corresponding spatially averaged system, and furthermore to make predictions. We also discuss ways in which our predictions could be improved. This section mo-

tivates a further, more detailed study into the suitability of non-spatial models to predict the behaviour of spatial phenomena, which we suggest as future work.

6.3.1 Parameter estimation

We attempt to estimate the vessel growth rate, η, as an example to investigate the predictive capability of the ODE model with respect to the behaviour of the PDE model. We suppose that in a clinical setting, a tumour evolves according to the PDE model in equations (6.3)-(6.4) with no therapy, and that tumour burden has been measured at five time-points since tumour initiation ($t = [10, 20, 30, 40, 50]$). We assume that the dimensionless parameter, η, characterises the growth of blood vessels, which characterise the growth of a vascular tumour, and that its estimation leads to predictions for subsequent tumour growth. We use the *fminsearch* function in Matlab where the objective function incorporates the sum of squared errors between simulations of the PDE model, where the parameters are known and the ODE model, for which we attempt to estimate η. Figure 6.2 shows that more accurate estimates for η are obtained for the simulations of larger values of D_T for the control simulations. We repeat the same method to estimate η including both vessel burden data and tumour burden data and this leads to an improvement in the estimates for η for the control simulations, but not for the AA treatment simulations. In Chapter 3, we showed that the parameters of the ODE model presented in that chapter were better estimated from treatment data than control data: here we demonstrate that for the current model and fixing all other parameters to their true values, estimates of η are not improved using treatment data compared to control data. In a more detailed study, the estimates for η may be improved by including more time-points for the least squares minimisation or using different initial estimates of η.

6.3.2 Model predictions

Using the value of η estimated from the PDE model control simulations where $D_T = 1$ with only $\langle T \rangle$ data, and with $\langle T \rangle$ and $\langle V \rangle$ data, we simulate the ODE

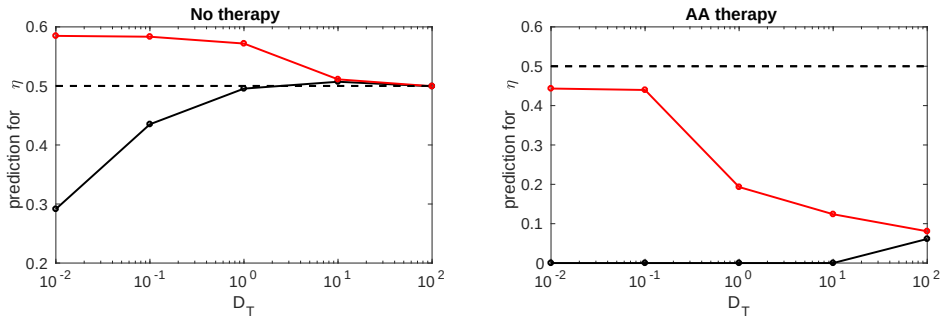
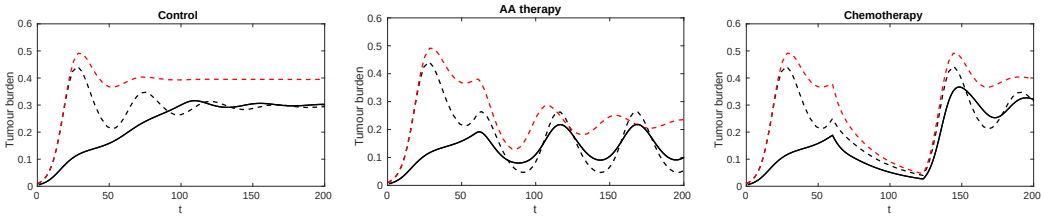


Figure 6.2: Estimates for η using the minimisation function *fminsearch* in Matlab. The parameter η in equations (6.1)-(6.2) was estimated from tumour burden (black line) or tumour and vessel burden (red line) data from simulations of equations (6.3)-(6.4), at time points $t = [10, 20, 30, 40, 50]$. The true value of η for all simulations was 0.5, as indicated by the dashed line. Initial conditions as in Figure 6.1 and model parameters as per Table 5.2. For AA therapy simulations, $d_V = 0.2$ from $t = 0$ as in Figure 6.1.

model with AA therapy or chemotherapy, and compare with the tumour burden calculated from PDE simulations with the true value of η. Figure 6.3 shows the predictions for tumour evolution without therapy and treatment outcome from ODE simulations compared with the outcome from PDE simulations. For AA therapy, there is good agreement with the ODE and PDE simulations for the value of η obtained from $\langle T \rangle$ data, where limit cycle oscillations are observed in both the ODE and PDE simulations. However, for the value of η obtained from $\langle T \rangle$ and $\langle V \rangle$ data, damped oscillations occur for the ODE simulations. There is good agreement between the ODE model predictions and the PDE model simulation for the effect of chemotherapy for both values of η simulated, and the value of η that was estimated using $\langle T \rangle$ data only produces the best agreement with the PDE model simulation.

Estimates for the model parameter η may be improved by using different parameter fitting algorithms or by using more data points for parameter fitting. However, for values of D_T such that the propagating wavefront does not reach the end of the domain in the time frame simulated (i.e. the system does not become well mixed), a different parameter set may fit the data more closely: in Figure 6.1, we illustrated that the average tumour burden per unit volume depends heavily on the diffusion coefficient of tumour cells, since the well-mixed assumption does not hold in these cases. The error in parameter estimates is likely to lead to unreliable predictions of



(a) **(b)** **(c)**

Figure 6.3: Simulations of the ODEs (6.1)-(6.2) with values of η estimated in Figure 6.2 for the no treatment case with $D_T = 1$. Solid black lines indicate the average tumour burden data as defined in equation (6.5) calculated from simulations of PDEs (6.3)-(6.4) with $D_T = 1, \eta = 10, L = 50$. Dashed black lines show ODE model simulation results with $\eta = 0.4955$ (from tumour burden data only) and dashed red lines show ODE model simulation results with $\eta = 0.5718$ (from tumour and vessel burden data). (a) No therapy. (b) AA therapy where $d_V = 0.1$ is administered at $t = 60$. (c) Chemotherapy where $C_b = 0.11$ for $60 \leq t < 123$.

model behaviour from a spatially averaged model simulation.

6.4 Discussion

We have developed spatially averaged models in Chapters 2, 3 and 4 of this thesis. In this chapter our goal was to suggest further study into the suitability of spatially averaged models for representing spatial phenomena. We have demonstrated that using data from the PDE model to estimate parameters of the ODE model can lead to discrepancies. Our simulations for various values of D_T show that agreement is obtained for the ODE and PDE simulations when the system is well mixed, and for our simulations this can occur when the tumour has filled the domain. For a tumour growing within an organ, the domain by which its growth is constrained is likely to be large, and this case is not well represented by our ODE simulations, but may be better represented by our PDE simulations where the domain can be prescribed according to the constraints of the cancerous organ.

We demonstrated a simple case where an ODE model parameter was estimated using tumour burden data from one-dimensional PDE simulations on a small domain, showing that our predictions provided a reasonable representation of the treatment effect according to PDE model simulations.

When using tumour burden data only, the estimate for a model parameter was of greater accuracy when using data from the control simulations than when using data from treatment simulations. This suggests that, unlike our findings in Chapter 3, a sequential approach for parameter estimation is more appropriate than a pooled approach for this particular scenario, since the oscillatory dynamics present under AA treatment make parameter estimation difficult when using a limited number of time points for least squares minimisation. Our parameter fitting method could be improved by taking more pre-treatment tumour and vessel burden measurements, by implementing a more sophisticated parameter fitting algorithm that is less severely affected by local minima, such as the SAEM algorithm described in Chapter 3, or by using several different initial estimates for the parameter to be estimated, in an attempt to avoid local minima.

This chapter has motivated future work, in which we plan to investigate further

the predictive power of the ODE model with respect to tumour burden in the PDE model by including experimental noise on tumour burden measurements, using a larger domain for PDE model simulations, fitting multiple parameters simultaneously, and by employing expectation maximisation algorithms for parameter fitting. Furthermore, we plan to use the tumour extent as a measure of tumour size, i.e. the point in space at which the propagating tumour front has half maximal tumour cell density, to compare the ODE and PDE simulations. This may be a more realistic representation of clinical and preclinical measurements of tumour diameter. In addition, future work could explore how ODE model parameters could be adapted to better represent simulations of the PDE model on a larger domain. In this work we have taken initial steps to address the wider question of whether non-spatial models that represent spatial systems are capable of producing predictions that provide a good representation of the 'true' dynamics.

Chapter 7

Discussion

In this thesis we have developed a range of ODE and PDE models of angiogenesis, vessel normalisation and anti-angiogenic treatments. We have drawn conclusions regarding anti-angiogenic (AA) treatment and combined AA and chemotherapeutic regimens, and our models have focussed on the role of vessel normalisation. In this chapter, we summarise our findings, put our work into the context of current research and identify future directions.

7.1 Summary and contextualisation

In Chapter 2 we developed a spatially averaged model of angiogenesis from current hypotheses regarding the onset of neovascularisation. We accounted for biochemical interactions and cellular dynamics in a set of 16 ODEs. We analysed a simplified version of the model, where biochemical interactions were assumed to be in equilibrium, and from the simplified system we identified four possible vessel phenotypes. These phenotypes were also exhibited by the full model. We used the results of a linear stability and steady state analysis to identify routes in parameter space from angiogenic phenotypes to non-angiogenic phenotypes. Furthermore, we showed that our model results were in qualitative agreement with experimental results for pericyte coverage and vessel density after treatment with anti-VEGF and anti-Ang2 antibodies. Our model built on work from Zheng *et al.* in which a continuous

model of biochemical and biomechanical aspects of angiogenesis is presented [91]. Recent hybrid models that integrate similar biochemical interactions and mechanical processes are presented in [38, 92].

As technology advances and computational power increases, numerical simulations are increasingly more straightforward to implement and run, and as a result, mathematical models of biological processes such as angiogenesis are increasingly complex, and rarely analysed in depth. As such, discrete and modular approaches are popular in the literature, such as those presented in [28, 186]. These complex models incorporate realistic vascular structures, and some simulate blood flow through an early-stage angiogenic blood vessel network. The model that we proposed in Chapter 2 could be extended to form part of a more complex, modular model of angiogenesis, with the benefit of understanding the behaviour of the model equations from our analysis.

Our collaboration with experimentalists and modellers at Roche played a key role in the development of the mixed effects model in Chapter 3. We implemented methods for mathematical modelling and parameter estimation that are widely used in the pharmaceutical industry. Furthermore, we were able to access preclinical datasets. In the field of clinical pharmacology, mixed effects modelling is widely used to model drug uptake and effect, and increasingly to model aspects of disease progression. Mixed effects modelling is a useful technique to leverage experimental data taken from a population of subjects such that data from all of the individuals is used to parametrise the model. However, the approach has limitations, for example, the quantity and type of data available limits the complexity of model for which parameters can be reliably identified. We developed a simple model of vascular tumour growth that we proposed may be used to identify a transient window of enhanced tumour growth that could correspond to the vessel normalisation window.

The model presented in Chapter 3 represents the growth of a tumour at a time when it has established its vasculature, i.e. a later stage of development than the model presented in Chapter 2. We considered that the carrying capacity of the tumour depends on the vessel density, which increases with tumour size. In contrast

to the model in Chapter 2, the details of biochemical interactions involved in angiogenesis were neglected. We assumed that the tumour has a positive effect on vessels in this model and we incorporated two forms of vessel regulation resulting from AA therapy: vessel kill and vessel normalisation. We demonstrated that a model incorporating vessel normalisation described the experimental data better than a model of tumour growth that did not. We selected the normalisation model on the basis that diagnostic plots, such as residuals against time, and individual fits showed less bias at specific time-points compared to the model without normalisation, even though the BIC suggested that the model without normalisation fit the data more closely. In particular, residuals plots showed that specific time-points were consistently overestimated or underestimated using the model without normalisation, and this information is not incorporated to the BIC, since the absolute difference between observed and simulated values are used to inform the information criterion. Furthermore the parameters for the normalisation model were estimated with closer precision (smaller r.s.e.) than those for the no-normalisation model.

Without further preclinical data, we were not able to validate whether the transient window of enhanced tumour growth that we identified was due to vessel normalisation. However, we proposed that further experiments wherein chemotherapy is administered alongside AA therapy could indicate whether the efficacy of chemotherapy is maximal when administered within the transient window. Similar models of vascular tumour growth that do not take into account vessel normalisation have been proposed by [133, 184]. Tackling cancer by combining several types of therapy is an increasingly popular approach in the pharmaceutical industry, and models such as ours could be combined to predict experimental outcomes [26, 127, 187]. This approach has the potential to guide experiments and increase efficiency in drug design. A limitation of data-driven tumour modelling approaches is often the lack of breadth of data; usually tumour size is the only observed variable and therefore, to avoid over-fitting, proposed models must be simple. Other useful, measurable observations could include vessel density or circulating biomarkers. In general more detailed data could enable more detailed modelling approaches and improved specificity of model

predictions.

In Chapters 4 and 5 we developed a model of vascular tumour growth in a well oxygenated region such that the net effect of tumour cells on vessels is negative due to vessel occlusion and destabilisation. The model was adapted from one presented by Stamper *et al.*, in which the authors investigated oscillatory dynamics that arise as a result of vessel occlusion [161]. We neglected spatial detail and incorporated AA therapy and normalisation for our model in Chapter 4, where we showed that, similarly to the original model presented in [161], our model admits limit cycle behaviour in certain parameter regimes. For the corresponding spatially resolved model presented in Chapter 5, we showed that tumour spatial heterogeneity arises in simulations for which the model parameters are part of the oscillatory regime in the well-mixed model. We demonstrated that for some values of the vessel kill parameter, and for no normalisation or a transient normalisation function, oscillatory behaviour of the non-spatial model leads to heterogeneous tumour cell density in the spatial model. A sustained normalisation function gives rise to inhomogeneous behaviour in the short term that stabilises in time for a more homogeneous tumour cell density. Such information on spatial heterogeneity was not possible to obtain via the well-mixed model.

The non-spatial model presented in Chapter 4 has some features in common with the non-spatial model presented in Chapter 3: both models include tumour and vessel growth, where vessels have a positive effect on tumour growth (in the model in Chapter 4 this was via oxygen delivery which was simplified via the quasi-steady state approximation). An assumption for the model in Chapter 3 was that the net effect of tumour cells on vessels was positive, i.e. tumour cells promote vessel growth. However, for the model in Chapter 4, we assumed that vessels obey logistic growth that does not depend on tumour size and that the net effect of tumour cells on vessels is negative due to occlusion and destabilisation. Our contrasting approaches represent different scenarios under which AA therapy may be administered. In Chapter 3 our simulations represent the case where AA therapy is applied to implanted tumours that have been growing for some time and have established

their own vasculature, whereas in Chapter 4, we assume that AA therapy is administered at an early stage of metastasis formation in a well vascularised region. The model in Chapter 4 was more complex than that in Chapter 3, and as a result, we uncovered interesting dynamics such as the oscillatory regime, which was not present in the model in Chapter 3.

We introduced tumour burden as a comparator for several treatment regimens in the PDE model, and we demonstrated that, similarly to the ODE model simulations, the timing of chemotherapy administration relative to the normalisation window does not affect long term tumour burden. This result is in contrast to a similar experiment in Chapter 3 where we showed that for a particular chemotherapy model and using our normalisation model, simulations of chemotherapy administered within the normalisation window resulted in a significantly reduced tumour size compared to chemotherapy administered outside the window. For the ODE and PDE models presented in this thesis, we attempted to obtain analytical results for expected model behaviour by analysing the steady states and linear stability where possible, and by performing $\lambda - \omega$ analysis for the PDE model in Chapter 5. Several early models of angiogenesis incorporate PDEs that represent endothelial cell density, such as those presented in [7, 143]. More recently, the model presented by Lignet *et al.* comprises a set of PDEs that represent biochemical species, endothelial cells and tumour cells [105]. The complexity of the model presented in [105] is such that analysis of possible model behaviours is not possible. Commonly, PDEs form the basis of modular models of vascular tumour growth [134, 139].

Although current technology and computing capacity allows for detailed modelling of vascular tumour growth, the usefulness of mathematical models is often limited by the quality and quantity of available experimental data. It is therefore important to resolve the dichotomy between complex computational approaches and tractable, data-driven modelling techniques. On one hand, most multi-scale models developed by mathematicians and computer scientists contain many key processes involved in tumour growth and vascularisation, and are capable of simulating, in detail, the expected effects of AA therapies. However, these models often involve

too many unknown parameters for proper parametrisation and therefore may not produce reliable predictions. On the other hand, modellers in the pharmaceutical industry are usually forced to make simplifying assumptions in their models in order to describe the limited data available, and this results in using simple ODE models to describe complex biological processes, and sometimes important biological detail may be lost in such simplifications.

In this thesis we have presented several mathematically based models of angiogenesis and vascular tumour growth that are analytically tractable to some extent. With further experimental data, our models could be extended and validated, and may be used to make meaningful, quantitative predictions for the effects of anti-angiogenic therapy. Such extensions could constitute a step towards reconciliation of available modelling techniques and biological accuracy.

7.2 Future directions

In Chapter 6, we introduced the concept of using non-spatial mathematical models to represent spatial phenomena as a potential direction for future research. In this section we summarise how the models presented in this thesis could be extended or improved, and we summarise the directions for future work motivated in Chapter 6.

There are extensions to the models presented in Chapters 2-5 that could provide a more realistic representation of the biological systems that they represent. A natural extension for the model presented in Chapter 2 is the inclusion of tumour cells. This would enable further predictions regarding response to AA therapy. Furthermore, a spatial component could be incorporated to account for the migration of vessels. As we mentioned above, the biochemical and cellular dynamics equations could be incorporated in a more complex, modular model of angiogenesis, where the treatment effect on vasculature could be compared closely with imaging studies such as the high-resolution ultramicroscopy images of vessel growth in tumours before and after AA treatment presented in [49].

Due to lack of data availability, the model in Chapter 3 was necessarily a highly

simplified approximation to vascular tumour growth. Extensions to this model could incorporate alternative, potentially more realistic, normalisation functions such as the Gaussian functions introduced in Chapter 4, or more detail of the factors that drive normalisation. By incorporating more biochemical detail in the model, elucidation of the mechanisms by which AA therapy induces vessel normalisation may be possible. Adding spatial information would provide insight into the model dynamics and tumour spatial heterogeneity. Furthermore, different populations of tumour cells could be introduced, similar to the model presented in [21], where quiescent, proliferative and apoptotic tumour cells behave differently. Such approaches are likely to provide a more realistic representation of vascular tumour growth and AA therapy.

In Chapters 4 and 5 we presented a model of vascular tumour growth that accounts for oxygen tension throughout the tumour. This model could be extended to include aspects of biochemistry involved in vascular tumour growth, such as VEGF and Ang2 mediated vessel growth and destabilisation. As an extension to the work in Chapter 4, mixed effects modelling techniques could be used to parametrise the model with preclinical or clinical data. Similarly to the model in Chapter 3, this model could benefit from the inclusion of several populations of tumour cells, as described above.

In Chapter 6, we introduced the concept of directly comparing ODE models and PDE models that represent the same biological system. We obtained preliminary results for our investigation into how ODE simulations can be used to recover known parameters from PDE model simulations, and the effects of these estimates on subsequent model predictions. Techniques such as averaging and homogenization have been applied to reaction-diffusion type PDEs [3, 4] and these techniques, described in PDE textbooks such as [30, 115], would be a starting point for further investigation. Further questions that arise from our preliminary comparison are:

- How can we quantify the biological detail lost by assuming a spatially evolving system is well-mixed?

- How should the parameter set for the non-spatial model account for spatial effects? For instance, smoothed functional forms may represent local variations for variables such as oxygen concentration.

- Are parameter estimates for the non-spatial model realistic representations of the behaviour in the spatial model?

The questions above are also relevant to other models in the field of mathematical biology. The well-mixed approximation is not always reasonable. We conclude that consideration of whether a system is truly well-mixed should be taken before introducing simplified models of spatially evolving systems.

Appendix A

Parameter values for Chapter 2

In this appendix we explain how we chose the parameter values for the model in Chapter 2. The reference values for variables are given in Table A.1 and these give rise to the initial conditions stated in Table 2.1 in Chapter 2.

VEGF parameters

We take the VEGF parameters from three primary sources: [42], [179] and [155].

The binding rates, k^v_{on} and k^v_{off} were measured in an *in-vitro* study in [42], using a BIAcore 2000, a device which allows measurement of binding rates using a sensor chip. The association constant, k^v_{on}, was measured as $3.6\pm0.07\times10^6$ $\text{M}^{-1}\text{s}^{-1} = 1.3\pm 0.03\times10^4\mu\text{M}^{-1}\text{h}^{-1}$ and the dissociation constant, k^v_{off}, was measured as $1.34\pm0.19\times 10^{-4}$ $\text{s}^{-1} = 0.48 \pm 0.07\text{h}^{-1}$; several orders of magnitude lower than the association constant. The dissociation constant, $k_d = k^v_{\text{off}}/k^v_{\text{on}}$ is therefore roughly 36pM.

An investigation by Wang *et al* in 2002 [179] compares the binding of VEGF to its receptor in HUCMEC (human colonic microvascular endothelial cells) and HUVEC (human umbilical vein endothelial cells). HUCMECs are present in the smaller vessels in the colon which express VEGF, and HUVECs are present in larger vessels in the umbilical vein. It was found that HUCMECs internalise VEGF at a lower rate, and release (dissociate) VEGF at a higher rate than HUVECs. The authors suggest that there appear to be two types of cell present; those with high affinity

and those with a lower affinity, and the dissociation constants ($k_d = k^v_{\text{off}}/k^v_{\text{on}}$) for these are 130 ± 14pM and 675 ± 66pM respectively.

VEGF internalisation, (rate k^v_{int} in our model), was also measured by Wang *et al.*, and it was noted that both HUCMECs and HUVECs internalised VEGF at 37 °C after 20 and 30 minutes respectively, and after this time, HUCMECs had internalised about 15% of the bound VEGF and HUVECs had internalised around 60% of the bound VEGF [179]. Translating these results we assume linear internalisation and say that for HUVECs, 60% had internalised at 20 minutes, so the rate of internalisation is $\frac{0.6}{20}$ $\text{min}^{-1} = 1.8\text{h}^{-1}$ and for HUCMECs, since 15% had internalised after 30 minutes, the internalisation rate is $\frac{0.15}{30}$ $\text{min}^{-1} = 0.3\text{h}^{-1}$. We note that internalisation of VEGF differs in endothelial cells compared with different vessels, and is unlikely to occur linearly in time. We chose a value of $k^v_{\text{int}} = 0.86h^{-1}$ for our model simulations.

The reference value for the number of receptors per cell, ϕ, is estimated at 10^5, since this is within the range of receptors per cell in both HUVECs and HUCMECs in [179].

The parameter for the decay rate of VEGF, δ_v, is taken from an in-vitro study in [155], where exogenous VEGF was added to plates seeded with HUVECs. The half life of VEGF was 64 ± 7min which leads to a decay parameter of about 1h^{-1}.

The parameters for the delivery of VEGF from the tumour, and the thresholds for proliferation and death of ECs due to bound VEGF were estimated.

Ang1 and Ang2 parameters

The main sources of parameters for the angiopoietins submodel were [59] and [114], and other useful studies were [12] and [23].

Two of the parameters associated with Ang1 and Ang2 production and binding were taken from *in-vitro* experiments in [59]. In this study, several human endothelial cell types and one smooth muscle cell type were cultured and the expression of Ang1 and Ang2, as well as the storage in WPBs, were observed. Ang2 was present

in HUVECs in a granular pattern, suggesting WPBs were present. There is no quantification of processes in this study, so we take statements such as "Granular Ang-2 is still prominently detectable after 16 hours...indicating a long half-life of stored Ang-2." to infer a half life of intracellular Ang2 of around 18 hours. From this we assume that the decay rate of Ang2 in WPBs $\delta_{aw} = 0.031\text{h}^{-1}$. The authors also state that on stimulation, WPBs release Ang2 so that the maximum concentration in the supernatant is reached in 20 minutes. From this, we infer the parameter α_{a_2}, the release rate of Ang2 is 3h^{-1}.

The reference concentration of Ang1 and Ang2 is based upon *in vitro* experiments in [12], where HUVECs were seeded on Matrigel, and the effects of adding 80ng/ml and 500ng/ml of Ang1 and Ang2 were observed. In units relevant to our model, this corresponds to $1.14-7.14\times10^{-3}\mu$M, which led us to take the reference concentration as a value in this range.

A key reference for the biology of Ang1 and Ang2 is [114]. In this study the binding of both ligands was studied in depth. From BIAcore experiments, the binding affinity for both Ang1 and Ang2 was found to be around 3nM, but the individual "on" and "off" rates are not given. Another parameter that can be estimated from this study is the ratio of Ang2 to Ang1 for dematuration of ECs, λ. By increasing the concentration of Ang2 added to ECs that were exposed to Ang1, an eight-fold higher Ang-2 concentration was found to block all phosphorylation of Tie-2 (Ang1 activates Tie-2 on binding, but Ang2 binds and does not activate the receptor).

In [23], HUVECs are incubated for 15 minutes at 37 $^{\circ}C$ and the binding of various concentrations of Ang1 and Ang2 is measured. From these experiments, we infer the internalisation rate of Ang1. The authors showed that around 70% of bound Ang1 is internalised over the course of 1 hour, and from this we estimate the internalisation rate of Ang1, $k_{\text{int}}^{a_1} = 1\text{h}^{-1}$.

The production rate of Ang2 can be inferred from [129], where a 4.6 fold increase in Ang2 mRNA expression in bovine retinal endothelial cells (BRECs) was observed after 2 hours of stimulation. However, the study does not mention the amount of Ang2 which is produced, but only a fold increase in Ang2 mRNA.

This leaves the decay rates of Ang1 and Ang2 in the ECM to be estimated, and the precise binding rates of Ang1 and Ang2 to be estimated, although the ratio $k_{\text{off}}^{a_1}/k_{\text{on}}^{a_1} = k_{\text{off}}^{a_2}/k_{\text{on}}^{a_2}$ is given in [114].

PDGF parameters

The production of PDGF was studied explicitly in an *in-vitro* study in [61]. A rate of $0.69ng$ per 10^6cells per day for the production of PDGF by bovine aortic ECs was calculated, and from this we estimate $\alpha_p = 6.7 \times 10^6 \text{h}^{-1}$. We estimated the value for δ_p within the ranges of the other ligands in our model.

In-vitro experiments performed in [9] measure the dissociation constants for PDGF/PDGFRβ for three types of smooth muscle cells at various stages in their lifetimes. We choose the rate which corresponds to 60% of the cells' lifespan, and take an average of the dissociation rates for two cell types. This leads to a dissociation rate of 45.75pM. Since this is similar to the VEGF dissociation rate, and the molecular weight of VEGF and PDGF are similar (45kDa for VEGF [57], 31kDa for PDGF [191]). We estimate the association rate, $k_{\text{on}}^p = 1.88 \times 10^4 \mu\text{M}^{-1}h^{-1}$ and the dissociation rate, $k_{\text{off}}^p = 0.86h^{-1}$.

Cell dynamics parameters

The interactions of ECs and PCs in the model is depends on a mixture of real and phenomenological parameters.

The proliferation rate of ECs was taken from a study of retinal angiogenesis in mice from [122]. This study measured the sprout area, the area subject to remodelling and the vessel covered area over 16 days. The authors produced sigmoidal curves for the growth of vessels. Simulating the simplified model in equations (2.17)-(2.20), we found that the proliferation rate $\theta = 0.0417h^{-1}$ produced good agreement with the experimental data.

The proliferation rates of ECs and PCs are compared in an in-vitro study in

[146], where both cell types were grown in culture. It was seen that PCs proliferated at a faster rate than ECs. Therefore, in the absence of experimental data for the proliferation rate of PCs, we choose a value that is twice as fast than the proliferation rate of ECs.

Death rates of ECs and PCs are difficult to estimate, since cells die for a variety of reasons, and it is challenging to find parameters that encompass all types of cell death. In particular, we propose in the model that PCs die when the Ang2 concentration is too high. Consequently the parameter ϵ is difficult to identify, and we make an order of magnitude estimate assuming that the maximum death rate is half of the maximum proliferation rate.

The parameters for the binding and detachment of PCs to ECs (ζ and ν), and the rates of maturity increase and decrease of ECs (η and μ) are all phenomenological, and have been given values based on the behaviour they produce.

Param	Description	Value	Units	Reference
V_0	Reference VEGF concentration	8×10^{-3}	μM	50ng/ml used *in-vitro* [119] . Assumed 10 times larger for *in-vivo* since our model represents a well mixed portion of tumour tissue where the concentrations of tumour factors is likely to be much higher than in the *in-vitro* experiment.
A_0	Reference Ang1/2 concentration	3×10^{-3}	μM	80-500ng/ml used *in-vitro* [12], Assumed 10 times larger for *in-vivo* since our model represents a well mixed portion of tumour tissue where the concentrations of tumour factors is likely to be much higher than in the *in-vitro* experiment.
p_0	Reference PDGF concentration	8×10^{-3}	μM	Order of magnitude estimate from *in-vitro* experiments [61].
E_0	Reference EC density	8×10^{-8}	μM	Assuming 10^5 receptors per cell, and one molecule of ligand binding to one receptor gives relative EC density in micromolar units. Binding kinetics described in *in-vitro* experiments.[59].
P_0	Reference PC density	4×10^{-8}	μM	Half reference EC density
ϕ	Average receptors per cell	10^5		Suggested by [179].
k^v_{on}	VEGF/VEGFR2 association	1.88×10^4	$\mu M^{-1} h^{-1}$	Real-time kinetics measured by using BIAcore equipment to record protein interactions on sensor chip [42].
k^v_{off}	VEGF/VEGFR2 dissociation	0.99	h^{-1}	Real-time kinetics measured by using BIAcore equipment to record protein interactions on sensor chip [42].
k^v_{int}	VEGF internalisation	0.86	h^{-1}	Estimate based on *In-vitro* experiments [179] using two types of endothelial cells.
α_v	VEGF delivery	0.375	$\mu M h^{-1}$	Fraction of reference value produced each hour from *in-vitro* experiments [119].
δ_v	VEGF decay	1	h^{-1}	Observed *in-vitro* [155]

Table A.1: Default parameter set with units and references where applicable. Continued overleaf.

Param	Description	Value	Units	Reference
$k_{\text{on}}^{a_1}$	Ang1/Tie2 association	417	$\mu M^{-1}h^{-1}$	*In-vitro* from k_d value [114] using BIAcore sensor chips to measure binding kinetics
$k_{\text{off}}^{a_1}$	Ang1/Tie2 dissociation	1.25	h^{-1}	*In-vitro* from k_d value [114] using BIAcore sensor chips to measure binding kinetics
$k_{\text{int}}^{a_1}$	Ang1 internalisation	1	h^{-1}	*In-vitro* HUVECs: 70% of Ang1 internalised in one hour [23].
$k_{\text{on}}^{a_2}$	Ang2/Tie2 association	417	$\mu M^{-1}h^{-1}$	*In-vitro* from k_d value [114] using BIAcore sensor chips to measure binding kinetics
$k_{\text{off}}^{a_2}$	Ang2/Tie2 dissociation	1.25	h^{-1}	*In-vitro* from k_d value [114] using BIAcore sensor chips to measure binding kinetics
δ_{a_1}	Ang1 decay	4.69	h^{-1}	Order of magnitude estimate from [59]
δ_{a_2}	Ang2 decay	0.0625	h^{-1}	Half life of extracellular Ang2 assumed shorter than intracellular Ang2 (below) described in [59]
δ_{a_w}	Intracellular Ang2 decay	0.031	h^{-1}	*In-vitro* subcellular Ang2 still visible after 15 hours [59].
α_{a_1}	Ang1 production	1×10^6	h^{-1}	Order of magnitude estimate from [59]
α_{a_w}	Ang2 production	0.8	h^{-1}	Order of magnitude estimate from [59]
α_{a_2}	Ang2 release	3	h^{-1}	*In-vitro* extracellular Ang2 reaches maximum after 20 minutes [59].
α_p	PDGF production	6.7×10^3	h^{-1}	Order of magnitude inferred from *in-vitro* experiments [61].
k_{on}^{p}	PDGF/PDGFRβ association	1.88×10^4	$\mu M^{-1}h^{-1}$	Assumed same as VEGF
k_{off}^{p}	PDGF/PDGFRβ dissociation	0.86	h^{-1}	Used k_d from *in-vitro* experiments [61].
δ_p	PDGF decay	1.2	h^{-1}	Order of magnitude estimate.

Table A.1: Default parameter set with units and references where applicable. Continued overleaf.

Param	Description	Value	Units	Reference
θ	EC proliferation	0.0417	h^{-1}	Comparison of logistic growth curves for *in-vitro* EC proliferation [122].
ρ	EC death	0.02	h^{-1}	Half of the maximal proliferation rate.
κ	PC proliferation	0.08	h^{-1}	*In-vitro* study of the growth of ECs and PCs [146].
ϵ	PC death	0.04	h^{-1}	Half the maximal proliferation rate.
ζ	PC attachment	5×10^5	$\mu M^{-1} h^{-1}$	Order of magnitude estimate.
ν	PC detachment	5×10^{-3}	h^{-1}	Order of magnitude estimate.
η	maturity increase	0.01	h^{-1}	Order of magnitude estimate.
μ	maturity decrease	0.01	h^{-1}	Order of magnitude estimate.
c_{ep}	Threshold bound VEGF for EC proliferation	0.3		Order of magnitude estimate.
c_d	Threshold bound VEGF for EC death	0.1	-	Order of magnitude estimate.
c_a	Threshold bound Ang2 for EC proliferation	0.3	-	Order of magnitude estimate.
c_{pp}	Threshold bound PDGF for PC proliferation	0.02	-	Order of magnitude estimate.
λ	Ang2/Ang1 ratio for maturity decrease	8		Based on experiments in [114]

Table A.1: Continued: Default parameter set with units and references where applicable.

Appendix B

Individual fits for the no-normalisation model

In this appendix we show the individual fits of the monotonic model described in Chapter 3 to the preclinical data. Below, we show the simulated results using individual parameter estimations alongside the experimental data.

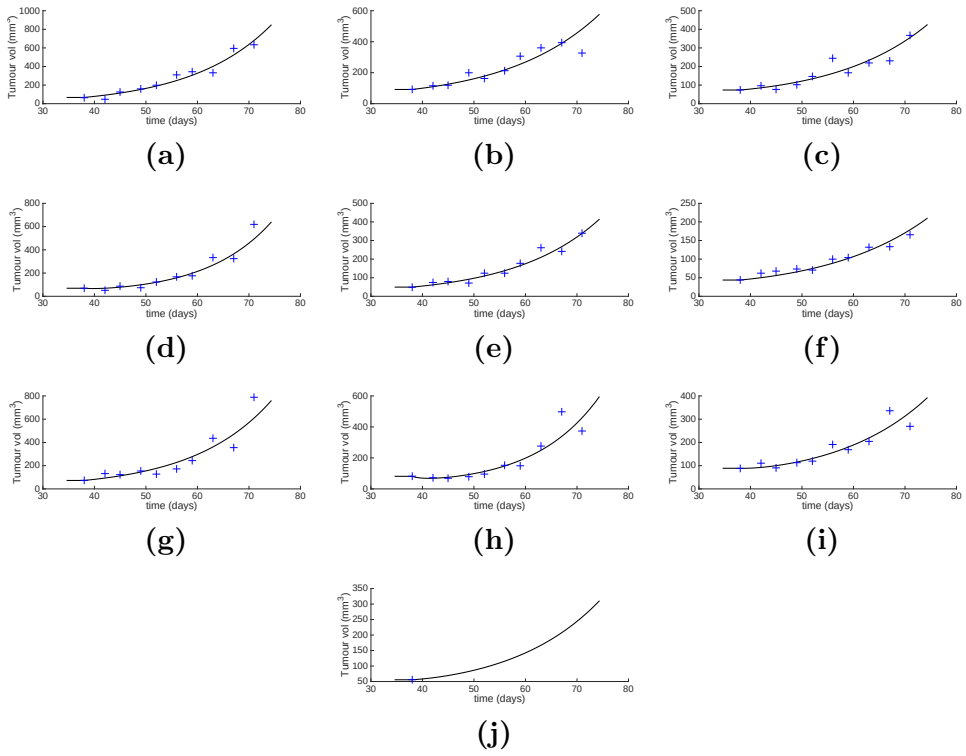


Figure B.1: Individual fits from simulations of equations (3.3)-(3.5). Individual fits for the control group using experimental data. Key: Blue '+' - experimental data, solid black lines - predicted tumour volume, T.

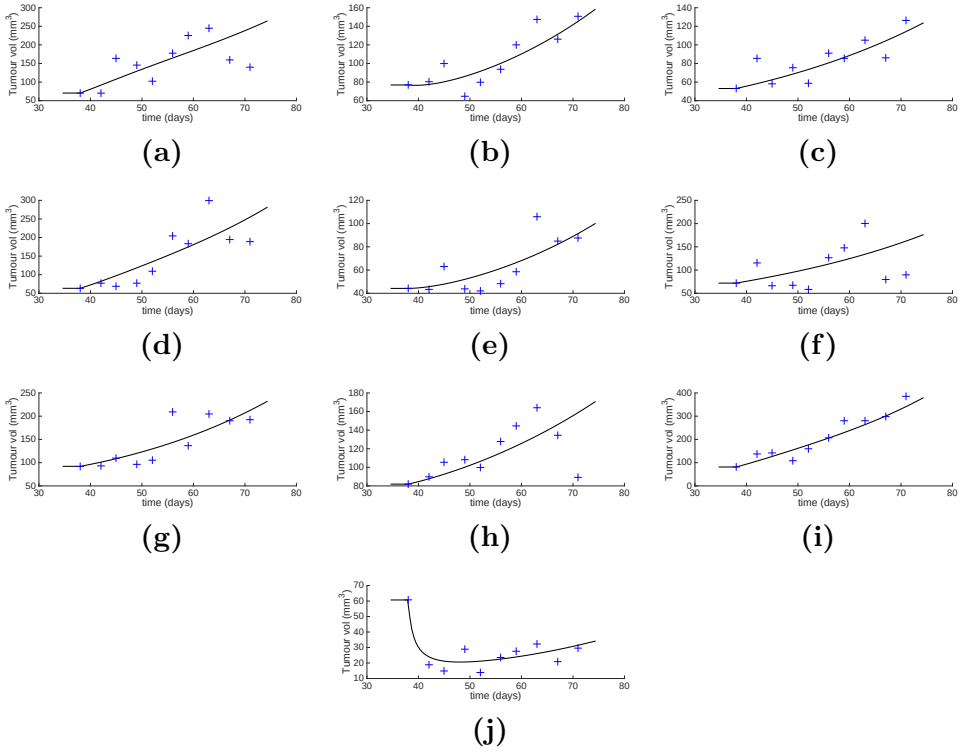


Figure B.2: Individual fits from simulations of equations (3.3)-(3.5). Individual fits for the bevacizumab group using experimental data. Key: Blue '+' - experimental data, solid black lines - predicted tumour volume, T, red dashed lines - normalisation windows for individuals.

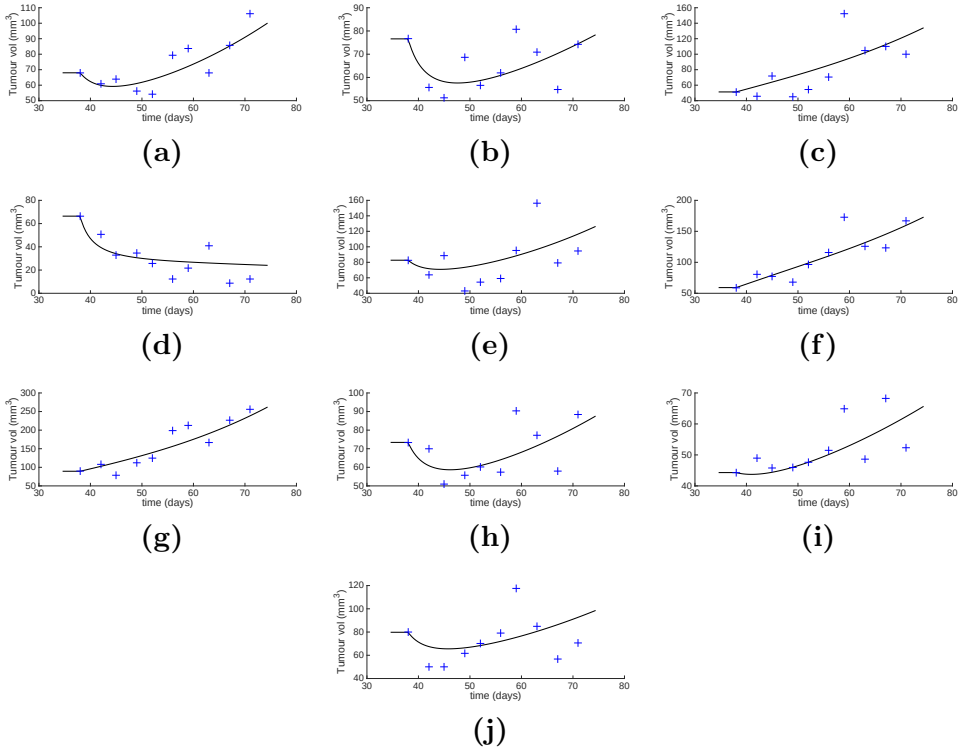


Figure B.3: Individual fits from simulations of equations (3.3)-(3.5). Individual fits for the vanucizumab group using experimental data. Key: Blue '+' - experimental data, solid black lines - predicted tumour volume, T, red dashed lines - normalisation windows for individuals.

Appendix C

Model selection for Chapter 3

In Chapter 3 we used Monolix software to estimate the parameters for a model of vascular tumour growth under anti-angiogenic therapy including vessel normalisation. In this appendix we include the results of using Monolix software to attempt to fit the model to the experimental data under various assumptions. The assumptions that we tested were

- Assuming the vessel kill rate, d_V, is the same for both treated groups/ assuming that d_V is different for each treated group;
- Assuming the maximum normalisation level, N_{max} is the same for both treated groups/ assuming that N_{max}, is different for each treated group;
- Assuming the timing of the normalisation window, characterised by t_{norm1} and t_{norm2} is the same for both treated groups/ assuming that t_{norm1} and t_{norm2} are different for each treated group;
- Assuming that the inter-individual variability (IIV) for t_{norm1} and t_{norm2}, should be fixed to 0.1/assuming that IIV for t_{norm1} and t_{norm2} can be estimated.

Combining these assumptions, we made eight attempts at model fitting using monolix software. For each attempt, we recorded the estimated values for the population parameters, the IIV for model parameter and the relative standard error (r.s.e.)

of on the population and IIV estimates. The table below details the results of all attempts at model fitting. Population parameters are indicated with a "pop" suffix and IIV values corresponding to parameters are indicated with an "omega" suffix in the table. The assumptions for each model are described in the first four rows, where "Y" indicates that the assumption was made and "N" indicates that the assumption was not made. In the table we write "na" where a parameter was not estimated for that model due to the assumptions indicated. Relative standard error is recorded as a percentage. The model that was selected is highlighted in yellow: it was selected based on diagnostic plots (see Chapter 3), low r.s.e. values for parameter estimation and on the basis of closeness of fit to the data from the individual fits.

Parameter	Model 1	Model 2	Model 3	Model 4	Model 5	Model 6	Model 7	Model 8
delta_V treatment specific?	Y	Y	N	N	Y	Y	Y	Y
N_max treatment specific?	Y	N	Y	N	N	N	N	N
tnorm treatment specific?	N	N	N	N	Y	Y	Y	Y
tnorm IIV fixed to 0?	Y	Y	Y	Y	Y	N	N	N
alpha_T_pop	0.0834	0.108	0.0979	0.0808	0.101	0.109	0.111	0.0968
alpha_T_pop_rse	8	10	10	8	9	12	8	7
alpha_T_omega	0.264	0.299	0.297	0.23	0.359	0.422	0.273	0.237
alpha_T_omega_rse	23	32	29	29	21	25	25	26
alpha_V_pop	0.133	0.11	0.106	0.179	0.107	0.119	0.0734	0.0987
alpha_V_pop_rse	9	7	8	8	3	7	6	7
alpha_V_omega	0.178	0.142	0.183	0.201	0.0661	0.177	0.204	0.202
alpha_V_omega_rse	40	44	36	31	36	34	27	31
K_pop	1.39	1.2	1.31	1.48	1.23	1.14	1.18	1.23
K_pop_rse	18	14	16	21	14	15	13	14
K_omega	0.9	0.723	0.795	1.04	0.749	0.711	0.666	0.74
K_omega_rse	15	15	15	15	13	15	14	14
N_max_pop	na	0.11	na	354	2.72	6.7	6.71	15.7
N_max_pop_rse	na	8	na	68	11	27	24	20
N_max_omega	na	0.231	na	1.57	0.459	0.55	0.935	0.63
N_max_omega_rse	na	66	na	31	18	41	20	26
N_max_bev_pop	626	na	13.2	na	na	na	na	na
N_max_bev_pop_rse	64	na	26	na	na	na	na	na
N_max_bev_omega	0.824	na	0.525	na	na	na	na	na
N_max_bev_omega_rse	59	na	38	na	na	na	na	na
N_max_van_pop	664	na	199	na	na	na	na	na
N_max_van_pop_rse	84	na	125	na	na	na	na	na
N_max_van_omega	1.63	na	2.77	na	na	na	na	na
N_max_van_omega_rse	38	na	33	na	na	na	na	na
tnorm1_pop	53	53	53.6	52.6	na	na	na	na
tnorm1_pop_rse	2	1	1	1	na	na	na	na
tnorm1_omega	FIX 0	FIX 0	FIX 0	FIX 0	na	na	na	na
tnorm1_omega_rse	na	na	na	na	na	na	na	na
tnorm2_pop	61.4	61.8	61.4	61.5	na	na	na	na
tnorm2_pop_rse	1	1	2	1	na	na	na	na
tnorm2_omega	FIX 0	FIX 0	FIX 0	FIX 0	na	na	na	na
tnorm2_omega_rse	na	na	na	na	na	na	na	na
tnorm1_bev_pop	na	na	na	na	51.7	53.3	53.3	52.6
tnorm1_bev_rse	na	na	na	na	4	4	3	6
tnorm1_bev_omega	na	na	na	na	FIX 0	FIX 0.1	0.0352	FIX 0.1
tnorm1_bev_omega_rse	na	na	na	na	na	na	115	na
tnorm2_bev_pop	na	na	na	na	62.3	59.2	61.9	59.6
tnorm2_bev_rse	na	na	na	na	2	3	2	4
tnorm2_bev_omega	na	na	na	na	FIX 0	FIX 0.1	0.0289	FIX 0.1
tnorm2_bev_omega_rse	na	na	na	na	na	na	63	na
tnorm1_van_pop	na	na	na	na	54.5	na	54.7	53.8
tnorm1_van_rse	na	na	na	na	204	na	4	nan
tnorm1_van_omega	na	na	na	na	FIX 0	na	0.0753	FIX 0.1
tnorm1_van_omega_rse	na	na	na	na	na	na	41	na
tnorm2_van_pop	na	na	na	na	60	na	56.4	49.4
tnorm2_van_rse	na	na	na	na	34	na	9	nan
tnorm2_van_omega	na	na	na	na	FIX 0	na	0.0335	FIX 0.1
tnorm2_van_omega_rse	na	na	na	na	na	na	721	na
delta_V_pop	na	na	0.114	0.213	na	na	na	na
delta_V_pop_rse	na	na	9	7	na	na	na	na
delta_V_omega	na	na	0.198	0.115	na	na	na	na
delta_V_omega_rse	na	na	34	59	na	na	na	na
delta_V_bev_pop	0.144	0.11	na	na	0.114	0.113	0.0719	0.0854
delta_V_bev_pop_rse	11	8	na	na	8	11	8	15
delta_V_bev_omega	0.0693	0.128	na	na	0.191	0.208	0.118	0.33
delta_V_bev_omega_rse	253	50	na	na	35	47	66	39
delta_V_van_pop	0.159	0.123	na	na	0.106	0.115	0.0652	0.0909
delta_V_van_pop_rse	13	11	na	na	12	12	17	17
delta_V_van_omega	0.231	0.248	na	na	0.301	0.293	0.409	0.436
delta_V_van_omega_rse	46	33	na	na	31	33	33	30

Appendix D

Individual fits for the normalisation model

In this appendix we show the individual fits of the non-monotonic (normalisation) model described in Chapter 3 to the preclinical data. Below, we show the simulated results using individual parameter estimations alongside the experimental data. The individuals are presented in the same order as in Appendix B.

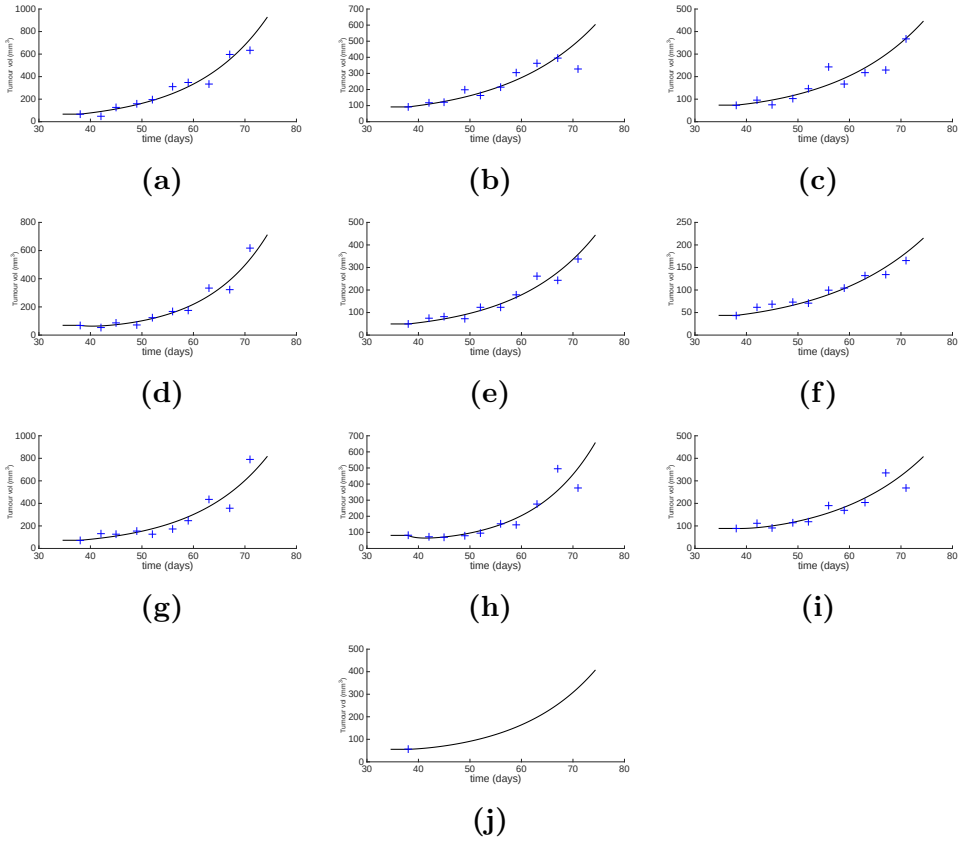


Figure D.1: Individual fits from simulations of equations (3.3)-(3.5). Individual fits for the control group using experimental data. Key: Blue '+' - experimental data, solid black lines - predicted tumour volume, T.

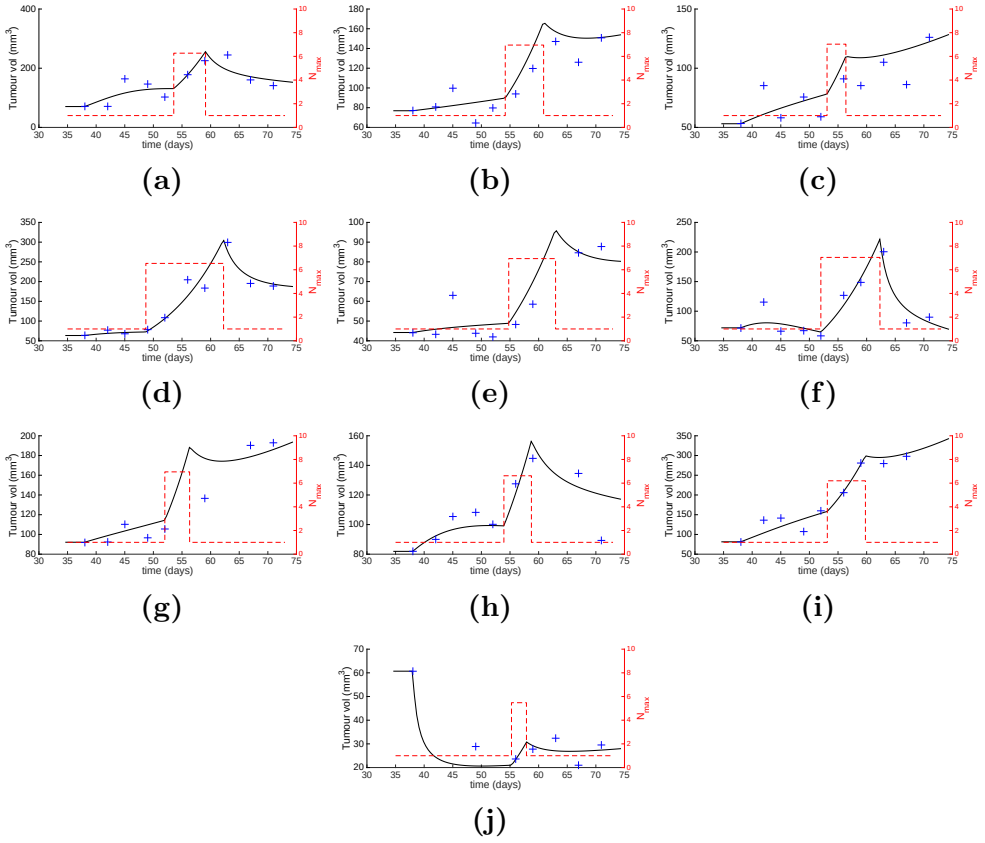


Figure D.2: Individual fits from simulations of equations (3.3)-(3.5). Individual fits for the bevacizumab group using experimental data. Key: Blue '+' - experimental data, solid black lines - predicted tumour volume, T, red dashed lines - normalisation windows for individuals.

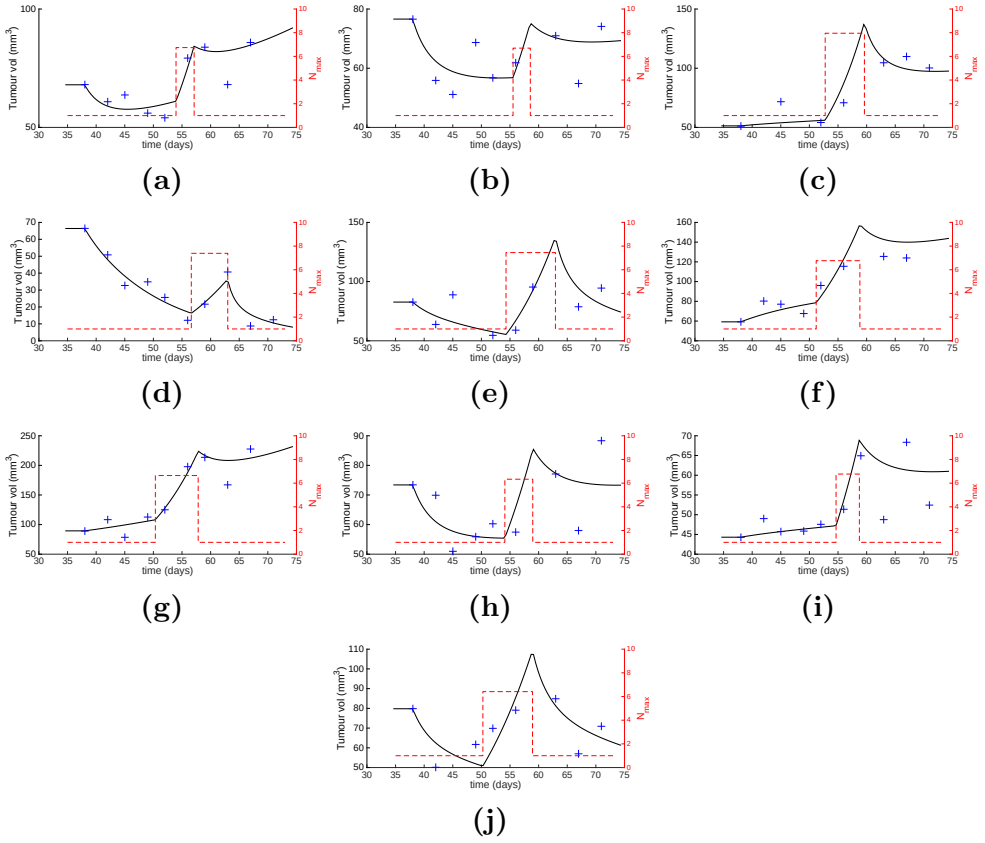


Figure D.3: Individual fits from simulations of equations (3.3)-(3.5). Individual fits for the vanucizumab group using experimental data. Key: Blue '+' - experimental data, solid black lines - predicted tumour volume, T, red dashed lines - normalisation windows for individuals.

Appendix E

$\lambda - \omega$ analysis for Chapter 5

We show how the model presented in Chapter 5 can be approximated by one of the appropriate type for $\lambda - \omega$ analysis, a standard method used to investigate the wavetrain solutions to a reaction-diffusion type model that exhibits limit cycle behaviour. From our analysis, we derive the specific conditions for which we should expect stable and unstable wavetrain solutions to our PDEs in the region of a Hopf bifurcation.

The simplified PDE model from equations (5.10)-(5.11) in Chapter 5 are

$$\frac{\partial T}{\partial t} = \frac{\partial^2 T}{\partial x^2} + f_s(T, V), \tag{E.1}$$

$$\frac{\partial V}{\partial t} = \frac{\partial^2 V}{\partial x^2} + g_s(T, V), \tag{E.2}$$

where

$$f_s(T, V) = \frac{NVT}{NV(1 + s_\beta) + s_\beta d_S} - d_p T,$$

$$g_s(T, V) = \eta V(1 - V) - \frac{\delta TV}{N(V + T)} - d_V V,$$

and in the case of no therapy, $N = 1$ and $d_V = 0 \; \forall \, t$. We state the specific conditions for linear stability of the coexistence steady state of the non-spatial system given

by:

$$\frac{\mathrm{d}T}{\mathrm{d}t} = f_s(T,V), \tag{E.3}$$

$$\frac{\mathrm{d}V}{\mathrm{d}t} = g_s(T,V), \tag{E.4}$$

here for completeness.

The solution for the general coexistence steady state of equations (E.3)-(E.4), (T_{ss}, V_{ss}), is obtained by setting $f_s(T,V) = g_s(T,V) = 0$:

$$T_{ss} = \frac{\eta V_{ss}(1-V_{ss}) - d_V V_{ss}}{d_V + \frac{\delta}{N} - \eta(1-V_{ss})}, \quad V_{ss} = \frac{d_P d_S s_\beta}{N(1-d_P - s_\beta d_P)},$$

and the corresponding Jacobian matrix is given by

$$J = \begin{pmatrix} \frac{\partial f_s}{\partial T} & \frac{\partial f_s}{\partial V} \\ \frac{\partial g_s}{\partial T} & \frac{\partial g_s}{\partial V} \end{pmatrix}, \tag{E.5}$$

where

$J_{11} = \frac{\partial f_s}{\partial T} = \frac{NV}{NV(1+s_\beta)+s_\beta d_S} - d_P$;

$J_{12} = \frac{\partial f_s}{\partial V} = \frac{s_\beta d_S NT}{(NV(1+s_\beta+s_\beta d_S))^2}$ (always ≥ 0);

$J_{21} = \frac{\partial g_s}{\partial T} = -\frac{\delta V^2}{N(T+V)^2}$ (always ≤ 0);

$J_{22} = \frac{\partial g_s}{\partial V} = \eta(1-2V) - \frac{\delta T^2}{N(T+V)^2} - d_V$.

The critical values of d_V for which a Hopf bifurcation occurs can be found by setting the trace of the Jacobian matrix (E.5) evaluated at (T_{ss}, V_{ss}) equal to zero and solving the arising quadratic expression for the critical value of $d_V = d_V^{crit}$:

$$\begin{aligned} J_{11}\Big|_{(T_{ss},V_{ss})} + J_{22}\Big|_{(T_{ss},V_{ss})} &= \frac{N}{\delta}(d_V^{crit})^2 + \left(1 + 2\eta\frac{N}{\delta}(1-V_{ss})\right) d_V^{crit} + \eta(1-2V_{ss}) \\ &\quad -\frac{N}{\delta}[\eta(1-V_{ss})]^2 \\ &= 0, \end{aligned}$$

where, for the remainder of our analysis we focus on the root of the quadratic for which the value of d_V^{crit} is smaller, although our analysis can be applied to either root.

We wish to approximate the model in equations (E.1)-(E.2) by a $\lambda - \omega$ system described by [157], which takes the form

$$\frac{\partial \hat{T}}{\partial t} = \frac{\partial^2 \hat{T}}{\partial x^2} + \lambda_0 \hat{T} - \omega_0 \hat{V} - (\lambda_1 \hat{T} + \omega_1 \hat{V})(\hat{T}^2 + \hat{V}^2), \tag{E.6}$$

$$\frac{\partial \hat{V}}{\partial t} = \frac{\partial^2 \hat{V}}{\partial x^2} + \omega_0 \hat{T} + \lambda_0 \hat{V} + (\omega_1 \hat{T} - \lambda_1 \hat{V})(\hat{T}^2 + \hat{V}^2), \tag{E.7}$$

where $\hat{T}$ and $\hat{V}$ are transformed variables such that the steady state solution of the corresponding spatially homogeneous system at $(\hat{T}, \hat{V}) = (0, 0)$ is unstable and admits a limit cycle solution of radius $\sqrt{\frac{\lambda_0}{\lambda_1}}$. According to [156], the full spatial system has a family of periodic wave train solutions

$$\hat{T} = R\cos[\omega(R)t \pm \sqrt{\lambda(R)}x], \quad \hat{V} = R\sin[\omega(R)t \pm \sqrt{\lambda(R)}x],$$

where R is the amplitude of the waves and

$$\lambda(r) = \lambda_0 - \lambda_1 r^2, \quad \omega(r) = \omega_0 + \omega_1 r^2, \quad r = \sqrt{\hat{T}^2 + \hat{V}^2}.$$

The condition for stable waves as derived in [98] is

$$\left(\frac{\omega_1}{\lambda_1}\right)^2 < 1.148, \tag{E.8}$$

where we derive λ_1 and ω_1 for our system below. From [157],

$$\lambda_0 = (d_V^{crit} - d_V)\frac{1}{2}\frac{\partial(J_{11} + J_{22})}{\partial d_V}\bigg|_{d_V = d_V^{crit}} \tag{E.9}$$

where J_{11}, J_{22} are evaluated at (T_{ss}, V_{ss}). Furthermore, from [157],

$$\omega_0 = \sqrt{J_{12}|J_{21}|}\bigg|_{d_V = d_V^{crit}} \tag{E.10}$$

where J_{12} and J_{21} are evaluated at (T_{ss}, V_{ss}). To obtain ω_1, λ_1 for the stability condition (E.8), we approximate our system by the form given by (E.6)-(E.7). For this, we make the linear change of variables

$$\hat{T} = \frac{T - T_{ss}}{\alpha}, \ \hat{V} = \frac{V - V_{ss}}{\beta}, \tag{E.11}$$

where β and α are constants to be determined below. For what follows, we assume that we are close to the Hopf bifurcation point, and therefore $d_V = d_V^{crit}$ such that $\lambda_0 = 0$, and therefore the equations that we wish to satisfy, given by (E.6)-(E.7), become

$$\frac{\partial \hat{T}}{\partial t} = \frac{\partial^2 \hat{T}}{\partial x^2} - \omega_0 \hat{V} + F(\hat{T}, \hat{V}), \tag{E.12}$$

$$\frac{\partial \hat{V}}{\partial t} = \frac{\partial^2 \hat{V}}{\partial x^2} + \omega_0 \hat{T} + G(\hat{T}, \hat{V}), \tag{E.13}$$

where F and G are functions of the transformed variables $\hat{T}$ and $\hat{V}$ that we must derive. Substituting (E.11) into (E.1)-(E.2), we obtain

$$\begin{aligned}
\frac{\partial \hat{T}}{\partial t} &= \frac{\partial^2 \hat{T}}{\partial x^2} + \frac{1}{\alpha} f_s(\hat{T}, \hat{V}) = \frac{\partial^2 \hat{T}}{\partial x^2} - \omega_0 \hat{V} + \frac{1}{\alpha} f_s(\hat{T}, \hat{V}) + \omega_0 \hat{V}, \\
\frac{\partial \hat{V}}{\partial t} &= \frac{\partial^2 \hat{V}}{\partial x^2} + \frac{1}{\beta} g_s(\hat{T}, \hat{V}) = \frac{\partial^2 \hat{V}}{\partial x^2} + \omega_0 \hat{T} + \frac{1}{\beta} g_s(\hat{T}, \hat{V}) - \omega_0 \hat{T},
\end{aligned}$$

and since we wish to approximate our model in equations (E.1)-(E.2) by one of the form given by equations (E.12)-(E.13), we must choose α, β such that

$$F(\hat{T}, \hat{V}) = \frac{1}{\alpha} f_s(\hat{T}, \hat{V}) + \omega_0 \hat{V}, \tag{E.14}$$

$$G(\hat{T}, \hat{V}) = \frac{1}{\beta} g_s(\hat{T}, \hat{V}) - \omega_0 \hat{T}. \tag{E.15}$$

From the definition of the $\lambda - \omega$ form in equations (E.6)-(E.7), we can say that the following conditions must be satisfied in order to approximate our model in $\lambda - \omega$

form:

$$F(0,0) = \frac{\partial F(\hat{T},\hat{V})}{\partial \hat{T}}\bigg|_{(0,0)} = \frac{\partial F(\hat{T},\hat{V})}{\partial \hat{V}}\bigg|_{(0,0)} = 0, \tag{E.16}$$

$$G(0,0) = \frac{\partial G(\hat{T},\hat{V})}{\partial \hat{V}}\bigg|_{(0,0)} = \frac{\partial G(\hat{T},\hat{V})}{\partial \hat{T}}\bigg|_{(0,0)} = 0. \tag{E.17}$$

It can be shown that $\frac{\partial f_s(T,V)}{\partial T}\big|_{(T_{ss},V_{ss})} = 0$, and since we are considering the region near the Hopf bifurcation, where $\mathrm{Tr}(J)\big|_{(T_{ss},V_{ss})} = 0$, we can say that $\frac{\partial g_s(T,V)}{\partial V}\big|_{(T_{ss},V_{ss})} = 0$ also. Therefore, from (E.14) and (E.15),

$$\frac{\partial F(\hat{T},\hat{V})}{\partial \hat{T}}\bigg|_{(0,0)} = \frac{1}{\alpha}\frac{\partial f_s(T,V)}{\partial T}\bigg|_{(T_{ss},V_{ss})} = 0,$$
$$\frac{\partial G(\hat{T},\hat{V})}{\partial \hat{V}}\bigg|_{(0,0)} = \frac{1}{\beta}\frac{\partial g_s(T,V)}{\partial T}\bigg|_{(T_{ss},V_{ss})} = 0,$$

in line with the conditions (E.16)-(E.17). Furthermore, we wish to find values of α and β for which (E.16)-(E.17) are satisfied. To satisfy $\frac{\partial F(\hat{T},\hat{V})}{\partial \hat{V}}\Big|_{(0,0)} = 0$, we apply $\frac{\partial}{\partial \hat{V}} \equiv \beta\frac{\partial}{\partial V}$ to (E.14) to obtain

$$\frac{1}{\alpha}\frac{\partial f_s(\hat{T},\hat{V})}{\partial \hat{V}}\bigg|_{(\hat{T},\hat{V})=(0,0)} + \omega_0 = \frac{\beta}{\alpha}\frac{\partial f_s(T,V)}{\partial V}\bigg|_{(T,V)=(T_{ss},V_{ss})} + \omega_0 = 0,$$

and therefore we obtain the expression containing β and α

$$\frac{\beta}{\alpha}J_{12}\bigg|_{(T,V)=(T_{ss},V_{ss})} = -\omega_0.$$

To satisfy $\frac{\partial G(\hat{T},\hat{V})}{\partial \hat{T}}\Big|_{(0,0)} = 0$, we apply $\frac{\partial}{\partial \hat{T}} \equiv \alpha\frac{\partial}{\partial T}$ to (E.15) to obtain

$$\frac{1}{\beta}\frac{\partial g_s(T,V)}{\partial \hat{T}}\bigg|_{(\hat{T},\hat{V})=(0,0)} - \omega_0 = \frac{\alpha}{\beta}\frac{\partial g_s(T,V)}{\partial T}\bigg|_{(T,V)=(T_{ss},V_{ss})} - \omega_0 = 0,$$

and therefore we obtain another expression containing β and α

$$\frac{\alpha}{\beta}J_{21}\bigg|_{(T,V)=(T_{ss},V_{ss})} = \omega_0.$$

By choosing

$$\beta = 1,$$

we have

$$\alpha = -\frac{J_{12}}{\omega_0} = \frac{\omega_0}{J_{21}},$$

where J_{12} and J_{21} are evaluated at $(T, V) = (T_{ss}, V_{ss})$. By substituting the values for α and β into the expressions for $F(\hat{T}, \hat{V})$ and $G(\hat{T}, \hat{V})$ in (E.14)-(E.15), we obtain

$$\begin{aligned} F(\hat{T}, \hat{V}) &= -\frac{\omega_0}{J_{12}} f_s(\hat{T}, \hat{V}) + \omega_0 \hat{V}, \\ G(\hat{T}, \hat{V}) &= g_s(\hat{T}, \hat{V}) - \omega_0 \hat{T}. \end{aligned}$$

The expressions for F and G that we have derived are used to evaluate the expressions given in [156] to find λ_1 and ω_1:

$$\begin{aligned} \lambda_1 &= -\frac{1}{16}\Big(F_{\hat{T}\hat{T}\hat{T}} + F_{\hat{T}\hat{V}\hat{V}} + G_{\hat{T}\hat{T}\hat{V}} + G_{\hat{V}\hat{V}\hat{V}}\Big) \\ &\quad + \frac{1}{16\omega_0}\Big(F_{\hat{T}\hat{T}} G_{\hat{T}\hat{T}} - F_{\hat{V}\hat{V}} G_{\hat{V}\hat{V}} - F_{\hat{T}\hat{V}}(F_{\hat{T}\hat{T}} + F_{\hat{V}\hat{V}}) + G_{\hat{T}\hat{V}}(G_{\hat{V}\hat{V}} + G_{\hat{T}\hat{T}})\Big), \qquad \text{(E.18)} \\ \omega_1 &= \frac{1}{16}\Big(G_{\hat{T}\hat{T}\hat{T}} + G_{\hat{T}\hat{V}\hat{V}} - F_{\hat{T}\hat{T}\hat{V}} - F_{\hat{V}\hat{V}\hat{V}}\Big) + \frac{1}{48\omega_0}\Big(F_{\hat{T}\hat{T}}(G_{\hat{T}\hat{V}} - F_{\hat{V}\hat{V}}) + G_{\hat{V}\hat{V}}(F_{\hat{T}\hat{V}} - G_{\hat{T}\hat{T}}) \\ &\quad -3F_{\hat{V}\hat{V}}(G_{\hat{T}\hat{V}} + F_{\hat{V}\hat{V}}) - 3G_{\hat{T}\hat{T}}(F_{\hat{T}\hat{V}} + G_{\hat{T}\hat{T}}) - 2(F_{\hat{T}\hat{T}} + F_{\hat{V}\hat{V}} - G_{\hat{T}\hat{V}})^2 \\ &\quad -2(G_{\hat{T}\hat{T}} + G_{\hat{V}\hat{V}} - F_{\hat{T}\hat{V}})^2\Big), \qquad \text{(E.19)} \end{aligned}$$

where subscripts represent derivatives with respect to $\hat{T}$ and $\hat{V}$ and all derivatives are evaluated at $(\hat{T}, \hat{V}) = (0, 0)$. The derivatives were calculated analytically (and are not shown here) and most terms are equal to zero when evaluated at $(\hat{T}, \hat{V}) = (0, 0)$. Accounting only for non-zero terms, the expressions (E.18)-(E.19) become

$$\begin{aligned} \lambda_1 &= -\frac{1}{16} F_{\hat{T}\hat{V}\hat{V}}, \\ \omega_1 &= \frac{1}{48\omega_0}\Big(G_{\hat{V}\hat{V}} F_{\hat{T}\hat{V}} - 2(G_{\hat{V}\hat{V}} - F_{\hat{T}\hat{V}})^2\Big), \end{aligned}$$

which can be evaluated numerically. A map of the region of parameter space for which stable and unstable travelling waves are predicted, as well as example simu-

lations of each case, are shown in Chapter 5.

References

[1] A. P. Adamis, J. W. Miller, M.-T. Bernal, D. J. D'Amico, J. Folkman, T.-K. Yeo and K.-T. Yeo. Increased Vascular Endothelial Growth Factor Levels in the Vitreous of Eyes With Proliferative Diabetic Retinopathy. *Am. J. Ophthalmol.*, 118(4):445–450, 1994. doi:10.1016/S0002-9394(14)75794-0.

[2] Z. Agur, L. Arakelyan, P. Daugulis and Y. Ginosar. Hopf point analysis for angiogenesis models. *Discret. Contin. Dyn. Syst. - Ser. B*, 4(1):29–38, 2003. doi:10.3934/dcdsb.2004.4.29.

[3] G. Allaire and A. Piatnitski. Homogenization of nonlinear reaction-diffusion equation with a large reaction term. *Analli Dell Univ. Di Ferrara*, 56(1):141–161, 2010. doi:10.1007/s11565-010-0095-z.

[4] B. Amaziane and L. Pankratov. Homogenization of a reactiondiffusion equation with Robin interface conditions. *Appl. Math. Lett.*, 19(11):1175–1179, 2006. doi:10.1016/j.aml.2005.04.021.

[5] J. Ambati, B. K. Ambati, S. H. Yoo, S. Ianchulev and A. P. Adamis. Age-Related Macular Degeneration: Etiology, Pathogenesis, and Therapeutic Strategies. *Surv. Ophthalmol.*, 48(3):257–293, 2003. doi:10.1016/S0039-6257(03)00030-4.

[6] L. Amit, I. Ben-Aharon, L. Vidal, L. Leibovici and S. Stemmer. The impact of bevacizumab (Avastin) on survival in metastatic solid tumors - a meta-analysis and systematic review. *PLoS One*, 8(1):e51780, 2013. doi:10.1371/journal.pone.0051780.

[7] A. R. A. Anderson. A hybrid mathematical model of solid tumour invasion: the importance of cell adhesion. *Math. Med. Biol.*, 22(2):163–86, 2005. doi:10.1093/imammb/dqi005.

[8] A. R. A. Anderson and M. A. J. Chaplain. Continuous and discrete mathematical models of tumor-induced angiogenesis. *Bull. Math. Biol.*, 60:857–900, 1998. doi:10.1006/bulm.1998.0042.

[9] M. Aoyagi, N. Fukai, K. Ogami, M. Yamamoto and K. Yamamoto. Kinetics of 125I-PDGF binding and down-regulation of PDGF receptor in human arterial smooth muscle cell strains during cellular senescence in vitro. *J. Cell. Physiol.*, 164(2):376–384, 1995. doi:10.1002/jcp.1041640218.

[10] M. Arjaans, T. H. Oude Munnink, S. F. Oosting, A. G. T. Terwisscha van Scheltinga, J. a. Gietema, E. T. Garbacik, H. Timmer-Bosscha, M. N. Lub-de

Hooge, C. P. Schröder and E. G. E. de Vries. Bevacizumab-induced normalization of blood vessels in tumors hampers antibody uptake. *Cancer Res.*, 73(11):3347–55, 2013. doi:10.1158/0008-5472.CAN-12-3518.

[11] A. Armulik, A. Abramsson and C. Betsholtz. Endothelial/pericyte interactions. *Circ. Res.*, 97(6):512–23, 2005. doi:10.1161/01.RES.0000182903.16652.d7.

[12] E. Audero, I. Cascone, I. Zanon, S. C. Previtali, R. Piva, D. Schiffer and F. Bussolino. Expression of Angiopoietin-1 in human glioblastomas regulates tumor-induced angiogenesis: in vivo and in vitro studies. *Arterioscler. Thromb. Vasc. Biol.*, 21(4):536–541, 2001. doi:10.1161/01.ATV.21.4.536.

[13] S. Audoly, L. D'Angio, M. Saccomani and C. Cobelli. Global identifiability of linear compartmental models-a computer algebra algorithm. *IEEE Trans. Biomed. Eng.*, 45(1):36–47, 1998. doi:10.1109/10.650350.

[14] L. C. Baker, J. K. Boult, M. Thomas, A. Koehler, T. Nayak, J. Tessier, C.-H. Ooi, F. Birzele, A. Belousov, M. Zajac, C. Horn, C. LeFave and S. P. Robinson. Acute tumour response to a bispecific Ang-2-VEGF-A antibody: insights from multiparametric MRI and gene expression profiling. *Br. J. Cancer*, 115:691–702, 2016. doi:10.1038/bjc.2016.236.

[15] D. Balding and D. McElwain. A mathematical model of tumour-induced capillary growth. *J. Theor. Biol.*, 114(1):53–73, 1985. doi:10.1016/S0022-5193(85)80255-1.

[16] K. Bartha and H. Rieger. Vascular network remodeling via vessel cooption, regression and growth in tumors. *J. Theor. Biol.*, 241(4):903–18, 2006. doi:10.1016/j.jtbi.2006.01.022.

[17] T. Bastogne, A. Samson, P. Vallois, S. Wantz-Mézières, S. Pinel, D. Bechet and M. Barberi-Heyob. Phenomenological modeling of tumor diameter growth based on a mixed effects model. *J. Theor. Biol.*, 262(3):544–52, 2010. doi:10.1016/j.jtbi.2009.10.008.

[18] T. T. Batchelor, A. G. Sorensen, E. di Tomaso, W.-T. Zhang, D. G. Duda, K. S. Cohen, K. R. Kozak, D. P. Cahill, P.-J. Chen, M. Zhu, M. Ancukiewicz, M. M. Mrugala, S. Plotkin, J. Drappatz, D. N. Louis, P. Ivy, D. T. Scadden, T. Benner, J. S. Loeffler, P. Y. Wen and R. K. Jain. AZD2171, a pan-VEGF receptor tyrosine kinase inhibitor, normalizes tumor vasculature and alleviates edema in glioblastoma patients. *Cancer Cell*, 11(1):83–95, 2007. doi:10.1016/j.ccr.2006.11.021.

[19] A. L. Bauer, T. L. Jackson and Y. Jiang. A Cell-Based Model Exhibiting Branching and Anastomosis during Tumor-Induced Angiogenesis. *Biophys. J.*, 92(9):3105–3121, 2007. doi:10.1529/biophysj.106.101501.

[20] R. Bellman and K. Åström. On structural identifiability. *Math. Biosci.*, 7(3-4):329–339, 1970. doi:10.1016/0025-5564(70)90132-X.

[21] F. Billy, B. Ribba, O. Saut, H. Morre-Trouilhet, T. Colin, D. Bresch, J.-P. Boissel, E. Grenier and J.-P. Flandrois. A pharmacologically based multiscale mathematical model of angiogenesis and its use in investigating the efficacy of a new cancer treatment strategy. *J. Theor. Biol.*, 260(4):545–562, 2009. doi:http://dx.doi.org/10.1016/j.jtbi.2009.06.026.

[22] J. L. Blum, S. E. Jones, A. U. Buzdar, P. M. LoRusso, I. Kuter, C. Vogel, B. Osterwalder, H. U. Burger, C. S. Brown and T. Griffin. Multicenter phase II study of capecitabine in paclitaxel-refractory metastatic breast cancer. *J. Clin. Oncol.*, 17(2):485–93, 1999. doi:10.1200/JCO.1999.17.2.485.

[23] E. Bogdanovic, V. P. K. H. Nguyen and D. J. Dumont. Activation of Tie2 by angiopoietin-1 and angiopoietin-2 results in their release and receptor internalization. *J. Cell Sci.*, 119(17):3551–3560, 2006. doi:10.1242/jcs.03077.

[24] C. Breward, H. M. Byrne and C. E. Lewis. A Multiphase Model Describing Vascular Tumour Growth. *Bull. Math. Biol.*, 65(4):609–640, 2003. doi:10.1016/S0092-8240(03)00027-2.

[25] A. M. Brufsky, S. Hurvitz, E. Perez, R. Swamy, V. Valero, V. O'Neill and H. S. Rugo. RIBBON-2: a randomized, double-blind, placebo-controlled, phase III trial evaluating the efficacy and safety of bevacizumab in combination with chemotherapy for second-line treatment of human epidermal growth factor receptor 2-negative metastatic breast c. *J. Clin. Oncol.*, 29(32):4286–93, 2011. doi:10.1200/JCO.2010.34.1255.

[26] R. Bruno, L. Lindbom, F. Schaedeli Stark, P. Chanu, F. Gilberg, N. Frey and L. Claret. Simulations to assess Phase II noninferiority trials of different doses of capecitabine in combination with docetaxel for metastatic breast cancer. *CPT Pharmacometrics Syst. Pharmacol.*, 1(12):e19, 2012. doi:10.1038/psp.2012.20.

[27] L. Bueno, D. P. de Alwis, C. Pitou, J. Yingling, M. Lahn, S. Glatt and I. F. Trocóniz. Semi-mechanistic modelling of the tumour growth inhibitory effects of LY2157299, a new type I receptor TGF-β kinase antagonist, in mice. *Eur. J. Cancer*, 44(1):142–150, 2008. doi:10.1016/j.ejca.2007.10.008.

[28] Y. Cai, J. Wu, Z. Li and Q. Long. Mathematical modelling of a brain tumour initiation and early development: A coupled model of glioblastoma growth, pre-existing vessel co-option, angiogenesis and blood perfusion. *PLoS One*, 11(3):e0150296, 2016. doi:10.1371/journal.pone.0150296.

[29] Y. Cai, J. Zhang, J. Wu, Z.-y. Li, Y. Cai, J. Zhang, J. Wu and Z.-y. Li. Oxygen transport in a three-dimensional microvascular network incorporated with early tumour growth and preexisting vessel cooption: numerical simulation study. *Biomed Res. Int.*, 2015:1–10, 2015. doi:10.1155/2015/476964.

[30] R. S. Cantrell and C. Cosner. *Spatial Ecology via Reaction-Diffusion Equations*. John Wiley & Sons ltd, 1 edition, 2003. ISBN 0-471-49301-5.

[31] P. Carmeliet and R. K. Jain. Principles and mechanisms of vessel normalization for cancer and other angiogenic diseases. *Nat. Rev. Drug Discov.*, 10(6):417–427, 2011. doi:10.1038/nrd3455.

[32] M. J. Chappell, K. R. Godfrey and S. Vajda. Global identifiability of the parameters of nonlinear systems with specified inputs: A comparison of methods. *Math. Biosci.*, 102(1):41–73, 1990. doi:10.1016/0025-5564(90)90055-4.

[33] D. Chen and I. Mellman. Oncology Meets Immunology: The Cancer-Immunity Cycle. *Immunity*, 39(1):1–10, 2013. doi:10.1016/j.immuni.2013.07.012.

[34] L. Cheng, Z. Huang, W. Zhou, Q. Wu, S. Donnola, J. K. Liu, X. Fang, A. E. Sloan, Y. Mao, J. D. Lathia, W. Min, R. E. McLendon, J. N. Rich and S. Bao. Glioblastoma stem cells generate vascular pericytes to support vessel function and tumor growth. *Cell*, 153(1):139–152, 2013. doi:10.1016/j.cell.2013.02.021.

[35] S. Chicklore, V. Goh, M. Siddique, A. Roy, P. K. Marsden and G. J. R. Cook. Quantifying tumour heterogeneity in 18F-FDG PET/CT imaging by texture analysis. *Eur. J. Nucl. Med. Mol. Imaging*, 40(1):133–40, 2013. doi:10.1007/s00259-012-2247-0.

[36] L. Q. M. Chow and S. G. Eckhardt. Sunitinib: from rational design to clinical efficacy. *J. Clin. Oncol.*, 25(7):884–896, 2007. doi:10.1200/JCO.2006.06.3602.

[37] L. Claret, P. Girard, P. M. Hoff, E. Van Cutsem, K. P. Zuideveld, K. Jorga, J. Fagerberg and R. Bruno. Model-based prediction of Phase III overall survival in colorectal cancer on the basis of Phase II tumor dynamics. *J. Clin. Oncol.*, 27(25):4103–4108, 2009. doi:10.1200/JCO.2008.21.0807.

[38] A. J. Connor, R. P. Nowak, E. Lorenzon, M. Thomas, F. Herting, S. Hoert, T. Quaiser, E. Shochat, J. Pitt-Francis, J. Cooper, P. K. Maini and H. M. Byrne. An integrated approach to quantitative modelling in angiogenesis research. *J. R. Soc. Interface*, 12(110), 2015. doi:10.1098/rsif.2015.0546.

[39] O. Coutelle, L. M. Schiffmann, M. Liwschitz, M. Brunold, V. Goede, M. Hallek, H. Kashkar and U. T. Hacker. Dual targeting of Angiopoetin-2 and VEGF potentiates effective vascular normalisation without inducing empty basement membrane sleeves in xenograft tumours Excellence Cluster on Cellular Stress Responses in Aging-Associated Diseases. *Br. J. Cancer*, 112:495–503, 2015. doi:10.1038/bjc.2014.629.

[40] S. Cox and P. Matthews. Exponential Time Differencing for Stiff Systems. *J. Comput. Phys.*, 176(2):430–455, 2002. doi:10.1006/jcph.2002.6995.

[41] C. H. Crane, L. M. Ellis, J. L. Abbruzzese, C. Amos, H. Q. Xiong, L. Ho, D. B. Evans, E. P. Tamm, C. Ng, P. W. T. Pisters, C. Charnsangavej, M. E. Delclos, M. O'Reilly, J. E. Lee and R. A. Wolff. Phase I trial evaluating the safety of bevacizumab with concurrent radiotherapy and capecitabine in locally advanced pancreatic cancer. *J. Clin. Oncol.*, 24(7):1145–51, 2006. doi:10.1200/JCO.2005.03.6780.

[42] S. A. Cunningham. Characterization of Vascular Endothelial cell Growth Factor interactions with the kinase insert domain-containing receptor tyrosine kinase. A real time kinetic study. *J. Biol. Chem.*, 274(26):18421–18427, 1999. doi:10.1074/jbc.274.26.18421.

[43] B. G. Czito, J. C. Bendell, C. G. Willett, M. A. Morse, G. C. Blobe, D. S. Tyler, J. Thomas, K. A. Ludwig, C. R. Mantyh, J. Ashton, D. Yu and H. I. Hurwitz. Bevacizumab, oxaliplatin, and capecitabine with radiation therapy in rectal cancer: Phase I trial results. *Int. J. Radiat. Oncol.*, 68(2):472–478, 2007. doi:10.1016/j.ijrobp.2007.02.001.

[44] C. Daly, A. Eichten, C. Castanaro, E. Pasnikowski, A. Adler, A. S. Lalani, N. Papadopoulos, A. H. Kyle, A. I. Minchinton, G. D. Yancopoulos and G. Thurston. Angiopoietin-2 functions as a Tie2 agonist in tumor models, where it limits the effects of VEGF inhibition. *Cancer Res.*, 73(1):108–118, 2013. doi:10.1158/0008-5472.CAN-12-2064.

[45] C. V. Dang and G. L. Semenza. Oncogenic alterations of metabolism. *Trends Biochem. Sci.*, 24(2):68–72, 1999. doi:10.1016/S0968-0004(98)01344-9.

[46] B. Delyon, M. Lavielle and E. Moulines. Convergence of a stochastic approximation version of the EM algorithm. *Ann. Stat.*, 27(1):94–128, 1999. doi:10.1214/aos/1018031103.

[47] P. V. Dickson, J. B. Hamner, T. L. Sims, C. H. Fraga, C. Y. C. Ng, S. Rajasekeran, N. L. Hagedorn, M. B. McCarville, C. F. Stewart and A. M. Davidoff. Bevacizumab-induced transient remodeling of the vasculature in neuroblastoma xenografts results in improved delivery and efficacy of systemically administered C chemotherapy. *Clin. Cancer Res.*, 13(13):3942–3950, 2007. doi:10.1158/1078-0432.CCR-07-0278.

[48] R. P. M. Dings, M. Loren, H. Heun, E. McNiel, A. W. Griffioen, K. H. Mayo and R. J. Griffin. Scheduling of radiation with angiogenesis inhibitors anginex and Avastin improves therapeutic outcome via vessel normalization. *Clin. Cancer Res.*, 13(11):3395–402, 2007. doi:10.1158/1078-0432.CCR-06-2441.

[49] M. Dobosz, V. Ntziachristos, W. Scheuer and S. Strobel. Multispectral fluorescence ultramicroscopy : three- dimensional visualization and automatic quantification of tumor morphology , drug penetration , and antiangiogenic treatment response. *Neoplasia*, 16(1):1–13, IN1–IN7, 2014. doi:10.1593/neo.131848.

[50] B. Döme, M. J. Hendrix, S. Paku, J. Tóvári and J. Tímár. Alternative vascularization mechanisms in cancer: pathology and therapeutic implications. *Am. J. Pathol.*, 170(1):1–15, 2007. doi:10.2353/ajpath.2007.060302.

[51] M. Dominietto, M. Dobosz, S. Bürgi, A. Renner, G. Zahlmann, W. Scheuer and M. Rudin. Quantification of antiangiogenic treatment effects on tissue heterogeneity in glioma tumour xenograft model using a combination of DCE-MRI and 3D-ultramicroscopy. *Eur. Radiol.*, pages 1–9, 2016. doi: 10.1007/s00330-016-4629-3.

[52] A. W. El-Kareh and T. W. Secomb. A mathematical model for comparison of bolus injection, continuous infusion, and liposomal delivery of doxorubicin to tumor cells. *Neoplasia*, 2(4):325–38, 2000.

[53] L. M. Ellis. Mechanisms of action of bevacizumab as a component of therapy for metastatic colorectal cancer. *Semin. Oncol.*, 33(Supp. 10):S1–S7, 2006.

[54] R. Erber, A. Thurnher, A. D. Katsen, G. Groth, H. Kerger, H.-P. Hammes, M. D. Menger, A. Ullrich and P. Vajkoczy. Combined inhibition of VEGF and PDGF signaling enforces tumor vessel regression by interfering with pericyte-mediated endothelial cell survival mechanisms. *FASEB J.*, 18(2):338–40, 2004. doi:10.1096/fj.03-0271fje.

[55] B. L. Falcón, H. Hashizume, P. Koumoutsakos, J. Chou, J. V. Bready, A. Coxon, J. D. Oliner, D. M. McDonald, B. L. Falcon, H. Hashizume, P. Koumoutsakos, J. Chou, J. V. Brady, A. Coxon, J. D. Oliner and D. M. McDonald. Contrasting actions of selective inhibitors of angiopoietin-1 and angiopoietin-2 on the normalization of tumor blood vessels. *Am. J. Pathol.*, 175(5):2159–70, 2009. doi:10.2353/ajpath.2009.090391.

[56] N. Ferrara and A. P. Adamis. Ten years of anti-vascular endothelial growth factor therapy. *Nat. Rev. Drug Discov. Discov.*, 15:385–403, 2016. doi:10.1038/nrd.2015.17.

[57] N. Ferrara, H.-P. Gerber and J. LeCouter. The biology of VEGF and its receptors. *Nat. Med.*, 9(6):669–76, 2003. doi:10.1038/nm0603-669.

[58] N. Ferrara, K. J. Hillan and W. Novotny. Bevacizumab (Avastin), a humanized anti-VEGF monoclonal antibody for cancer therapy. *Biochem. Biophys. Res. Commun.*, 333(2):328–35, 2005. doi:10.1016/j.bbrc.2005.05.132.

[59] U. Fiedler, M. Scharpfenecker, S. Koidl, A. Hegen, V. Grunow, J. M. Schmidt, W. Kriz, G. Thurston and H. G. Augustin. The Tie-2 ligand angiopoietin-2 is stored in and rapidly released upon stimulation from endothelial cell Weibel-Palade bodies. *Blood*, 103(11):4150–4156, 2004. doi:10.1182/blood-2003-10-3685.

[60] J. Folkman, E. Merler, C. Abernathy and G. Williams. Isolation of a tumor factor responsible for angiogenesis. *J. Exp. Med.*, 133:275–288, 1971. doi:10.1084/jem.133.2.275.

[61] P. L. Fox and P. E. DiCorletto. Regulation of production of a Platelet-Derived Growth Factor-like protein by cultured bovine aortic endothelial cells. 308, 1984.

[62] N. Frances, L. Claret, R. Bruno and A. Iliadis. Tumor growth modeling from clinical trials reveals synergistic anticancer effect of the capecitabine and docetaxel combination in metastatic breast cancer. *Cancer Chemother. Pharmacol.*, 68(6):1413–1419, 2011. doi:10.1007/s00280-011-1628-6.

[63] J. Fuxe, S. Tabruyn, K. Colton, H. Zaid, A. Adams, P. Baluk, E. Lashnits, T. Morisada, T. Le, S. O'Brien, D. M. Epstein, G. Y. Koh and D. M. McDonald. Pericyte requirement for anti-leak action of angiopoietin-1 and vascular remodeling in sustained inflammation. *Am. J. Pathol.*, 178(6):2897–2909, 2011. doi:10.1016/j.ajpath.2011.02.008.

[64] D. I. Gabrilovich, T. Ishida, S. Nadaf, J. E. Ohm and D. P. Carbone. Antibodies to vascular endothelial growth factor enhance the efficacy of cancer immunotherapy by improving endogenous dendritic cell function. *Clin. Cancer Res.*, 5(10):2963–70, 1999.

[65] K. Gaengel, G. Genové, A. Armulik and C. Betsholtz. Endothelial-mural cell signaling in vascular development and angiogenesis. *Arterioscler. Thromb. Vasc. Biol.*, 29(5):630–8, 2009. doi:10.1161/ATVBAHA.107.161521.

[66] G. Gasparini, F. Torino, T. Ueno, S. Cascinu, T. Troiani, A. Ballestrero, R. Berardi, J. Shishido, A. Yoshizawa, Y. Mori, S. Nagayama, P. Morosini and M. Toi. A phase II study of neoadjuvant bevacizumab plus capecitabine and concomitant radiotherapy in patients with locally advanced rectal cancer. *Angiogenesis*, 15(1):141–50, 2012. doi:10.1007/s10456-011-9250-0.

[67] Y. Gazit, J. W. Baish, N. Safabakhsh, M. Leunig, L. T. Baxter and R. K. Jain. Fractal characteristics of tumor vascular architecture during tumor growth and regression. *Microcirculation*, 4(4):395–402, 1997.

[68] H. Gerhardt, M. Golding, M. Fruttiger, C. Ruhrberg, A. Lundkvist, A. Abramsson, M. Jeltsch, C. Mitchell, K. Alitalo, D. Shima and C. Betsholtz. VEGF guides angiogenic sprouting utilizing endothelial tip cell filopodia. *J. Cell Biol.*, 161(6):1163–77, 2003. doi:10.1083/jcb.200302047.

[69] P. Gerlee. The model muddle: in search of tumor growth laws. *Cancer Res.*, 73(8):2407–11, 2013. doi:10.1158/0008-5472.CAN-12-4355.

[70] S. Goel, D. Duda, L. Xu and L. Munn. Normalization of the vasculature for treatment of cancer and other diseases. *Physiol Rev*, 91(3):1071–1121, 2011. doi:10.1152/physrev.00038.2010.

[71] V. L. Goodman, E. P. Rock, R. Dagher, R. P. Ramchandani, S. Abraham, J. V. S. Gobburu, B. P. Booth, S. L. Verbois, D. E. Morse, C. Y. Liang, N. Chidambaram, J. X. Jiang, S. Tang, K. Mahjoob, R. Justice and R. Pazdur. Approval summary: sunitinib for the treatment of imatinib refractory or intolerant gastrointestinal stromal tumors and advanced renal cell carcinoma. *Clin. Cancer Res.*, 13(5):1367–73, 2007. doi:10.1158/1078-0432.CCR-06-2328.

[72] P. Hahnfeldt, D. Panigrahy, J. Folkman and L. Hlatky. Tumor development under angiogenic signaling: a dynamical theory of tumor growth, treatment response, and postvascular dormancy. *Cancer Res.*, 59(19):4770–5, 1999.

[73] D. Hanahan and R. A. Weinberg. The hallmarks of cancer. *Cell*, 100:57–70, 2000.

[74] W. Hao, L. S. Schlesinger and A. Friedman. Modeling granulomas in response to infection in the lung. *PLoS One*, 11(3):e0148738, 2016. doi: 10.1371/journal.pone.0148738.

[75] A. L. Harris. Hypoxia–a key regulatory factor in tumour growth. *Nat. Rev. Cancer*, 2(1):38–47, 2002. doi:10.1038/nrc704.

[76] L. B. Harrison, M. Chadha, R. J. Hill, K. Hu and D. Shasha. Impact of tumor hypoxia and anemia on radiation therapy outcomes. *Oncologist*, 7(6):492–508, 2002. doi:10.1634/theoncologist.7-6-492.

[77] H. Hashizume, P. Baluk, S. Morikawa, J. W. McLean, G. Thurston, S. Roberge, R. K. Jain and D. M. McDonald. Openings between defective endothelial cells explain tumor vessel leakiness. *Am. J. Pathol.*, 156(4):1363–80, 2000. doi:10.1016/S0002-9440(10)65006-7.

[78] W. K. Hastings. Monte Carlo sampling methods using Markov chains and their applications. *Biometrika*, 57(1):97–109, 1970. doi:10.1093/biomet/57.1.97.

[79] A. Hegen, S. Koidl, K. Weindel, D. Marmé, H. G. Augustin and U. Fiedler. Expression of angiopoietin-2 in endothelial cells is controlled by positive and negative regulatory promoter elements. *Arterioscler. Thromb. Vasc. Biol.*, 24(10):1803–9, 2004. doi:10.1161/01.ATV.0000140819.81839.0e.

[80] P. Hinow, P. Gerlee, L. J. McCawley, V. Quaranta, M. Ciobanu, S. Wang, J. M. Graham, B. P. Ayati, J. Claridge, K. R. Swanson, M. Loveless and A. R. A. Anderson. A spatial model of tumor-host interaction: application of chemotherapy. *Math. Biosci. Eng.*, 6(3):521–46, 2009.

[81] M. Höckel and P. Vaupel. Tumor hypoxia: definitions and current clinical, biologic, and molecular aspects. *J. Natl. Cancer Inst.*, 93:266–276, 2001. doi:10.1093/jnci/93.4.266.

[82] J. Holash, P. C. Maisonpierre, D. Compton, P. Boland, C. R. Alexander, D. Zagzag, G. D. Yancopoulos and S. J. Wiegand. Vessel cooption, regression, and growth in tumors mediated by angiopoietins and VEGF. *Science (80-.).*, 284(5422):1994–8, 1999.

[83] A. C. Hooker, C. E. Staatz and M. O. Karlsson. Conditional weighted residuals (CWRES): a model diagnostic for the FOCE method. *Pharm. Res.*, 24(12):2187–97, 2007. doi:10.1007/s11095-007-9361-x.

[84] Y. Huang, S. Goel, D. G. Duda, D. Fukumura and R. K. Jain. Vascular normalization as an emerging strategy to enhance cancer immunotherapy. *Cancer Res.*, 73(10):2943–8, 2013. doi:10.1158/0008-5472.CAN-12-4354.

[85] Y. Huang, J. Yuan, E. Righi, W. S. Kamoun, M. Ancukiewicz, J. Nezivar, M. Santosuosso, J. D. Martin, M. R. Martin, F. Vianello, P. Leblanc, L. L. Munn, P. Huang, D. G. Duda, D. Fukumura, R. K. Jain and M. C. Poznansky. Vascular normalizing doses of antiangiogenic treatment reprogram the immunosuppressive tumor microenvironment and enhance immunotherapy. *Proc. Natl. Acad. Sci. U. S. A.*, 109(43):17561–6, 2012. doi:10.1073/pnas.1215397109.

[86] L. G. Hutchinson, E. A. Gaffney, P. K. Maini, J. Wagg, A. Phipps and H. M. Byrne. Vascular phenotype identification and anti-angiogenic treatment recommendation: A pseudo-multiscale mathematical model of angiogenesis. *J. Theor. Biol.*, 398:162–180, 2016. doi:10.1016/j.jtbi.2016.03.002.

[87] L. G. Hutchinson, H. Mueller, E. A. Gaffney, P. K. Maini, J. Wagg, A. Phipps, C. Boetsch, H. M. Byrne and B. Ribba. Modeling longitudinal preclinical tumor size data to identify transient dynamics in tumor response to antiangiogenic drugs. *CPT Pharmacometrics Syst. Pharmacol.*, 5(11):636–645, 2016. doi:10.1002/PSP4.12142.

[88] T. Inai, M. Mancuso, H. Hashizume, F. Baffert, A. Haskell, P. Baluk, D. D. Hu-Lowe, D. R. Shalinsky, G. Thurston, G. D. Yancopoulos and D. M. McDonald. Inhibition of Vascular Endothelial Growth Factor (VEGF) signaling in cancer causes loss of endothelial fenestrations, regression of tumor vessels, and appearance of basement membrane ghosts. *Am. J. Pathol.*, 165(1):35–52, 2004. doi:10.1016/S0002-9440(10)63273-7.

[89] M. Jaberi-Douraki, M. Pietropaolo and A. Khadra. Continuum model of T-cell avidity: Understanding autoreactive and regulatory T-cell responses in type 1 diabetes. *J. Theor. Biol.*, 383:93–105, 2015. doi:10.1016/j.jtbi.2015.07.032.

[90] T. Jackson and X. Zheng. A cell-based model of endothelial cell migration, proliferation and maturation during corneal angiogenesis. *Bull. Math. Biol.*, 72(4):830–868, 2010. doi:10.1007/s11538-009-9471-1.

[91] T. L. Jackson and X. Zheng. *Modeling tumor vasculature*. Springer New York, New York, NY, 2012. ISBN 978-1-4614-0051-6. doi:10.1007/978-1-4614-0052-3.

[92] H. V. Jain and T. L. Jackson. A hybrid model of the role of VEGF binding in endothelial cell migration and capillary formation. *Front. Oncol.*, 3:102, 2013. doi:10.3389/fonc.2013.00102.

[93] H. V. Jain, J. E. Nör and T. L. Jackson. Quantification of endothelial cell-targeted anti Bcl-2 therapy and its suppression of tumor growth and vascularization. *Mol. Cancer Ther.*, 8(10):2926–2936, 2009. doi:10.1158/1535-7163.MCT-08-1223.

[94] R. K. Jain. Normalizing tumor vasculature with anti-angiogenic therapy: a new paradigm for combination therapy. *Nat. Med.*, 7(9):987–989, 2001. doi:10.1038/nm0901-987.

[95] R. K. Jain. Normalization of tumor vasculature: an emerging concept in antiangiogenic therapy. *Science (80-.).*, 307(5706):58–62, 2005. doi:10.1126/science.1104819.

[96] Y. Kienast, C. Klein, W. Scheuer, R. Raemsch, E. Lorenzon, D. Bernicke, F. Herting, S. Yu, H. H. The, L. Martarello, C. Gassner, K.-G. G. Stubenrauch, K. Munro, H. G. Augustin and M. Thomas. Ang-2-VEGF-A CrossMab, a novel bispecific human IgG1 antibody blocking VEGF-A and Ang-2 functions simultaneously, mediates potent antitumor, antiangiogenic, and antimetastatic efficacy. *Clin. Cancer Res.*, 19(24):6730–6740, 2013. doi:10.1158/1078-0432.CCR-13-0081.

[97] E. A. Kleibeuker, A. W. Griffioen, H. M. Verheul, B. J. Slotman and V. L. Thijssen. Drug Resistance Updates Combining angiogenesis inhibition and radiotherapy: A double-edged sword. *Drug Resist. Updat.*, 15:173–182, 2012. doi:10.1016/j.drup.2012.04.002.

[98] N. Kopell and L. N. Howard. Plane wave solutions to reaction-diffusion equations. *Stud. Appl. Math.*, 52(4):291–328, 1973. doi:10.1002/sapm1973524291.

[99] E. Kuhn and M. Lavielle. Coupling a stochastic approximation version of EM with an MCMC procedure. *ESAIM Probab. Stat.*, 8:115–131, 2004. doi: 10.1051/ps:2004007.

[100] E. Kuhn and M. Lavielle. Maximum likelihood estimation in nonlinear mixed effects models. *Comput. Stat. Data Anal.*, 49(4):1020–1038, 2005. doi: 10.1016/j.csda.2004.07.002.

[101] M. Lavielle. Mixed effects models for the population approach: Models, tasks, methods and tools. chapter 9, pages 231–276. CRC Press, Boca Raton, 1 edition, 2015. ISBN 978-1-4822-2651-5.

[102] D. W. Leung, G. Cachianes, W. J. Kuang, D. V. Goeddel and N. Ferrara. Vascular endothelial growth factor is a secreted angiogenic mitogen. *Science*, 246(4935):1306–9, 1989. doi:10.1126/science.2479986.

[103] H. A. Levine, B. D. Sleeman and M. Nilsen-Hamilton. A mathematical model for the roles of pericytes and macrophages in the initiation of angiogenesis. I. The role of protease inhibitors in preventing angiogenesis. *Math. Biosci.*, 168(1):77–115, 2000.

[104] H. A. Levine, B. D. Sleeman and M. Nilsen-Hamilton. Mathematical modeling of the onset of capillary formation initiating angiogenesis. *J. Math. Biol.*, 42(3):195–238, 2001.

[105] F. Lignet, S. Benzekry, S. Wilson, F. Billy, O. Saut, M. Tod, B. You, A. Adda Berkane, S. Kassour, M. X. Wei, E. Grenier and B. Ribba. Theoretical investigation of the efficacy of antiangiogenic drugs combined to chemotherapy in xenografted mice. *J. Theor. Biol.*, 320:86–99, 2013. doi: 10.1016/j.jtbi.2012.12.013.

[106] E. Limpert, W. A. Stahel and M. Abbt. Log-normal Distributions across the Sciences: Keys and Clues. *Bioscience*, 51(5):341–352, 2001. doi:10.1641/0006-3568.

[107] Y. S. Lin, C. Nguyen, J.-L. Mendoza, E. Escandon, D. Fei, Y. G. Meng and N. B. Modi. Preclinical pharmacokinetics, interspecies scaling, and tissue distribution of a humanized monoclonal antibody against vascular endothelial growth factor. *J. Pharmacol. Exp. Ther.*, 288(1):371–378, 1999.

[108] P. Lindahl, B. R. Johansson, P. Levéen and C. Betsholtz. Pericyte loss and microaneurysm formation in PDGF-B-deficient mice. *Science (80-.).*, 277(5323):242–245, 1997. doi:10.1126/science.277.5323.242.

[109] G. Liu, A. a. Qutub, P. Vempati, F. Mac Gabhann and A. S. Popel. Module-based multiscale simulation of angiogenesis in skeletal muscle. *Theor. Biol. Med. Model.*, 8(1):6, 2011. doi:10.1186/1742-4682-8-6.

[110] L. Ljung and T. Glad. On global identifiability for arbitrary model parametrizations. *Automatica*, 30(2):265–276, 1994. doi:10.1016/0005-1098(94)90029-9.

[111] M. Lorger and B. Felding-Habermann. Capturing changes in the brain microenvironment during initial steps of breast cancer brain metastasis. *Am. J. Pathol.*, 176(6):2958–2971, 2010. doi:10.2353/ajpath.2010.090838.

[112] J.-F. Lu, R. Bruno, S. Eppler, W. Novotny, B. Lum and J. Gaudreault. Clinical pharmacokinetics of bevacizumab in patients with solid tumors. *Cancer Chemother. Pharmacol.*, 62(5):779–786, 2008. doi:10.1007/s00280-007-0664-8.

[113] F. Mac Gabhann and A. S. Popel. Model of competitive binding of vascular endothelial growth factor and placental growth factor to VEGF receptors on endothelial cells. *Am. J. Physiol. Heart Circ. Physiol.*, 286(1):H153–64, 2004. doi:10.1152/ajpheart.00254.2003.

[114] P. C. Maisonpierre. Angiopoietin-2, a natural antagonist for Tie2 that disrupts in vivo angiogenesis. *Science (80-.).*, 277(5322):55–60, 1997. doi:10.1126/science.277.5322.55.

[115] H. Malchow, S. V. Petrovski and E. Venturino. *Spatiotemporal Patterns in Ecology and Epidemiology*. Chapman & Hall/CRC, 1 edition, 2008. ISBN 1-58488-674-9.

[116] N. V. Mantzaris, S. Webb and H. G. Othmer. *Mathematical modeling of tumor-induced angiogenesis*, volume 187. Springer-Verlag, 2003. ISBN 0028500302622. doi:10.1007/s00285-003-0262-2.

[117] S. Marino, I. B. Hogue, C. J. Ray and D. E. Kirschner. A methodology for performing global uncertainty and sensitivity analysis in systems biology. *J. Theor. Biol.*, 254(1):178–96, 2008. doi:10.1016/j.jtbi.2008.04.011.

[118] S. Matsumoto, S. Batra, K. Saito, H. Yasui, R. Choudhuri, C. Gadisetti, S. Subramanian, N. Devasahayam, J. P. Munasinghe, J. B. Mitchell and M. C. Krishna. Antiangiogenic agent sunitinib transiently increases tumor oxygenation and suppresses cycling hypoxia. *Cancer Res.*, 71(20), 2011.

[119] K. Matsushita, M. Yamakuchi, C. N. Morrell, M. Ozaki, B. O'Rourke, K. Irani and C. J. Lowenstein. Vascular endothelial growth factor regulation of Weibel-Palade-body exocytosis. *Blood*, 105(1):207–14, 2005. doi:10.1182/blood-2004-04-1519.

[120] M. C. McGee, J. B. Hamner, R. F. Williams, S. F. Rosati, T. L. Sims, C. Y. Ng, M. W. Gaber, C. Calabrese, J. Wu, A. C. Nathwani, C. Duntsch, T. E. Merchant and A. M. Davidoff. Improved Intratumoral Oxygenation Through Vascular Normalization Increases Glioma Sensitivity to Ionizing Radiation. *Int. J. Radiat. Oncol.*, 76(5):1537–1545, 2010. doi:10.1016/j.ijrobp.2009.12.010.

[121] M. Melter, M. E. Reinders, M. Sho, S. Pal, C. Geehan, M. D. Denton, D. Mukhopadhyay and D. M. Briscoe. Ligation of CD40 induces the expression of vascular endothelial growth factor by endothelial cells and monocytes and promotes angiogenesis in vivo. *Blood*, 96(12):3801–8, 2000.

[122] F. Milde, S. Lauw, P. Koumoutsakos and M. L. Iruela-Arispe. The mouse retina in 3D: quantification of vascular growth and remodeling. *Integr. Biol.*, 5(12):1426–38, 2013. doi:10.1039/c3ib40085a.

[123] D. W. Miles, A. Chan, L. Y. Dirix, J. Cortés, X. Pivot, P. Tomczak, T. Delozier, J. H. Sohn, L. Provencher, F. Puglisi, N. Harbeck, G. G. Steger, A. Schneeweiss, A. M. Wardley, A. Chlistalla and G. Romieu. Phase III study of bevacizumab plus docetaxel compared with placebo plus docetaxel for the first-line treatment of human epidermal growth factor receptor 2-negative metastatic breast cancer. *J. Clin. Oncol.*, 28(20):3239–47, 2010. doi: 10.1200/JCO.2008.21.6457.

[124] H. Mizutani, S. Tada-Oikawa, Y. Hiraku, M. Kojima and S. Kawanishi. Mechanism of apoptosis induced by doxorubicin through the generation of hydrogen peroxide. *Life Sci.*, 76(13):1439–1453, 2005. doi:10.1016/j.lfs.2004.05.040.

[125] B. J. Monk, A. Poveda, I. Vergote, F. Raspagliesi, K. Fujiwara, D.-S. Bae, A. Oaknin, I. Ray-Coquard, D. M. Provencher, B. Y. Karlan, C. Lhommé, G. Richardson, D. G. Rincón, R. L. Coleman, T. J. Herzog, C. Marth, A. Brize, M. Fabbro, A. Redondo, A. Bamias, M. Tassoudji, L. Navale, D. J. Warner and A. M. Oza. Anti-angiopoietin therapy with trebananib for recurrent ovarian cancer (TRINOVA-1): a randomised, multicentre, double-blind, placebo-controlled phase 3 trial. *Lancet. Oncol.*, 15(8):799–808, 2014. doi: 10.1016/S1470-2045(14)70244-X.

[126] A. Montero, F. Fossella, G. Hortobagyi and V. Valero. Docetaxel for treatment of solid tumours: a systematic review of clinical data. *Lancet Oncol.*, 6(4):229–239, 2005. doi:10.1016/S1470-2045(05)70094-2.

[127] D. Mould, A.-C. Walz, T. Lave, J. Gibbs and B. Frame. Developing exposure/response models for anticancer drug treatment: special considerations. *CPT Pharmacometrics Syst. Pharmacol.*, 4(1):12–27, 2015. doi: 10.1002/psp4.16.

[128] A. L. Myers, R. F. Williams, C. Y. Ng, J. E. Hartwich and A. M. Davidoff. Bevacizumab-induced tumor vessel remodeling in rhabdomyosarcoma xenografts increases the effectiveness of adjuvant ionizing radiation. *J. Pediatr. Surg.*, 45(6):1080–5, 2010. doi:10.1016/j.jpedsurg.2010.02.068.

[129] H. Oh, H. Takagi, K. Suzuma, A. Otani, M. Matsumura and Y. Honda. Hypoxia and Vascular Endothelial Growth Factor selectively up-regulate angiopoietin-2 in bovine microvascular endothelial cells. *J. Biol. Chem.*, 274(22):15732–15739, 1999. doi:10.1074/jbc.274.22.15732.

[130] M. E. Orme and M. A. J. Chaplain. A mathematical model of the first steps of tumour-related angiogenesis: Capillary sprout formation and secondary branching. *Math. Med. Biol.*, 13(2):73–98, 1996. doi: 10.1093/imammb/13.2.73.

[131] J. O'Shaughnessy, D. Miles, S. Vukelja, V. Moiseyenko, J.-P. Ayoub, G. Cervantes, P. Fumoleau, S. Jones, W.-Y. Lui, L. Mauriac, C. Twelves, G. Van Hazel, S. Verma and R. Leonard. Superior survival with capecitabine plus docetaxel combination therapy in anthracycline-pretreated patients with advanced breast cancer: phase III trial results. *J. Clin. Oncol.*, 20(12):2812–23, 2002.

[132] Z. K. Otrock, R. A. R. Mahfouz, J. A. Makarem and A. I. Shamseddine. Understanding the biology of angiogenesis: Review of the most important molecular mechanisms. *Blood Cells, Mol. Dis.*, 39(2):212–220, 2007. doi: 10.1016/j.bcmd.2007.04.001.

[133] A. Ouerdani, H. Struemper, A. Suttle, D. Ouellet and B. Ribba. Preclinical modeling of tumor growth and angiogenesis inhibition to describe pazopanib clinical effects in renal cell carcinoma. *CPT Pharmacometrics Syst. Pharmacol.*, 4(11):660–668, 2015. doi:10.1002/psp4.12001.

[134] M. R. Owen, T. Alarcón, P. K. Maini and H. M. Byrne. Angiogenesis and vascular remodelling in normal and cancerous tissues. *J. Math. Biol.*, 58(4-5):689–721, 2009. doi:10.1007/s00285-008-0213-z.

[135] T. P. Padera, B. R. Stoll, J. B. Tooredman, D. Capen, E. di Tomaso and R. K. Jain. Pathology: Cancer cells compress intratumour vessels. *Nature*, 427(6976):695–695, 2004. doi:10.1038/427695a.

[136] S. W. Park, J.-H. Yun, J. H. Kim, K.-W. Kim, C.-H. Cho and J. H. Kim. Angiopoietin 2 induces pericyte apoptosis via $\alpha 3\beta 1$ integrin signaling in diabetic retinopathy. *Diabetes*, 63(9):3057–3068, 2014. doi:10.2337/db13-1942.

[137] S. M. Peirce. Computational and mathematical modeling of angiogenesis. *Microcirculation*, 15(8):739–51, 2008. doi:10.1080/10739680802220331.

[138] S. M. Peirce, E. J. Van Gieson and T. C. Skalak. Multicellular simulation predicts microvascular patterning and in silico tissue assembly. *FASEB J.*, 18:731–733, 2004. doi:10.1096/fj.03-0933fje.

[139] H. Perfahl, H. M. Byrne, T. Chen, V. Estrella, T. Alarcón, A. Lapin, R. a. Gatenby, R. J. Gillies, M. C. Lloyd, P. K. Maini, M. Reuss and M. R. Owen. Multiscale modelling of vascular tumour growth in 3D: the roles of domain size and boundary conditions. *PLoS One*, 6(4):e14790–e14790, 2011. doi: 10.1371/journal.pone.0014790.

[140] G. C. Pillai, F. Mentré and J.-L. Steimer. Non-linear mixed effects modeling from methodology and software development to driving implementation in drug development science. *J. Pharmacokinet. Pharmacodyn.*, 32(2):161–183, 2005. doi:10.1007/s10928-005-0062-y.

[141] V. K. Piotrovsky. Population pharmacodynamic and pharmacokinetic modeling via mixed effects. *Curr. Opin. Drug Discov. Devel.*, 3(3):314–30, 2000.

[142] M. Plank and B. Sleeman. A reinforced random walk model of tumour angiogenesis and antiangiogenic strategies. *Math. Med. Biol.*, 20:135–181, 2003.

[143] M. J. Plank, B. D. Sleeman and P. F. Jones. A mathematical model of tumour angiogenesis, regulated by vascular endothelial growth factor and the angiopoietins. *J. Theor. Biol.*, 229(4):435–54, 2004. doi:10.1016/j.jtbi.2004.04.012.

[144] H. Pohjanpalo. System identifiability based on the power series expansion of the solution. *Math. Biosci.*, 41(1-2):21–33, 1978. doi:10.1016/0025-5564(78)90063-9.

[145] D. Posada and T. R. Buckley. Model selection and model averaging in phylogenetics: advantages of akaike information criterion and bayesian approaches over likelihood ratio tests. *Syst. Biol.*, 53(5):793–808, 2004. doi: 10.1080/10635150490522304.

[146] S. A. Prokopiou. *Integrative modelling of angiogenesis in the bovine corpus luteum*. Ph.D. thesis, University of Nottingham, 2013.

[147] A. a. Qutub, F. Mac Gabhann, E. Karagiannis, P. Vempati and A. S. Popel. Multiscale models of angiogenesis: integration of molecular mechanisms with cell- and organ-level models. *IEEE Eng. Med. Biol. Mag.*, 28(2):14–31, 2009. doi:10.1109/MEMB.2009.931791.

[148] E. Raymond, L. Dahan, J.-L. Raoul, Y.-J. Bang, I. Borbath, C. Lombard-Bohas, J. Valle, P. Metrakos, D. Smith, A. Vinik, J.-S. Chen, D. Hörsch, P. Hammel, B. Wiedenmann, E. Van Cutsem, S. Patyna, D. R. Lu, C. Blanckmeister, R. Chao and P. Ruszniewski. Sunitinib Malate for the treatment of pancreatic neuroendocrine tumors. *N. Engl. J. Med.*, 364(6):501–513, 2011. doi:10.1056/NEJMoa1003825.

[149] B. Ribba, N. H. Holford, P. Magni, I. Trocóniz, I. Gueorguieva, P. Girard, C. Sarr, M. Elishmereni, C. Kloft and L. E. Friberg. A review of mixed-effects models of tumor growth and effects of anticancer drug treatment used in population analysis. *CPT Pharmacometrics Syst. Pharmacol.*, 3(5):1–10, 2014. doi:10.1038/psp.2014.12.

[150] B. Ribba, G. Kaloshi, M. Peyre, D. Ricard, V. Calvez, M. Tod, B. Cajavec-Bernard, A. Idbaih, D. Psimaras, L. Dainese, J. Pallud, S. Cartalat-Carel, J.-Y. Delattre, J. Honnorat, E. Grenier and F. Ducray. A tumor growth inhibition model for low-grade glioma treated with chemotherapy or radiotherapy. *Clin. Cancer Res.*, 18(18):5071–80, 2012. doi:10.1158/1078-0432.CCR-12-0084.

[151] M. Rocchetti, M. Germani, F. Del Bene, I. Poggesi, P. Magni, E. Pesenti and G. De Nicolao. Predictive pharmacokinetic-pharmacodynamic modeling of tumor growth after administration of an anti-angiogenic agent, bevacizumab, as single-agent and combination therapy in tumor xenografts. *Cancer Chemother. Pharmacol.*, 71(5):1147–57, 2013. doi:10.1007/s00280-013-2107-z.

[152] C. Ruhrberg, H. Gerhardt, M. Golding, R. Watson, S. Ioannidou, H. Fujisawa, C. Betsholtz and D. T. Shima. Spatially restricted patterning cues provided by heparin-binding VEGF-A control blood vessel branching morphogenesis. *Genes Dev.*, 16(20):2684–98, 2002. doi:10.1101/gad.242002.

[153] M. Scharpfenecker, U. Fiedler, Y. Reiss and H. G. Augustin. The Tie-2 ligand angiopoietin-2 destabilizes quiescent endothelium through an internal autocrine loop mechanism. *J. Cell Sci.*, 118(Pt 4):771–80, 2005. doi: 10.1242/jcs.01653.

[154] M. Scianna, C. G. Bell and L. Preziosi. A review of mathematical models for the formation of vascular networks. *J. Theor. Biol.*, 333:174–209, 2013. doi:10.1016/j.jtbi.2013.04.037.

[155] G. Serini, D. Ambrosi, E. Giraudo, A. Gamba, L. Preziosi and F. Bussolino. Modeling the early stages of vascular network assembly. *EMBO J.*, 22(8):1771–1779, 2003.

[156] J. Sherratt. Periodic travelling waves in cyclic predator-prey systems. *Ecol. Lett.*, 4(1):30–37, 2001. doi:10.1046/j.1461-0248.2001.00193.x.

[157] J. A. Sherratt. Invading wave fronts and their oscillatory wakes are linked by a modulated travelling phase resetting wave. *Phys. D Nonlinear Phenom.*, 117(1-4):145–166, 1998. doi:10.1016/S0167-2789(97)00317-5.

[158] L. M. Sherwood, E. E. Parris and J. Folkman. Tumor angiogenesis: therapeutic implications. *N. Engl. J. Med.*, 285(21):1182–1186, 1971. doi:10.1056/NEJM197111182852108.

[159] M. Simeoni, P. Magni, C. Cammia, G. De Nicolao, V. Croci, E. Pesenti, M. Cermani, I. Poggesi and M. Rocchetti. Predictive pharmacokinetic-pharmacodynamic modeling of tumor growth kinetics in xenograft models after administration of anticancer agents. *Cancer Res.*, 64(3):1094–1101, 2004. doi:10.1158/0008-5472.CAN-03-2524.

[160] B. Speed, H.-Z. Bu, W. F. Pool, G. W. Peng, E. Y. Wu, S. Patyna, C. Bello and P. Kang. Pharmacokinetics, distribution, and metabolism of [14C]sunitinib in rats, monkeys, and humans. *Drug Metab. Dispos.*, 40(3):539–55, 2012. doi:10.1124/dmd.111.042853.

[161] I. J. Stamper, M. R. Owen, P. K. Maini and H. M. Byrne. Oscillatory dynamics in a model of vascular tumour growth–implications for chemotherapy. *Biol. Direct*, 5(1):27, 2010. doi:10.1186/1745-6150-5-27.

[162] A. Stein, W. Wang, A. A. Carter, O. Chiparus, N. Hollaender, H. Kim, R. J. Motzer and C. Sarr. Dynamic tumor modeling of the doseresponse relationship for everolimus in metastatic renal cell carcinoma using data from the phase 3 RECORD-1 trial. *BMC Cancer*, 12(1):311, 2012. doi:10.1186/1471-2407-12-311.

[163] A. Stéphanou, S. R. McDougall, A. R. A. Anderson and M. A. J. Chaplain. Mathematical modelling of flow in 2D and 3D vascular networks: Applications to anti-angiogenic and chemotherapeutic drug strategies. *Math. Comput. Model.*, 41(10):1137–1156, 2005. doi:10.1016/j.mcm.2005.05.008.

[164] C. L. Stokes and D. A. Lauffenburger. Analysis of the roles of microvessel endothelial cell random motility and chemotaxis in angiogenesis. *J. Theor. Biol.*, 152(3):377–403, 1991. doi:10.1016/S0022-5193(05)80201-2.

[165] M. Stroh, D. Carlile, C.-C. Li, J. Wagg, B. Ribba, S. Ramanujan, J. Jin, J. Xu, J.-E. Charoin, Z.-X. Xhu, P. Morcos, J. Davis and A. Phipps. Challenges and opportunities for quantitative clinical pharmacology in cancer immunotherapy: something old, something new, something borrowed, and something blue. *CPT Pharmacometrics Syst. Pharmacol.*, 4(9):495–497, 2015. doi:10.1002/psp4.12014.

[166] C. Sundberg, M. Kowanetz, L. F. Brown, M. Detmar and H. F. Dvorak. Stable expression of angiopoietin-1 and other markers by cultured pericytes: phenotypic similarities to a subpopulation of cells in maturing vessels during later stages of angiogenesis in vivo. *Lab. Invest.*, 82(4):387–401, 2002.

[167] C. Suri, P. F. Jones, S. Patan, S. Bartunkova, P. C. Maisonpierre, S. Davis, T. N. Sato and G. D. Yancopoulos. Requisite Role of Angiopoietin-1, a Ligand for the TIE2 Receptor, during Embryonic Angiogenesis. *Cell*, 87(7):1171–1180, 1996. doi:10.1016/S0092-8674(00)81813-9.

[168] U. Tateishi, H. Nishihara, E. Tsukamoto, T. Morikawa, N. Tamaki and K. Miyasaka. Lung tumors evaluated with FDG-PET and dynamic CT: the relationship between vascular density and glucose metabolism. *J. Comput. Assist. Tomogr.*, 26(2):185–190, 2002.

[169] M. Thomas, Y. Kienast, W. Scheuer, M. Bähner, K. Kaluza, C. Gassner, F. Herting, U. Brinkmann, S. Seeber, A. Kavlie, M. Welschof, S. Ries, K. M. Weidner, J. T. Regula and C. Klein. A novel angiopoietin-2 selective fully human antibody with potent anti-tumoral and anti-angiogenic efficacy and superior side effect profile compared to Pan-Angiopoietin-1/-2 inhibitors. *PLoS One*, 8(2):e54923, 2013. doi:10.1371/journal.pone.0054923.

[170] R. H. Thomlinson and L. H. Gray. The histological structure of some human lung cancers and the possible implications for radiotherapy. *Br. J. Cancer*, 9(4):539–49, 1955.

[171] S. M. Tolaney, Y. Boucher, D. G. Duda, J. D. Martin, G. Seano, M. Ancukiewicz, W. T. Barry, S. Goel, J. Lahdenrata, S. J. Isakoff, E. D. Yeh, S. R. Jain, M. Golshan, J. Brock, M. Snuderl, E. P. Winer, I. E. Krop, R. K. Jain, H. Chen and G. W. Sledge. Role of vascular density and normalization in response to neoadjuvant bevacizumab and chemotherapy in breast cancer patients. *Proc. Natl. Acad. Sci.*, 112(46):14325–14330, 2015. doi:10.1073/pnas.1518808112.

[172] R. T. Tong, Y. Boucher, S. V. Kozin, F. Winkler, D. J. Hicklin and R. K. Jain. Vascular normalization by vascular endothelial growth factor receptor 2 blockade induces a pressure gradient across the vasculature and improves drug penetration in tumors. *Cancer Res.*, 64(11):3731–6, 2004. doi:10.1158/0008-5472.CAN-04-0074.

[173] K. Turetschek, A. Preda, V. Novikov, R. C. Brasch, H. J. Weinmann, P. Wunderbaldinger and T. P. L. Roberts. Tumor microvascular changes in antiangiogenic treatment: assessment by magnetic resonance contrast media of different molecular weights. *J. Magn. Reson. Imaging*, 20(1):138–44, 2004. doi:10.1002/jmri.20049.

[174] P. H. Van Der Graaf and N. Benson. Systems Pharmacology: Bridging systems biology and Pharmacokinetics-Pharmacodynamics (PKPD) in Drug Discovery and Development. *Pharm. Res.*, 28:1460–1464, 2011. doi:10.1007/s11095-011-0467-9.

[175] A. A. Van der Veldt, M. Lubberink, I. Bahce, M. Walraven, M. P. de Boer, H. N. Greuter, N. H. Hendrikse, J. Eriksson, A. D. Windhorst, P. E. Postmus, H. M. Verheul, E. H. Serné, A. A. Lammertsma and E. F. Smit. Rapid decrease in delivery of chemotherapy to tumors after anti-VEGF therapy: implications for scheduling of anti-angiogenic drugs. *Cancer Cell*, 21(1):82–91, 2012. doi: 10.1016/j.ccr.2011.11.023.

[176] L. von Baumgarten, D. Brucker, A. Tirniceru, Y. Kienast, S. Grau, S. Burgold, J. Herms and F. Winkler. Bevacizumab has differential and dose-dependent effects on glioma blood vessels and tumor cells. *Clin. Cancer Res.*, 17(19):6192–205, 2011. doi:10.1158/1078-0432.CCR-10-1868.

[177] T. Voron, O. Colussi, E. Marcheteau, S. Pernot, M. Nizard, A.-L. Pointet, S. Latreche, S. Bergaya, N. Benhamouda, C. Tanchot, C. Stockmann, P. Combe, A. Berger, F. Zinzindohoue, H. Yagita, E. Tartour, J. Taieb and M. Terme. VEGF-A modulates expression of inhibitory checkpoints on CD8+ T cells in tumors. *J. Exp. Med.*, 212(2):139–48, 2015. doi: 10.1084/jem.20140559.

[178] S. Wakui, K. Yokoo, T. Muto, Y. Suzuki, H. Takahashi, M. Furusato, H. Hano, H. Endou and Y. Kanai. Localization of Ang-1, -2, Tie-2, and VEGF expression at endothelial-pericyte interdigitation in rat angiogenesis. *Lab. Invest.*, 86(11):1172–84, 2006. doi:10.1038/labinvest.3700476.

[179] D. Wang, R. E. Lehman, D. B. Donner, M. R. Matli, R. S. Warren and M. L. Welton. Expression and endocytosis of VEGF and its receptors in human colonic vascular endothelial cells. *Am. J. Physiol. - Gastrointest. Liver Physiol.*, 282(6):G1088–G1096, 2002.

[180] M. Welter, K. Bartha and H. Rieger. Vascular remodelling of an arteriovenous blood vessel network during solid tumour growth. *J. Theor. Biol.*, 259(3):405–22, 2009. doi:10.1016/j.jtbi.2009.04.005.

[181] S. M. Wilhelm, C. Carter, L. Tang, D. Wilkie, A. McNabola, H. Rong, C. Chen, X. Zhang, P. Vincent, M. McHugh, Y. Cao, J. Shujath, S. Gawlak, D. Eveleigh, B. Rowley, L. Liu, L. Adnane, M. Lynch, D. Auclair, I. Taylor, R. Gedrich, A. Voznesensky, B. Riedl, L. E. Post, G. Bollag and P. A. Trail. BAY 43-9006 exhibits broad spectrum oral antitumor activity and targets the RAF/MEK/ERK pathway and receptor tyrosine kinases involved in tumor progression and angiogenesis. *Cancer Res.*, 64(19):7099–109, 2004. doi: 10.1158/0008-5472.CAN-04-1443.

[182] C. G. Willett, Y. Boucher, E. di Tomaso, D. G. Duda, L. L. Munn, R. T. Tong, D. C. Chung, D. V. Sahani, S. P. Kalva, S. V. Kozin, M. Mino, K. S. Cohen, D. T. Scadden, A. C. Hartford, A. J. Fischman, J. W. Clark, D. P. Ryan, A. X. Zhu, L. S. Blaszkowsky, H. X. Chen, P. C. Shellito, G. Y. Lauwers and R. K. Jain. Direct evidence that the VEGF-specific antibody bevacizumab has antivascular effects in human rectal cancer. *Nat. Med.*, 10(2):145–147, 2009.

[183] C. G. Willett, Y. Boucher, D. G. Duda, E. di Tomaso, L. L. Munn, R. T. Tong, S. V. Kozin, L. Petit, R. K. Jain, D. C. Chung, D. V. Sahani, S. P. Kalva, K. S. Cohen, D. T. Scadden, A. J. Fischman, J. W. Clark, D. P. Ryan, A. X.

Zhu, L. S. Blaszkowsky, P. C. Shellito, M. Mino-Kenudson and G. Y. Lauwers. Surrogate markers for antiangiogenic therapy and dose-limiting toxicities for bevacizumab with radiation and chemotherapy: continued experience of a phase I trial in rectal cancer patients. *J. Clin. Oncol.*, 23(31):8136–9, 2005. doi:10.1200/JCO.2005.02.5635.

[184] S. Wilson, M. Tod, A. Ouerdani, A. Emde, Y. Yarden, A. Adda Berkane, S. Kassour, M. Wei, G. Freyer, B. You, E. Grenier and B. Ribba. Modeling and predicting optimal treatment scheduling between the antiangiogenic drug sunitinib and irinotecan in preclinical settings. *CPT Pharmacometrics Syst. Pharmacol.*, 4(12):720–727, 2015. doi:10.1002/psp4.12045.

[185] F. Winkler, S. V. Kozin, R. T. Tong, S.-S. Chae, M. F. Booth, I. Garkavtsev, L. Xu, D. J. Hicklin, D. Fukumura, E. di Tomaso, L. L. Munn and R. K. Jain. Kinetics of vascular normalization by VEGFR2 blockade governs brain tumor response to radiation: role of oxygenation, angiopoietin-1, and matrix metalloproteinases. *Cancer Cell*, 6(6):553–63, 2004. doi:10.1016/j.ccr.2004.10.011.

[186] J. Xu, G. Vilanova and H. Gomez. Full-scale, three-dimensional simulation of early-stage tumor growth: The onset of malignancy. *Comput. Methods Appl. Mech. Eng.*, 2016. doi:10.1016/j.cma.2016.07.010.

[187] J. Yang, H. Tang, Y. Li, R. Zhong, T. Wang, S. Wong, G. Xiao and Y. Xie. DIGRE: Drug-Induced Genomic Residual Effect Model for Successful Prediction of Multidrug Effects. *CPT Pharmacometrics Syst. Pharmacol.*, 4(2):91–97, 2015. doi:10.1002/psp4.1.

[188] E. G. Zhang, S. K. Smith, P. N. Baker and D. S. Charnock-Jones. The regulation and localization of angiopoietin-1, -2, and their receptor Tie2 in normal and pathologic human placentae. *Mol. Med.*, 7(9):624–635, 2001.

[189] Q. Zhang, V. Bindokas, J. Shen, H. Fan, R. M. Hoffman and H. R. Xing. Time-course imaging of therapeutic functional tumor vascular normalization by antiangiogenic agents. *Mol. Cancer Ther.*, 10(7):1173–84, 2011. doi:10.1158/1535-7163.MCT-11-0008.

[190] W. Zhang and A. Edwards. Oxygen transport across vasa recta in the renal medulla. *Am. J. Physiol. Heart Circ. Physiol.*, 283(3):H1042–55, 2002. doi:10.1152/ajpheart.00074.2002.

[191] X. Zheng, G. Young Koh and T. Jackson. A continuous model of angiogenesis: Initiation, extension, and maturation of new blood vessels modulated by vascular endothelial growth factor, angiopoietins, platelet-derived growth factor-B, and pericytes. *Discret. Contin. Dyn. Syst. - Ser. B*, 18(4):1109–1154, 2013. doi:10.3934/dcdsb.2013.18.1109.